R-04-17

Respect distances

Rationale and means of computation

Raymond Munier, Svensk Kärnbränslehantering AB

Harald Hökmark, Clay Technology

December 2004

Svensk Kärnbränslehantering AB
Swedish Nuclear Fuel
and Waste Management Co
Box 5864
SE-102 40 Stockholm Sweden
Tel 08-459 84 00
+46 8 459 84 00
Fax 08-661 57 19
+46 8 661 57 19

ISSN 1402-3091
SKB Rapport R-04-17

Respect distances

Rationale and means of computation

Raymond Munier, Svensk Kärnbränslehantering AB

Harald Hökmark, Clay Technology

December 2004

Contents

1 Introduction

The Baltic shield is the westernmost sub-unit in a platform called the Fennosarmatian craton /Müller et al. 1992./ and borders the latter to the north on the Scandinavian Caledonides. Two other sub-units are contained in Fennosarmatia: the Russian Table and the Ukrainian Shield. The craton extends from the Tornquist line, a late Precambrian suture zone /Pegrum, 1984/, in the west, to the Ural Mountains in the east. To the south, the craton borders between the Northern Caucasus and the Southern Ural. The lithosphere of the craton varies in thickness between c 90 km in the south and east to more than 170 km in Scandinavia /Babuska et al. 1987/. The shield was eroded to a peneplain, about 600 million years ago, on which Paleozoic sedimentary rocks were deposited. Remnants of these rocks and of the exhumed peneplain surface show that, since the Precambrian era, tectonic activity has consisted of minor vertical movements /e.g. Tirén et al. 1987/, with displacements along widely spaced faults amounting to at most tens of meters. This fact, together with the infrequency and size of recorded contemporary earthquakes gives a strong presumption of adequate tectonic stability for hosting a repository in most of the country.

However, despite the present distance to plate boundaries, Swedish bedrock is only inactive to a first approximation. Cratons, such as the Fennosarmatian, are not tectonically dead as is often assumed. It has long been recognised that the Baltic shield sinks and rises in response to loading and removal of platform sediments and ice sheets. It has been shown that the rate of isostatic recovery after the last Quaternary ice cap melted, briefly exceeded the fastest subduction rates at plate margins /Mörner, 1979/. Vertical movements are now much slower but still in the order of cm per year. However, fault scarps, tens of m high and hundreds of km long in Lapland that are associated with tens of major landslides indicate large earthquakes only about 9,000 years ago /Lagerbäck, 1988; Muir Wood, 1993; Stanfors and Ericsson, 1993/. It has been suggested that these were triggered by deglaciation after a period of suppression of rock failure beneath a km-thick ice cap /Johnston, 1987; Talbot and Slunga, 1989/. Such young faults of such unexpected size challenge the view that the Baltic Shield has been, is, or will ever be tectonically dead. Current intraplate earthquakes in Sweden are small (< M 5) and relatively rare /e.g. Skordas, 1992; Skordas and Kulhánek, 1992; Wahlström and Grünthal, 2000a,b/. Since SKB's nationwide monitoring began in 2001, 6 events larger than M = 3 have been recorded with a record of M = 3.6 as the largest /e.g. Bödvarsson, 2004/. This can be interpreted such, that fault strength degraded with time, earthquakes became smaller and by now, small tectonic stresses, that are attributed to relative plate motions, are responsible for the minor earthquakes occurring /e.g. Skordas, 1992/.

Crustal deformation after the next glaciation is anticipated to predominantly exploit pre-existing deformation zones by jostling the intervening blocks. Though the evidence for reactivation of zones is overwhelming /see e.g. Larsson and Tullborg, 1993, for an exposé/ the possibility of creation of new glacio-isostatic faults in pristine rock can certainly not be excluded. However, despite some reports implying the contrary /e.g. Mörner, 1989/ none of the glacio-isostatic faults mapped in Sweden so far have been, upon closer investigations /e.g. SKB, 1990/, unequivocally shown to have been created in pristine rock.

Canisters with spent nuclear fuel can obviously not be located within deformation zones as this might jeopardise their long term mechanical stability and thereby constitute a potential hazard to the biosphere /e.g. Andersson et al. 2000/. Less apparent, but equally important, is the fact that earthquakes trigger reactivation, slip, of structures some distance from their hypocentres due to, among many other factors, stress redistribution. Fault slip across a

deposition hole might damage the isolation capacity of the canister and thereby jeopardise the overall integrity of the barrier system. Therefore, the following question might be posed: What is the distance from a deformation zone beyond which a canister can be safely emplaced? This respect distance cannot be readily computed because, unknown future events aside, there are some complicated aspects that need to be addressed e.g. degree of conservatism, scale, our ability to model ice sheets and earthquakes, etc.

In this report we discuss various aspects of the assignment of respect distances, propose a methodology for its assignment and apply the methodology to the Forsmark Site as a worked example. The report is organised as follows:

A definition of the term respect distance is presented in Chapter 2. We also present a brief summary of its use and definitions in previous SKB projects. The different approaches that have been used to address the computation of respect distances are summarised in Chapter 3. Some computation efforts have been reported to SKB as consultancy reports and not been previously published. These are included as appendices (Appendix 1a, 1b, 2a, 2b).

The definition of the width of deformation zones may steer how the notion of respect distance is perceived and used. We therefore discuss zone geometry, from a zone growth perspective, in Chapter 4.

SKB have earlier addressed respect distances from an empirical point of view, by compiling research on the damage on underground constructions due to earthquakes and adding some new findings. This work is briefly summarised in Chapter 5.

Many of the simplifications and assumptions used in modelling are conservative. Due to the potentially large impact on the repository layout, this aspect is discussed separately in Chapter 6 and the overall implications are discussed in the summary of this report, presented in Chapter 7. In Chapter 8 we apply the proposed methodology to the Forsmark site using real, but preliminary, data as a worked example.

Our main concern, in the context discussed in this report, is the postglacial faults anticipated to occur after the next glaciations. To properly address conservativeness, analysis of risk, and its implementation in safety analysis, we provide an extensive compilation of our current knowledge on postglacial faults as an appendix (Appendix 3).

2 Definition

The first attempt to define a the notion “respect distance” was made in the application for KBS-3 /KBS, 1983a,b,c,d,e/ in which the respect distance to “…zones with appreciably elevated permeability…” was set to 100 m and to “…zones with moderately elevated permeability …” was set to 25 m. No coupling to earthquakes was explicitly expressed though the mechanical instability from an engineering perspective was addressed.

A similar approach, though more thoroughly argued for, was presented in SKB 91 /SKB, 1992, and references therein/, also based on the hydraulic properties of the zones.

In the safety report SR-97 /SKB, 1999/ respect distances were set to 100 m from regional deformation zones and 50 m from major local deformation zones, respectively, based on reasoning of /Almén et al. 1996/ in which deformation zones were classified according to their expected function in a repository. The respect distances were used in a hypothetical repository layout /Munier et al. 1997/ which constituted one of many inputs to SR-97 /SKB, 1999/. The work of /Munier et al. 1997/ did, however, not elaborate on how the different aspects of respect distance should be computed and these were subjectively assigned values of 50 m (local deformation zones) and 100 m (regional deformation zones). Later work /La Pointe et al. 1997/ addressed the mechanical (tectonic) aspect by computing and applying seismic influence volumes to hypothetical repository layouts /La Pointe et al. 1999/.

The respect distance was originally intended to eventually include many aspects of potential importance including: Thermal-, hydraulic- and seismic influence. In addition, the broader definition also included the geometric uncertainty of deformation zones. Later work /Munier et al. 2003/ elaborated on geometric uncertainty of deformation zones but it was concluded that this aspect should not be included in the notion of respect distance; the two issues are judged to be entirely unrelated. However, uncertainty in e.g. position of a deformation zone will naturally be reflected in an uncertainty of the position of the respect volume.

The thermal aspects were partly addressed in /Hakami and Olofsson, 2002/ and we conclude that thermal aspects, though locally important, would not have any significant impact on respect distance to deformation zones.

Rapid changes of water pressures could potentially cause damage to the repository should the buffer liquefy. The liquefaction of the buffer turns the material from a solid state into a liquid state that could create a risk that the canisters tilt or sink. SKB has in a previous report /Pusch, 2000/ treated this issue with the conclusion that the necessary prerequisite for liquefaction of buffer does exist, but that the density of buffer and stress conditions practically eliminates the risk for liquefaction, assuming earthquakes up to magnitude 7–8 with normal duration time. Further, the SKB design with saturated buffer density, ≈ 2,000 kg/m^3, well exceeds the critical density (1,700–1,800 kg/m^3). Similarly, /JNC, 2000a,b/ studied seismic stability of the engineered barriers during an earthquake. Engineering-scale models (scales 1:10 and 1:5) of the canister and buffer were shaken according to a well-defined earthquake spectrum to verify and validate advanced numerical values. In a numerical model accounting for pore water pressure in the buffer, no rise of pore water pressure in the buffer material could be demonstrated, and the possibility of liquefaction in the buffer was considered remote.

From a nuclide transport point of view, it is desirable to obtain a transport resistance, $F > 10^4$years/m, along the path from a canister to the biosphere. This resistance could be expressed as a "functional distance" to a hydraulically active deformation zone and could as such form a component of the respect distance. However, our studies so far /Andersson et al. 2002a,b; Poteri et al. 2002; Winberg et al. 2003/ have indicated that this distance is probably smaller than the seismic influence.

Unless ongoing research demonstrates other wise, it appears that the seismic influence on canister integrity overshadows the mechanical, thermal and hydraulic aspects discussed above. The notion of respect distance can therefore be said to reflect our desire to avoid mechanical damage of the canister, should future, presumably postglacial, earthquakes of significance occur near or within the repository.

Based on the reasoning above, respect distance is here therefore defined as follows:

"The respect distance is the perpendicular distance from a deformation zone that defines the volume within which deposition of canisters is prohibited, due to anticipitated, future seismic effects on canister integrity".

3 Computation of respect distances

3.1 Statement of the problem

3.1.1 General

For calculation of the risk of earthquake–induced canister damage, the following question is relevant:

- If a potential repository site is located at a given distance from a fault that is large enough to create an earthquake of a given magnitude M, what is the maximum size of repository host rock fractures that can be allowed to intersect deposition holes?

If it is necessary due to layout considerations that a given maximum fracture size must be allowed, then the question should be:

- What is the minimum acceptable distance between the intersecting fracture and a fault, large enough to create an earthquake of magnitude M?

This minimum distance between an earthquake fault and the repository is, using SKB nomenclature, referred to as “respect distance”. The respect distance can have a fixed value, for a given size of a fault, but only if coupled to the maximum acceptable size of fracture intersecting a canister position.

For numerical studies, the problem must be reduced, for instance as follows:

- If an earthquake of given magnitude, M, occurs at a given distance from a fracture of given extension, what is the maximum induced displacement on that fracture?

To arrive at respect distance estimates, it is necessary to perform many analyses of the above kind. There are many aspects to be considered and the scope of possible parameter variation is large. In the following, the fractures in the host rock are called “target fractures”. The following parameters have been identified as relevant:

- Earthquake magnitude.
- Earthquake fault geometry (strike, dip, position and dimensions of the rupture zone).
- Source mechanism (average displacement of the rupture area, stress drop, rupture speed, mode of slip).
- Orientation of the target fracture (dip and strike).
- Position of the target fracture (distance from edge of rupture area, distance from epicentre).
- Mechanical properties of the target fracture (shear strength parameters).
- Size of the target fracture.
- Mechanical properties of the of the host rock (elastic parameters and viscous damping parameters).
- Host rock initial stresses.
- Maximal allowable displacement that the canister-bentonite system can accommodate.

3.1.2 Parameter overview

General

Due to the requirement of conservativeness, and with regards to the geological context, the number of possible parameters that need to be varied can be significantly reduced. In some cases the range of parameter values can also be reduced. Some parameters such as magnitude, fault dimension and fault average displacement are correlated.

Canister failure criterion

The buffer material in a deposition hole acts as a damper between the canister and the rock, and may substantially reduce the effect of shearing across the deposition hole.

A number of numeric and analogue models and tests have been performed to assess how much mechanical damage the canister/bentonite system can withstand yet maintaining its isolating capabilities /Börgesson, 1986; Takase et al. 1998; Werme and Sellin, 2001,2003/. Based on these investigations SKB used a failure criterion of 0.1 m shear deformation across the canister in the safety report SR-97 and subsequent modelling efforts.

Recently, a series of laboratory tests was performed with shearing of water saturated bentonite samples at different densities and shear rates to investigate the stiffness and shear strength of the buffer material /Börgesson et al. 2004/. From those tests a material model of the buffer, that takes into account the density and shear rate, was formulated using shear rates up to 6 m/s. Shearing across the deposition hole was then modelled using 3D finite element calculations with the code ABAQUS. In this work, shearing was modelled to take place perpendicular to the canister axis in either the centre of the deposition hole or at the quarter point. Using four buffer densities between 1,950 and 2,100 kg/m^3 at water saturation and shear rates between 0.0001 and 1,000 mm/s, the shear calculations were driven to a total of 20 cm of shear without reaching the breaking threshold of the canister. The results of /Börgesson et al. 2004/ also show that the influence of the buffer density and the location of the shear plane is very strong but also that the shear rate and magnitude of the shear displacement have a significant effect. The results of this work indicate that the previously used failure criterion of 0.1 m of shear might be conservative. For practical purposes, however, mainly to ensure compatibility between various models, we still use the criterion 0.1 m shear displacement across the canister position.

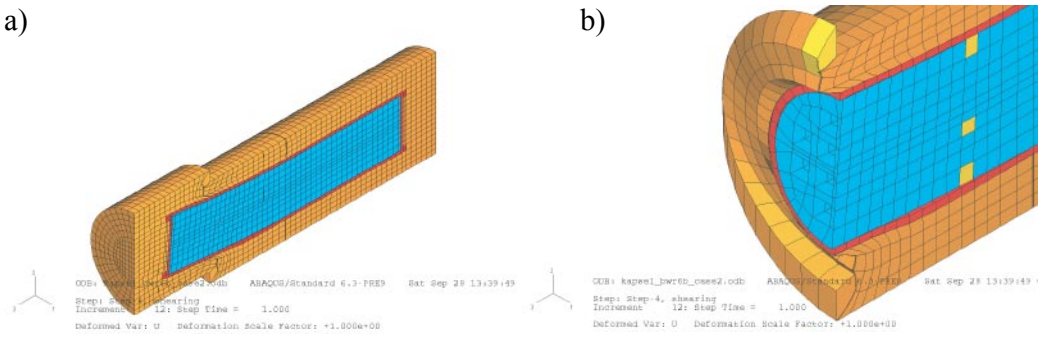

Figure 3-1. *Deformed structure after 20 cm rock displacement (a) and a detail cut at the shear plane (b). The three elements in the cast iron insert that are studied in more detail are marked yellow. /From Figure 5-1 in Börgesson et al. 2004/.*

Earthquake magnitude and fault dimensions

The moment magnitude M is given by /Thatcher and Hanks, 1973/:

$$M = \frac{2}{3}\log_{10}\left(M_0\right) - 6.07 \qquad \text{Equation 3-1}$$

where M_0 (SI units) is the seismic moment given by:

$$M_0 = G \cdot d \cdot A \qquad \text{Equation 3-2}$$

This is the definition of the moment magnitude, which approximates other magnitude measures, for instance the Richter magnitude, reasonably well. Here, G (Pa) is the rock mass elastic shear modulus, d (m) is the mean relative displacement of the fault surfaces and A (m^2) is the rupture area.

A large average displacement on a small rupture area can produce the same seismic moment as a small displacement on a large rupture area, but average displacements can not be arbitrarily large: regression relations can be found between moment magnitude, average slip and rupture area /see e.g. La Pointe et al. 1999, for a compilation/. Large displacements on small rupture areas create larger stress drops, more effects on the surrounding rock and are more representative of intraplate events /Scholz, 1990/. Therefore, to analyze effects of an event of a given magnitude it is expedient and conservative to look at the maximum fault displacement that is consistent with that magnitude according to the regression relations, and to a prescribe the rupture area accordingly.

According to published relations between earthquake magnitude and displacement /e.g. Wells and Coppersmith, 1994/, the displacement on the primary fault does not exceed the threshold value 0.1 m for earthquakes of magnitude 5 and smaller. That is, no canisters would be damaged, even if the earthquake originated on a fault intersecting one or many deposition holes. Analysis of small earthquakes is therefore not meaningful.

Earthquake fault orientation

We anticipate that the main hazard stems from post glacial earthquakes. We therefore find it necessary to mimic the geometry of known post glacial faults (see Appendix 3 for an exposé). The predominant strike of mapped postglacial faults are perpendicular to the orientation of the major (tectonically accumulated) horizontal stress. This is consistent with dip-slip motions on steeply dipping faults. In our models we therefore orient the earthquake–generating faults accordingly.

Earthquake source mechanism

The default schematic mechanism is that the rupture originates from a hypocenter in the central part of the rupture area and then propagates towards the boundaries of that area with a speed that is a fraction, about 70%, of the shear wave velocity /Scholz, 1990/. Although there may be variations, there does not seem to be any reasons for assuming differently.

Target fracture orientation

The orientation of the target fracture is a key parameter that needs to be varied.

Target fracture position

The distance between target fracture and the rupture area is a key parameter and needs to be varied systematically.

Target fracture mechanical properties

The most conservative assumption is that of frictionless fractures. If this assumption gives too large respect distances, then more realistic, but still conservative, assumptions must be tried, e.g. Mohr Coulomb fractures with moderate friction angles. However, it is probably sufficient to examine the role of friction for a few reference cases. If the reduction of target fracture displacement is found to be considerable and systematic because of friction, then the zero friction results can be downscaled schematically.

Target fracture size

The size of the target fracture can be fixed to a reference value that is reasonably relevant to the problem. Looking at very large target fractures is not meaningful, because such fractures, or more properly, fracture zones, would not be allowed to intersect deposition holes for other reasons. Here, target fractures of 100 m radius are used as reference. Within reasonable size ranges, induced displacements are proportional to fracture size, so results can be up-scaled or down-scaled as needed.

Target fracture shape

In all simulation, target fractures are perfectly planar discs or rectangles.

Host rock properties

The most conservative and reasonable approach is to assume the host rock to be linearly elastic.

Host rock stresses

In a postglacial type stress state, the major horizontal stress is generally assumed to be large compared to present day conditions: The ice increases the vertical stresses by an amount that corresponds to the weight of the ice cover and the horizontal stress by a fraction (given by Poisson's ratio) of that vertical stress increase. However, the ice-load will slowly bend the crust, and this will increase the horizontal stresses further. The rate and scope of that deformation is controlled by the interaction between the elastic/brittle crust and the viscous mantle. Tectonic strain may also contribute to the slow increase in horizontal stresses under the ice cover.

When the stabilizing ice cover disappears at the end of the glacial cycle, the vertical stress will decrease at the same rate and soon correspond to the rock overburden only, while the horizontal stresses will remain high. If the duration of the glacial load is long, the horizontal stress excess may create potential instability of fault zones, in particular of zones striking normal to the major stress. Therefore, for post-glacial faulting, a relevant stress field is one with low vertical stress but high horizontal stress in the fault dip direction.

3.1.3 Problem statement summary

Figure 3-2 shows the problem, schematically idealized and structured for numerical simulation studies.

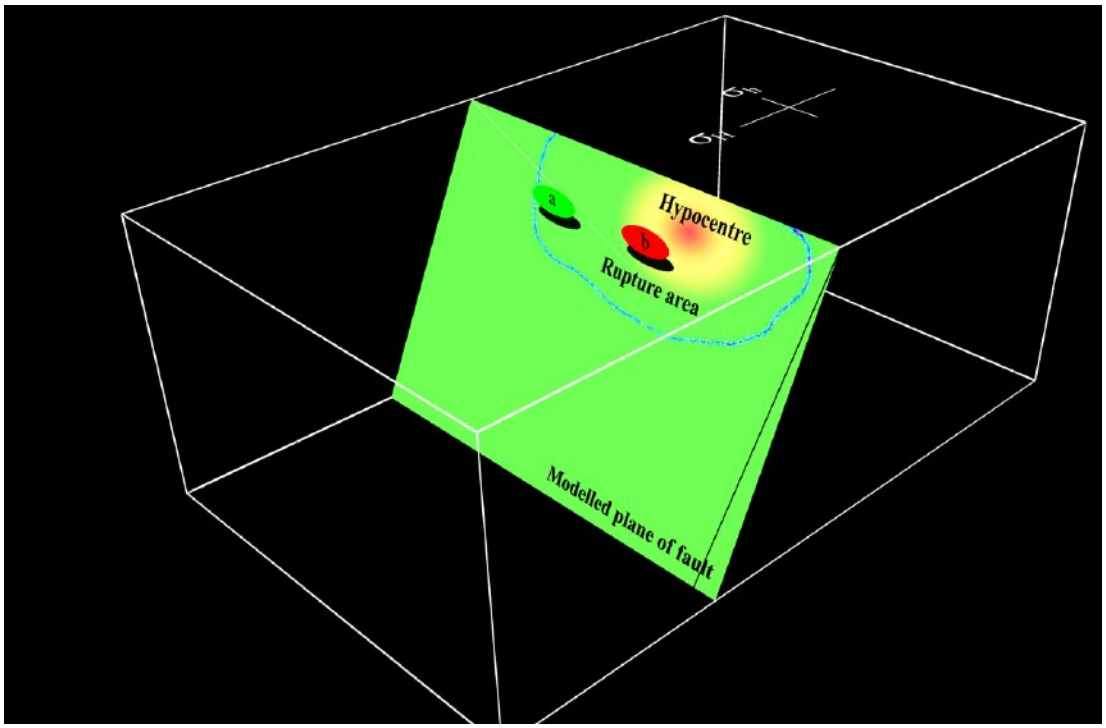

Figure 3-2. *Schematic cartoon of the numerical problem addressed here, which is to find the maximum induced displacement on a 100 m radius target fractures located at different distances from an earthquake that can be of different magnitude and originate at rupture areas of different size and shape. The primary fault movement is assumed to be dip-slip along steeply dipping fault planes that are potentially unstable because of the high horizontal stress in the fault dip direction. Target fractures may be located close to the edge of the rupture area (a) or close to the hypocentre (b).*

3.1.4 Modelling approaches

The seismic respect distance problem can be analysed using many different approaches, with different degrees of idealisation or simplification. Table 3-1 shows an overview of the modelling work that has been performed up to the present day (December 2004). These modelling efforts have yielded results of the types summarised in Table 3-2.

Table 3-1. Overview of modelling approach.

Representation of earthquake		Effects analysed		
		Static effects only	Dynamic effects only	Both static and dynamic effects
Enforcing movement on primary fault. The magnitude is determined by setting the rupture area and the average displacement at relevant values. (Primary fault movement is unrelated to the initial stresses, although the initial stresses will contribute to control the response of target fractures with non-zero friction).	Schematic, instantaneous.	Poly3D analyses reported and used as main background material in SR-97.		
	With rupture control to mimic typical source mechanism.		Step 1 FLAC3D analyses, (Appendix 1a). Step 2 FLAC3D analyses, (Appendix 2a). Both steps performed using Wave results (Appendix 1b) to define dynamic boundary conditions.	Wave analyses (Appendix 2b)
Letting movement on primary fault occur as result of stresses and primary fault properties. (To obtain a given magnitude, it is necessary to calibrate stress field and primary fault properties).	With rupture control to mimic typical source mechanism.			Step 3 FLAC3D analyses (this report)

Table 3-2. Summary of different sets of results.

Code/ study	Type of result	Event	Target fracture	Main limitations of code/study	Description
Poly3D	Induced displacement on target fractures	All types of events	All sizes, all orientations. frictionless	Dynamic effects not considered. Statistical approach makes direct derivation of respect distances difficult. No account of initial stress field	SKB reports TR-97-07 TR 99-03
FLAC3D step 1	Induced displacement on target fractures.	M = 6, Dip-slip on vertical fault	100 m radius, frictionless	Static effects not considered. Oscillations approximated by plane wave. No account of initial stress field	Appendix 1a (this report)
FLAC3D step 2	Induced displacement on target fractures	M = 6, Dip-slip on vertical fault	100 m radius, friction 15° friction 30°	Static effects not considered. Oscillations approximated by plane wave. No relevant account of initial stress field.	Appendix 2a (this report)
Wave step 1	Velocity records to be used as boundary conditions in FLAC3D models	M = 6, Dip-slip on vertical fault	No target	Faults must be either vertical or horizontal. No relevant account of initial stress field.	Appendix 1b (this report)
Wave step 2	Induced displacements on 200 m fractures	M = 6, Dip-slip on vertical fault	100 m radius, frictionless, friction 15°, friction 30°	Faults can only be either vertical or horizontal. Target fractures must be either horizontal or vertical. No relevant account of initial stress field.	Appendix 2b (this report)

Code/ study	Type of result	Event	Target fracture	Main limitations of code/study	Description
FLAC3D step 3	Induced displacements on 200 m fractures	M = 6, Dip-slip on 70 degr dipping fault	100 m radius, frictionless, friction 15°	Preliminary study with few results.	this report

3.2 Evaluation of static analysis results used in SR97

The earthquake scenario risk analysis in the SR 97 safety report is based upon a static method of calculating secondary (induced) displacement on target fractures. The numerical tool used to calculate the displacement is a Displacement Discontinuity code called Poly3D /Thomas, 1993/.

In the Poly3D analyses, an earthquake is represented in the following way:

- The bedrock is represented by a stress-free, linearly elastic, semi-infinite (or infinite) half space with prescribed values of E and ν (Modulus of elasticity and Poisson's ratio).
- A shear displacement is enforced on a rectangular discontinuity which represents the fault on which the seismic event originates. The area of the discontinuity is the earthquake rupture area.
- The movement creates stresses in the initially stress-free medium. These stresses cause secondary displacements on target fractures, which are located in the rock volume hosting the repository.

A schematic simulation setup is illustrated in Figure 3-3: A strike-slip earthquake of magnitude 6.1 occurred at a horizontal distance of 2 km from the edge of a box-shaped repository with a fracture population derived from statistical fracture network models.

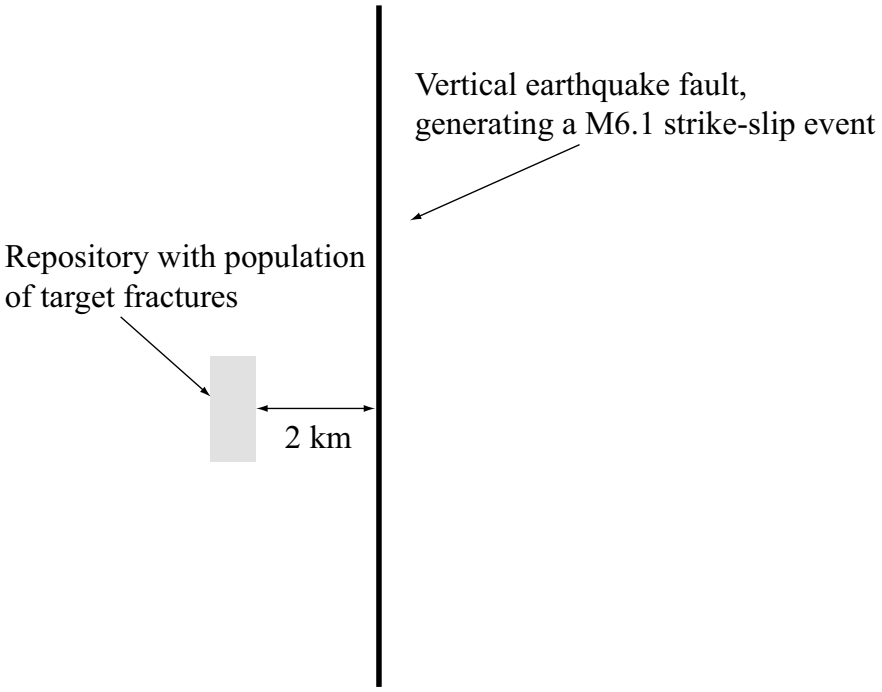

Figure 3-3. *Schematic plan view of repository volume and earthquake fault.*

The target fractures were planar, circular and with varying radii. Figure 3-4 shows the result of the simulations. The plot symbols represent the maximum induced shear displacement (at the centre of the circular fractures) of the individual target fractures. The figure confirms that there is a relation between fracture size and possible displacement. The spread, obvious in the figure, can be attributed to the following:

- Target fractures are not at the same distance from the earthquake. Some are close to the repository edge at 2 km distance, while others are close to the opposite edge at 2.4 km distance.
- Target fractures have different dip and strike. The stresses generated in the elastic medium give different shear normal loads on differently oriented fractures even if they are at the same distance from the earthquake.

The largest displacement shown in Figure 3-4 is about 2.2 mm and occurs for a fracture of 40 m radius. The largest fracture did not move more than 2.1 mm. However, since there is very strong coupling between the size and maximum displacement, 2.2 mm is not the maximum possible displacement on this modelling setup; Had the largest fracture been located and oriented as the 40 m fracture, or as the fractures giving the largest displacement per unit fracture radius (worst case size-/displacement relation) then the displacement of that fracture would have been much larger. This reasoning is illustrated in Figure 3-5 which can be used to estimate the slope of such a worst case relation; The figure shows an estimate of the relation and the corresponding potential maximum displacement of a 100 m radius fracture.

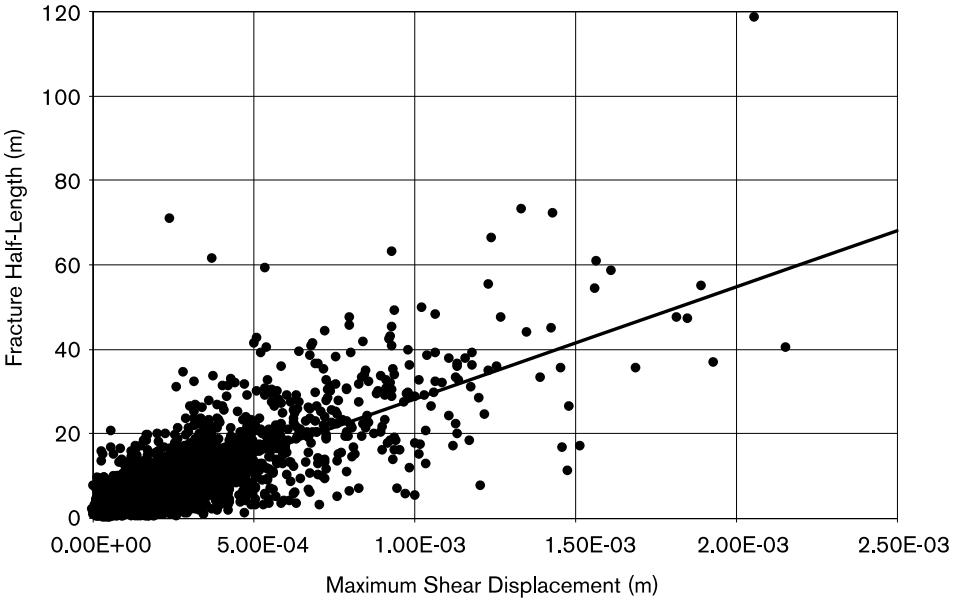

Figure 3-4. *Induced shear displacements in population of target fractures within box-shaped rock volume at 2 km distance from a fault generating a M6.1 earthquake /from La Pointe et al. 1997/.*

The maximum displacement value suggested in Figure 3-5 for a 100 m radius fracture, at 2 km horizontal distance from the earthquake fault, 12.5 mm, is an upper bound estimate for the assumed source mechanism. It should be noted, however, that the probability of simulating a fracture that is both large, and suitably oriented is quite small, especially in the light of the commonly used powerlaw size distribution.

Additionally, the maximum displacement for a 100 m radius fracture at 2 km distance found above (12.5 mm) must not necessarily be the absolute maximum due to the following: An earthquake of a given magnitude can be generated in many different ways; a small average dislocation on a large rupture area and large average dislocation on a small rupture area, for instance, can generate the same seismic moment. Figure 3-6 shows the result of representing a M6 earthquake in ten different stochastically selected ways and applying the resulting stress change to a fracture population, similar to the one shown in Figure 3-4. For the 2 km distance the maximum value is about 2.8 mm. Here, it is not clear what the size of the particular target fracture was that moved 2.8 mm, and there is no way of establishing a "worst case size/displacement relation". It is therefore not possible to infer from the results shown in Figure 3-6 if the maximum possible displacement of a 100 m radius fracture, located at 2 km from the centre of magnitude 6 earthquake as shown in Figure 3-3, is larger than the value of 12.5 mm suggested in Figure 3-5.

In summary, The Poly3D study suggests that an earthquake of moment magnitude 6 induces a maximum static displacement of about 15 mm on frictionless fractures of 100 m radius at an epicentre distance of 2 km.

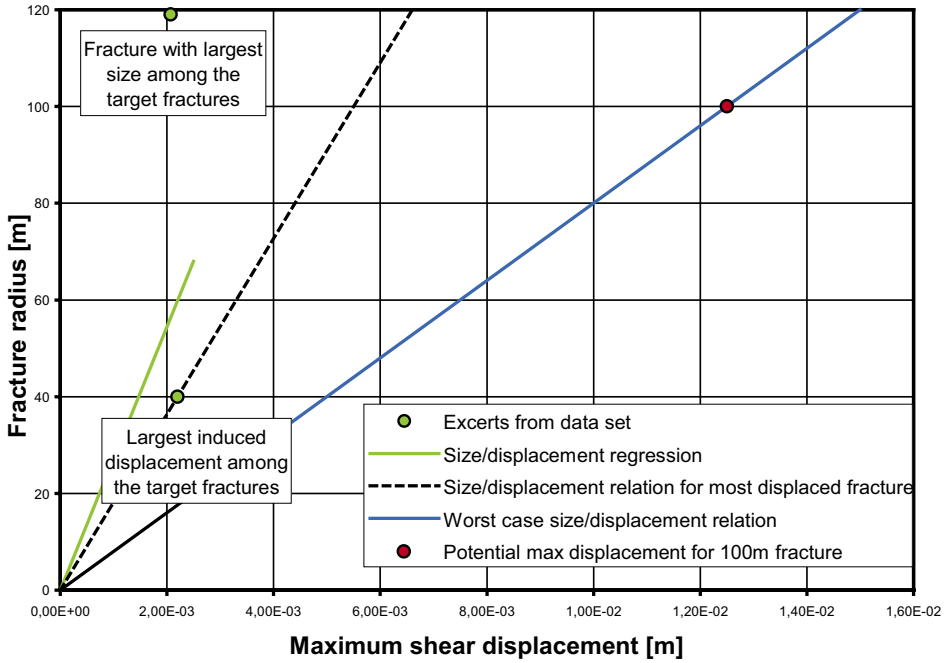

Figure 3-5. *Maximum possible displacement of a fracture with a 100 m radius. Worst case size/displacement relation is assumed to apply for fractures at closest possible distance from the earthquake fault (i.e. 2 km). See also Figure 3-4.*

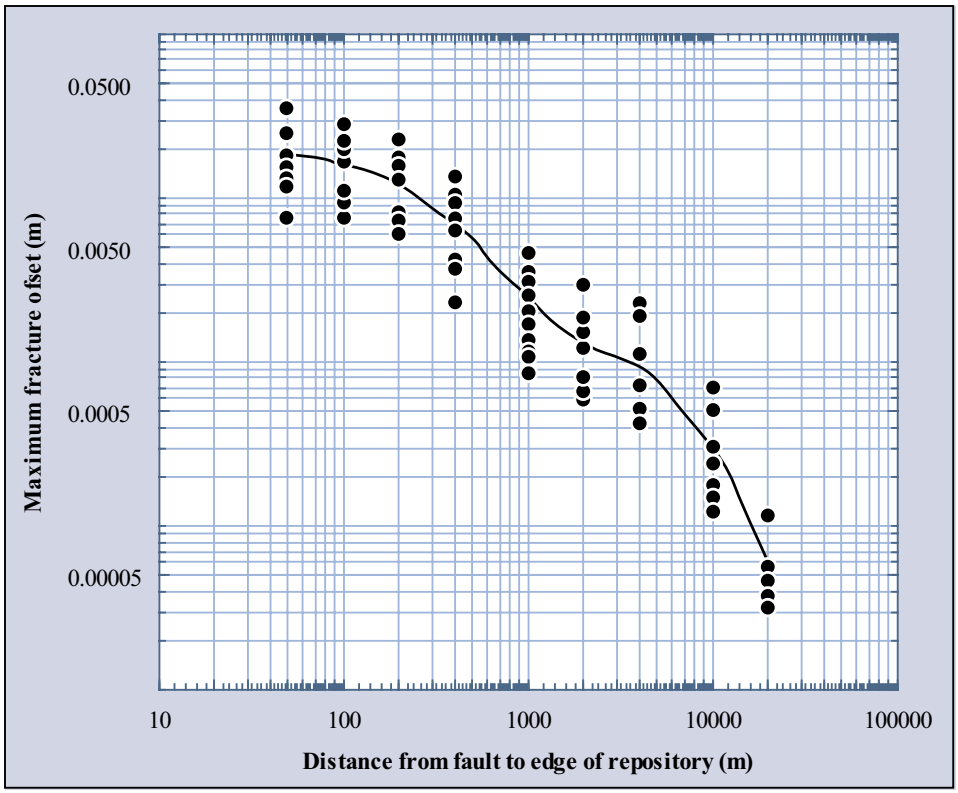

Figure 3-6. *Maximum induced displacement in a statistical fracture population for ten different Monte Carlo simulations of a Magnitude 6 earthquake. At a distance of 2 km, the maximum induced displacement is about 2.28 mm.*

3.3 Results from dynamic calculations

3.3.1 General

Results from three modelling approaches are presented here:

- FLAC3D step 1 and step 2 results with dynamic boundary conditions generated with the WAVE code. Step 1 includes only friction-free fractures.
- WAVE results.
- FLAC3D step 3 results.

3.3.2 FLAC3D – step 1 and step 2

All results were generated for the reference case, i.e. target fracture size of 100 m radius and earthquakes of moment magnitude 6. The experiment setup is summarised in Table 3-3.

Table 3-3. Summary of assumptions and parameters used in FLAC3D models.

FLAC3D parameters	
Target fracture strength	• Zero friction • 15 degrees of friction • 30 degrees of friction
Target fracture orientation	• Horizontal • Dipping 45 degrees in fault strike direction • Dipping 45 degrees normal to fault strike
Initial stress state	Stress state 1 • σ_1 = 35 MPa (horizontal and normal to fault strike) • σ_2= 20 MPa (horizontal and parallel with fault strike) • σ_3 =13 MPa (vertical) Stress state 2 • σ_1 = 55 MPa (horizontal and normal to fault strike) • σ_2= 20 MPa (horizontal and parallel with fault strike) • σ_3 =7 MPa (vertical)
WAVE parameters	
Source – target distance	2 km, 6 km and 10 km
Rupture area	Rectangular 8.6 km by 4 km, with upper boundary 1 km below ground surface
Source mechanism	Dip-slip on vertical fault
Rupture control	Rupture propagates across the plane of fault with a prescribed rupture velocity

Full descriptions of the modelling results are given in Appendices 1a and 2a. The FLAC3D models did not include the primary fault, just a rock volume around the target fracture.

The following procedure was used:

- Velocity records were generated using the WAVE code (Appendix 1b). Velocity records were determined for all source to target distances above.
- The velocity records were translated into stress history boundary conditions of a FLAC3D model. The FLAC3D model was analysed using these boundary conditions, and the response of the target fracture was recorded (Appendix 1a; Appendix 2a).

To generate the velocity records, a number of different parameter settings (rupture area, mode of slip, etc) were tried, all producing the intended Magnitude 6 event. The velocity records with the highest amplitudes were then used in the FLAC3D models. These records correspond to a dip-slip event on an 8 km by 4.6 km rupture area.

The high amplitude velocity records were translated into stress boundary conditions, applied to the base of the FLAC3D models, such that all base points moved together and in phase. However, the use of WAVE/FLAC3D has limitations:

- The plane wave approximation is valid for large source to target distances. Here, that distance is on the same order of magnitude as the size of the rupture.
- The method cannot capture the static effects of an earthquake, i.e. the permanent change of the stress state at the location of the target fracture that follows from the forced displacement of the primary fault.
- The WAVE code can generate seismic input from faults that are either vertical or horizontal, not from arbitrarily dipping faults.

Figure 3-7 shows examples of results. The maximum shear displacement occurs for the friction-free horizontal fracture and amounts to less than 6mm. The effect of a 15 degree friction angle is very significant. For stress state 1, the 13 MPa vertical stress (acting normally on the target fracture) was sufficient to completely prevent slip. The oscillations are purely elastic. For stress state 2, the initial vertical stress was much smaller, and the target fracture slipped about 1mm.

Figure 3-8 shows corresponding results for the 6 km source to target distance. For the friction models, no slip occurred for any of the stress states.

Figure 3-9 shows a summary of the results for the horizontal target fracture and for one of the inclined fracture cases. The following observations can be made:

Displacements were small for all analysed cases. The maximum displacement amounted to about 6 mm on the horizontal target fracture and about 2.8 mm on the inclined target fracture, both at a distance of 2 km from the fault. The inclusion of friction dramatically decreases displacement to less than one mm.

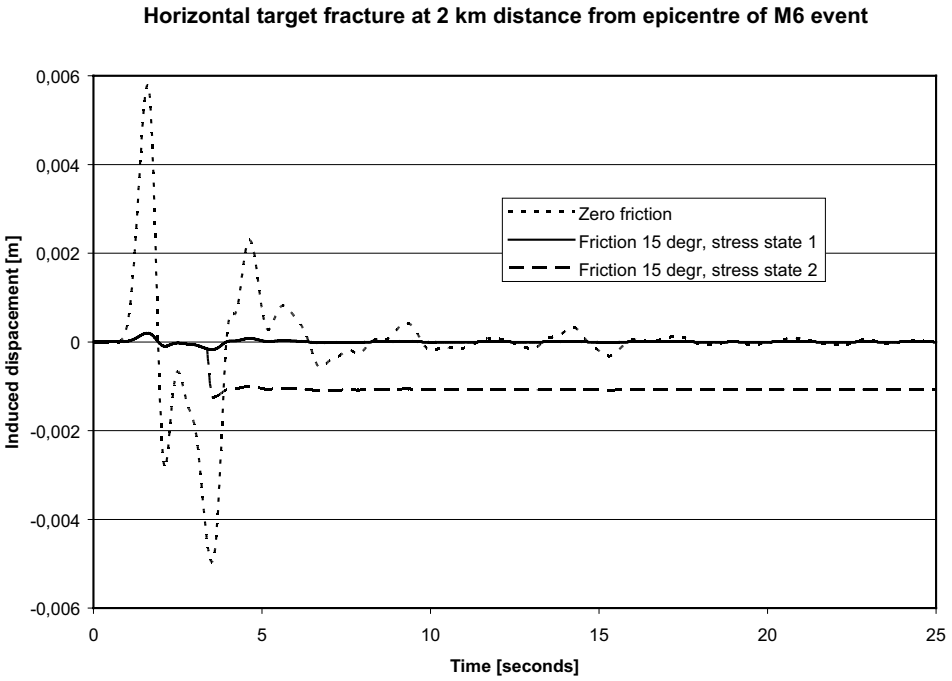

Figure 3-7. *Displacement induced by magnitude 6 event at 2 km distance.*

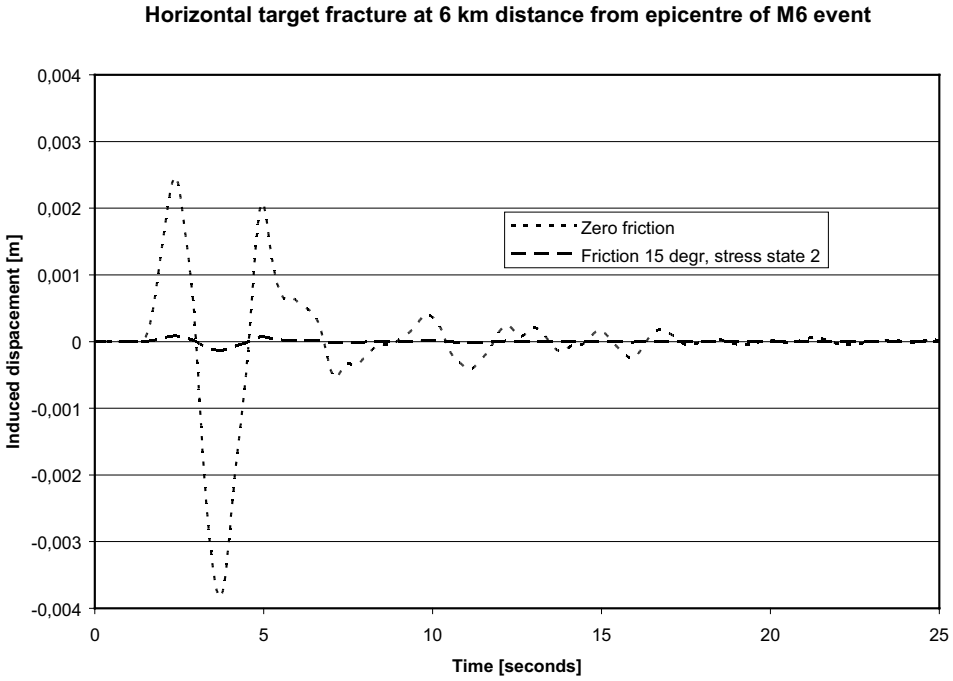

Figure 3-8. *Displacement induced by magnitude 6 event at 6 km distance*

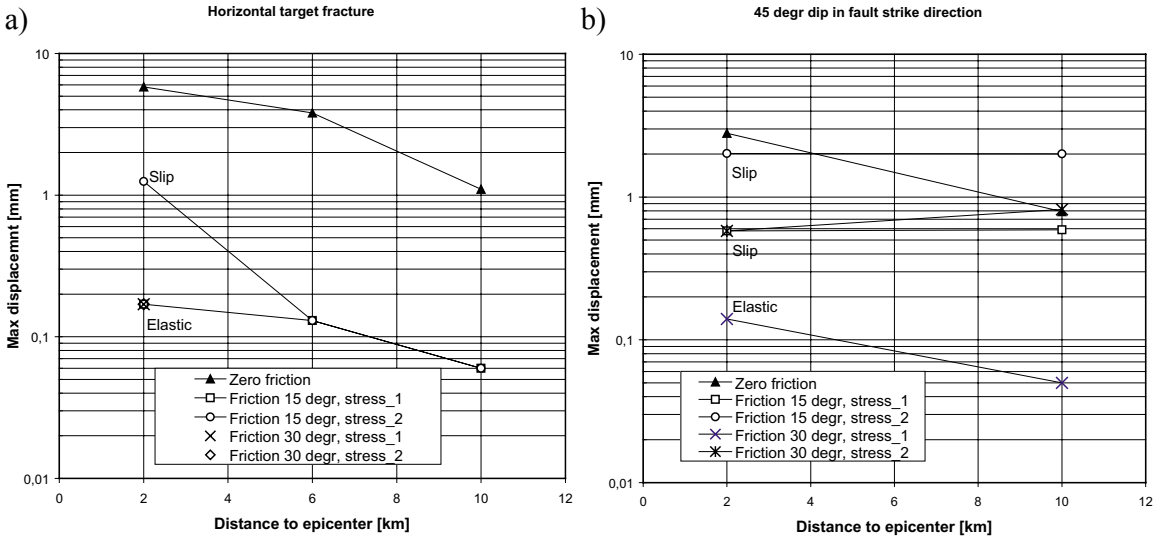

Figure 3-9. *a) Maximum displacement for the horizontal target fracture. b) Maximum displacement for one of the cases with inclined target fractures.*

3.3.3 Wave

In the previous section we described how the WAVE code was used to generate velocity records that were used as seismic input to FLAC3D models. The effects on the target fracture were then analysed in the FLAC3D model using the FLAC3D logic for representation of fractures. Target fractures can also be included directly in WAVE models such that the WAVE code itself is used to calculate induced displacements. There are two advantages of this approach in comparison to the approach described above:

- Since there is no implicit plane wave assumption, the source to target distance can be arbitrarily small.
- Static effects are automatically included.

There is one major disadvantage:

- The target fracture and the fault must be aligned with the same Cartesian grid. This means that target fractures must be perpendicular to the primary fault and either horizontal or vertical.

A number of analyses of induced displacement on 100 m radius fractures are described in Appendix 2b. Two geometries were considered as shown in Figure 3-10. Figure 3-11 and Figure 3-12 show maximum shear displacements and maximum shear velocities, respectively, for some of the WAVE analyses.

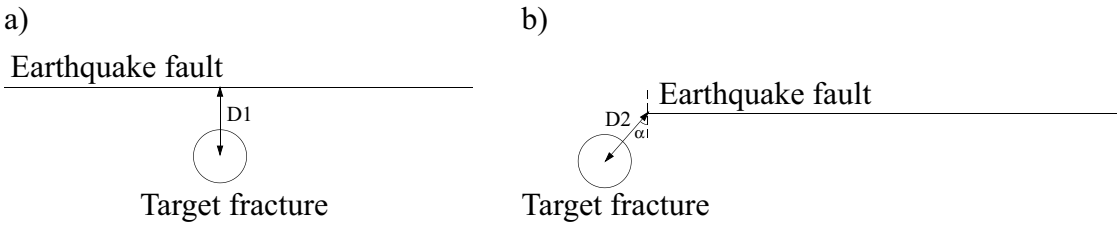

Figure 3-10. *a) Model geometry 1: Source to target distance D1 was varied between 200 m and 7,000 m. b) Model geometry 2. Two values of D2 were considered: 200 m and 800 m. Azimuth from fault tip was varied between 0 and 90 degrees.*

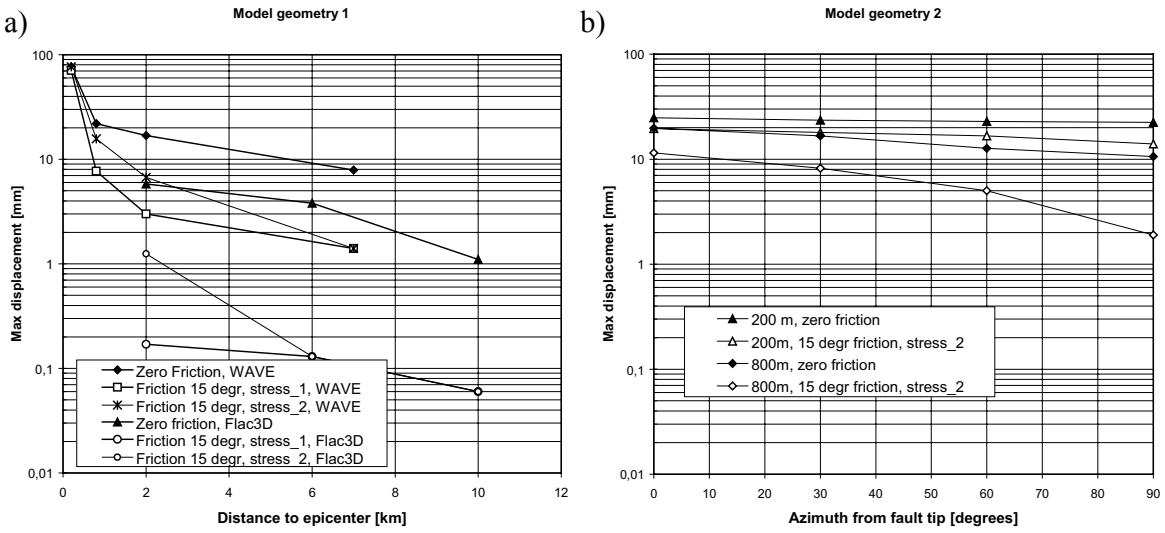

Figure 3-11. *a) Results from WAVE analyses, model geometry 1. Corresponding FLAC3D results are included for comparison. b) Results from WAVE analyses, model geometry 2.*

Figure 3-11 illustrates the importance of target fracture friction. For all cases except for the smallest distance (200 m), the 15 degree friction angle reduced the maximum displacement by at least 50% compared to the zero friction case. In most cases, the effects of friction were much larger.

The shear velocity results shown in Figure 3-12 are relevant to the question of the canister failure criterion. The mechanical properties of the bentonite buffer are strain rate dependant, which means that loads that are transferred to the canister as a result of fracture shear displacements will be different for different shear velocities. A high velocity gives high bentonite stiffness and more canister deformations than a low shear velocity. This means that modelling work aimed at revising the canister criterion that is now being applied (0.1 m displacement counts as canister failure) should be based on realistic upper bound estimates of the fracture shear velocity. For the models analysed here no velocities exceeded 0.08 m/s.

In Figure 3-11 and Figure 3-12 only maximum displacements and maximum shear velocities are shown. Figure 3-13 shows the target fracture displacement in more detail as function of time for the zero friction case, model geometry 1. Figure 3-14 shows corresponding shear velocities. The results shown in Figure 3-13 and Figure 3-14 are selected examples. A full result description is found in Appendix 2b.

A general observation of the WAVE results shown in Figure 3-13 is that the residual displacement is approximately equal to the maximum displacement. This shows that the effects of the permanent change of the static stress field are more important than the oscillating load. This is an important finding, because it seems to support the relevance of the approach used in previous work, i.e. to base estimates of target fracture displacements on results obtained from static analyses /La Pointe et al. 1997; La Pointe et al. 1999/.

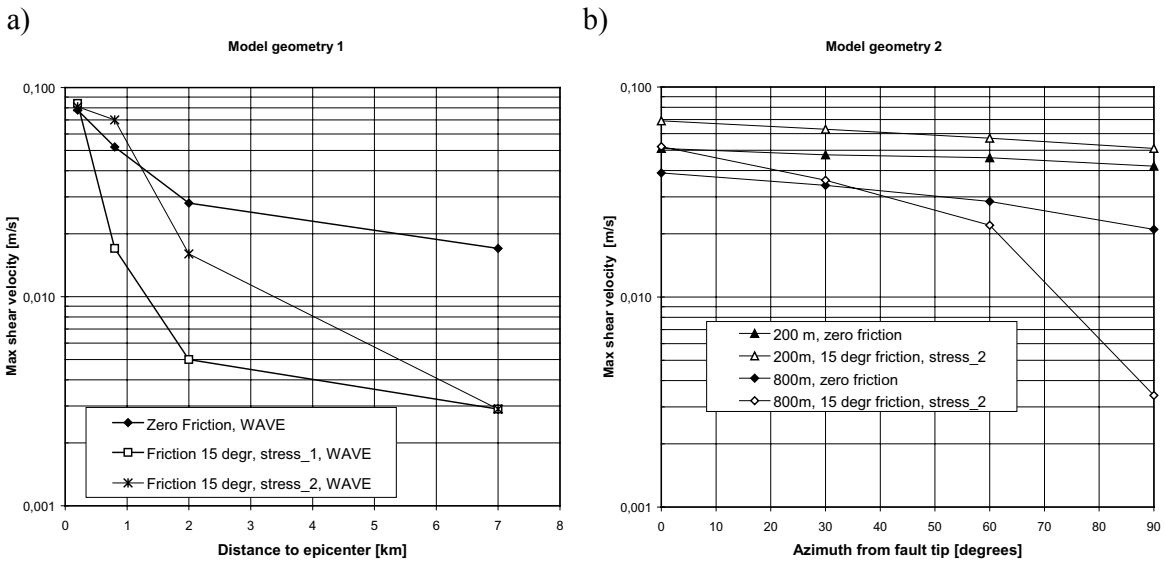

Figure 3-12. *a) Results from WAVE analyses, model geometry 1. b) Results from WAVE analyses, model geometry 2.*

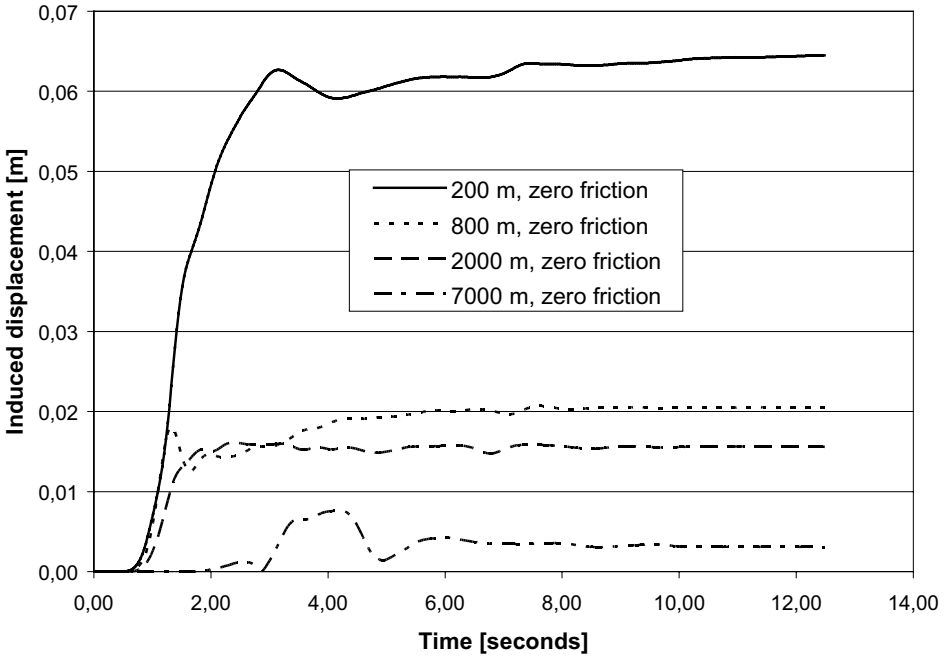

Figure 3-13. *Induced target fracture shear displacements as function of time for different source to target assumptions.*

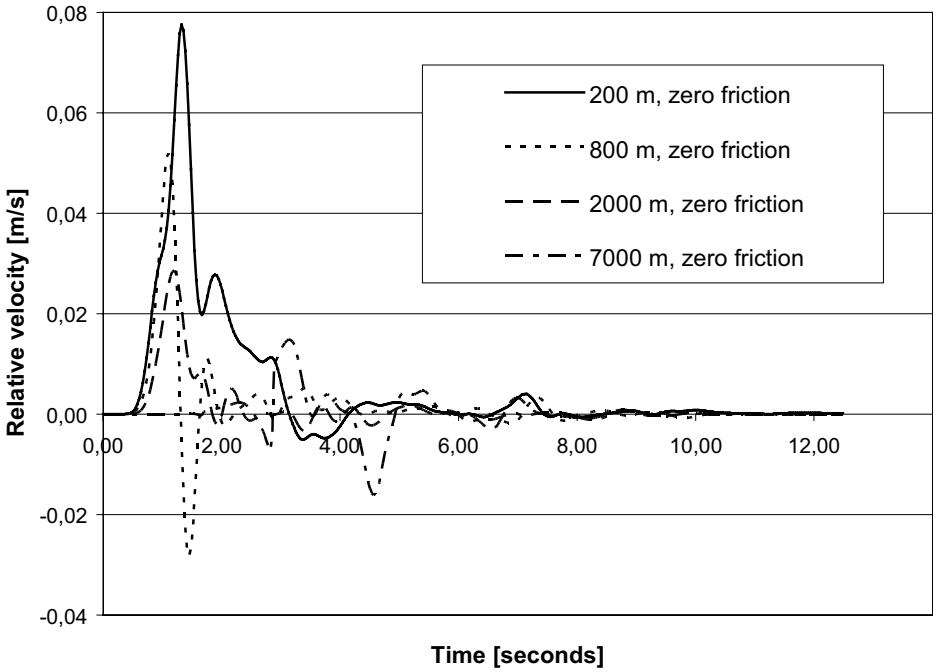

Figure 3-14. *Shear velocities.*

Figure 3-15 illustrates how the oscillating component is singled out in the FLAC3D solution, while the WAVE solution includes the static as well as the oscillating component. The two solutions are based on the same source mechanism. The diagram shows, in a lucid way, that the static component overshadows the oscillating component at small distances. It is also interesting to note that the maximum displacement, 15 mm, is in agreement with the estimate derived from the Poly3D results (cf Chapter 3.2). A brief summary of maximum displacements is given in Table 3-4.

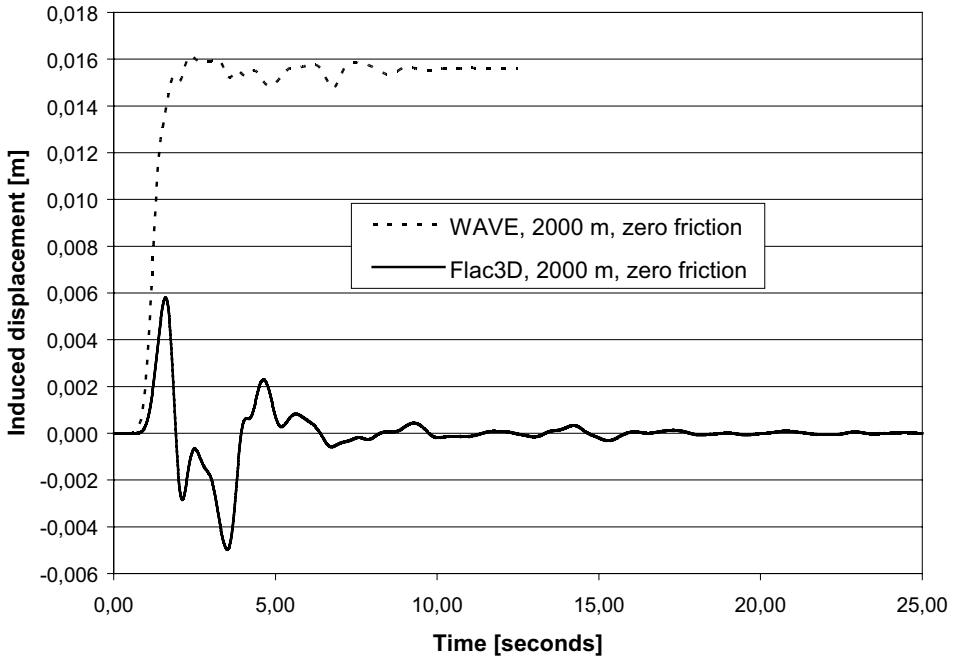

Figure 3-15. *Comparison between FLAC3D and WAVE results.*

Table 3-4. Summary of maximum displacements.

Dip angle	10 km	2 km	Dip direction	Component		Code
	Max displacement			Oscill	Static	
0°	1.6 mm	5.8 mm		X		FLAC3D (Wave input)
45°	0.7 mm	1.8 mm	Perpendicular to fault strike	X		FLAC3D (Wave input)
45°	0.8 mm	2.8 mm	Parallel to fault strike	X		FLAC3D (Wave input)
?	3.5 mm	15.0 mm			X	Derived from Poly3D results
0°		16.9 mm		X	X	Wave
0°		16.6 mm			X	Wave

In summary, for reasonably comparable cases, the static Poly3D method seems to give target fracture displacement that are on the same order of magnitude as those calculated by use of Wave. Note that the FLAC3D results do not include the static component, only the oscillatory part of the displacement. The implication of this is that the oscillatory component is relatively unimportant and largely overshadowed by the static component.

3.3.4 FLAC3D – step 3

In all modelling approaches described above, earthquakes are simulated by forcing a part of the primary fault (the rupture area) to move in a way that is consistent with the intended magnitude and the intended source mechanism. This can be done arbitrarily without regard to the initial stress field; also for a medium that is stress-free initially. In reality, however, the movement along the primary fault requires that it is potentially unstable under the initial stresses.

A more realistic way of simulating an earthquake is to lock shear movements on the primary fault temporarily, then subject it to a stress field and finally release the bonds and allow for slip in a controlled sequence. The stress field and the residual strength of the primary fault must be combined to produce the amount of total slip that corresponds to the intended seismic moment. The sequence of bond releases must be designed to mimic a typical rupture propagation from the hypocenter outwards across the plane of the fault (e.g. in the way shown in Appendix 1b).

A preliminary study aiming at modelling earthquakes in this more physically correct way, i.e. with consideration of the coupling between the initial stress field and the movement of the primary fracture, has been conducted by use of the FLAC3D code. Figure 3-16 shows the FLAC3D model. As opposed to the models described above, the primary fault has a non-zero dip (cf Figure 3-2).

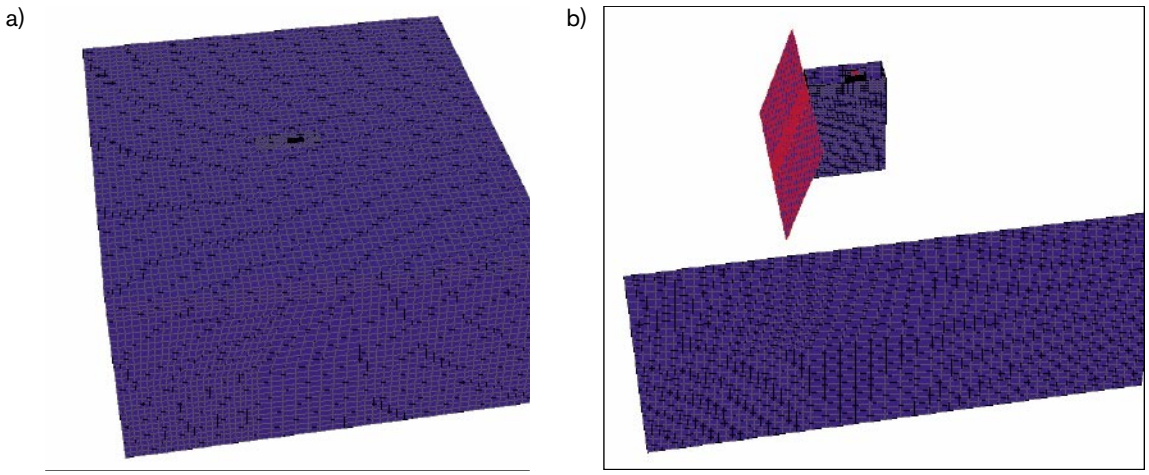

Figure 3-16. *a): The entire model volume of the FLAC3D model (20,000 m x 20,400 m x 10,000 m). b): Same as left, but only selected parts visible to display the 8.0 km by 4.6 km rupture area and the horizontal target fracture. The horizontal fault-target distance is 2,000 m, while the epicentre distance is about 3,000 m.*

The model allows for full representation of:

- The earthquake itself, i.e. the slip on the primary fault caused by potential instability under a postglacial type stress field, and
- The effects, dynamic and residual, on a nearby target fracture.

The rupture area was the same as the one assumed for the magnitude 6 events generated with the 15 MPa stress drop WAVE model. To allow for comparison with corresponding WAVE results, the following was specified:

- The target fracture was horizontal,
- The rock was elastic with Young's modulus = 75 GPa, Poisson's ratio = 0.25 and density = 2,700 kg/m^3. These values are identical to the ones assumed in the WAVE model.
- The upper edge of the rupture area was 1,000 m below ground surface.
- The rupture was simulated by reducing the cohesive strength of the primary fault. The motion was initiated at the center of the 4 km by 8 km rupture area. The rupture front was allowed to move outwardly in a radial direction at a speed 70% of the shear wave velocity. The strength was ramped down from a value equal to the elastic shear stress to a value of zero over a period of 0.5 second. This is similar to the way in which the fault motions were simulated in the WAVE model.

The initial stress field was set such that the shear stress acting on the primary fault was sufficient to give a 1.16 m average fault shear displacement, corresponding to a seismic moment of 1.34E18 J and a moment magnitude of 6.02 (Equation 3 1 and Equation 3 2). The stresses were set according to Table 3-5, and the properties of the two discontinuities according to Table 3-6. An overview of the four conducted analyses is presented in Table 3-7.

Table 3-5. Initial stresses.

Stress component	Value at depth Y m (Pa)	
σ_v	2,700 * 9.81 * Y	Vertical stress
σ_H	17.25e6 + 3.6101e4 * Y	Horizontal stress perpendicular to the strike of the earthquake fault
σ_h	4.31e6 + 1.5647e4 * Y	Horizontal stress parallel to the earthquake fault

Table 3-6. Fault and target fracture properties.

	Friction	Cohesion	Tensile strength	Normal stiffness (GPa/m)	Shear stiffness (GPa/m)
Target fracture	0 degr 15 degr	0	0	10	10
Primary fault	0	0 (final after completed rupture)	0	10	10

Table 3-7. Analysis overview.

Model description			Result (maximum target fracture shear displacement)	
Model nr	Target fracture fiction angle	Horizontal distance between target fracture and top of primary fault	Peak	Residual
1	0 degr	1,000 m	8.0 mm	6.4 mm
2	15 degr	1,000 m	0.3 mm	0.02 mm
3	0 degr	2,000 m	8.7 mm	7.1 mm
4	15 degr	2,000 m	0.03 mm	0.02 mm

The difference in results between the 1,000 m fault distance and the 2,000 m fault distance is very small. Figure 3-17 shows an explanation: the shear stress acting on the plane of the target fracture has a local maximum at about 1,500 m distance. The shear stresses are high only a couple of hundred meters from the fault. This is in agreement with corresponding WAVE results (cf Figure 3-12).

Figure 3-18 shows results from model nr 3 in more detail. Corresponding WAVE results are included for comparison. In the WAVE model, the primary fault is vertical, which means that the horizontal distance between the top of the fault and the target fracture (2,000 m) equals the epicenter distance. In the FLAC3D model, the epicenter distance is about 3,000 m. Both results are based on very similar source mechanisms, the difference being the dip of the primary fault. The FLAC3D results seem to verify the WAVE results qualitatively and with respect to order of magnitude. The oscillating component of the effects on the target fracture is small compared to the residual effects in both analyses. This does seem to support the assumption made by La Pointe, i.e. that static analyses may be sufficient to predict near-field events (cf Section 3.3.3).

Figure 3-19 shows FLAC3D results for models nr 3 and 4. The influence of target fracture friction is very significant at this distance. This is in agreement with the WAVE results shown in Figure 3-12.

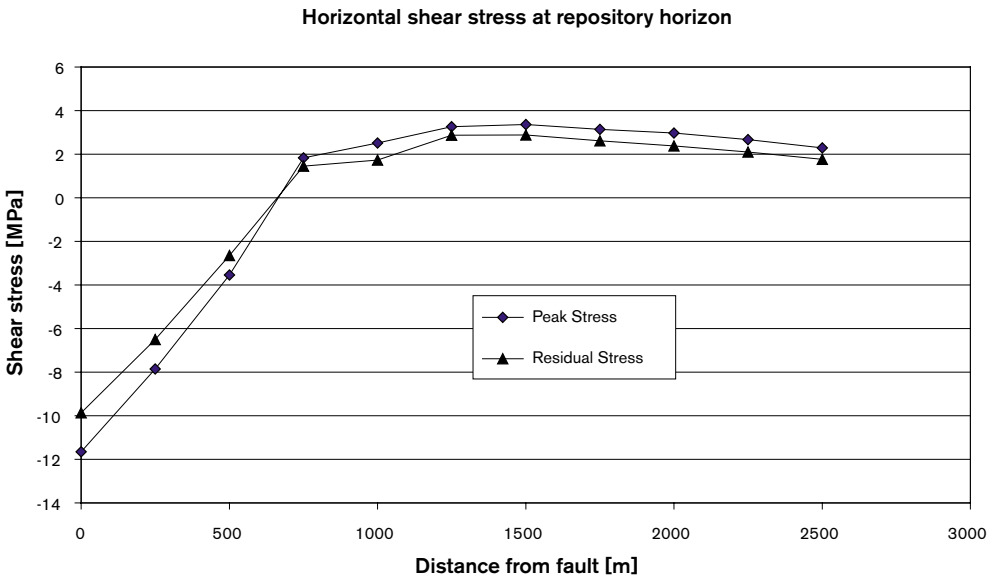

Figure 3-17. *Shear stress acting in the plane of the horizontal target fracture.*

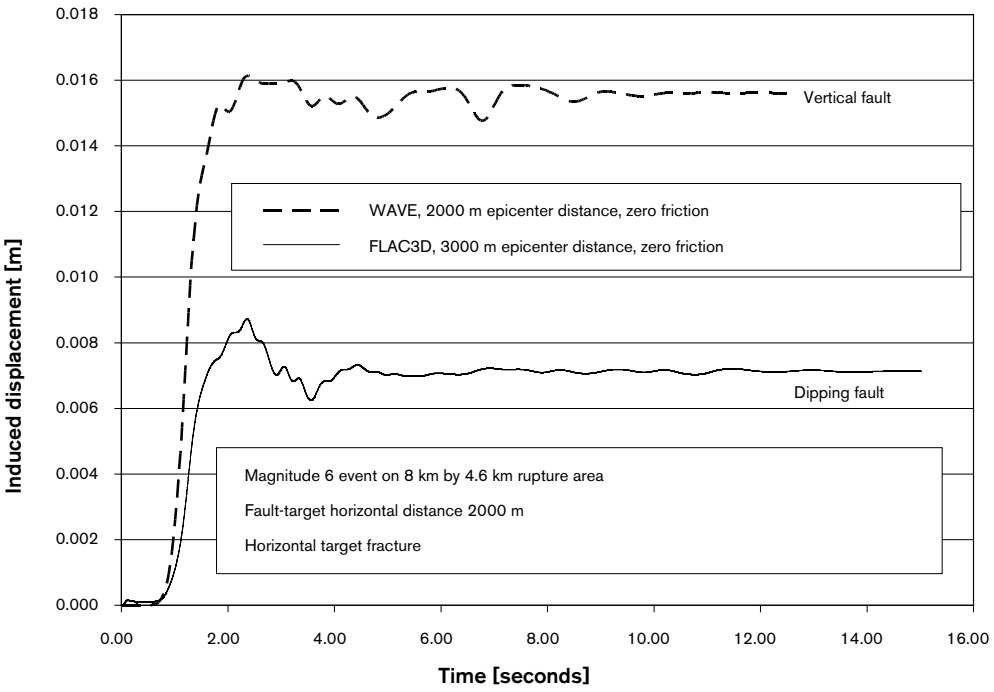

Figure 3-18. *Shear displacement on target fracture, calculated with account of initial stress and primary fault properties (FLAC3D). Corresponding WAVE result is included for comparison.*

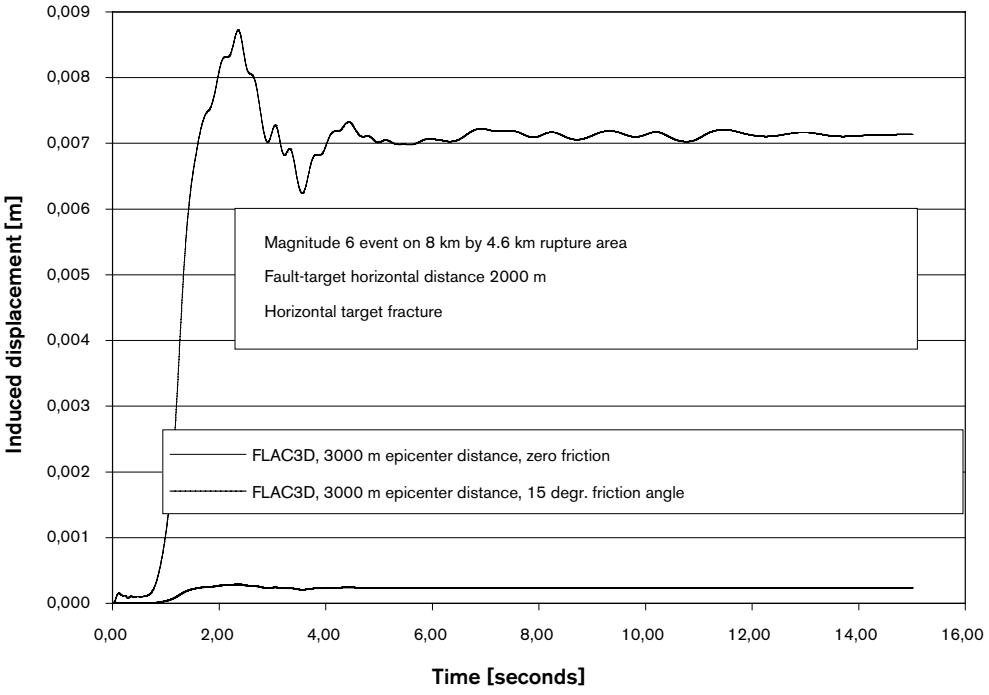

Figure 3-19. *Shear displacement on target fracture, calculated with account of initial stress and primary fault properties. Two cases are shown: with and without target fracture friction.*

3.4 Modelling summary

3.4.1 Main observations

The results presented here were derived from different studies presented in Appendices 1a, 1b, 2a, 2b, and from the FLAC3D study presented at the end of the previous chapter. Some results were derived from the static simulations upon which the risk analysis in SR 97 is based. The following conclusions can be drawn for the reference case considered here, that is, a magnitude 6 event and a 100 m radius target fracture.

- A magnitude 6 event which, according to the regressions presented in /La Pointe et al. 1997/, corresponds to surface rupture length of about 5 km did not produce induced displacements in excess of the 0.1 m threshold value for any of the simulations. For the 200 m distance, the displacement was close (0.065 m) to the threshold (cf Figure 3-13). If the target fracture was located at the edge of the rupture area, rather than close to the epicentre, then even the 200 m distance gave insignificant (0.025 m) maximum, induced displacements (cf Figure 3-11b). Therefore, for a 5 km long potential zone, a respect distance of 200 m seems to be sufficient.
- The WAVE results show that the static response overshadows the dynamic effects (cf Figure 3-13 and Figure 3-15). This was confirmed by the FLAC3D –step 3 results.
- The WAVE results seem to agree well with the results of the static Poly3D analyses, provided that these results are re-evaluated to concern the reference fracture size (100 m radius). For instance, at 2 km distance, the maximum static Poly3D displacement for a friction-less target fracture is on the order of 15 mm. This is in agreement with the WAVE results shown in Figure 3-11a and with the FLAC3D step 3 results shown in Figure 3-18.
- Except for very close distances, the fracture friction is efficient also when dynamic oscillations disturb the mechanical interaction between the two fracture surfaces.
- Given the importance of the static component of the induced displacement, and the agreement between the purely static calculation (Poly3D) and the static/dynamic calculations (WAVE; FLAC3D step 3), it is possible that, for determination of respect distances, static calculations will be sufficient despite our initial doubts.
- The dynamic response is important for establishing shear velocity ranges. Figure 3-12 suggests that 0.1 m/s is an upper bound estimate, relevant for magnitude 6 events.

3.4.2 Validity and relevance of the results

There are limitations to some of the dynamic simulation methods tried so far:

- WAVE/FLAC3D. FLAC3D models can be analysed using arbitrary assumptions regarding the orientation of the target fracture. The target fracture can be realistically modelled with mechanical properties that are typical of rock fractures. The method used here in step 1 and step 2, i.e. to import dynamic boundary conditions from a separate WAVE model, appeared, however, to suppress the static displacement component which turned out to be the most important one. The method of applying a plane wave dynamic load as boundary condition to, for instance, a FLAC3D model is certainly relevant for earthquake problems involving large source to target distances where the dynamic load is the main concern. However, the method is not meaningful to estimate secondary induced movements on repository host rock fractures.

- WAVE. Because of the previous point, the conclusions here are based mainly on the WAVE results. However, in WAVE models, fractures must be either horizontal or vertical. This limits the general validity of the results. There are indications that horizontal target fractures, such as in the WAVE models analysed here, move less than inclined fractures when subjected to static stress changes induced by movements on steeply dipping faults /La Pointe et al. 2000/.
- FLAC3D. The physically most relevant representation of the source to target interaction is the one used in the FLAC3D –step 3 study. The movement of the primary fault takes place as a result of potential fault instability. The slip magnitude is related to the shear stress on the fault plane and to the residual strength of the fault. The primary fault as well as the target fracture can be arbitrarily oriented. At present, the method has been applied only to a small number of cases. In addition, the memory and runtime requirements of a model large enough to simulate a magnitude 8 event will probably exceed current computing capabilities. The practical model size limit has however not yet been determined.

3.4.3 Future simulation work

The continued work should be conducted with models similar to those analyzed in the FLAC3D step 3 study and be focused on the following:

- Run additional FLAC3D analyses of magnitude 6 events for a number of variations regarding the geometry. The radius of the target should be kept at 100 m, and the source mechanism should be identical to the one used so far. Shorter source to target distances (down to 200 m), and different assumptions of the relative orientation of primary fault and the target fracture should however be tried.
- Analyse effects of larger events. As described above, there is a practical limit to the model size. That practical limit needs to be determined. However, the requirements on computational capability may not be the only problem. The question of how one should quantify a large dip-slip event does not have a clear-cut answer, as discussed in the following section.
- Analyse the effect of increasing the canister failure criterion from 0.1 m to 0.2 m.

3.5 Large earthquakes

So far, the efforts have only regarded earthquakes of moment magnitude 6. There are practical reasons for not yet having included larger earthquakes. Analysing large earthquakes dynamically in the way attempted here would require very large models, because of the large fault dimensions required to release sufficient amounts of seismic moment. Regression relations between moment magnitude and surface rupture length suggest horizontal fault dimensions on the order of 300 km as compared to the 8 km horizontal extension of the magnitude 6 event considered here. For dynamic analyses, the mesh cannot be made coarser to compensate for the increased model volume, since this would impede the propagation of the mechanical oscillations. This means that the requirements on computing power seem to be at the limit of what is available at present, at least for magnitude 8 earthquakes.

In addition to practical computational concerns, there are also fundamental aspects to consider on how earthquakes should be represented, e.g. how the seismic moment relates to the change in stress state in the vicinity of the slipping earthquake fault. These aspects become particularly important for large earthquakes.

3.5.1 Stress drop and magnitude

A rock fracture in the vicinity of an earthquake responds mechanically to the stress change caused by the slip on the nearby earthquake fault. Therefore, the stress drop, i.e. the change in shear stress acting on the fault plane, rather than the moment magnitude, is likely to be a key parameter when it comes to calculating induced displacements on target fractures. There are theories positing that the stress drop does not depend on the seismic moment, i.e. on the magnitude /Scholz, 1990/, but takes on values that are typical of the geological setting. For instance, typical interplate earthquakes have stress drops of around 3 MPa, while intraplate earthquakes have stress drops on the order of 15 MPa. For the magnitude 6 earthquakes analyzed with WAVE and FLAC3D the stress drop was conservatively set at 15 MPa (Appendix 1b), or rather: rupture dimensions and average fault slip was set to produce that stress drop.

If the stress drop is indeed independent of the magnitude, then the static effects on target fractures will also be independent of the magnitude, provided that the target fracture is close to the slipping fault and small compared to the dimensions of the rupture area. A rather provocative consequence of this is that large magnitude events would not give more calculated slip on target fractures than the slip amounts obtained here for magnitude 6 events, provided that the parameters are set such that the stress drop is kept at the same value, i.e at 15 MPa.

In the static Poly3D analyses performed by /La Pointe et al. 1997/, there are results indicating a clear dependence of induced target fracture displacements on earthquake magnitude also at small distances. This is in contrast to the above and a consequence of how the earthquakes were generated in the Poly3D study. Figure 3-20 shows that the stress drop was increased with increasing magnitude. There is no explicit account of the stress drop in the Poly3D report /La Pointe et al. 1997/. The stress drop, $\Delta\sigma$, scales, however, approximately with the fault slip/width ratio /Scholz, 1990/ according to:

$$\Delta\sigma = G \cdot \frac{\Delta\bar{u}}{W} \qquad \text{Equation 3-13}$$

where G is the rock shear modulus, $\Delta\bar{u}$ the mean fault slip and W the width (or small dimension) of the rupture. Equation 3 1 holds if the earthquake represents a rupture in an unbroken elastic medium. Values of $\Delta\bar{u}$ and W are explicitly given in the Poly3D study for the different events and are used below to indicate that stress drop was not constant, but increased systematically with magnitude.

The above does not mean that the results derived in the Poly3D study are wrong, only that the set of earthquake parameter values used in that study do not seem to agree with the theory of magnitude-independent stress drop.

The notion of stress drop being independent of magnitude is an approximate theory that can be supported by application of scaling relations to observations of events in the low magnitude range, but not equally well for large earthquakes. For large earthquakes that breach the ground surface and extend deep enough that the bottommost parts of the fault plane have already failed aseismically, it can be argued that the rupture is not constrained either on top or bottom /Scholz, 1990/. This would resolve the apparent stress drop difference between small and large earthquakes and allow for the assumption that stress drop does not increase with magnitude.

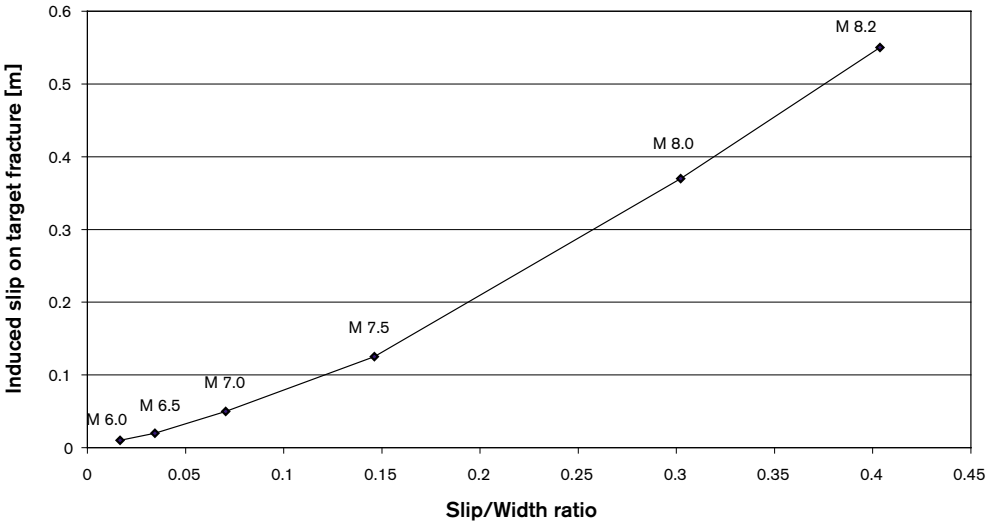

Figure 3-20. *Maximum slip on target fracture located within a repository with the repository edge at 50 m distance from the plane of the rupture. Results derived from /La Pointe et al 1997/.*

When modelling earthquakes of different magnitudes, and large magnitudes in particular, with the methods demonstrated in the previous chapters and associated appendices, it will be possible to adopt different approaches. The choice of approach may well turn out to be much more decisive of the effects on nearby target fractures than the earthquake magnitude. For instance:

- If an increase in magnitude is represented by an increased horizontal extension of the ruptured area, then the stress drop and the seismic moment per unit of rupture area will both be unchanged and the effects on nearby target fractures will change very little.
- If an increase in magnitude is represented by an increased width of the ruptured area, then the stress drop will decrease and the seismic moment per unit rupture will remain unchanged. This may reduce rather than increase the effects on nearby target fractures.
- If an increase in magnitude is represented by an increased average fault slip, then the stress drop and the seismic moment per unit of rupture area will both increase. This will increase the effects on nearby target fractures.

The type of large earthquakes that may be relevant to the safety analysis, i.e. future postglacial fault movements, cannot easily be categorized with respect to stress drop. The overall mechanical conditions will probably differ from those of typical 15 MPa stress drop intraplate events. If Equation 3 1 is applied to the large fault movements in northern Sweden that took place during the last deglaciation, using data provided by /Muir Wood, 1993/, the stress drops would amount to 6 MPa (Lansjärv) and 7.5 MPa (Pärvie). Note that these stress drop figures are still on the conservative side because no account is made of the possibility of preceding aseismic stress release around the lower parts of the fault planes.

3.5.2 Handling of large earthquakes

The general conclusion of the above is that there is a possibility that very large earthquakes will not give much larger induced displacements (on nearby target fractures) than those calculated previously for magnitude 6 events. That is: nearby target fractures do not respond to the net strain energy release, but to the local stress change. They are not affected by movements on remote parts of large fault zones, only by movements of the reasonably nearby parts. (Large earthquakes will however cause displacements on a larger number of fractures than smaller ones because the range of influence will be larger). In future analyses it may be sufficient to demonstrate this by use of static models, provided that it can be confirmed in a general way that the dynamic effects are small compared with the static effects.

4 Out of plane growth; the transition zone

In the previous chapter we presented various methods to compute respect distances and presented results of such computations. However, we must also clearly define the geometry of the deformation zone in order to apply respect distances on a real case. Or expressed differently, from where/what should the respect distance be calculated?

It is naturally essential to clearly having defined the geometry of the deformation zone before a respect distance can be applied. There is a complication, though, in the definition of the thickness of a deformation zone. Usually, the thickness of a fracture zone is defined on the basis of the most deformed part, its core (Figure 4-1). In general, only clay filled fractures, breccia, cataclasites and other results of shear deformation are addressed. This approach is common in engineering geology due to obvious stability issues. This approach is also common when mapping drill cores.

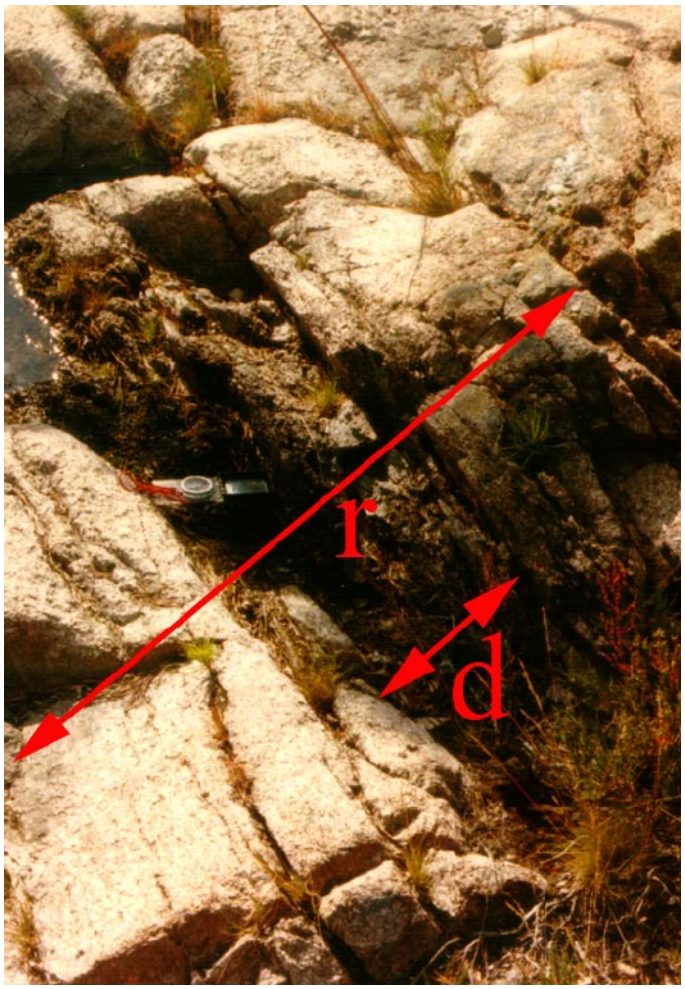

Figure 4-1. *The thickness of a fracture zone can be either be defined on the basis of its core "d", or defined as to include the damage zone "r". In the latter case, the core is only one of many components in a complex structure /picture from Munier, 1995/.*

But the thickness of a fracture zone can also be defined to include those parts of the surrounding rock that have been influenced by the presence of the zone. This is quite difficult, if at all possible, to address in macroscopic core mapping /Morad and Aldahan, 2002/, but well exposed fracture zones, e.g. by tunnelling or trenching, can reveal the magnitude of this influence (Figure 4-1). The fracture array in the immediate vicinity of the fracture zone, using the traditional definition of thickness, often differ markedly from the undisturbed rock mass /Chester and Logan, 1986; Koestler, 1994/. The term “damage zone”, “process zone”, or within SKB, “transition zone” /Munier et al. 2003; Thunehed and Lindqvist, 2003/ is used to address this particular aspect of fracture zones. Using this approach, the thickness of a fracture zone will be larger than traditionally mapped/modelled (Figure 4-2).

We favour this approach because, besides honouring conservativeness, it also takes into account the future evolution of the zone, i.e. future reactivations in terms of in-plane and out of plane growth /e.g. the growth model of Martel, 1989/. With other words, should a future glaciation trigger reactivation of a fracture zone, the faulting may not necessarily occur within its most deformed part, the core, but can very well be located somewhere within the transition zone. Therefore, respect distances should be defined such that the width of the transition zone constitutes a minimum respect distance from the core.

A concern is that it is hardly possible to address this aspect of fracture zones from studies of drill cores, and fracture zones are rarely exposed on outcrop. Geophysical anomalies (e.g. aeromagnetics) can under favourable conditions provide a rudimentary estimate of the maximum thickness. In the lack of other information, it would therefore be attractive to use a method to estimate the thickness using the trace length which is relatively easy to obtain from e.g. lineament maps. When necessary, the actual width can be investigated by trenching at surface or addressed at a later stage, during excavation of the tunnel system.

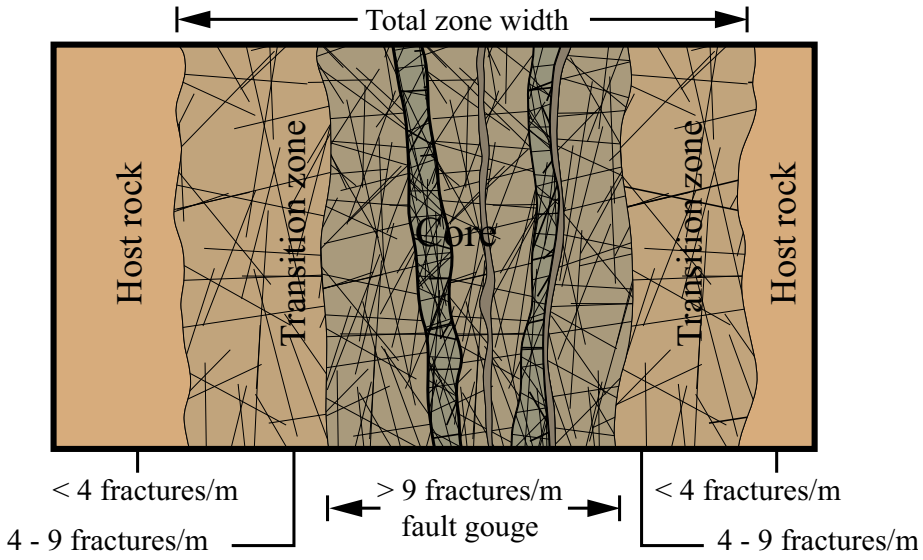

Figure 4-2. *Schematic cartoon showing different components of a fracture zone (see text for further explanation).*

We have, unfortunately, despite extensive searches in databases, only been able to find a few studies that directly relate the size of the transition zone to the size of the fracture zone. Studies by /Vermilye, 1996; Vermilye and Scholtz, 1998/ propose that the width of the transition zone scales linearly with fault length with a proportionality constant of the order of 10^{-2}. A work by /Cowie and Shipton, 1998/ modified the model of Vermilye by relating the transition zone to the dimension of the slip rather than to the dimension of the fault but this modification did not alter the proportionality constant of 10^{-2} between fault length and width of transition zone.

Another study records that the transition zone amounts to approximately twice the shear displacement /Knott et al. 1996/. Since other studies record that the shear displacement can amount to about 1–5% of the trace length /Cowie and Scholz, 1992a/, the transition zone could be approximated to vary in the range 2–10% thus partially confirming the work of /Vermilye, 1996/. However, the few exposed zones that we have studied, e.g. at the Äspö HRL, show that the transition zone is asymmetrical, i.e. it is usually larger on one side than on the other; and that the ratio between width of transition zone and fault length rather should lie in the lower part of this range. Unless it can be defined otherwise, we therefore recommend a preliminary assignment of a transition zone width that amounts to 2% of the zone length, i.e. 1% on each side of the zone core(s). Should this estimate be considered too conservative, the actual thickness of the transition zone at the rock volume of interest can be addressed by additional geophysics, studies of drill cores, etc.

5 Empirical knowledge

One way of estimating possible mechanical effects on the repository is to examine documented cases of earthquake-induced damage on underground facilities, such as tunnels and mines. Conclusions drawn from a systematic and worldwide literature survey, including underground constructions at small distances from large earthquakes suggest that, as a general rule, underground effects are insignificant compared to corresponding surface effects /Bäckblom and Munier, 2002/. There are two separate reasons for this:

- Oscillations have lower amplitudes at large depths. Because of wave reflections off the ground surface, mechanical oscillations are particularly intense close to-and at the surface, due to superposition of incident and reflected waves.
- Underground constructions are less sensitive to dynamic loads. To damage an underground structure significantly, the disturbance must be powerful enough to rupture the surrounding medium.
- The wavelength of the seismic waves is long compared to the size of the underground structure, so that little damage occur.

The repository will be at a much larger depth than most of the tunnels covered by the literature survey conducted by /Bäckblom and Munier, 2002/. In addition, the repository host rock will be of better quality than the rocks in the tunnel sections where damage was actually found and, as opposed to the tunnels in the survey, the repository cavities will all be backfilled. The literature survey included tunnels that intersect active fault zones on which earthquakes originated. In these cases, the damage was restricted to the nearest surroundings of the tunnel/fault intersection.

The study of /Bäckblom and Munier, 2002/ suggests that the respect distance, i.e. the distance between potential earthquake zones and deposition holes, may not have to be very large. This because the large distances over which dynamic oscillations are known to propagate and cause damage to surface structures are not relevant to the problem of estimating respect distances which are to be applied at relatively deep (400–700 m) underground constructions. To increase the confidence in the general conclusions drawn from /Bäckblom and Munier, 2002/ it is desirable to obtain quantitative respect distance estimates by the use of numerical analyses.

6 Discussion on conservatism

None of the studies cited in this report have included the geometry of the repository or, more importantly, the location of canisters in relation to the location of target fractures. Only a minor amount of the simulated fractures displaced more than the threshold value, 0.1 m. The risk for earthquake damage can be significantly reduced, or perhaps even eliminated, if such undesirable fractures are avoided in the canister holes. With other words, the nature of the fractures within the repository will steer the resource ratio, i.e. canister positions containing undesirable features (fractures) can be neglected. Since the number of canisters is constant, the disqualification of a canister position must be compensated by the addition of new positions. The required amount of rock will therefore increase. The resource ratio is a measure on how much of the rock is available for deposition and is expressed as the ratio between the amount of canister positions that can be accepted for loading and the total amount of canister positions. At the moment, 4,500 canisters are planned to be deposited. The resource ratio can thus be expressed as:

$$rr\left[\%\right] = 100 \cdot \frac{N_{can}}{N_{pos}} \qquad \text{Equation 6-1}$$

where N_{can} is the number of canisters, at the moment 4500, and N_{pos} the total amount of canister positions.

Simplifying the reasoning in previous chapters, the respect distance can be said to be a function of the geometry of the fault (and stress drop/magnitude) and the geometry (size and orientation) and location of the target fractures. The effect of earthquakes can be avoided by discriminating canister positions transected by large fractures. With other words, the respect distance can be balanced against the resource ratio in the panels between the deformation zones and is thus strongly coupled to repository layouts and optimisation. However, lowering the resource ratio has an associated cost. It is therefore essential not to use overly conservative assumptions. The aim is to compute respect distances that are sufficiently conservative to gain confidence in the scientific and public community, yet honouring reasonable engineering and economic considerations. Various aspects of conservativeness or lack thereof, is the main topic of this chapter.

6.1 Site specific stress fields

Our main concern is glacio-isostatic faulting during, or shortly after, the next glaciation(s) (see Appendix 3 for an exposé). Though some researchers have reported glacio-isostatic faults in central and southern Sweden /Mörner, 2003/ all unambiguous faults are located in northern Scandinavia /Tanner, 1930; Kujansuu, 1964; Lundqvist and Lagerbäck, 1976; Kuivamäki, 1986; Paananen, 1987; Vuorela et al. 1987; Olesen et al. 1989; Olesen et al. 1992a; Olesen et al. 1992b; Muir Wood, 1993/, where the ice-cap was thickest (Figure 6-1).

In the lack of hard evidence that such faults have occurred at our study sites Forsmark and Simpevarp, we need to model the next glaciation using realistic, site-specific data. Ongoing work /SKB, 2003/ will address this issue, specifically:

- What are the properties (thickness, temperature, etc) of the glacier above our study sites?
- How is the glacier likely to affect the rock stresses during and after the ice age?

- Is it at all possible, using reasonable assumptions, that glacio-isostatic faults can occur at our study sites?
- What is the probability for a (series of) glacio-isostatic fault at our sites?
- Which are the most likely candidates for reactivation at our sites?

Naturally, if there are no prerequisites for glacio-isostatic faulting at our study sites then respect distances to deformation zones due to earthquakes will no longer be an issue. While waiting for simulation results, we will assume that prerequisites will exist, and that all deformation zones large enough to harbour major earthquakes have the same probability, albeit low, to reactivate.

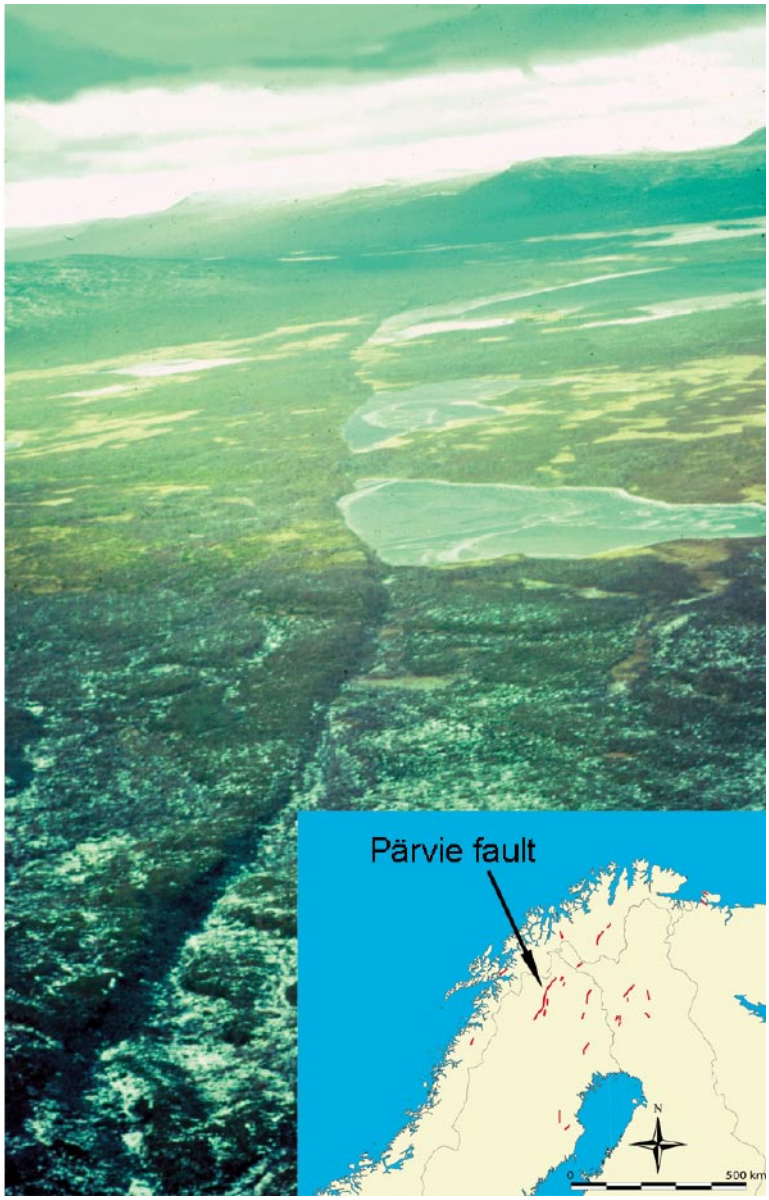

Figure 6-1. *The picture shows the Pärvie fault, looking NE offsetting the smooth Quarternary surface. The insert shows the location of the most prominent glacio-isostatic faults.*

6.2 Target fracture size

Generally, decreasing target fracture radius from 100 m to 50 m result in a 50% decrease of the respect distance from 200 m to approximately 100 m /La Pointe et al. 1997, e.g. Figure 4-7/. Thus, by increasing the requirements on how large fractures we can accept in our deposition hole, we will be able to considerably decrease respect distances to deformation zones. We have assumed that fractures exceeding 100 m radius can be detected in the deposition holes and the respect distances calculated so far have been based on that assumption. However, a 200 meter wide fracture is fairly large. Though there is a lower limit for what one possibly can map with confidence underground, despite extensive excavations and drilling, we believe that it is reasonable to assume that fractures with radii exceeding 50 m, can be detected using standard mapping techniques, with adequate accuracy. The mapping is greatly aided by numerous closely spaced deposition holes and tunnels (Figure 6-2).

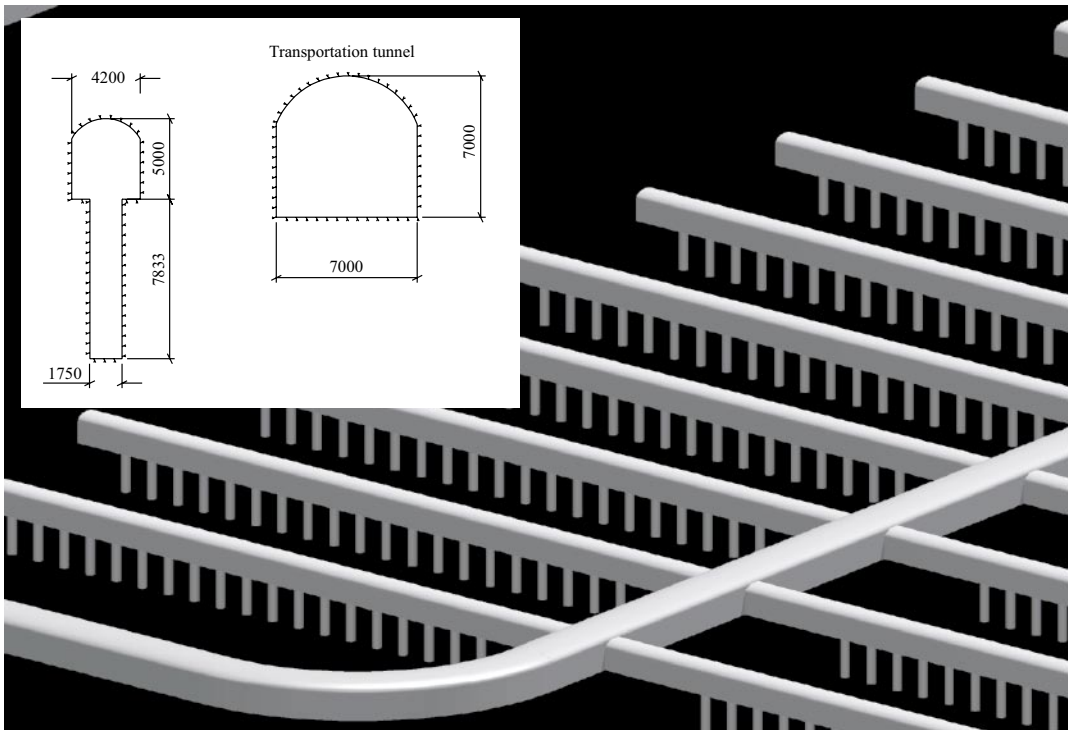

Figure 6-2. *Tentative repository layout. The spacing of deposition tunnels and canister holes spacing is, at the moment, 40 m and 6 m respectively. The insert shows the tunnel dimensions.*

6.3 Target fracture properties and host rock properties

The numerically calculated target fracture displacements were all obtained assuming conservative conditions:

- Target fracture were assumed to be friction-free or to have small values of the friction angle
- Target fractures were assumed to be planar.
- The host rock was assumed to be linearly elastic.

For some cases the role of fracture friction was analyzed. At reasonably large source-target distances, the role of friction appeared to be very important. At the smallest distance analyzed (200 m), however, the role was less clear. Considering more realistic values of friction may not necessarily reduce the calculated induced displacements at small distances much.

Non-planar fractures will move less than the idealized fractures considered in the numerical models. Taking non-planarity into account would be a reasonably simple way of arriving at smaller and more realistic results of calculated target fracture displacements.

If there are additional fractures in the rock surrounding the target fracture, these will absorb some of the strain and give less displacement of the target fracture itself. Taking this into account would also be a reasonably simple way of arriving at smaller target slip estimates.

There is also the question of fracturing around the tips of a slipping target fracture. In the conservativeness study conducted by /La Pointe et al. 2000/ this aspect was considered. The outcome of the study was that target fractures will slip only until a relevant fracture propagation criterion is met at the fracture tips. As soon as fracture propagation has been initiated, no more strain energy would be expended on slip, giving slip amounts much smaller than those found in the numerical analyses described in previous chapters. The effects of considering this aspect are large but difficult to quantify. In the conservativeness study, the fracture propagation criterion was schematic and approximate. The two processes (i.e. slip and fracture propagation) were uncoupled, while in reality the propagation will give changes in the stress state as well as in the fracture geometry.

6.4 Single versus multiple events

In previous estimates of canister failures due to earthquakes /e.g. La Pointe et al. 1999/ the maximum accumulated slip was computed on target fractures. A conservative assumption is that all increments of slips have the same direction and are additive. However, it is possible that this assumption is overly conservative and yield too large net slips. With regards to local stress redistributions in the blocks between zones, it is not self-evident that the driving force, σ_1, is constant in direction through time, at all locations within the repository. Consequently, the sense of induced shear, all other factors held equal, on the target fractures may vary; a dextral strike-slip of, say, 5 cm will be cancelled out by a sinistral strike-slip of the same amount. If this reasoning can be regarded acceptable, then only the maximum slip vector will be of interest for calculations of potential canister damage. Since the latter is strongly coupled to target fracture size, canister damage due to earthquakes can probably be completely avoided by the proper choice of discriminating fracture in the canister hole (see Section 6.2).

6.5 Scale

The analyses of canister failures are, to date, based on energy input (magnitude/stress drop) and induced slip on target fractures. We have assumed, conservatively, that all deformation zones have the potential of harbouring the maximum possible earthquake for a structure of that particular size (rupture area). But size is a scale dependent property. A deformation zone interpreted as a single, large structure in one scale, might be segmented into numerous smaller sections when interpreted in another scale.

The question is, of course, on what scale should the calculations be based on? Figure 6-3 illustrates schematically the concept. It is clear that by segmenting a deformation zone into its constituent strands, much smaller respect distances can be obtained. However, this reasoning can be expanded in absurdum. The presumably fractal nature of fragmentation in the Earths crust /e.g. Hirata, 1989; King, 1992; Korvin, 1992; Barton and La Pointe, 1995; Johnston and McCaffrey, 1996/ postulates that each segment consists of even smaller segments. Following this logic, the segment length will, as resolution increases, tend towards zero while their frequency will tend towards infinity. The inevitable conclusion, should this logic be followed throughout, is absurd: by choosing interpretation scale we will be able to steer the expected magnitude of earthquakes and, hence, respect distances. There is, in fact, not much of a choice. Most empirical studies relating earthquake magnitude to surface rupture length, width, etc, /Albee, 1969; Bonilla et al. 1984; Ambraseys, 1988; Blenkinsop and Hull, 1989; Cowie and Scholz, 1992a,b; Dong et al. 1993; Huang and Wang, 1993; Clark and Cox, 1996/ are based on regional studies with resolutions typically in the order of tens of meters. Accordingly, when computing respect distances for deformation zones in our sites, Forsmark and Simpevarp, computations should be based on regional models only. Adjustment of respect distances as resolution increases, going from regional models (versions 1.x) to local models (versions 2.x) is inappropriate. Adjustment of respect distances as information increase is, on the other hand, highly desirable.

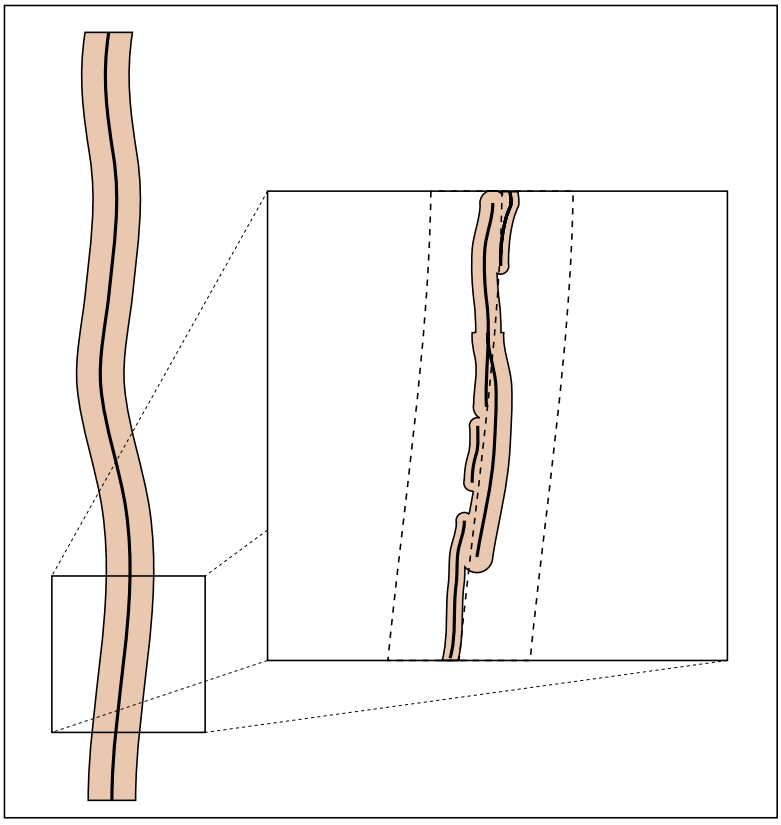

Figure 6-3. *The presumed fractal nature of deformation zones have a limited effect on calculations of respect distances. By increasing resolution of interpretation, faults strands decrease in size and, hence, the respect distances. However, we here advocate that respect distances should be based on regional models (versions 1.X) only.*

7 Summary, discussion and recommendations

An important finding of the dynamic numerical simulations conducted after the appearance of SR 97 with different tools, and by use of different simulation approaches, is that the dynamic effects are relatively unimportant at small distances. For target fractures, the static, residual, effects of the energy release overshadow effects of the dynamic load for all distances of any concern for the deep repository. This confirms the basic assumptions made in the seismic risk analysis in SR 97 /La Pointe et al. 1997; La Pointe et al. 2000/.

The reference target fracture used in all dynamic analyses conducted up to the present day is 100 m in radius. The reference magnitude is M6. According to the simulation results obtained so far, the numerically computed respect distance, would be 200 m for a zone capable of accommodating a M6 event given that it will be possible to detect and avoid fractures of 100 m in radius or larger. If it will be feasible to reject canister positions intersected by 50 m radius fractures, the respect distance can be reduced from 200 m to approximately 100 m.

The stress drop was set at a conservatively high value in the dynamic numerical models. The stress drop is the key quantity for estimating the residual, static, effects of fault movements. The implication of this is that the numerically calculated induced displacements along reference target fractures probably are representative also of larger events, such that the computed respect distance does not need to be larger for M7 and M8 events than for M6 events. In conclusion, a respect distance of 100 m from the plane of the potential fault will probably be defensible from the computational point of view. This conclusion is based on the notion that stress drop is a magnitude-independent quantity /Scholz, 1990/. However, the numerical analyses are not sufficiently realistic to fully support this argument.

The idealized representation of the source to target interaction used in the numerical models sets bounds to the range of distances that can be considered. Earthquake faults were represented by planar features in all models and seismic events were modelled as idealized and schematic relative movements along these planes. Attempting to analyze effects on target fractures at very small distances is not meaningful, since details in the fault geometry and in the source mechanism will become important in the vicinity of the fault. At small distances it is, for instance, not relevant to distinguish between induced displacements on target fractures and displacements on components of the seismogenic fault itself. Distances that are smaller than the measure used to describe the zone half-width should probably be considered too small in that respect.

To defend respect distances smaller than 100 m for M6 events and larger, the general conservativeness in the elastic stress/deformation model for rock fractures must be exploited and accounted for. Support of small respect distances is found in a conservativeness study conducted by /La Pointe et al. 2000/. That study addressed the effects of fracturing in the regions of the tips of a slipping target fracture, using fracture propagation criteria based on stress intensity factors derived by /Shen, 1993/. The results of the study suggested that the amount of maximum possible induced shear displacement on a given fracture is determined by the size of the fracture itself and is independent of the load on the fracture, i.e. of the earthquake magnitude and of the distance to the earthquake fault. For fractures of 50 m radius, the maximum displacement was found to be only a few millimeters. This result is not conservative, since the maximum displacements were calculated without consideration of the change in geometry that will follow from the processes around the fracture tips.

Qualitatively, however, the study points to the effects of strain energy being expended on fracturing rather than on elastic deformations and indicates that induced displacement will be significantly smaller than those obtained from the elastic source to target analyses. Taking full account of the results in /La Pointe et al. 2000/ means that earthquake-induced displacements on fractures transecting deposition holes will not be an issue for the determination of respect distances.

Table 7-1 shows a summary of the findings discussed above and should be read as follows: For each zone of a certain size the transition zone is calculated or, if possible, measured. Since the transition zone is here considered an integrated part of the deformation zone, deposition of canisters within the transition zone is prohibited by SKB design policy. As a consequence thereof, if the transition zone exceeds the seismic influence distance, then the respect distance equals the transition zone, otherwise the respect distance equals the seismic influence distance.

Table 7-1. The table relates respect distance (RD) and transition zone (TZ) to zone length using various assumptions.

Zone size	Estimate based on analyses of source to target interaction	Estimate based on findings of conservativeness study		Transition zone estimates		
	(50 m radius fracture)	Safe detection of 50 m radius fractures	Safe detection of 25 m radius fractures	W/L Ratio 2%	W/L Ratio 1%	
0 km– 3 km	–	–	–	0 m–30 m	0 m–15 m	Source movement does not exceed 0.1 m
3 km– 10 km	100 m	100 m	50 m	30 m–100 m	15 m–50 m	Respect distance = TZ half-width
>10 km	100 m	100 m	50 m	> 100 m–	> 50 m –	TZ half-width > RD

The respect distances in Table 7-1, based on numerical analyses, can all be reasonably well defended, from a numerical point of view, but not proven to be 100% safe. Some further work is needed to gain sufficient confidence in the general validity of the calculation-based conclusions. For layout planning purposes, an appropriate strategy may be to use the minimum respect distance and then, if permitted by available rock volumes, increase the respect distance for zones with half-widths that are larger than that first estimate. We would, however, like to stress the point that empirical observations show little or no damage to deep, underground, relatively small dimensioned, engineered structures. It is therefore fair to expect respect distances to be smaller, probably much smaller, than indicated in Table 7-1 even if we cannot support such statement with numerical arguments.

It will hardly be possible to model the source mechanism in sufficient detail (i.e. with full account of the distribution of mechanical properties on the plane of primary fault, of fault width and fault width variations, of host rock property variations with depth, etc) to be able to calculate the response of target fractures at very small distances. However, the general conservativeness in the target fracture representation points to the possibility that target fracture displacements will be significantly smaller than those calculated here, irrespective of details in the fault behaviour.

Figure 7-1 shows respect distance estimates based on interpretations of results from the dynamic numerical analyses. The schematic zone is intended to represent a 10 km long zone with a transition zone half-width of 100 m (W/L ratio = 2%). A zone of such dimensions may accommodate a M6 event, or larger. If it is possible to detect and avoid fractures of 100 m radius, but not fractures smaller than that, the respect distance is 200 m (Figure 7-1a). If, on the other hand, it is possible to detect and avoid fractures with 50 m radius, the respect distance will be approximately halved (Figure 7-1b). Reducing the detection limit further, for instance such that 25 m radius fractures and larger can be safely detected and avoided, would, however, not automatically result in reduced respect distances. A canister position such as the one indicated in Figure 7-1c, for instance, would not be allowed because the idealized representation of the source to target interaction used in the numerical models does not allow for conclusions relevant for very close distances. Additionally, the canister position in Figure 7-1c is entirely contained within the transition zone of the fault and thereby excluded by definition.

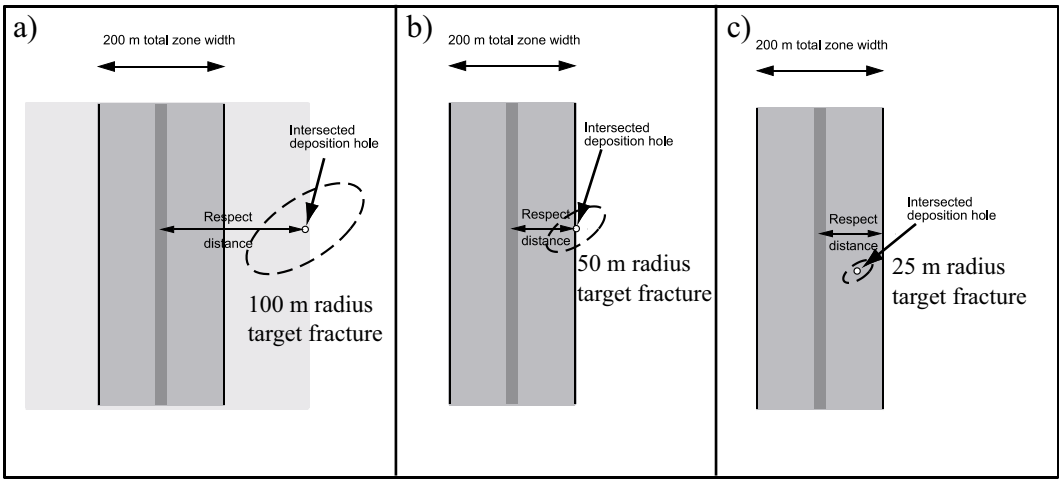

Figure 7-1. *Respect distances based on interpretations of static/dynamic source to target analyses.*

8 Worked example

For illustrative purposes, respect distances have been assigned to deformation zones of the site descriptive model FM V.1.1. Figure 8-1 shows the location of the Forsmark site and various model boundaries. The worked example presented in this chapter is limited in space to the local model volume, while using deformation zones interpreted in other scales.

The first step in assigning respect distances is the setup of appropriately defined rules that can be applied to the geological model. For this example the following principles have been followed:

- The discriminating fracture size in deposition holes is 50 m (radius), i.e. half that used in previous modelling.
- For deformation zones capable of hosting M5 or larger (i.e. longer than c 3.5 km), the minimum respect distance is set to 100 m.
- The width of the transition zone amounts to 1% of zone length. The length is based on interpretation in regional scales. The maximum width of transition zone was, however, set to 400 m, i.e. 200 m half-width for the largest zones in order not to obtain unrealistically wide transitions zones. This is partly backed up by observations from the constructions of SFR.

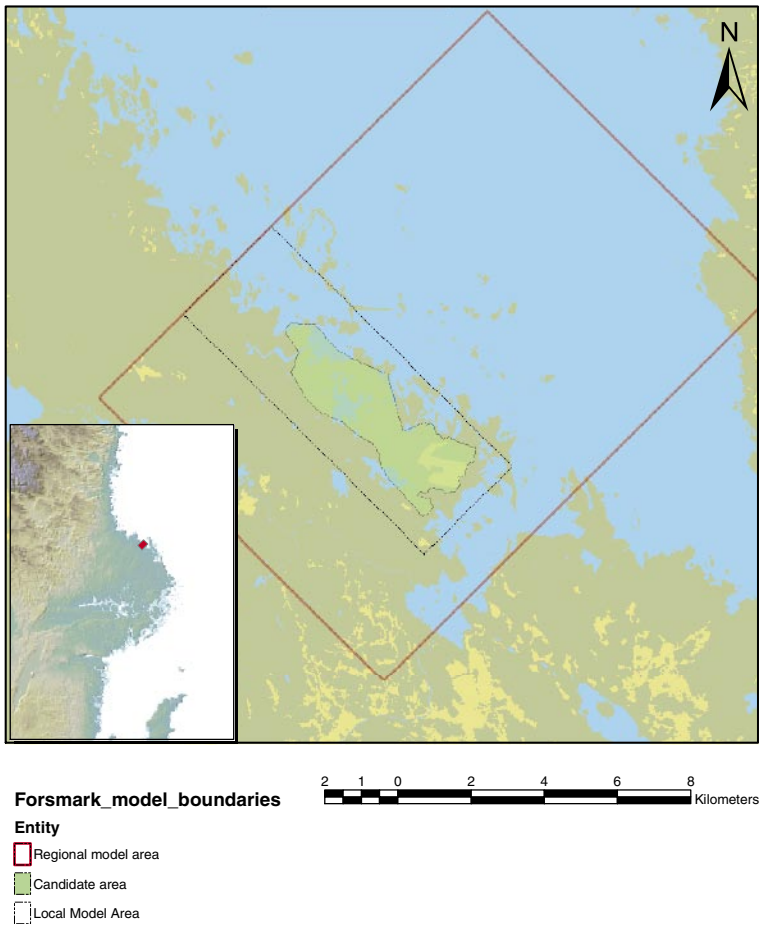

Figure 8-1. *Location of the Forsmark site.*

Figure 8-2 shows interpreted lineaments in the Forsmark site. Since it is essential to compute the width of the transition zone on the entire length of the lineament, we used a lineament interpretation performed on a larger scale (insert in Figure 8-2).

Lineaments coloured red in Figure 8-2 are those sufficiently close to the model volume as to have a potential impact on the calculation of respect distances. In the V.1.1 model, it is clear that regional deformation zones are made up of shorter zone segments. Still, we use the sum of zone segments lengths to honour the principle of conservativeness (see discussion on scale, section 6.5).

Figure 8-4 shows a 3D geological model (Figure 8-4a) with the respect distances from the map in Figure 8-3 superimposed (Figure 8-4b).

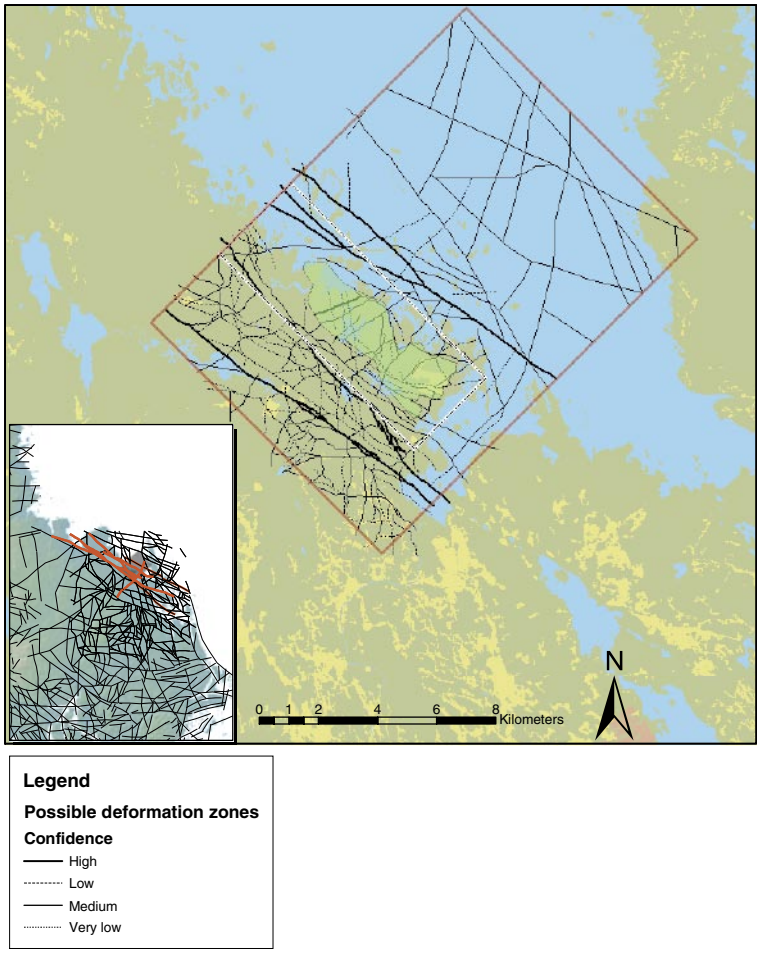

Figure 8-2. *Lineaments in Forsmark, V.1.1. The insert is a large scale interpretation of lineaments (SNA). Lineaments coloured red are those sufficiently close to the model volume as to have a potential impact on the calculation of respect distances.*

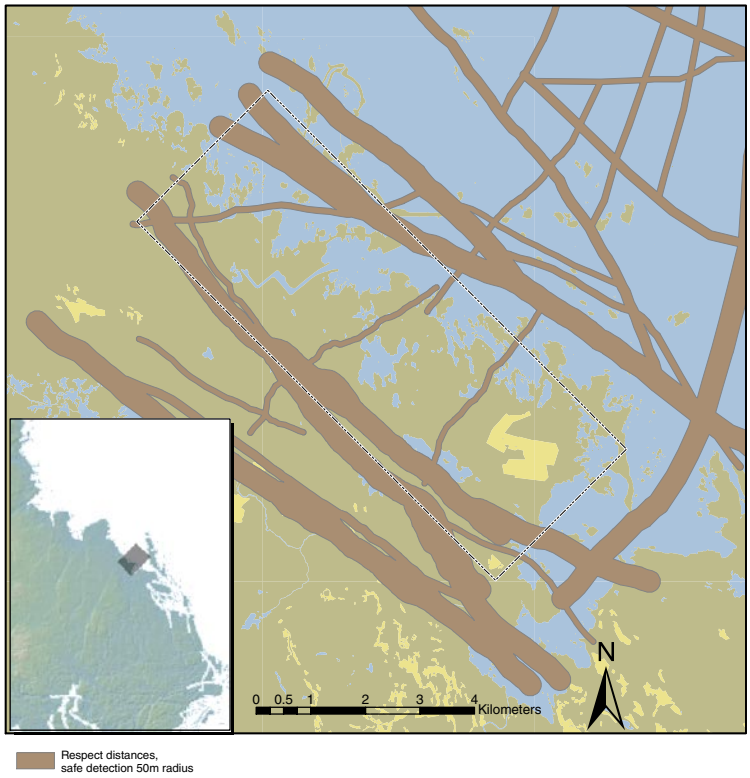

Figure 8-3. *Respect distances computed for deformation zones at Forsmark (model version V.1.1).*

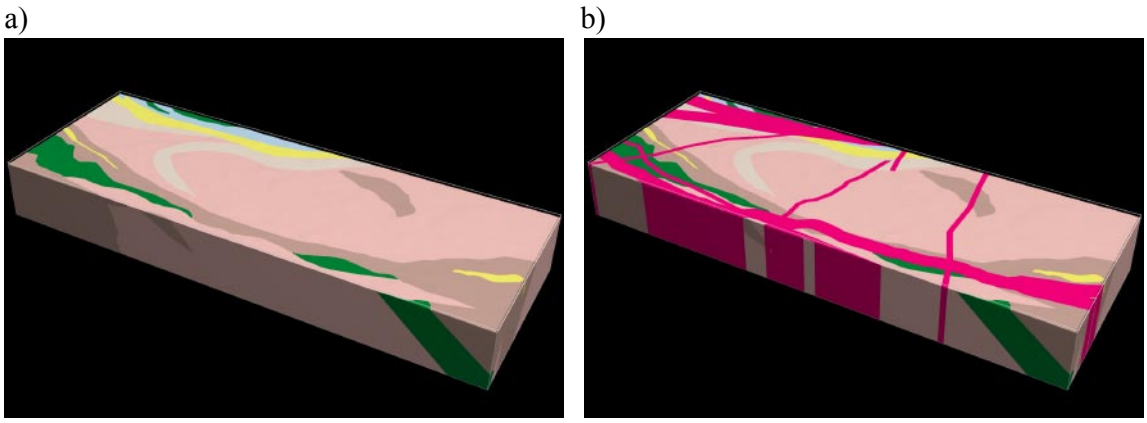

Figure 8-4. *The local model containing a) lithology and b) lithology and deformation zones.*

a) b)

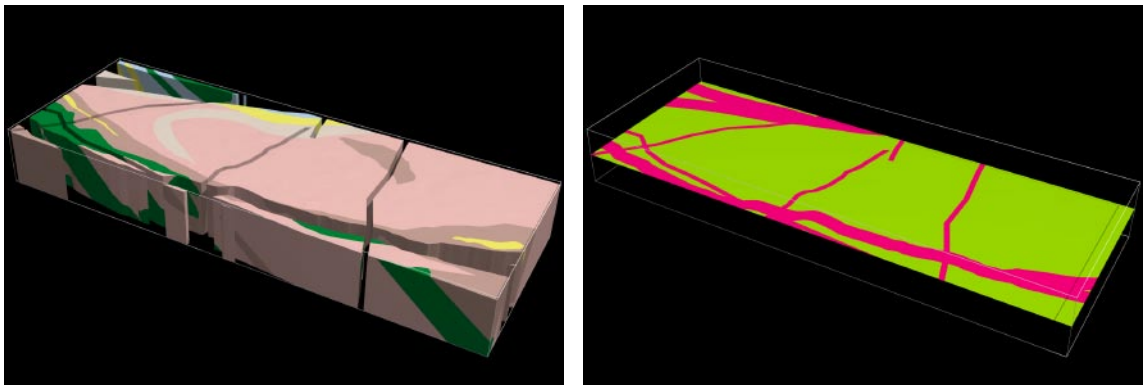

Figure 8-5. *a) Geological model (FM.V.1.1) with deformation zones removed. b) Available deposition panels at –500 m.*

By subtracting the confidence volumes from the geological model, we outline the rock volumes within which canisters can be safely emplaced from a seismic point of view. Figure 8-6 illustrates parts of a tentative repository layout. Note that small deformation zones (< 3.5 km in this study) have not been included in the computation of respect distances but these will also have some impact on the repository layout.

We believe it is essential to model the respect distances in 3D (i.e. respect volumes). Not obvious in this simple example, is the fact that respect distances should be computed for zones of all orientations including subhorisontal zones. The shape, and size of repository panels at repository depth can naturally become quite complex. A 3D model of respect volumes enables "slicing" at various depths to outline repository panels and therefore provide a useful tool for the planning the repository layout.

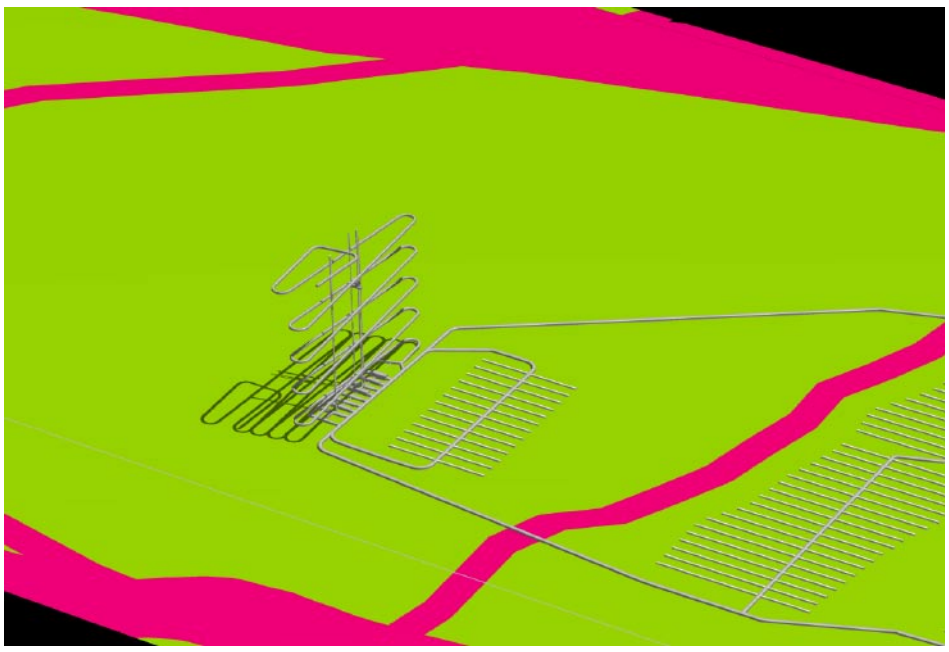

Figure 8-6. *Tentative repository layout. Only deformation zones with computed respect distances, i.e. large scale zones, are shown.*

9 References

Albee A L, 1969. Earthquake source dimensions and the relationships between the length and amount of displacement in historic surface faulting.

Almén K-E, Stanfors R, Svemar C, 1996. Nomenklatur och klassificering av geologiska strukturer vid platsundersökningar för SKB:s djupförvar. SKB Djupförvar Projektrapport PR D-96-029, Svensk Kärnbränslehantering AB.

Ambraseys N N, 1988. Magnitude-fault length relationships for earthquakes in the Middle East, in Historical seismograms and earthquakes of the world, Lee, W.H.K, Meyers, H, and Shimazaki, K, Editors. 1988, Acad. Press: San Diego, CA, United States. p 309–310.

Andersson J, Ström A, Svemar C, Almén K-E, Ericsson L O, 2000. What requirements does the KBS-3 repository make on the host rock? Geoscientific suitability indicators and criteria for siting and site evaluation. SKB TR-00-12, Svensk Kärnbränslehantering AB.

Andersson P, Byegård J, Winberg A, 2002a. Final report of the TRUE Block Scale project. 2. Tracer tests in the block scale. SKB TR-02-14, Svensk Kärnbränslehantering AB.

Andersson P, Byegård J, Dershowitz B, Doe T, Hermanson J, Meier P, Tullborg E-L, Winberg A, 2002b. Final report of the TRUE Block Scale project. 1. Characterisation and model development. SKB TR-02-13, Svensk Kärnbränslehantering AB.

Babuska V, Plomerova J, Sileny J, 1987. Structural model of the subcrustal lithosphere in central Europe,, in Composition, Structure and Dynamics of the Lithosphere-Asthenosphere Sysem, K, F. and C, F, Editors. 1987, American Geophysical Union: Washigton, D. C. p 239–272.

Barton C, La Pointe P, 1995. Ed. Fractals in the Earth Sciences. Plenum Press, New York. 265 p ISBN 0306448653.

Blenkinsop T G, Hull J, 1989. Thickness-displacement relationships for deformation zones; discussion and reply. Journal of Structural Geology. Vol. 11(8): p 1051–1054.

Bonilla M G, Mark R K, Lienkaemper J J, 1984. Statistical relations among earthquake magnitude, surface rupture length, and surface fault displacement. Bulletin of the Seismological Society of America. Vol. 74(6): p 2379–2411.

Bäckblom G, Munier R, 2002. Effects of Earthquakes on the Deep Repository for Spent Fuel in Sweden Based on Case Studies and Preliminary Model Results. SKB TR 02-24, Svensk Kärnbränslehantering AB.

Bödvarsson R, 2004. Swedish National Seismic Network (SNSN). A short report on recorded earthquakes during the fourth quarter of the year 2003. SKB P-04-24, Svensk Kärnbränslehantering AB.

Börgesson L, 1986. Model shear tests of canisters with smectite clay envelopes in deposition holes. SKB TR 86-26, Svensk Kärnbränslehantering AB.

Börgesson L, Johannesson L-E, Hernelind J, 2004. Earthquake induced rock shear through a deposition hole. Effect on the canister and the buffer. SKB TR-04-02, Svensk Kärnbränslehantering AB.

Chester F M, Logan J M, 1986. Implications for mechanical properties of brittle faults from observations of the Punchbowl fault zone, California, in International structure of fault zones, Wang, C.y, Editor. 1986, Birkhaeuser Verlag: Basel, Switzerland. p 79–106.

Clark R M, Cox S J D, 1996. A modern regression approach to determining fault displacement-length scaling relationships, in Special issue; Scaling laws for fault and fracture populations; analyses and applications, Cowie, P.A, Knipe, R.J, Main, I.G, and Wojtal, S.F, Editors. 1996, Pergamon: Oxford-New York, International. p 147–152.

Cowie P A, Scholz C H, 1992a. Displacement-length scaling relationship for faults; data synthesis and discussion. Journal of Structural Geology. Vol. 14(10): p 1149–1156.

Cowie P A, Scholz C H, 1992b. Physical explanation for the displacement-length relationship of faults using a post-yield fracture mechanics model. Journal of Structural Geology. Vol. 14(10): p 1133–1148.

Cowie P A, Shipton Z K, 1998. Fault tip displacement gradients and process zone dimensions. Journal of Structural Geology. Vol. 20(8): p 983–997.

Dong R, Ran H, Gao Z, 1993. The relationship between earthquake magnitude and length of active faults in China. Dizhen Dizhi = Seismology and Geology. Vol. 15(4): p 395–400.

Hakami E, Olofsson S-O, 2002. Numerical modelling of fracture displacements due to thermal load from a KBS-3 repository. SKB TR-02-08, Svensk Kärnbränslehantering AB.

Hirata T, 1989. Fractal dimension of fault systems in Japan; fractal structure in rock fracture geometry at various scales. Pure and Applied Geophysics. Vol. 131(1–2): p 157–170.

Huang F, Wang J, 1993. Relations of maximum fault displacement, maximum width of fault crush belt and fault length in northwestern Yunnan province. Xibei Dizhen Xuebao = Northwestern Seismological Journal. Vol. 15(2): p 71–75.

JNC, 2000a. Second progress report on research and development for the geological disposal of HLW in Japan. H12: Project to establish the scientific and technical basis for HLW disposal in Japan. Supporting Report 2 – Repository design and engineering technology. JNC TN1410 2000-003, JNC – Japan Nuclear Cycle Development Institute Japan.

JNC, 2000b. Second progress report on research and development for the geological disposal of HLW in Japan. H12: Project to establish the scientific and technical basis for HLW disposal in Japan. Supporting Report 3 – Safety assessment of the geological disposal system. JNC TN1410 2000-004, JNC – Japan Nuclear Cycle Development Institute Japan.

Johnston A C, 1987. Suppression of earthquakes by large continental ice sheets. Nature. Vol. 303: p 467–469.

Johnston J D, McCaffrey K J W, 1996. Fractal geometries of vein systems and the variation of scaling relationships with mechanism, in Special issue; Scaling laws for fault and fracture populations; analyses and applications, Cowie, P.A, Knipe, R.J, Main, I.G, and Wojtal, S.F, Editors. 1996, Pergamon: Oxford-New York, International. p 349–358.

KBS, 1983a. Final storage of spent nuclear fuel – KBS-3. Summary. KBS-3 Summary, Swedish Nuclear Fuel Supply Co/Division, SKBF/KBS.

KBS, 1983b. Final storage of spent nuclear fuel – KBS-3. Part III Barriers. KBS-3 Part III, Swedish Nuclear Fuel Supply Co/Division, SKBF/KBS.

KBS, 1983c. Final storage of spent nuclear fuel – KBS-3. Part IV Safety. KBS-3 Part IV, Swedish Nuclear Fuel Supply Co/Division, SKBF/KBS.

KBS, 1983d. Final storage of spent nuclear fuel – KBS-3. Part II Geology. KBS-3 Part II, Swedish Nuclear Fuel Supply Co/Division, SKBF/KBS.

KBS, 1983e. Final storage of spent nuclear fuel – KBS-3. Part I General. KBS-3 Part I, Swedish Nuclear Fuel Supply Co/Division, SKBF/KBS.

King G C P, 1992. Fractals and chaos in the earth sciences. Vol. 138. 1992, Basel, Switzerland: Birkhaeuser Verlag. ISBN.

Knott S D, Beach A, Brockbank P J, Brown J L, McCallum J E, Welbon A I, 1996. Spatial and mechanical controls on normal fault populations, in Special issue; Scaling laws for fault and fracture populations; analyses and applications, Cowie, P.A, Knipe, R.J, Main, I.G, and Wojtal, S.F, Editors. 1996, Pergamon: Oxford-New York, International. p 359–372.

Koestler A G, 1994. Scaling properties of extensional fault populations; the natural gap at the medium scale, in Fault populations, Anonymous, Editor. 1994, Geological Society of London: London, United Kingdom. p 21–23.

Korvin G, 1992. Fractal models in the earth sciences. 1992: Cambridge University Press. ISBN.

Kuivamäki A, 1986. Havaintoja Venejarven ja Ruosterjarven postglasiaalisista siirroksista Translated Title: Observations on the Venejarvi and Ruostejarvi postglacial faults. Tiedonanto YST. 1986, Espoo, Finland: Geologian Tutkimuskeskus, Ydinjatteiden Sijoitustutkimukset. p 20. ISBN.

Kujansuu R, 1964. Nuorista siirroksista Lapissa. (Recent Faulting in Lapland). Geologi Vsk. Vol. 16: p 30–36.

La Pointe P, Wallmann P, Thomas A, Follin S, 1997. A methodology to estimate earthquake effects on fractures intersecting canister holes. SKB TR 97-07, Svensk Kärnbränslehantering AB.

La Pointe P R, Cladouhos T, Follin S, 1999. Calculation of displacements on fractures intersecting canisters induced by earthquakes: Aberg, Beberg and Ceberg examples. SKB TR-99-03, Svensk Kärnbränslehantering AB.

La Pointe P R, Cladouhos T T, Outters N, Follin S, 2000. Evaluation of the conservativeness of the methodology for estimating earthquake-induced movements of fractures intersecting canisters. SKB TR-00-08, Svensk Kärnbränslehantering AB.

Lagerbäck R, 1988. Postglacial faulting and paleoseismicity in the Landsjärv area, northern Sweden. SKB TR 88-25, Svensk Kärnbränslehantering AB.

Larsson S Å, Tullborg E-L, 1993. Tectonic regimes in the Baltic Shield during the last 1200 Ma – A review. SKB TR 94-05, Svensk Kärnbränslehantering AB.

Lundqvist J, Lagerbäck R, 1976. The Pärve Fault: A late-glacial fault in the Precambrian of Swedish Lapland. GFF. Vol. 98(1): p 45–51.

Martel S J, 1989. Formation of segmented strike-slip fault zones, Mount Abbot Quadrangle, California, in Proceedings of Conference XLV; a workshop on Fault segmentation and controls of rupture initiation and termination, Schwartz, D.P. and Sibson, R.H, Editors. 1989, U. S. Geological Survey: Reston, VA, United States. p 246–259.

Morad S, Aldahan A, 2002. Djupförvarsteknik. Spatial and temporal distribution of mineral alterations in granitic bedrock around main deformation zones in the Äspö HRL, SE Sweden. SKB Technical Document TD-02-12, Svensk Kärnbränslehantering AB.

Muir Wood R, 1993. A review of the seismotectonics of Sweden. SKB TR 93-13, Svensk Kärnbränslehantering AB.

Munier R, 1995. Studies of geological structures at Äspö. Comprehensive summary of results. SKB HRL Progress Report 25-95-21, Svensk Kärnbränslehantering AB.

Munier R, Sandstedt H, Niland L, 1997. Förslag till principiella utformningar av förvar enligt KBS-3 för Aberg, Beberg och Ceberg. SKB Rapport R-97-09, Svensk Kärnbränslehantering AB.

Munier R, Stenberg L, Stanfors R, Milnes A G, Hermanson J, Triumf C-A, 2003. Geological site descriptive model. A strategy for the model development during site investigations. SKB R-03-07, Svensk Kärnbränslehantering AB.

Müller B, Zoback M-L, Fuchs K, Mastin L, Gregersen S, Pavoni N, Stephansson O, Ljungren C, 1992. Regional patterns of Tectonic stress in Europe, J. Geoph. Res. Vol. 97(B8): p 11783–11803.

Mörner N-A, 1979. The Fennoscandian uplift and late Cenozoic geodynamics: Geological evidence. Geojournal. Vol. 3.3.

Mörner N-A, 1989. Postglacial faults and fractures on Äspö. SKB HRL Progress report 25-89-24, Svensk Kärnbränslehantering AB.

Mörner N-A, 2003. Paleoseismicity of Sweden – a novel paradigm. 2003. ISBN 91-631-4072-1.

Olesen O, Lile O B, Henkel H, Ronning J S, Dalsegg E, 1989. Geophysical investigations of the postglacial Stuoragurra Fault, Finnmark, northern Norway, in 17th meeting of the Nordic Association for Applied Geophysics, Anonymous, Editor. 1989, Elsevier: Amsterdam, Netherlands. p 62–63.

Olesen O, Henkel H, Lile O B, Mauring E, Ronning J S, 1992a. Geophysical investigations of the Stuoragurra postglacial fault, Finnmark, northern Norway. Journal of Applied Geophysics. Vol. 29(2): p 95–118.

Olesen O, Henkel H, Lile O B, Mauring E, Ronning J S, Torsvik T H, 1992b. Neotectonics in the Precambrian of Finnmark, northern Norway, in Post-Cretaceous uplift and sedimentation along the western Fennoscandian Shield, Jensen, L.N, Riis, F, and Boyd, R, Editors. 1992b, Universitetsforlaget: Oslo, Norway. p 301–306.

Paananen M, 1987. Geophysical studies of the Venejärvi, Ruostejärvi, Suasselkä and Pasmajärvi postglacial faults in northern Finland. YST-59, Geological Survey of Finland Nuclear Waste Disposal Research Espoo.

Pegrum R M, 1984. Structural Development of the southwestern margin of the Russian-Fennoscandian Platform, in Petroleum Geology of the North European Margin. 1984, Norwegian Petrolium Society: Oslo. p 359 369.

Poteri A, Billaux D, Dershowitz W, Gómez-Hernández J J, Cvetkovic V, Hautojärvi A, Holton D, Medina A, Winberg A, 2002. Final report of the TRUE Block Scale projekt. 3. Modelling of flow and transport@ @. SKB TR-02-15, Svensk Kärnbränslehantering AB.

Pusch R, 2000. On the risk of liquefaction of buffer and backfill. SKB TR-00-18, Svensk Kärnbränslehantering AB.

Scholz C H, 1990. The mechanics of earthquakes and faulting. 1990, USA: Cambridge University Press USA. ISBN.

Shen B, 1993. Mechanics of fractures and intervening bridges in hard rocks, Engineering Geology Royal Institute of Technology Stockholm Sweden: Engineering Geology, Royal Institute of Technology, Stockholm

SKB, 1990. Granskning av Nils-Axel Mörners arbete avseende postglaciala strukturer på Äspö. SKB AR 90-18, Svensk Kärnbränslehantering AB.

SKB, 1992. SKB 91 – Final disposal of spent nuclear fuel. Importance of the bedrock for safety. SKB TR 92-20, Svensk Kärnbränslehantering AB.

SKB, 1999. Deep repository for spent nuclear fuel. SR 97 – Post-closure safety. Main report – Volume I, Volume II and Summary. SKB TR-99-06 Vol. I, Vol. II and Summary, Svensk Kärnbränslehantering AB.

SKB, 2003. Planning report for the safety assessment SR-Can. SKB TR-03-08, Svensk Kärnbränslehantering AB.

Skordas E, 1992. Some aspects of causes and effects of the seismicity in Fennoscandia with emphasis to Sweden. Doctoral dissertation. Uppsala University.

Skordas E, Kulhánek O, 1992. Spatial and temporal variations of Fennoscandian seismicity. Geophys. J. Int. Vol. 111: p 577–588.

Stanfors R, Ericsson L O, 1993. Post-glacial faulting in the Lansjärv area, Northern Sweden. Comments from the expert group on a field visit at the Molberget post-glacial fault area, 1991. SKB TR 93-11, Svensk Kärnbränslehantering AB.

Takase H, Benbow S, Grindrod P, 1998. Mechanical failure of SKB spent fuel disposal canisters. Mathematical modelling and scoping calculations. SKB TR-99-34, Svensk Kärnbränslehantering AB.

Talbot C J, Slunga R, 1989. Patterns of active shear in Fennoscandia, in Earthquakes at North-Atlantic passive margins: Neotectonics and postglacial rebound, Gregersen and Basham, Editors. 1989, Kluer Academic Publishers: Amsterdam. p 441–466.

Tanner V, 1930. Studier över kvartärsystemet i Fennoskandias nordliga delar IV. Bulletin de la Commission Géologique de Finlande. Vol. 88: p 594 pp.

Thatcher W, Hanks T C, 1973. Relation between earthquake magnitude and source parameters. Earthquake Notes. Vol. 44(1–2): p 63.

Thomas A L, 1993. Poly3D: A three dimensional polygonal element displacement discontinuity boundary element computer program with applications to fractures, faults and cavities in the earths crust, Version 1.0, Stanford University.

Thunehed H, Lindqvist L, 2003. Oskarshamn site investigation. Calculation of Fracture Zone Index (FZI) for KSH01A. SKB P-03-93, Svensk Kärnbränslehantering AB.

Tirén S A, Beckholmen M, Isaksson H, 1987. Structural analysis of digital terrain models, Simpevarp area, South-Eastern Sweden. Method study EBBA II. SKB HRL Progress report 25-87-21,

Wahlström R, Grünthal G, 2000a. Probabilistic seismic hazard assessment (horizontal PGA) for Sweden, Finland and Denmark using three different logic tree approaches, Soil Dynamics and Earthquake Engineering. Vol. 20: p 45–48.

Wahlström R, Grünthal G, 2000b. Probabilistic seismic hazard assessment (horizontal PGA) for Sweden, Finland and Denmark using the logic tree approach for regionalization and nonregionalization models, Seismological Research Letters. Vol. 72(1): p 33–45.

Wells D L, Coppersmith K J, 1994. New empirical relationships among magnitude, rupture length, rupture width, rupture area, and surface displacement. Bulletin of the Seismological Society of America. Vol. 84(4): p 974–1002.

Werme L O, Sellin P, 2001. The performance of a copper canister for geologic disposal of spent nuclear fuel in granitic rock. SKB, Svensk Kärnbränslehantering AB.

Werme L O, Sellin P, 2003. The performance of a copper canister for geologic disposal of spent nuclear fuel in granitic rock, In: Prediction of long term corrosion behaviour in nuclear waste systems. Proceedings of an international workshop Cadarache France 2002. pp 395–411: Svensk Kärnbränslehantering AB.

Vermilye J M, 1996. The growth of natural fracture systems: A fracture mechanics approach. Ph. D thesis. Colombia University.

Vermilye J M, Scholz C H, 1998. The Process zone. A microstructural view of fault growth, J. Geophys. Res. Vol. 103(B6): p 12223–12237.

Winberg A, Andersson P, Byegård J, Poteri A, Cvetkovic V, Dershowitz W, Doe T, Hermanson J, Gómez-Hernández J J, Hautojärvi A, Billaux D, Tullborg E-L, Holton D, Meier P, Medina A, 2003. Final report of the TRUE block scale project. 4. Synthesis of flow, transport and retention in the block scale. SKB TR-02-16, Svensk Kärnbränslehantering AB.

Vuorela P, Kuivamäki A, Paananen M, 1987. Neotectonic bedrock movements. A preliminary survey of the Pasmajärvi fault. YST-57, Geological Survey of Finland Nuclear Waste Disposal Research Espoo.

Appendix 1a

Flac3D analysis

Shear Displacement on Fractures due to Seismic Movements

Mark Christiansson, Itasca Consulting Inc
Minneapolis USA

January 2001

A1a Executive summary

Six FLAC3D /ITASCA, 1997/ models were run to establish the amount of dislocation that may occur across a frictionless fracture during an earthquake. The applied motions were calculated to represent a Richter 6.0 magnitude earthquake at distances of 2 km and 10 km from the fracture. The motions were applied to models containing either a horizontal fracture or a fracture dipping at 45°. The 45° fracture model was run with the dip direction oriented both parallel and perpendicular to the vertical plane of the earthquake fault. The table below shows the maximum dislocations that occur during the earthquake. Because the fracture is frictionless in this study, all dislocations relax to zero after the earthquake motions have ceased.

Maximum Shear Displacement of Fracture for Magnitude 6 Earthquake.

Dip Angle	10 km	2 km	
0°	0.16 cm	0.58 cm	
45°	0.07 cm	0.18 cm	(dip direction perpendicular to fault strike)
45°	0.08 cm	0.28 cm	(dip direction parallel to fault strike)

Contents

A1a-1 Introduction

/La Pointe et. al 1997/ conducted a numerical analysis on the potential for fracture displacements due to earthquake motions to investigate the concern that fracture displacements could cause damage to canisters placed in a radioactive waste repository. In the section entitled “Limitations,” the authors state that dynamic effects were ignored and that “The linear elasticity assumption should be conservative, in that all of the earthquake energy is dissipated in slip along existing fractures rather than in plastic or ductile rock deformation, thus maximizing estimated displacements.” This statement is misleading in the sense that it implies that the study is conservative because of the assumption of linear elasticity. The issue of whether the study is conservative when compared to a dynamic analysis is not addressed.

The study presented here is a simple demonstration of the expected magnitude of dislocations that may occur along pre-existing fractures when the effects of dynamics are not ignored. It is a physical fact that the effect of a static load or displacement applied to an area of a certain radius decays with distance within only a few multiples of that radius. The motions due to a dynamic source, such as an earthquake, will have effects at much greater distances. When shear waves generated by an earthquake encounter a rock fracture, some portion of the energy may not pass across the fracture. The amount of transmission is dependent on the properties of the fracture.

For the purposes of direct comparison, the models used in this study were designed to mimic the conditions used in the study by La Pointe. Of most significance is the lack of friction on the target fracture. A frictionless fracture cannot transfer shear waves; the shear waves are reflected by the fracture. The result of this is that the movements of one side of the fracture will be out of phase with the other side by approximately the amount of the shear-wave travel time. In addition, the model is assumed to be stress-free initially. This assumption has little effect when coupled with the assumption of the frictionless surface, but it would be significant if friction were included.

The transmission of earthquake motions is difficult to model for nearby epicenters. Ideally, the wave motions would be described uniquely for each gridpoint on the model boundary. This approach is not employed in this study, and it is assumed that the earthquake is deep and distant enough that the motions can be described by a planar wave applied on the bottom of the model.

The motions applied in the model were calculated by Applied Seismology Consultants Ltd. The assumptions used in the calculations of these movements are given in Appendix 1b. Of particular interest is the authors' recommendation that the most appropriate type of earthquake to be used in the study would be dip-slip. This is in contrast to the strike slip assumption used in the study by La Pointe.

A1a-2 FLAC3D model

FLAC3D is a fully dynamic three-dimensional finite-difference code. The decision to use FLAC3D rather than a discontinuum code such as 3DEC was based on FLAC3D's ability to model a limited number of fractures and its free-field boundary. Viscous boundary conditions are used on the sides and the bottom of the FLAC3D model. The viscous boundaries absorb energy, thereby preventing reflections. The free-field boundary prevents the viscous boundaries on the sides of the models from absorbing incident energy that is moving parallel to the edge. This helps maintain the shape of the input seismic wave.

Six FLAC3D /ITASCA, 1997/ models were run to establish the amount of dislocation that may occur across a frictionless fracture during an earthquake. The applied motions were calculated to represent a Richter 6.0 magnitude earthquake at distances of 2 km and 10 km from the fracture. The motions were applied to models containing either a horizontal fracture or a fracture dipping at 45°. The 45° fracture model was run with the dip direction oriented both parallel and perpendicular to the vertical plane of the earthquake fault.

An analysis of the frequencing spectrum in the earthquake data indicates that the maximum frequency is 1 Hz. The shear-wave velocity is 3.3 km/sec. Using Equation (A1a-1), this gives
a maximum zone length of 330 m:

$$\Delta l \leq \frac{f\, C_s}{10} \qquad \text{Equation A1a-1}$$

where Δl is the maximum zone dimension, f is the maximum frequency, and C_s is the shear-wave velocity. The zone sizes in the FLAC3D model are smaller than this value.

Figure A1a-1 shows the FLAC3D grid used to model the horizontal fracture orientations. The dimension of the entire model is 2,000 m × 2,000 m × 1,000 m. Figure A1a-2 shows the same model with the top removed to show the frictionless fracture in red. Figure A1a-3 shows the FLAC3D grid used in the 45° orientation case. Figure A1a-4 shows the model with the top removed to show the frictionless fracture in red. In all cases, the fracture is a 200-m square in the center of the model.

Viscous boundaries are applied on all sides and on the bottom. This prevents reflection of secondary seismic waves. The top surface is free and will reflect waves. The sides of the model also have a dynamic free-field boundary that prevents the absorption of the applied primary seismic wave.

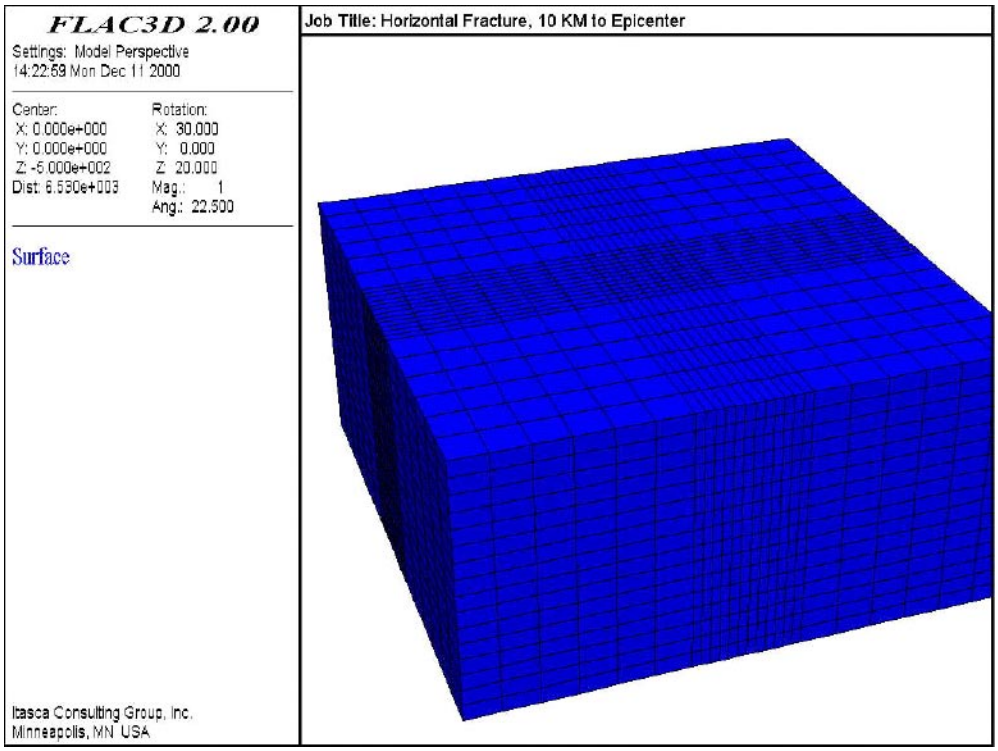

Figure A1a-1. *FLAC3D Grid for Horizontal Fracture Case.*

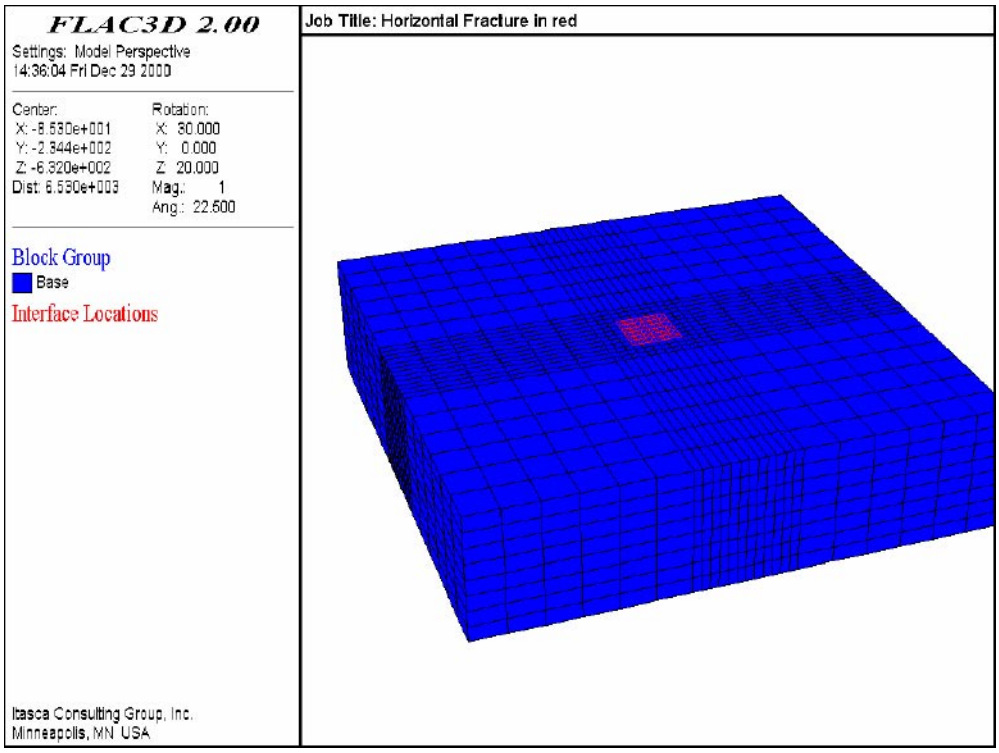

Figure A1a-2. *FLAC3D Grid for Horizontal Fracture Case. (The top is removed; the fracture is in red.)*

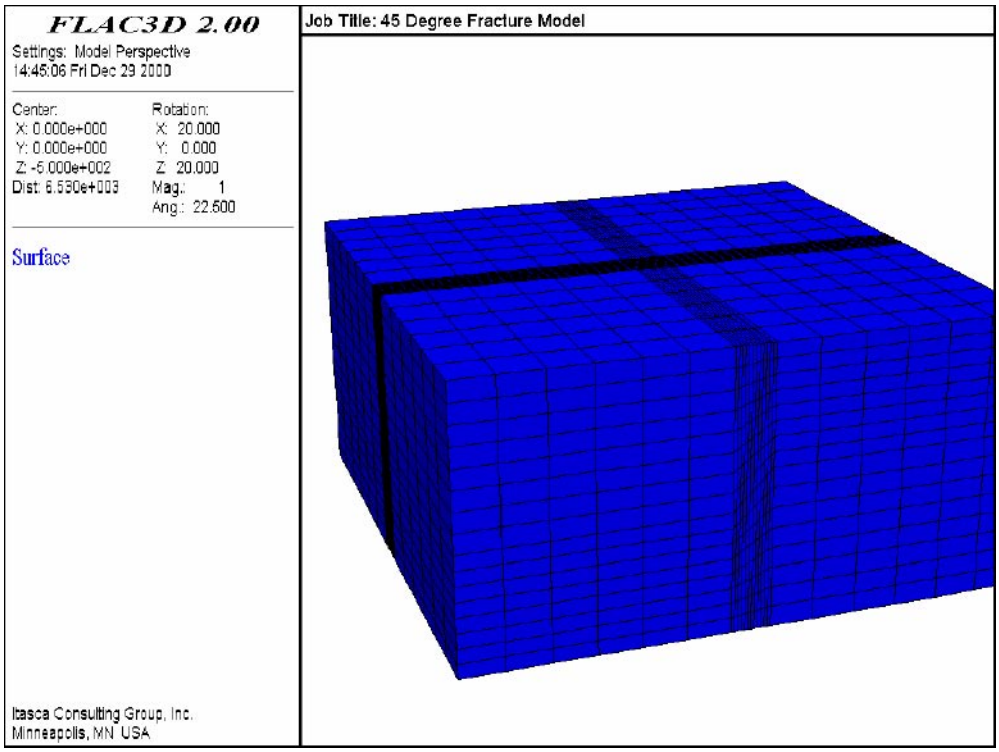

Figure A1a-3. *FLAC3D Grid for 45° Fracture Case.*

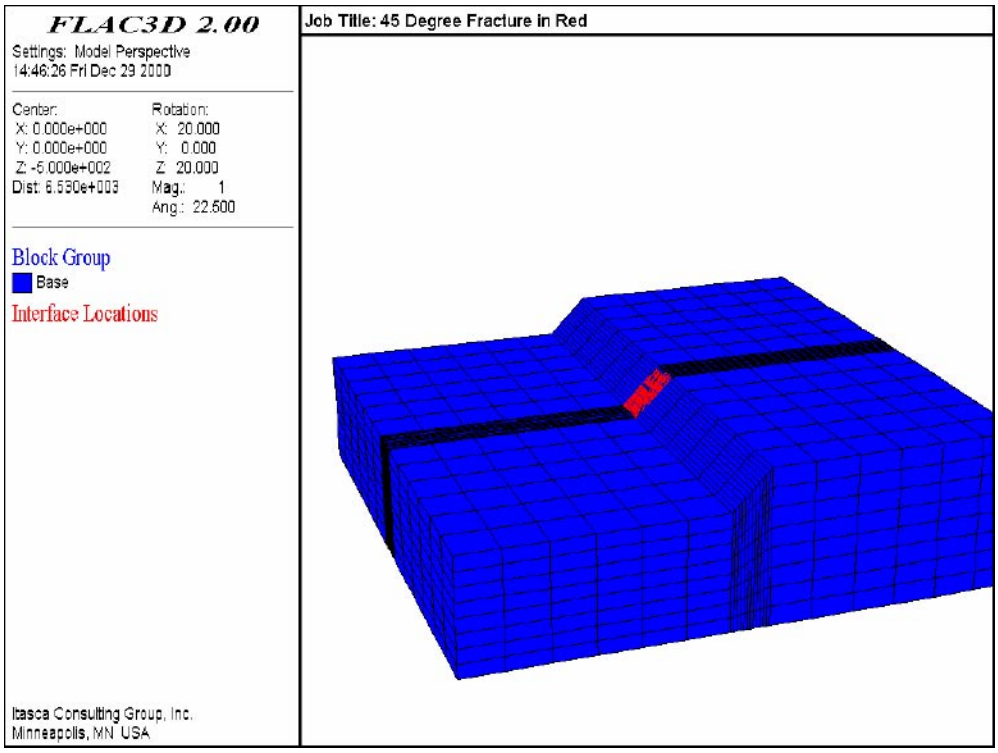

Figure A1a-4. *FLAC3D Grid for 45° Fracture Case. (The top is removed; the fracture is in red.)*

A1a-3 Properties

The rock mass is modeled as a homogeneous elastic mass with the following material properties:

Density	2,700 Kg/m^3
Young's Modulus	75 Gpa
Poisson's Ratio	0.25

The fracture has the following properties:

Friction	0.0
Cohesion	0.0
Tension	0.0
Normal Stiffness	10 GPa/m
Shear Stiffness	10 GPa/m

A1a-4 Seismic input

Because there is a viscous boundary at the base of the model, it is not possible to define the seismic input as a velocity-vs-time history, as is usual. In this case, a stress-vs-time history is applied, in which the stress corresponds to the velocity according to the following relations:

$$\Phi_n = 2\Delta C_p V_n \qquad \text{Equation A1a-2}$$

$$\Phi_s = 2\Delta C_s V_s \qquad \text{Equation A1a-3}$$

where:

F_n = applied normal stress,
F_s = applied shear stress,
D = mass density,
C_p = speed of p-wave propagation,
C_s = speed of s-wave propagation,
V_n = normal particle velocity in the incident wave, and
V_s = shear particle velocity in the incident wave.

Following the recommendation from the seismology report (Appendix 1b), the input record of a dip-slip earthquake was used. Note that the dip-slip mechanism results in significant motions in only the vertical and x-plane. There is no relative motion in the plane parallel to the fault. Figure A1a-5 shows the conceptual geometry of the analysis. The fault is at a distance of either 2 km or 10 km from the target fracture. In all cases, it is assumed that the motion at the base of the FLAC3D model is a plane wave and all base gridpoints move together. Figure A1a-6 shows the velocity-vs-time histories for the vertical and X-Y shear planes for the 2-km distance. The velocities for the 10-km distance can be seen in Figure A1a-7. Figure A1a-8 and Figure A1a-9 show the same data converted to stress-vs-time histories used as input to FLAC3D for the 2-km and 10-km cases, respectively.

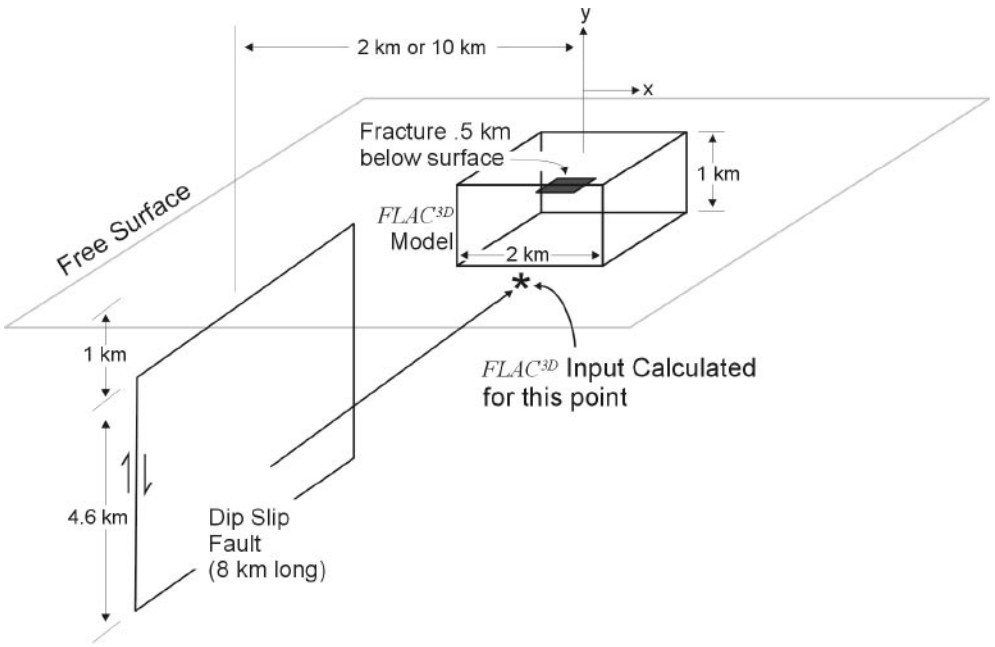

Figure A1a-5. *Conceptual Geometry.*

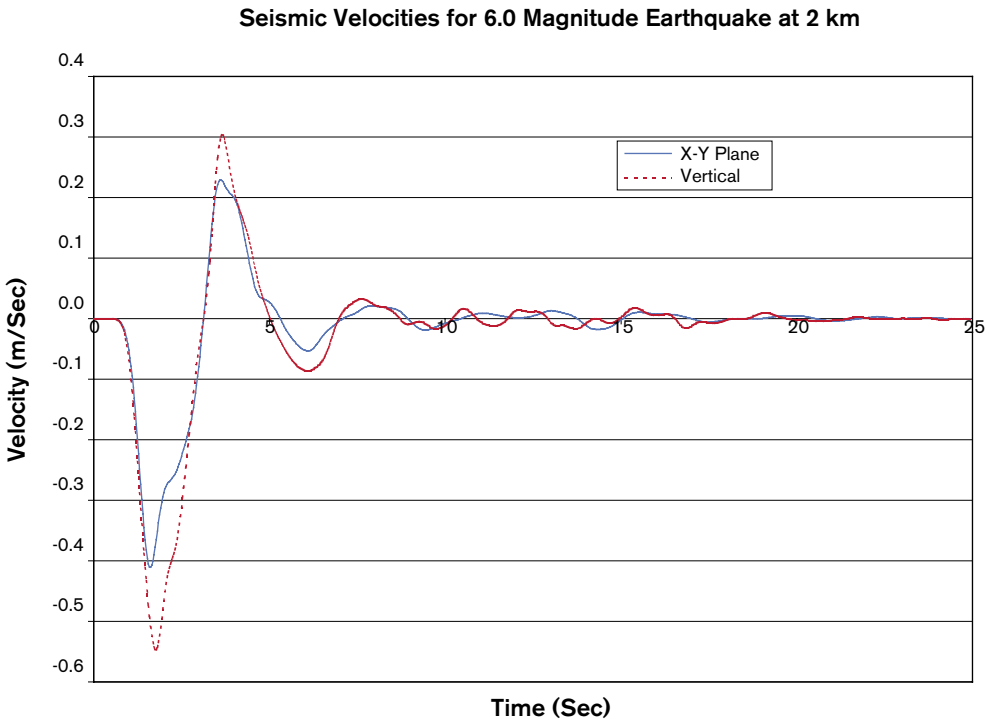

Figure A1a-6. *Velocity-Time Record for Magnitude 6.0 Earthquake at a Distance of 2 km.*

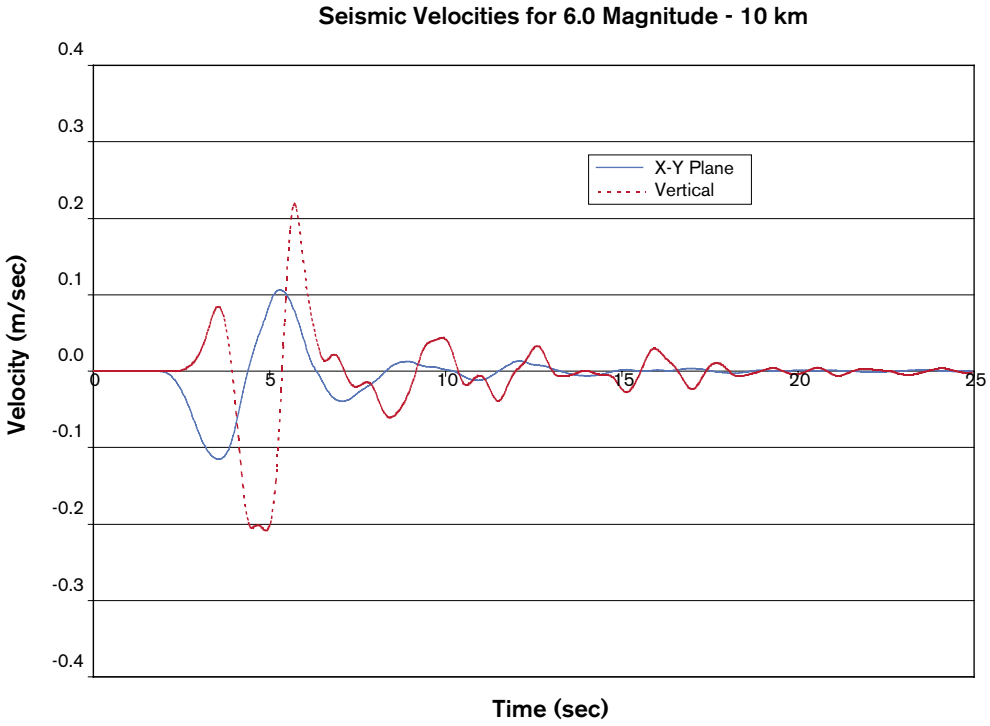

Figure A1a-7. *Velocity-Time Record for Magnitude 6.0 Earthquake at a Distance of 10 km.*

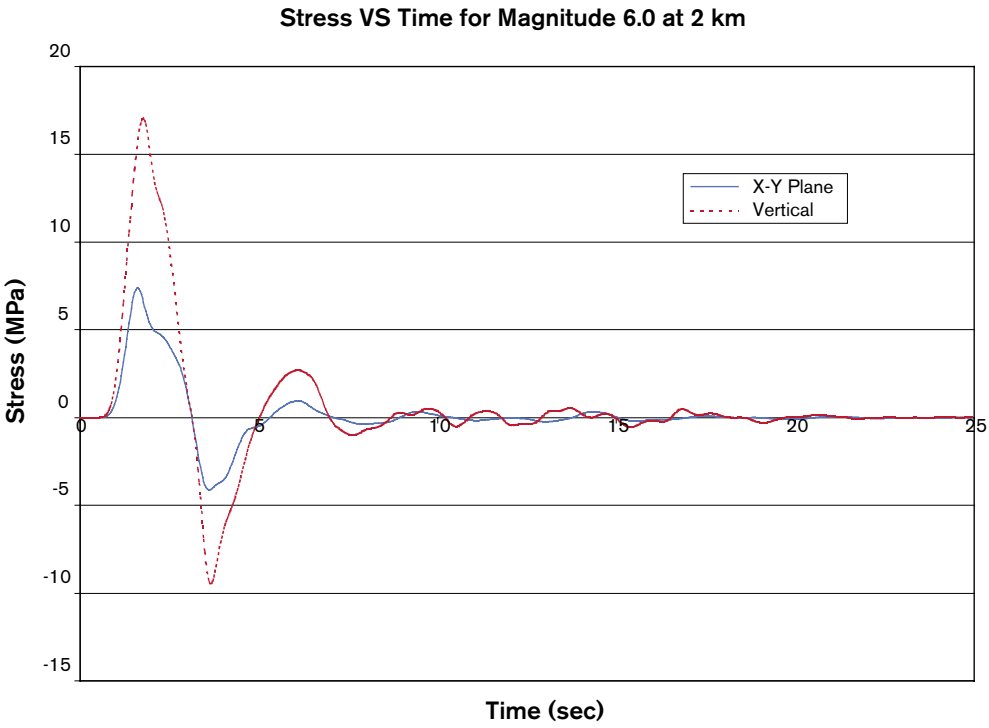

Figure A1a-8. *Stress-Time Record for Boundary Condition in FLAC3D. (Values are calculated from velocity record used in Equation A1a-2 and Equation A1a-3. This record is for a Magnitude 6.0 earthquake at a distance of 2 km.)*

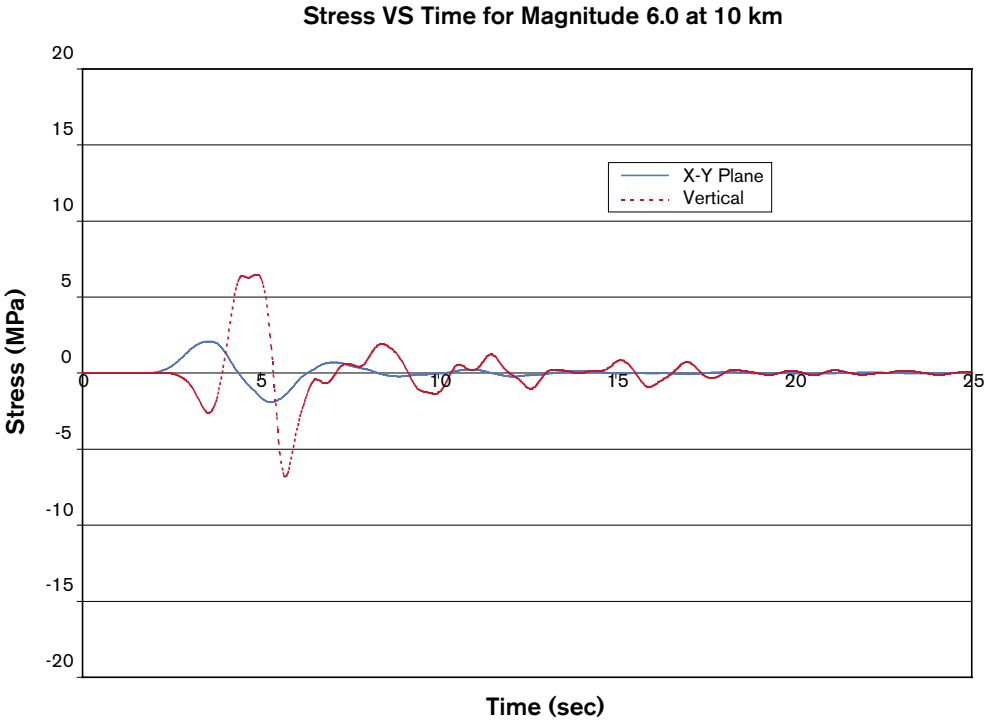

Figure A1a-9. *Stress-Time Record for Boundary Condition in FLAC3D. (Values are calculated from velocity record used in Equation A1a-2 and Equation A1a-3. This record is for a Magnitude 6.0 earthquake at a distance of 10 km.)*

A1a-5 Results

Six cases were analyzed. The horizontal fracture model was run with the input representing the 10-km and 2-km distances. The model with the 45° fracture was also run with the same 10-km and 2-km data. In addition to these two runs, the 45° model was also run for both distances, with the model rotated 90° so that the dip for the fracture was parallel to the earthquake fault. The shear displacements at the center of the fracture were calculated and saved as time histories.

Figure A1a-10 shows the history of the shear displacements at a point in the center of the fracture for a horizontal fracture at a distance of 2-km from the epicenter. The maximum shear displacement in this case was 0.58 cm. This is approximately double the 0.3-cm maximum (0.1-cm mean) displacement reported by La Pointe for this distance and seismic magnitude. Figure A1a-11 shows the time histories for the same model but with the input from the 10-km distant earthquake. Again, the maximum displacement of 0.16 cm is greater then the maximum of 0.07 cm (0.028-cm mean) reported by La Pointe.

Figure A1a-12 shows the maximum shear displacements for the case with a 45° fracture (dip direction perpendicular to the fault strike) at a distance of 2 km. The magnitude (0.18 cm) of the shear displacement is significantly smaller than the displacements of the horizontal fracture. For the 10-km distance, the shear displacement (0.07 cm), as shown in Figure A1a-13, is also smaller than that obtained for the horizontal fracture.

Figure A1a-14 and Figure A1a-15 show the shear displacements for the case in which the dip of the 45° fracture is parallel to the fault strike. For both distances (2 km and 10 km), the maximum shear displacements (0.28 cm and 0.08 cm) are similar to the case in which the dip direction is perpendicular to the fault strike.

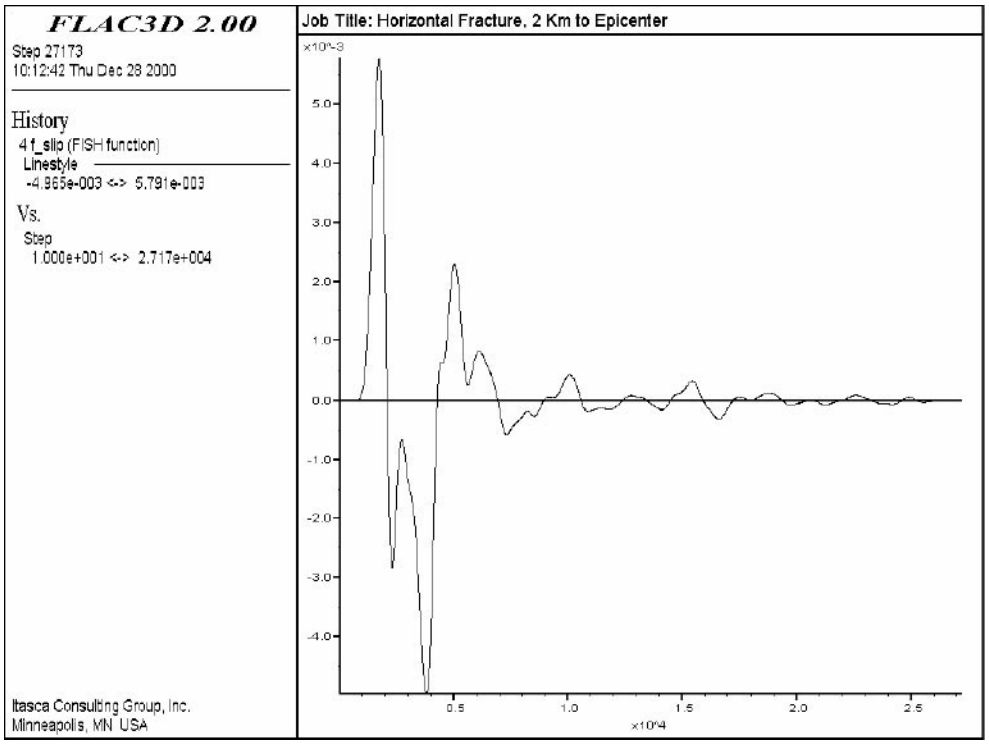

Figure A1a-10. *Shear Displacements at the Center of fracture for a 6.0 Magnitude Earthquake at a Distance of 2 km.*

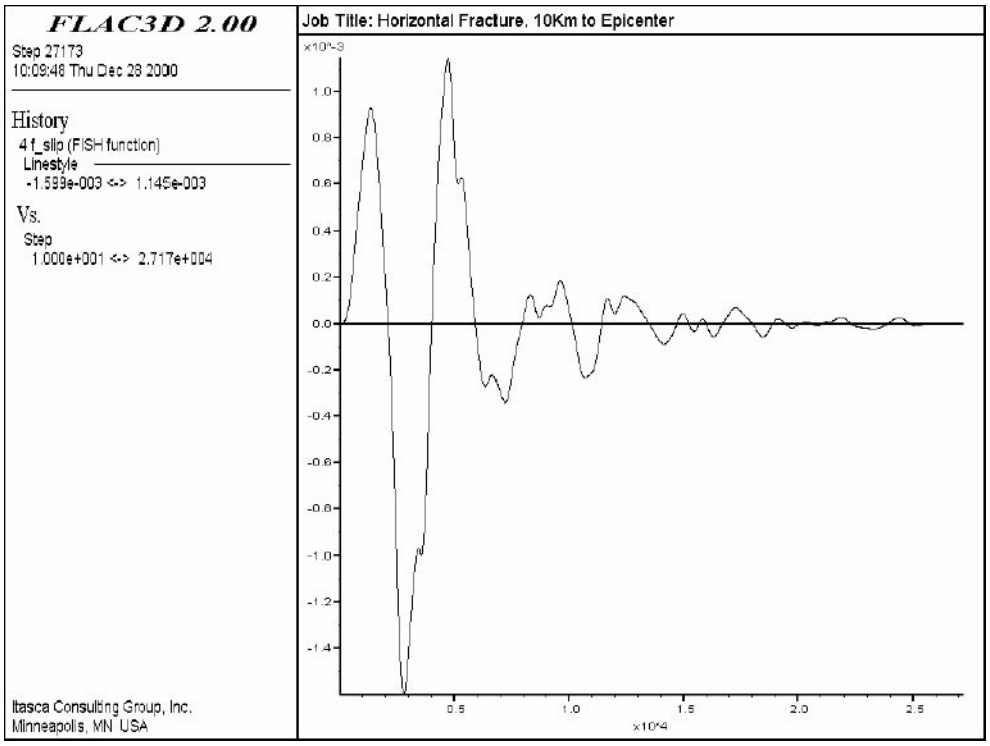

Figure A1a-11. *Shear Displacements at the Center of fracture for a 6.0 Magnitude Earthquake at a Distance of 10 km.*

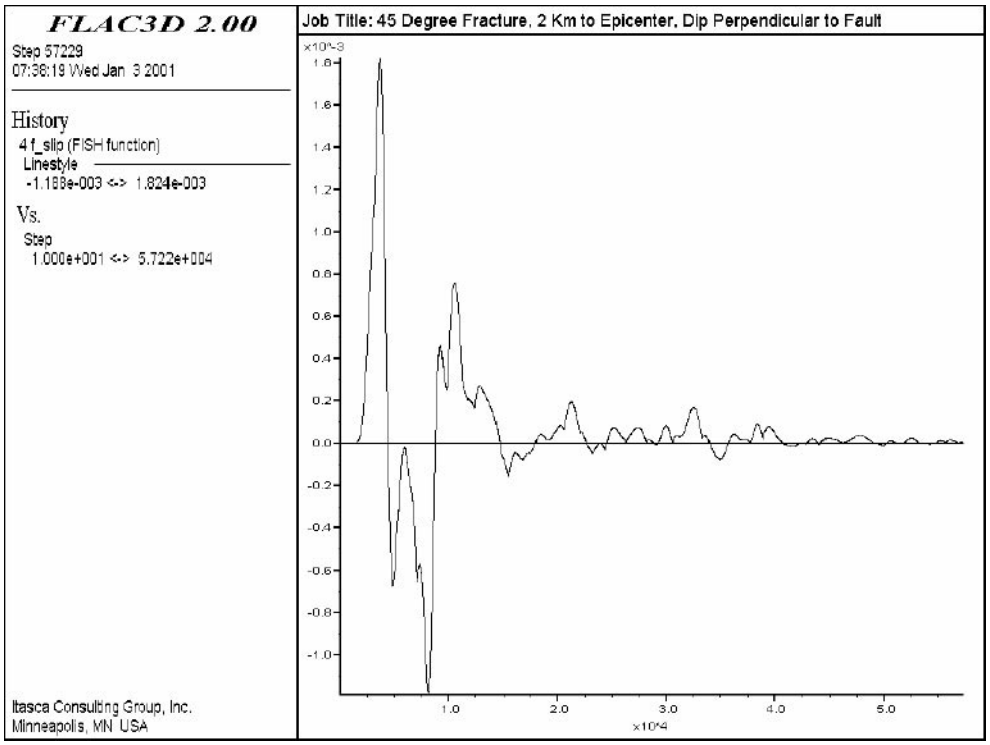

Figure A1a-12. *Shear Displacements at the Center of a 45° fracture for 6.0 Magnitude Earthquake at a Distance of 2 km (The dip direction of the fracture is perpendicular to the fault strike.).*

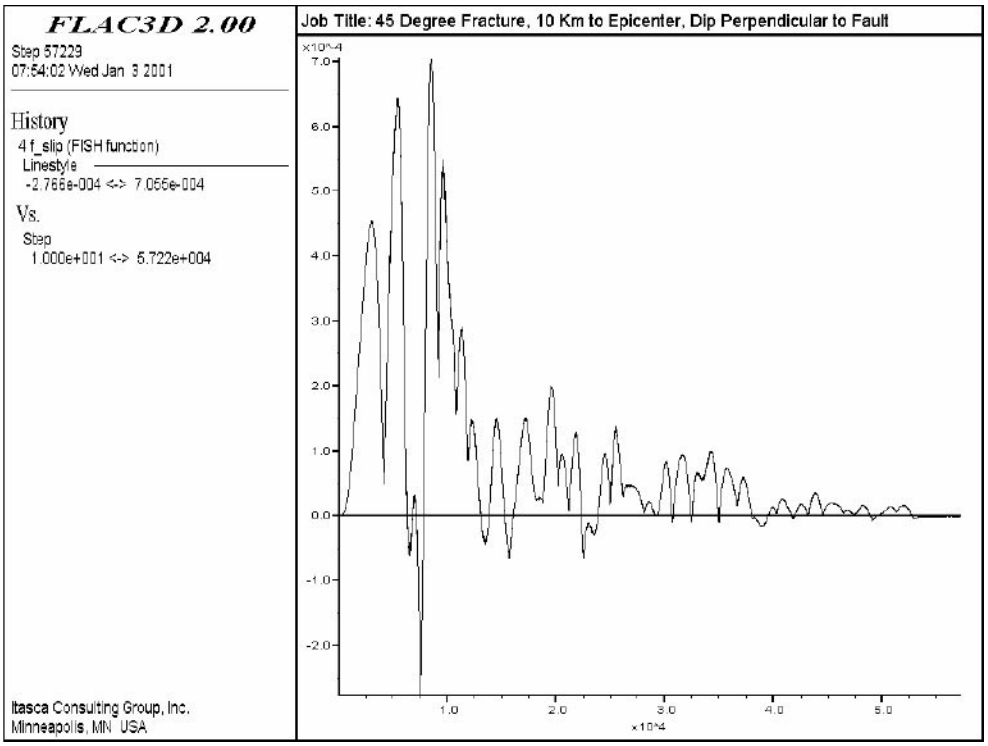

Figure A1a-13. *Shear Displacements at the Center of a 45° fracture for a 6.0 Magnitude Earthquake at a Distance of 10 km (The dip direction of the fracture is perpendicular to the fault strike.).*

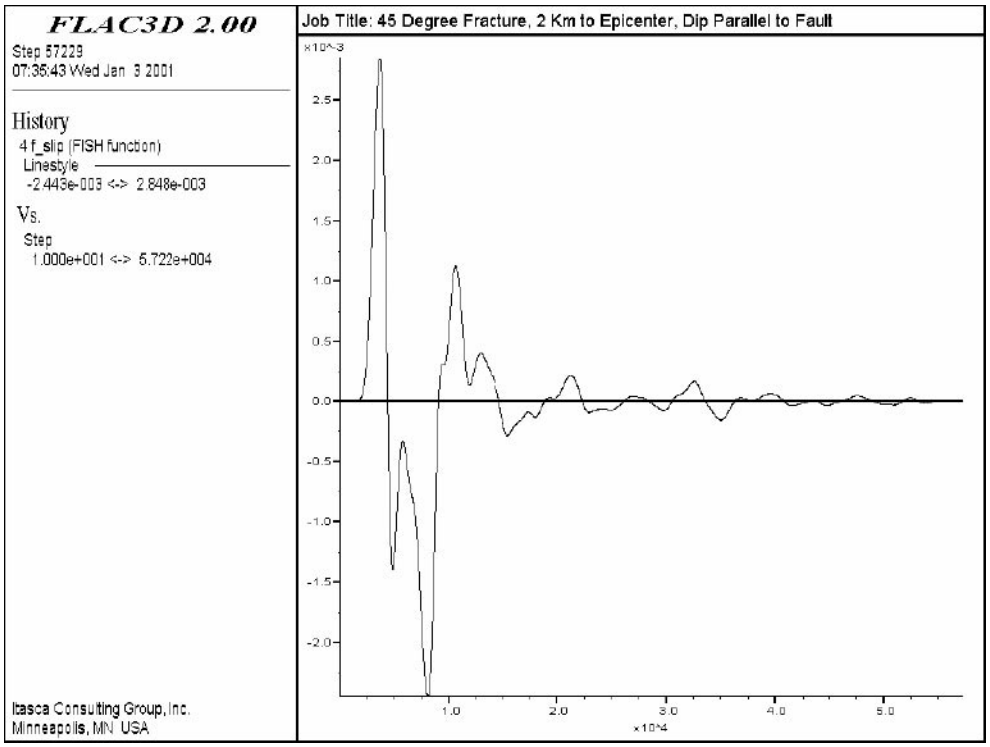

Figure A1a-14. *Shear Displacement at the Center of a 45° fracture for a 6.0 Magnitude Earthquake at a distance of 10 km (The dip direction of the fracture is parallel to the fault strike.).*

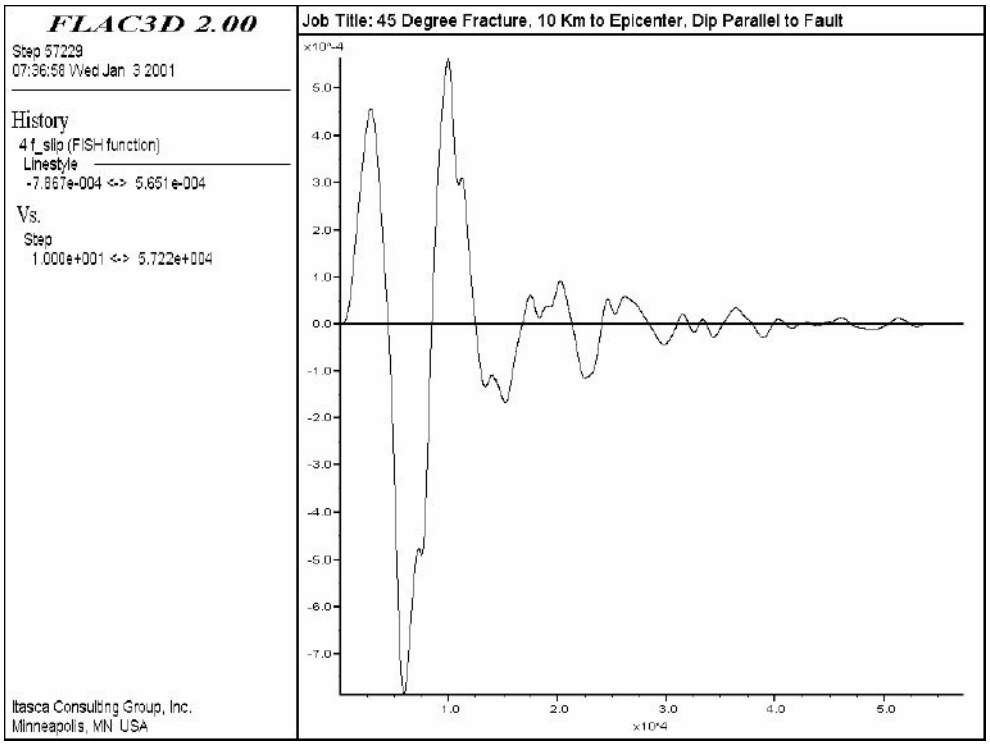

Figure A1a-15. *Shear Displacement at the Center of a 45° fracture for a 6.0 Magnitude Earthquake at a Distance of 10 km. (The dip direction is parallel to the fault strike.)*

A1a-6 References

ITASCA, 1997. FLAC3D, Fast Lagrangian Analysis of Continua in 3 Dimensions, Version 2.0,

LaPointe P, Wallmann P, Thomas A, Follin S, 1997. A methodology to estimate earthquake effects on fractures intersecting canister holes. SKB TR 97-07, Svensk Kärnbränslehantering AB.

Appendix 1b

WAVE analysis

Velocity-time histories resulting from a magnitude 6 earthquake in the vicinity of a sub-surface repository

Calum Baker, Applied Seismology Consultants Ltd, UK

Mark Hildyard, Department of Earth Sciences, Liverpool University, UK

Will Pettitt, Applied Seismology Consultants Ltd, UK

October 2000

A1b Executive Summary

The velocity field resulting from an earthquake on a fault located in the near-field (2–10 km distance) is modelled using a finite difference program /WAVE – Hildyard et al. 1995/. We have used rock mass properties supplied by the client and have assumed other model parameters using realistic values. Measurements of the velocity field are given that we feel are representative of an *intraplate* earthquake of Magnitude 6. This earthquake has a stress drop of 15 MPa that is bigger than would be expected in interplate tectonic regimes (3 MPa). The result is a higher amplitude velocity field with respect to earthquakes found at plate boundaries. We use a vertical fault, with dimensions calculated to produce the appropriate magnitude, and an aspect ratio (length/width) of 2. Considering that the modelling is for a repository positioned at approximately 400–1,000 m in depth, we also incorporate a free-surface, that represents the Earth's surface, 1 km above the fault. We test differences produced in the velocity field from the earthquake mechanism, by testing two mechanism end members; one has slip orientated parallel to the fault's strike, and one has slip parallel to the down-dip direction.

As would be expected from an earthquake in the near field we find the exact nature of the velocity field, as given by recorded waveforms, to vary considerably with azimuth and then to be different between the two mechanisms tested. However, the absolute amplitude of the velocity field does not vary considerably (within one order of magnitude) over the area of interest (2–10 km distance from the fault). For the majority of this area the velocity field is in the range 0.15–0.35 m/s for both mechanisms with a stress drop of 15 MPa. We find that the dip-slip earthquake produces a higher velocity field (approximately ×2) close to the free surface, and along the length of the fault out to approximately 5 km distance. This is due to amplification from reflections off the boundary. The velocity field therefore includes a considerable effect from this free surface and it is important to include this in the models, as we have done here. We also show there to be a difference in the velocity field experienced across a hypothetical repository volume of 800 × 800 m in plan generated by the time lag as it moves across. This will map into induced stresses across the repository.

We discuss differences anticipated in the velocity field through variations in the model parameters. We conclude that the exact nature of the velocity field (changes in waveform shape) is sensitive to the observation position relative to the earthquake mechanism and fault orientation, and the relative orientation of these to the free surface, of which there are an infinite number of possibilities to choose from. However, the general velocity field (variation in absolute amplitude across the model volume) described by Model 2a, produces measurements that are close to the maximum that could be produced by any earthquake/fault scenario relating to a Magnitude 6 earthquake, and gives a realistic representation for the velocity field in the immediate vicinity of such a large earthquake. This data should therefore be used by the client in further analysis.

Contents

A1b-1 Introduction

This report outlines results from the analysis of the dynamic velocity field resulting from slip on a fault in the vicinity of a proposed Underground Storage Facility/Repository. The velocity time histories resulting from this work are to be used as the inputs to a series of geomechanical models. The ultimate aim of these models is to assess whether the energy from an event close to a repository could result in significant displacement on fractures within the rock mass in which it is excavated, and thus whether the occurrence of a seismic event of this size represents a significant hazard to the safe operation of the facility.

A1b-2 Modelling procedure

The velocity time histories and associated results presented in this report have been computed using WAVE /Hildyard et al. 1995/, an explicit finite difference program developed by the CSIR division of mining and technology to model elastodynamic movements within rock masses. The reader is advised to reference /Hildyard et al. 1995/ for further information on WAVE, and for further related references.

A1b-3 Formulation of the model

A number of model parameters were specified for this modelling by the client in advance. These were chosen to reflect the properties of the rock mass at the site of interest. The size of the seismic event was also specified. The earthquake resulting from slip on the fault was to release energy equivalent to a Magnitude 6 event. The resulting wave-fields were to be recorded at distances of 2 and 10 km from the fault. Other parameters were not pre-defined. For these we have chosen realistic and appropriate values that we believe represent likely scenarios in the case of a real earthquake occurring. We have produced four different models in order to gauge the variation in results given by possible scenarios. Here we will present the formulation of the models.

In the case of a repository lying close to an active fault and at a depth of approximately 400 m, the velocity field, or equivalently, the maximum particle velocity experienced at a position in space, is primarily a function of the following:

a. the rock mass properties,
b. the stress drop of the earthquake (mapped into a fault area to produce an earthquake of Magnitude 6),
c. the seismic radiation pattern of the earthquake (this depends on the earthquake mechanism),
d. the orientation of the fault,
e. the proximity of the Earth's free surface.

The effect of these will be examined and their effect on the results will be discussed in Section 6

A summary of the rock mass properties is given in Table A1b-1. The primary assumptions of the modelling are that the material is elastic, linear and homogeneous. A discontinuity (fault) has then been built into the models. The fault has been chosen as a vertical plane of pre-defined dimension. In *WAVE*, the discontinuity must be aligned to a pre-defined

Cartesian grid. A vertical plane was chosen as the orientation of the fault rather than a horizontal plane for reasons discussed below. We will also describe the choice of fault size, and we will discuss the effect of fault orientation on the observed velocity field in Section 6.

We will show results from four models that vary in i) stress drop (fault size), ii) earthquake mechanism. Parameters for the models are given in Table A1b-2. We use two stress drops. The first, labelled Model 1, uses a stress drop ($\Delta\sigma$ = 3 MPa) consistent with typical tectonic earthquakes found at *interplate* boundaries. The second, labelled Model 2, uses a high stress drop ($\Delta\sigma$ = 15 MPa) that is the maximum that would be expected, and is consistent with *intraplate* earthquakes. For a discussion of earthquake stress drops, and further references, see /Scholz, 1990/. For each of the stress drops considered, we have chosen two earthquake mechanisms that represent the end members of slip orientation. The first (with suffix "a"), is a dip-slip (slip is vertical) mechanism, and the second (with suffix "b"), is a strike-slip (slip is horizontal) mechanism.

In the case of a repository close to the Earth's surface (400–1,000 m depth), another main contributor to increases in the velocity field is the location of the fault with respect to the free-surface. Increases in the velocity field are due to reflections off the free-surface that result in an amplification of the radiated energy. We have therefore included in the model such a free surface with the fault being positioned with its upper tip at 1 km below this surface. This approach, however, means that the velocity field recorded is also sensitive to the orientation of the fault with respect to the free surface as well as the position of the repository with respect to the radiation pattern from the earthquake. The repository is likely to be in an *intraplate* environment (i.e. away from tectonic margins) so, in this case, a near-vertical fault is more likely than a near-horizontal fault. We will discuss the effect of the free-surface on our results in Section 6.

The fault is defined within the model as two planar surfaces that move relative to one another. The slip initiates at a point (i.e. the hypocentre, defined as the centre of the fault) and moves out from this point across the fault surface at a velocity equal to $0.7 \times V_s$, the velocity of shear waves in the rock. The rise time for the slip (the time taken for the stress drop to occur at any point on the fault) has been defined. We have carried out tests that demonstrate that, within realistic limits, variations in the rise time do not affect the overall shape of the final waveforms. We have therefore chosen a value (0.5 seconds) that gives numerical advantages in the modelling.

The size of the fault is defined for each of the stress drops considered so that a Magnitude 6 earthquake is obtained with that stress drop. The fault size is calculated using the following approach:

1) An approximate fault size is defined depending upon an approximate area of the fault required.
2) The fault is then failed in *WAVE* as described above. The Seismic Moment, M_o, is then related to the slip on the fault by Equation A1b-1 where μ is the shear modulus of the medium and u is the slip observed over a small area of the fault, dA. The slip is integrated over the complete fault surface, of area A, to obtain the Seismic Moment. This, in turn, is related to the Shear-Wave Magnitude, M_s by Equation A1b-2 /Scholz, 1990/. The Surface-Wave magnitude is equivalent to a "Richter Magnitude" scale for earthquakes at this magnitude, and is a standard magnitude scale in seismology.

$$M_0 = \mu . \int u.dA \qquad \text{Equation A1b-1}$$

$$\log M_0 = 1.5 M_s + 9.1 \qquad \text{Equation A1b-2}$$

3) An iterative approach is then used to obtain a fault size that provides an earthquake of the defined stress drop and of Magnitude 6. The aspect ratio (L/W) of the fault is kept at approximately 2. This is realistic for faults in the upper crust.

The fault dimensions used for Models 1 and 2 respectively are given in Table A1b-2. Figure A1b-1 shows the fault-rupture time history for the $\Delta\sigma = 3$ MPa earthquake (Model 1) with the two mechanisms used. Figure A1b-2 shows Model 2 ($\Delta\sigma = 15$ MPa). Fault rupture occurs across the entire fault in approximately 2–3 seconds. The maximum slip on the fault occurs in the central region and is approximately 0.6 m for Model 1 and 2 m for Model 2. The strike-slip earthquake (e.g. Model 1b) has a slightly elongated rupture along the strike direction compared to the down-dip direction. The opposite is true for e.g. Model 1a. Note the differences in the fault size, for Model 1 and Model 2, that are required to generate the necessary earthquake of Magnitude 6 and the appropriate stress drop.

To produce the necessary Magnitude 6 earthquake the fault is large compared to the distances over which the velocity field measurements are taken. Recording at "2 and 10 km distance from the fault" therefore depends on the relative position of the fault with respect to the position in space at which the measurements are taken. In order to provide a representative selection of velocity records to the client, we have designed an array of 85 hypothetical seismic receivers around the fault (Figure A1b-3). The array covers all azimuths (0–90° from the fault plane, normal to parallel, due to symmetry) between

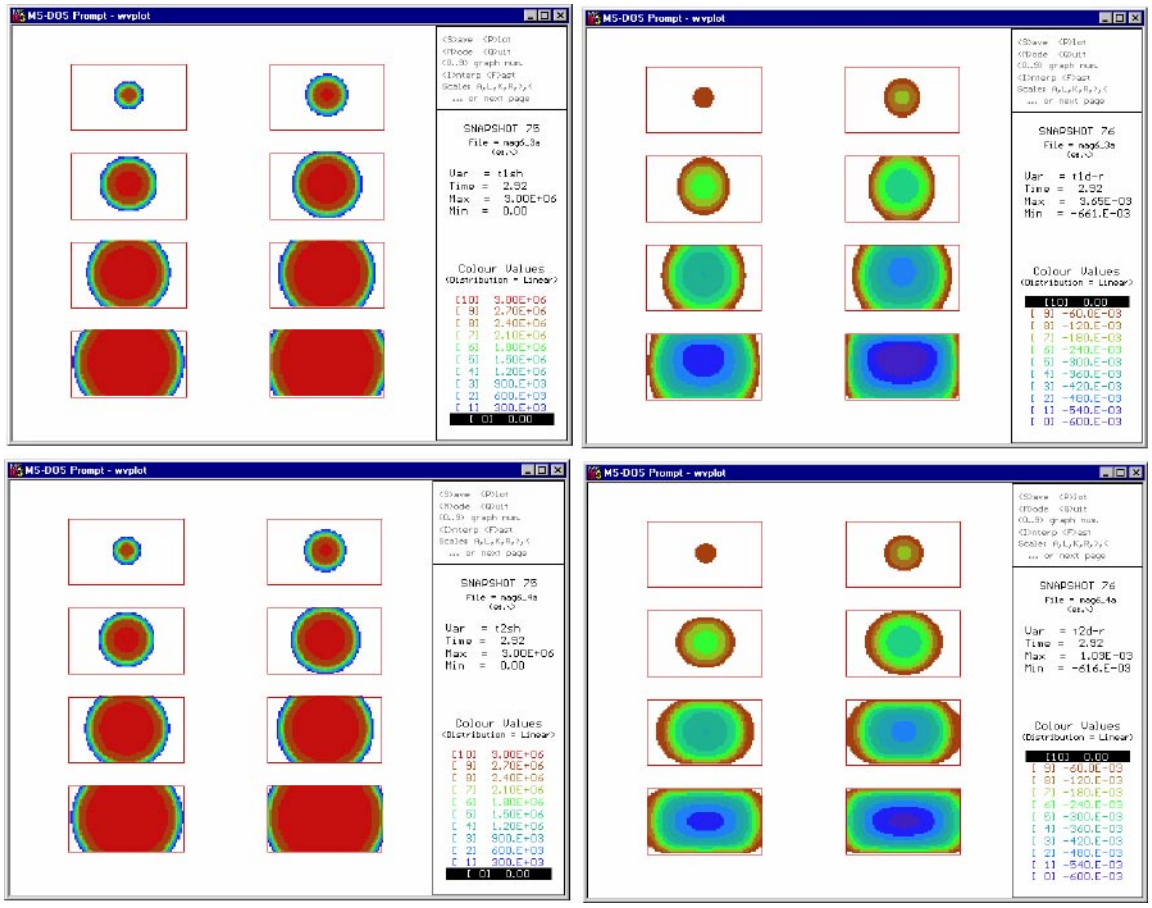

Figure A1b-1. *Rupture Time-history Sequence for Model 1 ($\Delta\sigma = 3$ MPa). Upper two plots are for Model 1a (dip-slip earthquake). Lower two plots are for Model 1b (strike-slip earthquake). Left hand two plots show shear stress (Pa) along the direction of slip. Right hand two plots show the slip displacement (m). For each plot, eight time-lapse images are shown, giving a longitudinal view of the fault at 0.75, 1.06, 1.37, 1.68, 1.99, 2.31, 2.62, 2.93 seconds after rupture initiation.*

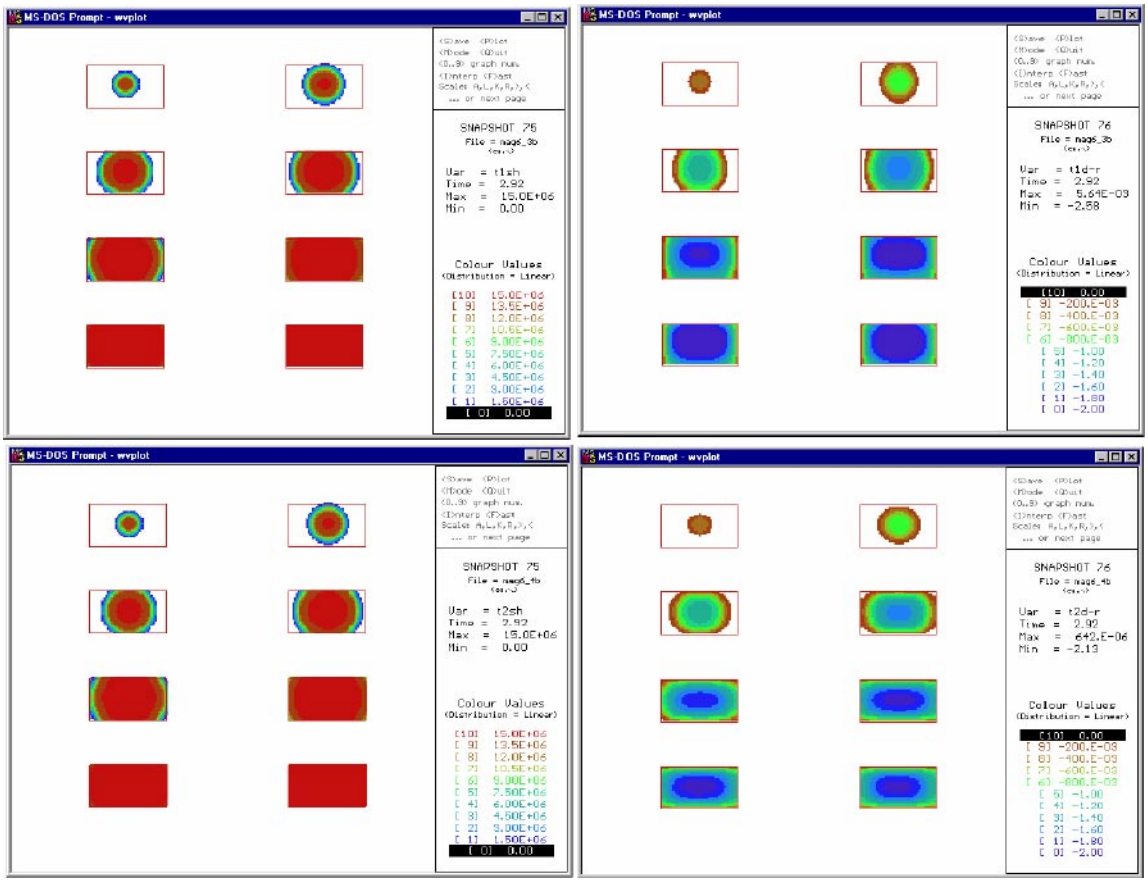

Figure A1b-2. *Rupture Time-history Sequence for Model 2 (Δσ = 15 MPa). Upper two plots are for Model 2a (dip-slip earthquake). Lower two plots are for Model 2b (strike-slip earthquake). Left hand two plots show shear stress (Pa) along the direction of slip. Right hand two plots show the slip displacement (m). For each plot, eight time-lapse images are shown, giving a longitudinal view of the fault at 0.75, 1.06, 1.37, 1.68, 1.99, 2.31, 2.62, 2.93 seconds after rupture initiation.*

2 and 10 km from both the vertical axis of the fault plane and from the tip of the fault plane. The sensors are located at the approximate depth of the repository of 400 m. This gives the concentric pattern of receivers shown in this figure. We have also included a grid of 50 seismic receivers (of dimensions 800 m northing × 800 m easting × 200 m depth) that represent a hypothetical repository, at an arbitrary position 10 km away from the fault's vertical axis. We shall use these receivers to test the effect of the velocity field travelling across such a repository. The model is a total of 140 × 50 × 140 finite difference zones in dimension, each zone being a 200 m cube, giving a 28 × 10 × 28 km model.

Two-dimensional plots of maximum particle velocity (defined here as the "velocity field") will be shown for each of the models performed. Variations in the velocity fields resulting from the models will be noted and used to show how the models depend on the parameters used. The maximum velocity is defined as:

$$V = \sqrt{V_x^2 + V_y^2 + V_z^2} \qquad \text{Equation A1b-3}$$

where e.g. V_x is the velocity recorded along the X Cartesian axis. The X, Y, Z co-ordinate system is defined with X in positive east, Y in positive up and Z in positive south. Velocity waveforms for each of the three components (and at each of the seismic receivers shown in Figure A1b-3) will be provided from the model with the highest observed velocity field.

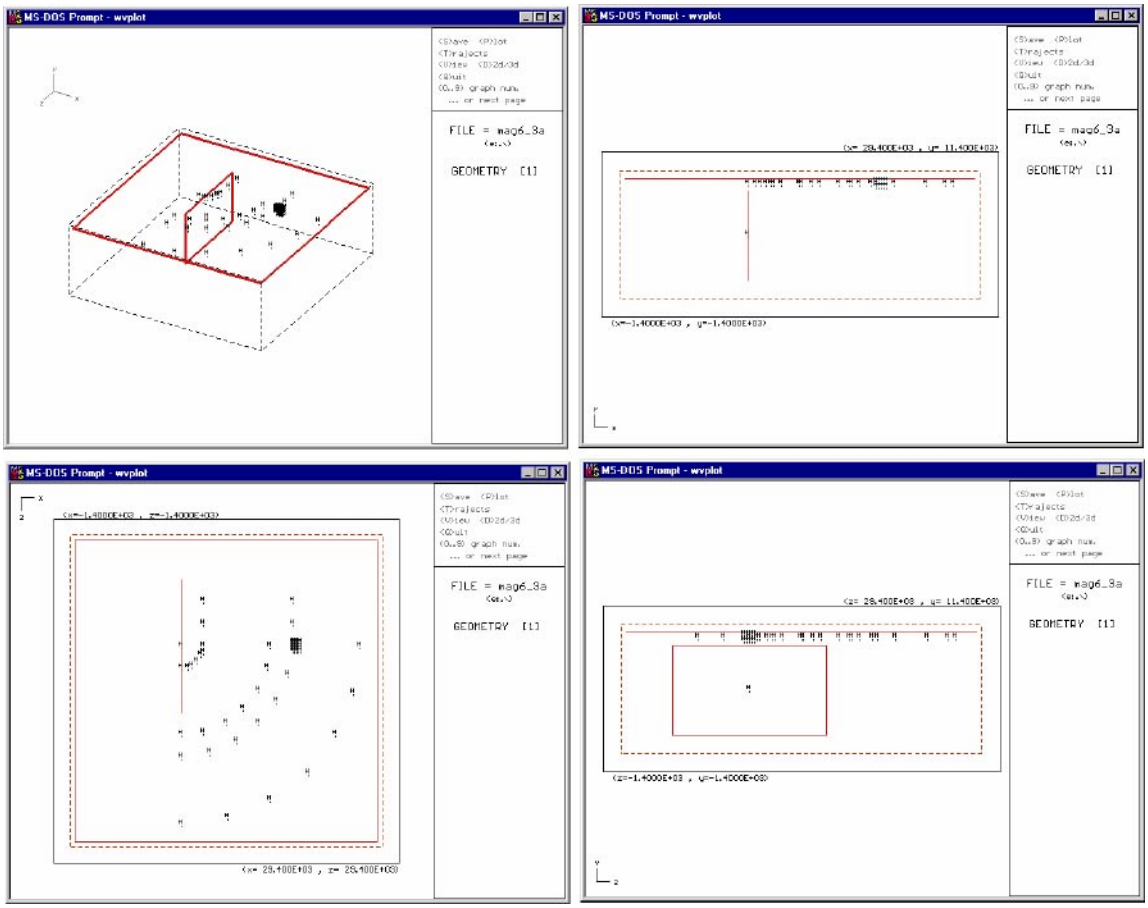

Figure A1b-3. *Locations for the 85 seismic receivers used in the model to provide velocity records. Upper Left: Perspective View. Upper right: cross sectional view. Lower Left: Plan view. Lower Right: Longitudinal View. The fault shown is for Model 1 with a dimension of Length (along strike) = 12 km, Width (down dip) = 7 km, and is positioned with its upper tip 1 km below the free surface.*

A1b-4 Results

Figure A1b-4 gives plots of the velocity field for Model 1a. It should be noted that the plots are not all contoured to the same velocity range in order to show the pattern of the velocity field across the area of interest (out to 10 km from the fault). The maximum in the velocity range is indicated on each plot. The red square is the projection of the fault boundaries onto the plot. The highest velocities are observed in the upper 0–2 km of Model 1a. This is due to reflections off the free surface causing an approximate amplification of ×2. It is therefore important that the free surface is included in the model.

Figure A1b-5 gives the velocity field for Model 1b, differing in only earthquake mechanism from Model 1a. The difference in the spatial variation of the velocity field between the two earthquake mechanisms is very apparent. For model 1a, high velocity zones are orthogonal to the fault orientation with velocities of 0.05 m/s observed at 10 km distance from the fault plane and at 400 m depth. For model 1b, velocities are highest along the strike direction with velocities of 0.05 m/s observed at 10 km from the fault tip. The overall range in the velocity field is not very different between the two models with the 0.05 m/s velocity contour covering the majority of the area of interest for both models.

(a) Vmax=0.2 m/s

(b) Vmax=0.2 m/s

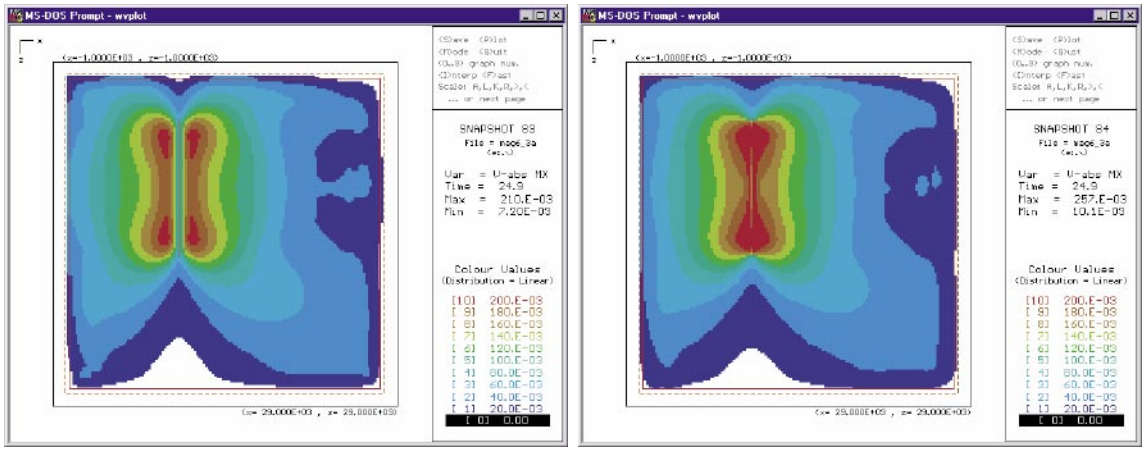

(c) Vmax=0.2 m/s

(d) Vmax=0.1 m/s

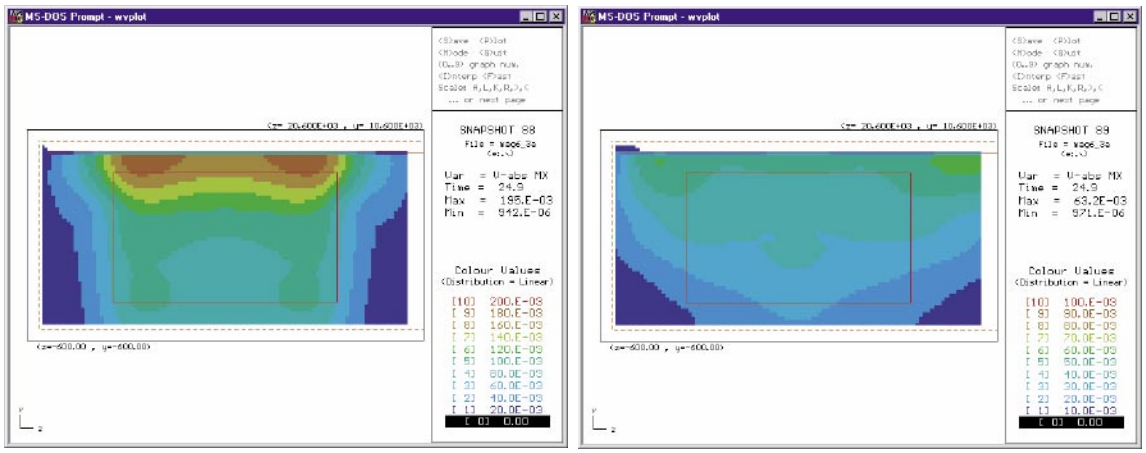

(e) Vmax=0.1 m/s

(f) Vmax=0.05 m/s

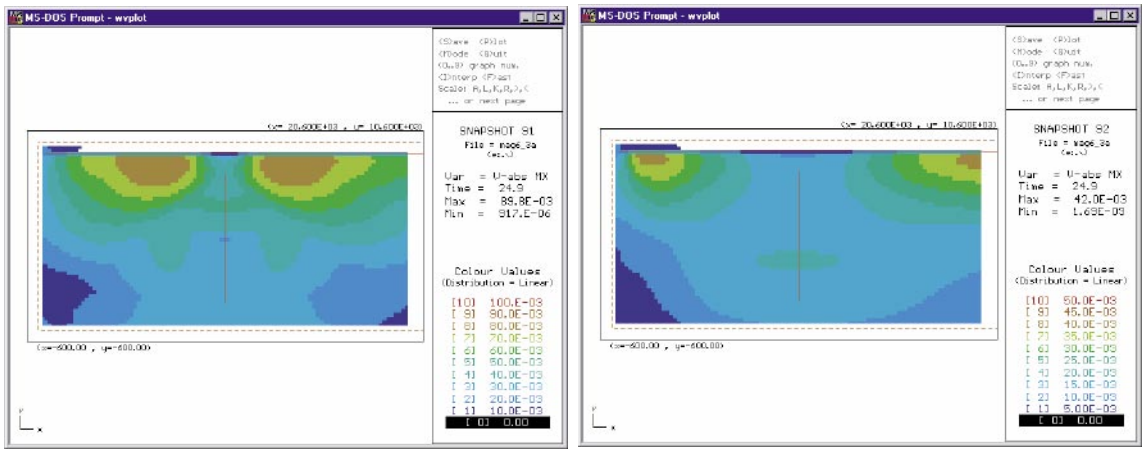

Figure A1b-4. *The velocity field generated by Model 1a. Plots show the maximum particle velocity experienced over the model volume. The fault has a length of 12 km and width of 7 km. The contour colour scale is chosen to view the variation in velocity across the volume and is not identical for each plot – Vmax gives upper velocity range. a) Plan view at 400 m depth. b) Plan view at 1,000 m depth. c) Longitudinal view at 2 km from the fault surface. d) Longitudinal view at 10 km from the fault surface. e) Cross sectional view at 2 km from the fault tip. f) Cross sectional view at 10 km from the fault tip.*

(a) Vmax=0.1 m/s

(b) Vmax=0.1 m/s

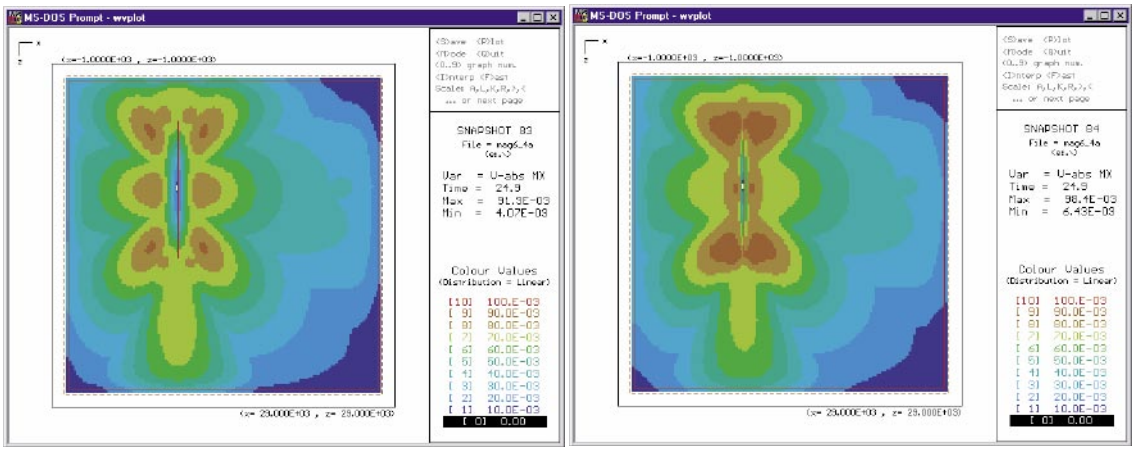

(c) Vmax=0.1 m/s

(d) Vmax=0.05 m/s

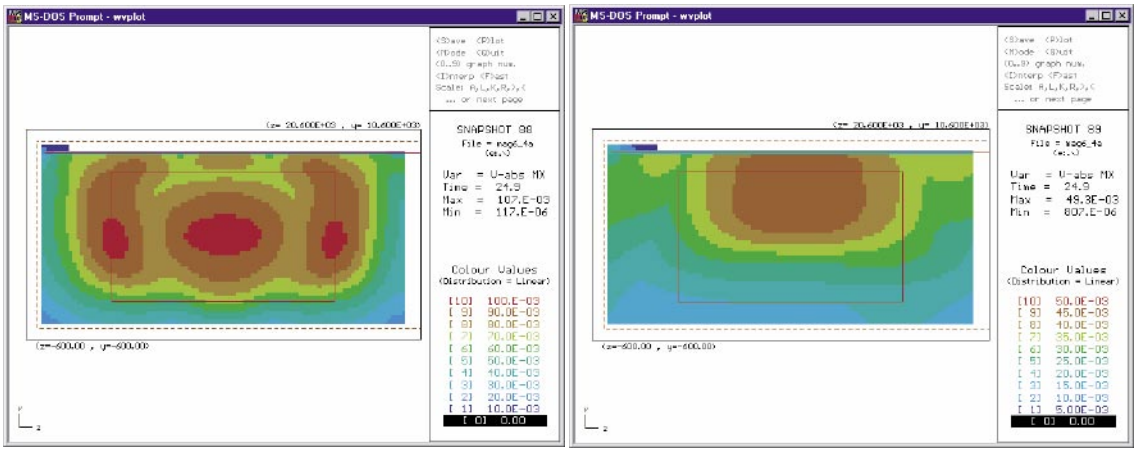

(e) Vmax=0.07 m/s

(f) Vmax=0.07 m/s

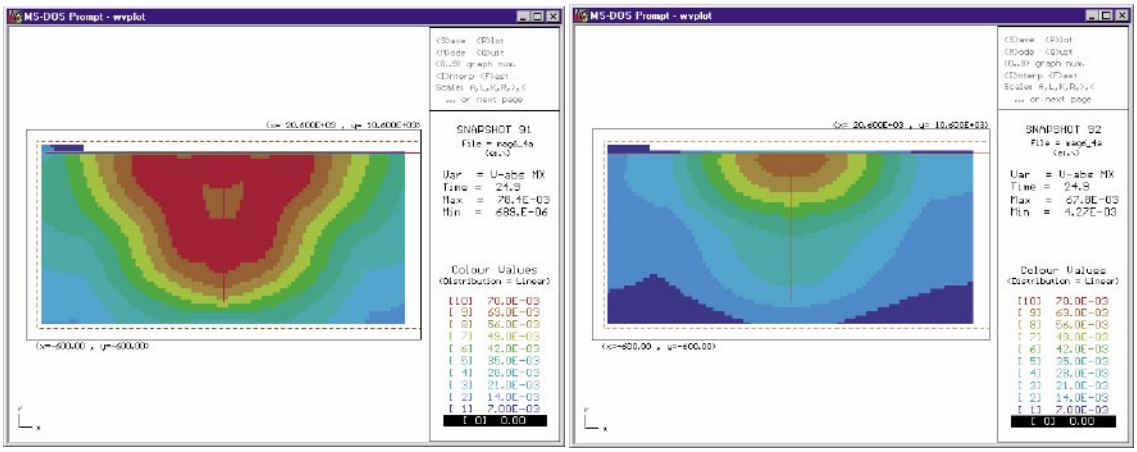

Figure A1b-5. *The velocity field generated by Model 1b. Plots show the maximum particle velocity experienced over the model volume. The fault has a length of 12 km and width of 7 km. The contour colour scale is chosen to view the variation in velocity across the volume and is not identical for each plot – Vmax gives upper velocity range. a) Plan view at 400 m depth. b) Plan view at 1,000 m depth. c) Longitudinal view at 2 km from the fault surface. d) Longitudinal view at 10 km from the fault surface. e) Cross sectional view at 2 km from the fault tip. f) Cross sectional view at 10 km from the fault tip.*

Figure A1b-6 and Figure A1b-7 give the velocity fields for Model 2a and 2b respectively. Differences in the radiation pattern between the two earthquake mechanisms are again visible in the models, with the same differences being evident as in Model 1. For Model 2a, the velocity observed at 10 km orthogonal to the fault plane is approximately 0.2 m/s, and for Model 2b, the velocity observed at 10 km from the fault tip is approximately 0.2 m/s. Again, the maximum velocities across the area are observed at azimuths orthogonal to the fault plane for the dip-slip earthquake, and along the strike direction for the strike-slip earthquake. This is what would be expected from such mechanisms. The observed velocities are also approximately 4x that seen in Model 1. This difference is attributed to the larger stress drop that is occurring on a smaller fault plane in order to get the equivalent moment to a Magnitude 6 earthquake.

Figure A1b-8 shows the velocity field from Model 2b on the same velocity range as that plotted for Model 2a in Figure A1b-6. These two figures can be directly compared. In general, it should be noted that the velocity fields for both mechanisms are very similar across the area of interest, and are within the range 0.15–0.35 m/s. However, it is also clearly evident that Model 2a generates much higher velocities close to the fault (within the first 5 km distance orthogonal to the fault plane), and at the repository depth range of 400–1,000 m. Much smaller velocities, relative to Model 2b, are generated in the direction of the fault's strike away from the fault tip. Amplification of the velocity field close to the Earth's surface is a result of confining the energy to the half-space.

Figure A1b-8 shows waveforms for the modelled velocity fields, in both Model 2a and 2b, at a distance of 10 km from the fault's vertical axis and at azimuths around the fault . There is a large amount of detail in the waveforms that changes with azimuth. This would be expected from an earthquake in the near field, with a complex source radiation pattern and the introduction of reflections off the free surface. This detail will also change if the ring of receivers was moved vertically, up or down. All the velocity amplitude changes are easily within the same order of magnitude around the complete 90° azimuth.

Figure A1b-10 compares velocity records from the opposite corners of the example repository volume that has been instrumented in the model (see Figure A1b-3). The two sets of waveforms appear qualitatively to be very similar, however there is a time lag between the two caused by the finite time it takes for the velocity field to move across the repository (assumed as 800 × 800 m in plan). This results in a reasonably large difference in particle velocity (approximately the same amplitude as the velocity field) across the repository volume. This will lead to induced stress in the volume.

(a) Vmax=0.75 m/s

(b) Vmax=0.75 m/s

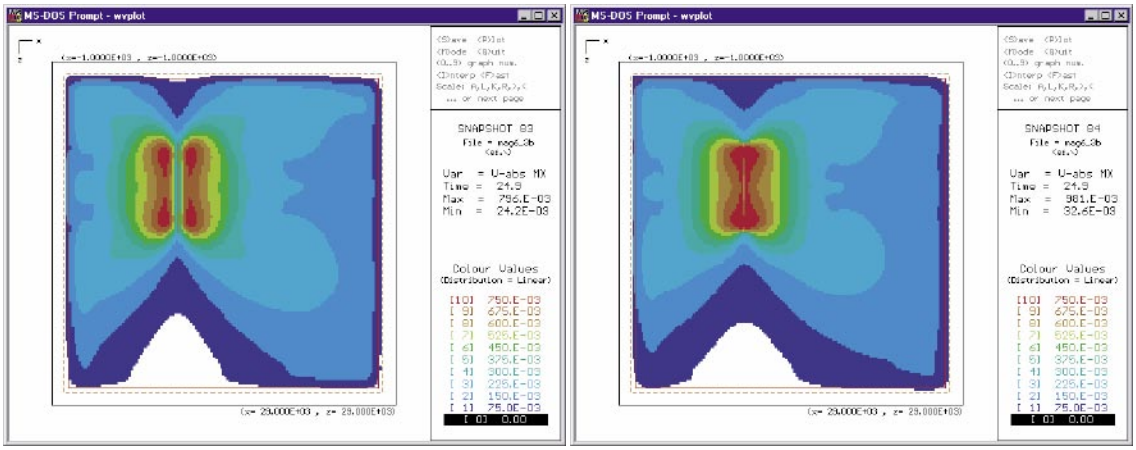

(c) Vmax=0.75 m/s

(d) Vmax=0.25 m/s

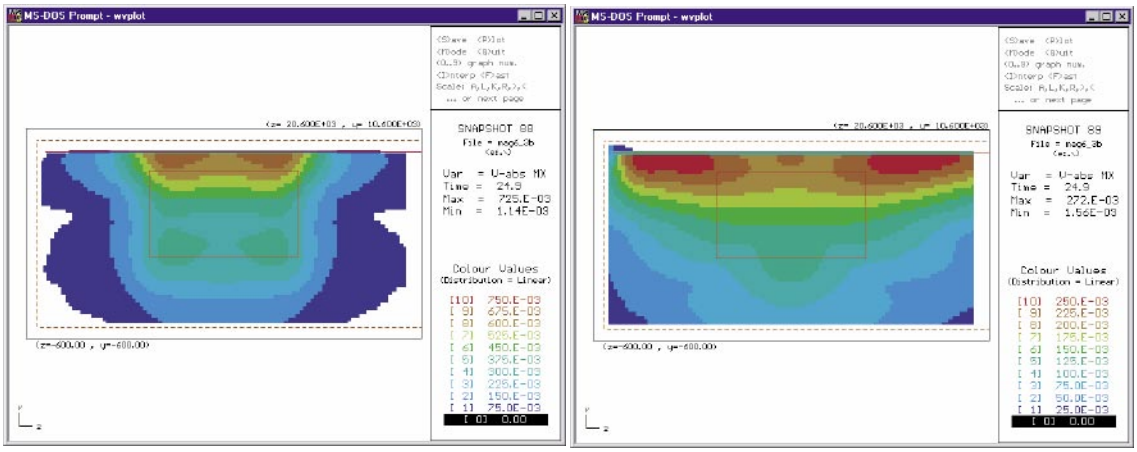

(e) Vmax=0.25 m/s

(f) Vmax=0.25 m/s

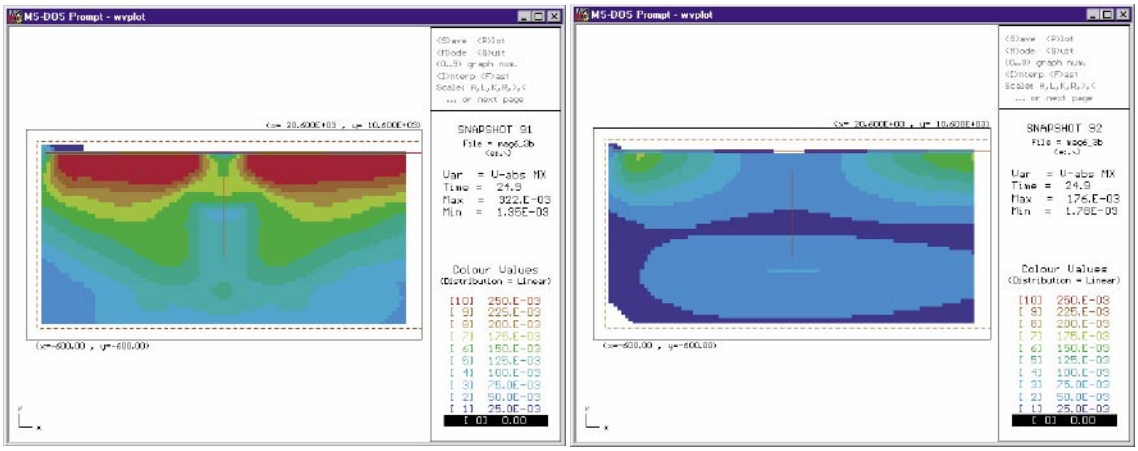

Figure A1b-6. *The velocity field generated by Model 2a. Plots show the maximum particle velocity experienced over the model volume. The fault has a length of 8 km and width of 4.6 km. The contour colour scale is chosen to view the variation in velocity across the volume and is not identical for each plot – Vmax gives upper velocity range. a) Plan view at 400 m depth. b) Plan view at 1,000 m depth. c) Longitudinal view at 2 km from the fault surface. d) Longitudinal view at 10 km from the fault surface. e) Cross sectional view at 2 km from the fault tip. f) Cross sectional view at 10 km from the fault tip.*

(a) Vmax=0.3 m/s

(b) Vmax=0.3 m/s

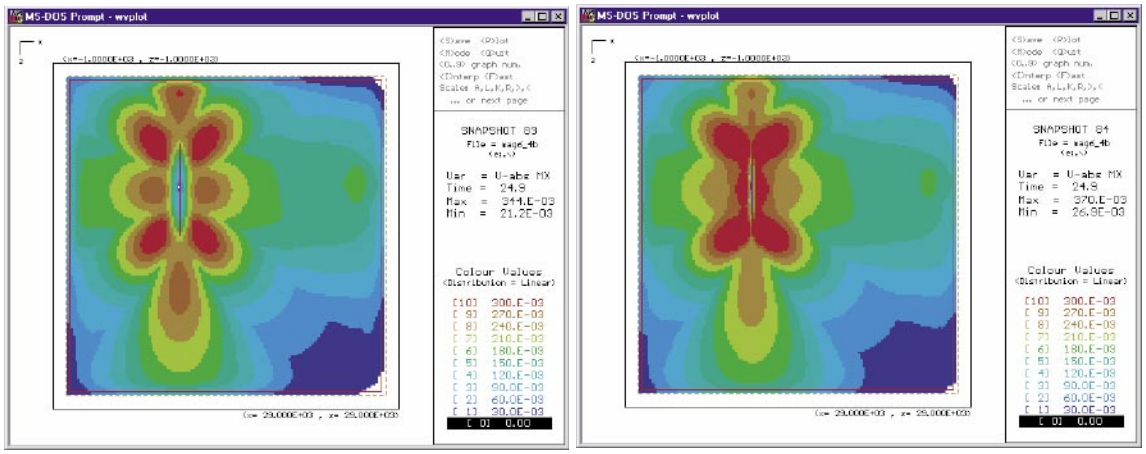

(c) Vmax=0.3 m/s

(d) Vmax=0.3 m/s

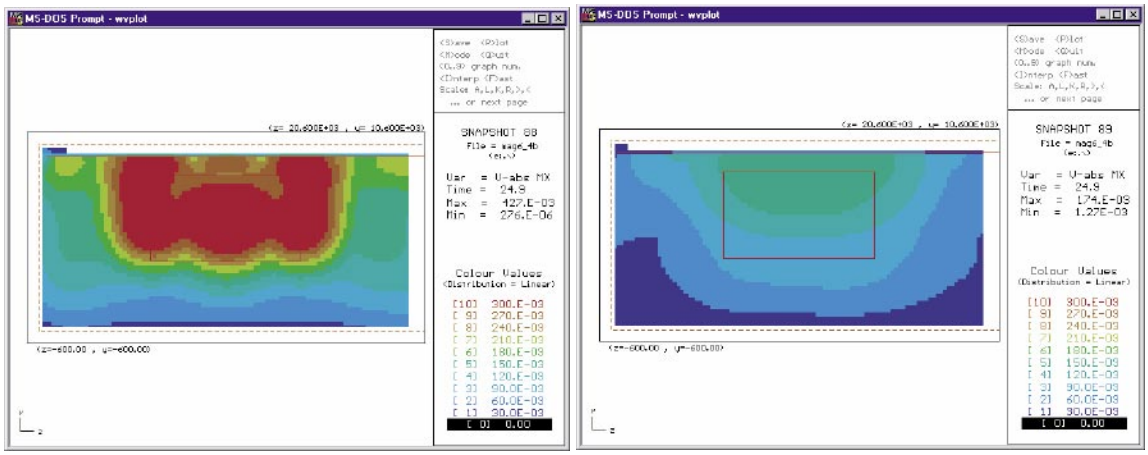

(e) Vmax=0.3 m/s

(f) Vmax=0.3 m/s

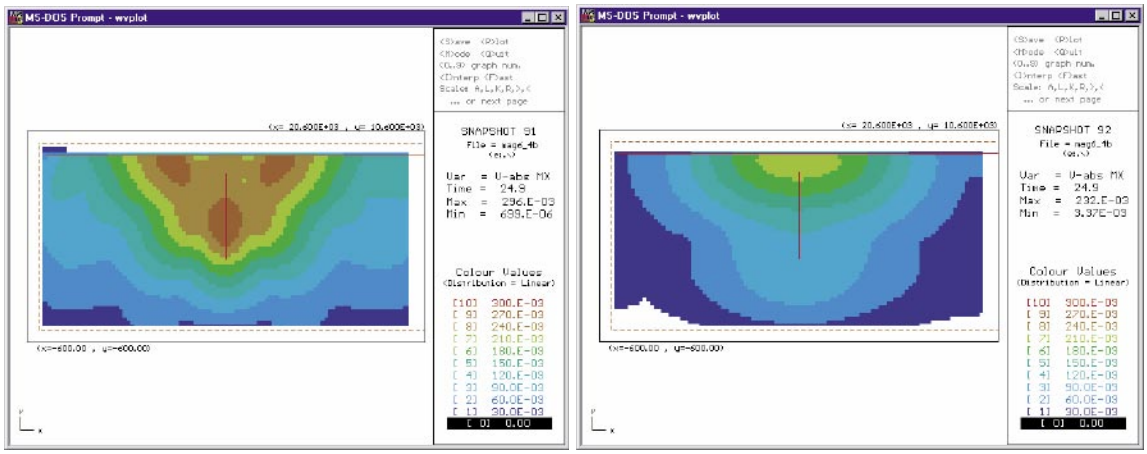

Figure A1b-7. *The velocity field generated by Model 2b. Plots show the maximum particle velocity experienced over the model volume. The fault has a length of 8 km and width of 4.6 km. The contour colour scale is chosen to view the variation in velocity across the volume and is not identical for each plot – Vmax gives upper velocity range. a) Plan view at 400 m depth. b) Plan view at 1,000 m depth. c) Longitudinal view at 2 km from the fault surface. d) Longitudinal view at 10 km from the fault surface. e) Cross sectional view at 2 km from the fault tip. f) Cross sectional view at 10 km from the fault tip.*

(a) Vmax=0.75 m/s

(b) Vmax=0.75 m/s

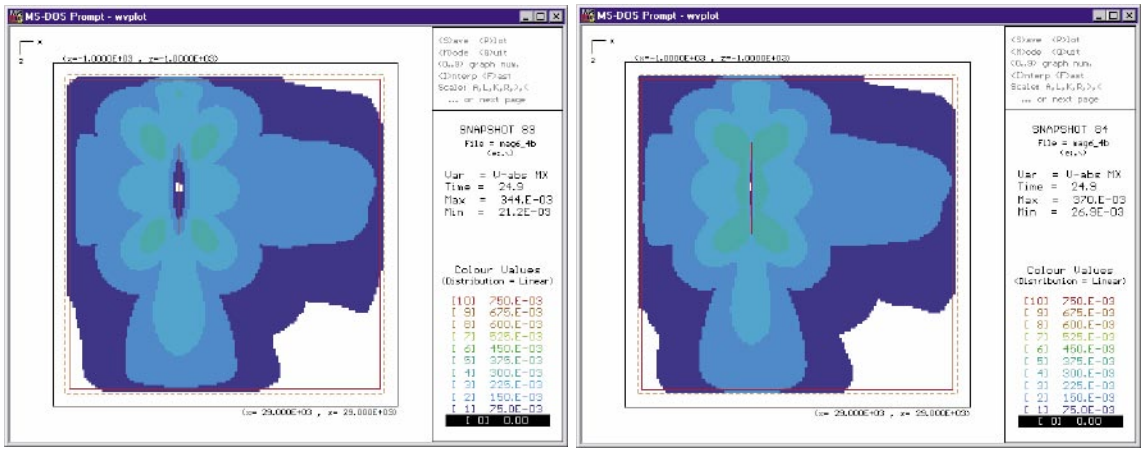

(c) Vmax=0.75 m/s

(d) Vmax=0.25 m/s

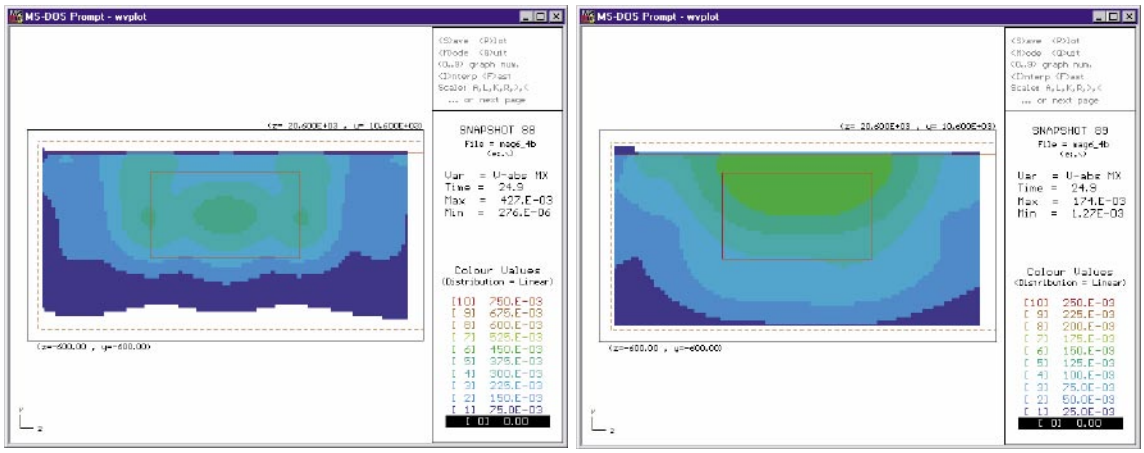

(e) Vmax=0.25 m/s

(f) Vmax=0.25 m/s

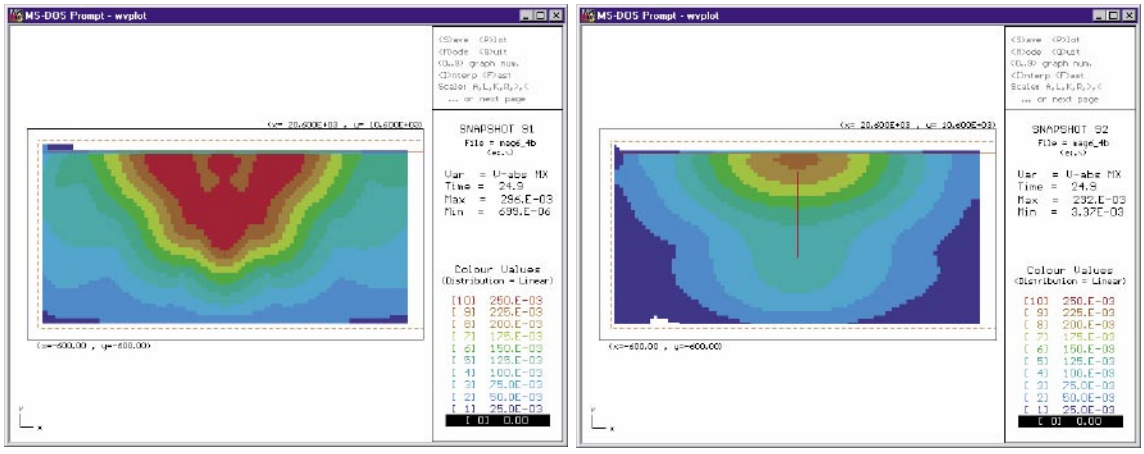

Figure A1b-8. *As previous figure. The velocity range is identical to that shown in Figure A1b-6 for Model 2a for comparison.*

(a)

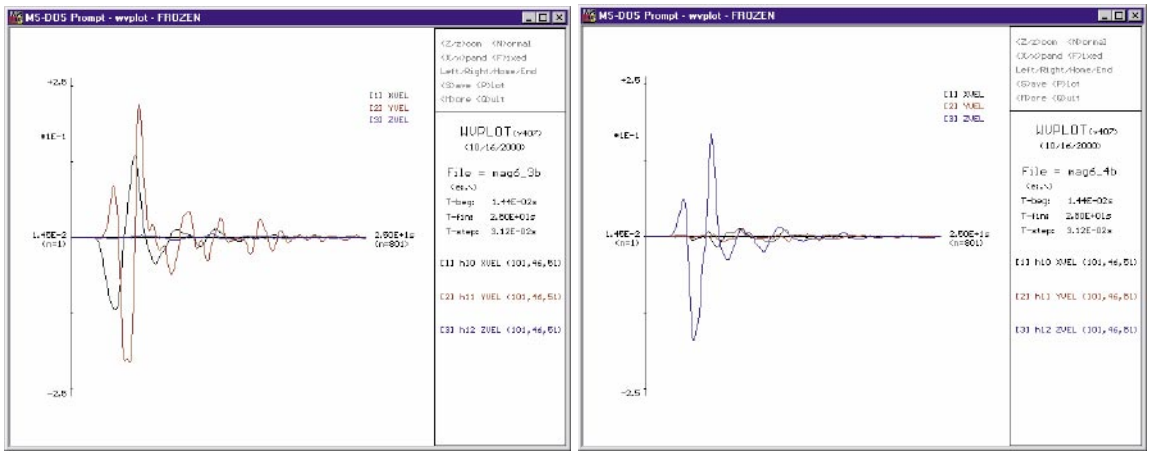
MS-DOS Prompt - wvplot - FROZEN
WUPLOT(v407)
File = mag6_3b
MS-DOS Prompt - wvplot - FROZEN
WUPLOT(v407)
File = mag6_4b

(b)

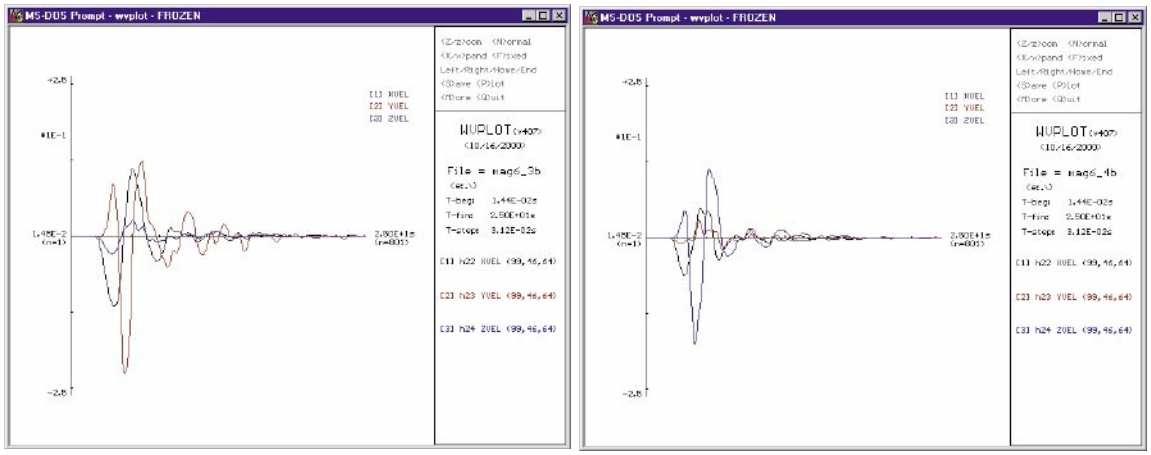
MS-DOS Prompt - wvplot - FROZEN
WUPLOT(v407)
File = mag6_3b
MS-DOS Prompt - wvplot - FROZEN
WUPLOT(v407)
File = mag6_4b

(c)

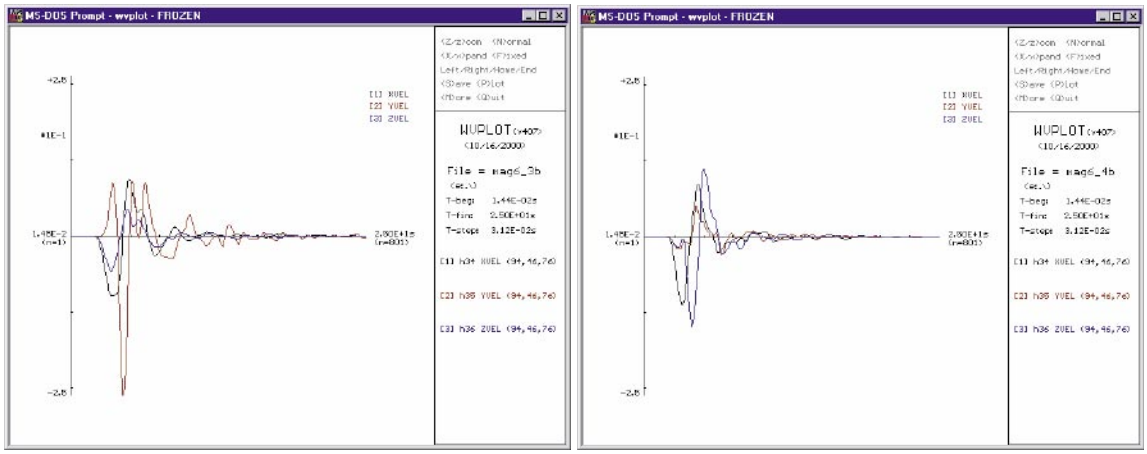
MS-DOS Prompt - wvplot - FROZEN
WUPLOT(v407)
File = mag6_3b
MS-DOS Prompt - wvplot - FROZEN
WUPLOT(v407)
File = mag6_4b

(d)

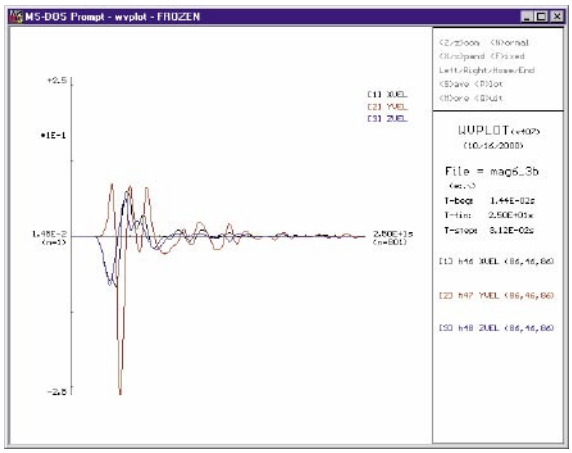
MS-DOS Prompt - wvplot - FROZEN
WUPLOT
File = mag6_3b

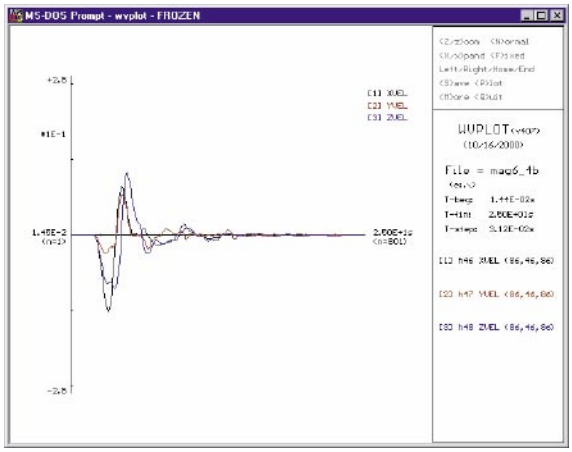
MS-DOS Prompt - wvplot - FROZEN
WUPLOT
File = mag6_4b

(e)

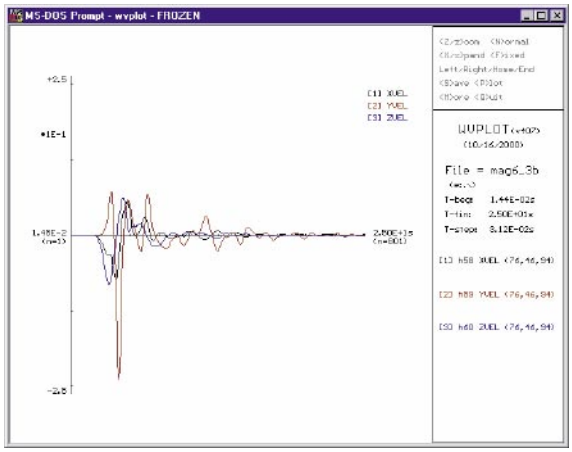
MS-DOS Prompt - wvplot - FROZEN
WUPLOT
File = mag6_3b

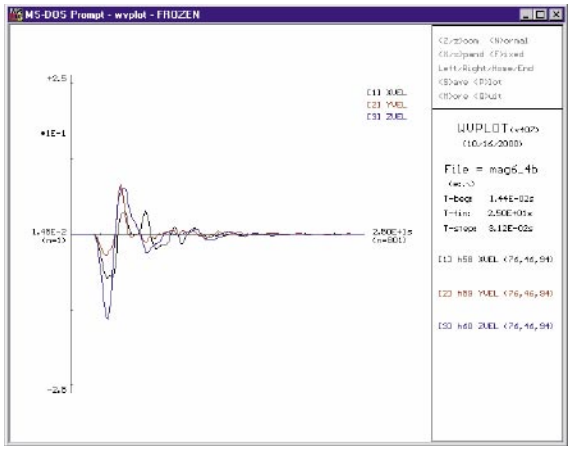
MS-DOS Prompt - wvplot - FROZEN
WUPLOT
File = mag6_4b

(f)

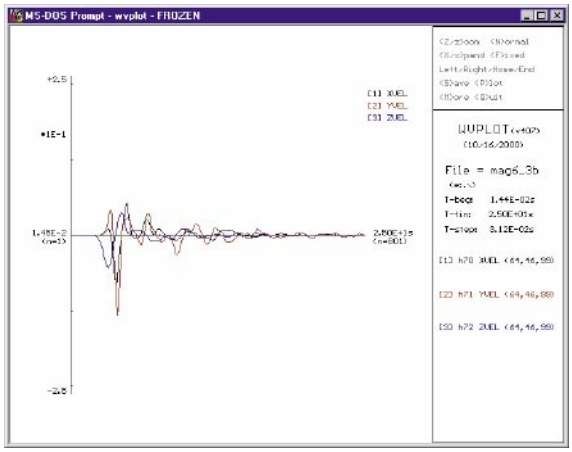
MS-DOS Prompt - wvplot - FROZEN
WUPLOT
File = mag6_3b

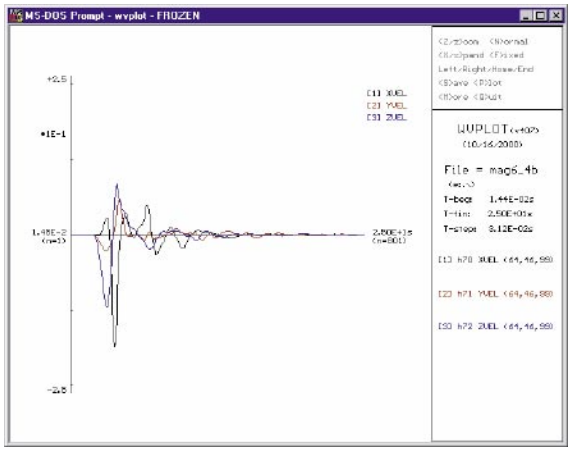
MS-DOS Prompt - wvplot - FROZEN
WUPLOT
File = mag6_4b

(g)

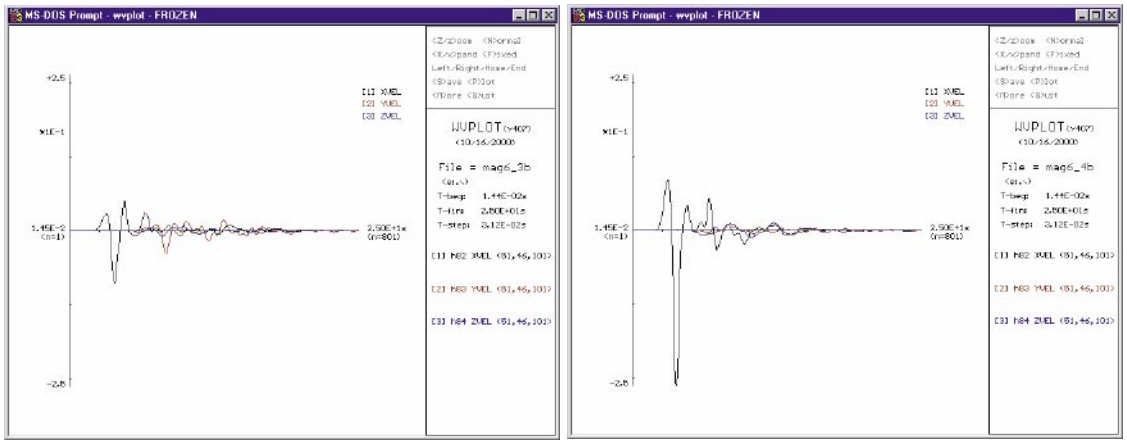

Figure A1b-9. *Velocity records observed at seismic receivers at a distance of 10 km from the fault's vertical axis (third concentric ring of seismic receivers shown in Figure A1b-3). The left hand plots are for Model 2a and the right hand plots for Model 2b. The Vx, Vy and Vz components are shown. The plots all have the same vertical scale, and are in order of increasing azimuth from normal to the fault (0°) to parallel to the fault's strike (90°); a) 0°, b) 15°, c) 30°, d) 45°, e) 60°, f) 75°, g) 90°.*

A1b-5 Recommended velocity field

In our recommendations to the client, as to which velocity model to use in further analysis, we consider two things.

1) *The client should utilise the model with the velocity records with the highest amplitudes.* The high stress drop models generate a considerably higher amplitude velocity field than the low stress drop models. Compared to Model 2b, Model 2a generates a velocity field with much greater amplitudes close to the fault, out to approximately 5 km normal to the fault surface, and in the repository depth range of 400–1,000 m. This is due to the free surface. However, it does generate velocity amplitudes that are much smaller at azimuths around the strike of the fault, especially at large distances (> 5 km), and so may not represent the maximum velocities that could occur for an observation at this location.
2) *The velocity records should be those that represent a likely earthquake scenario.* Both Model 2a and 2b represent possible earthquake scenarios. Model 2a is a pure dip-slip earthquake, which is very rare in nature. However, high-angle (up to 80° dip) dip-slip earthquakes are reasonably common. Strike-slip earthquakes are also very common occurrences.

Considering these two points we feel that the model which maximises the free surface effect should be used. We therefore recommend that the client utilises velocity field data from Model 2a. This uses a high stress drop, consistent with an *intraplate* earthquake, and a pure dip-slip mechanism.

(a) (b)

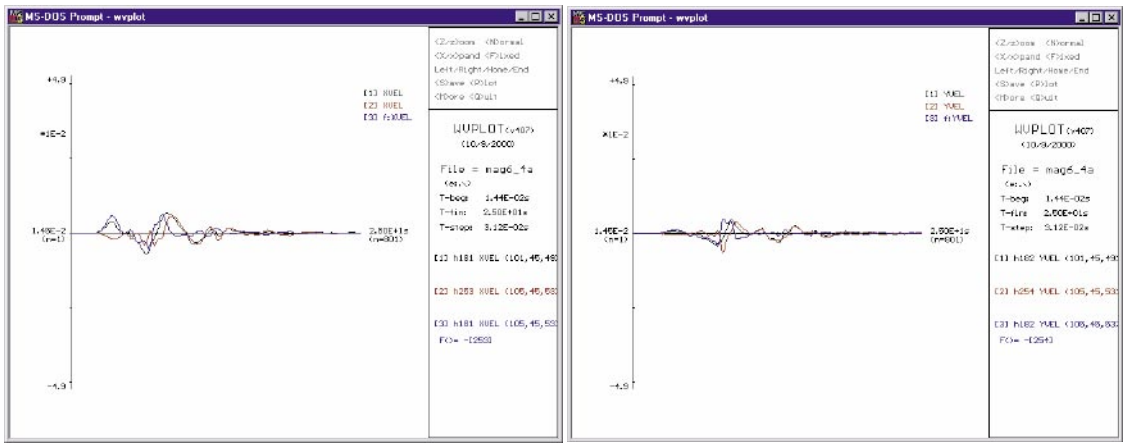

(c) (d)

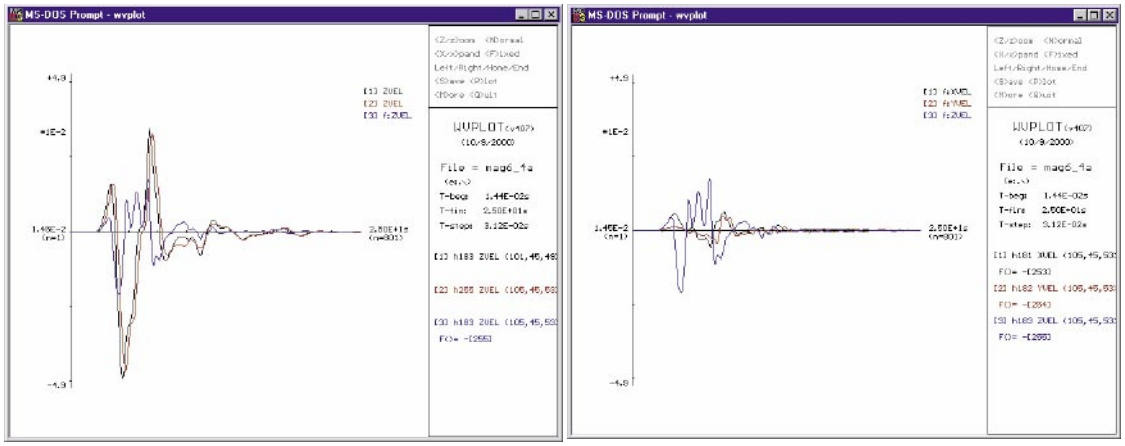

Figure A1b-10. *Comparison of velocity records observed across a hypothetical repository volume. Model 1b is used as an example. Black waveforms are for a receiver positioned at 10 km distance from the fault's vertical axis and normal to the fault's orientation. Red waveforms are for a receiver positioned at 800 m east and 800 m south of this. The blue waveforms are the difference between the two records. a) Vx. b) Vy. c) Vz. d) All X,Y,Z differences.*

A1b-6 Discussion

There are a number of parameters (boundary conditions) in the model that influence the velocity field, and which are assumed in Model 2a. We have shown the differences in the results that could be obtained from changing some of these parameters.

- **Orientation of the fault and the earthquake mechanism.** When investigating the exact nature of the velocity field, the position of the observation point with respect to the fault orientation, and the slip direction of the earthquake on this fault, has a very significant effect on the velocity record obtained. This is due to the radiation pattern of the energy emitted from the earthquake. Velocity records will fluctuate considerably if the observation point is moved around the fault/earthquake. This effect is widely used in seismology to invert for the earthquake mechanism, and hence back-calculate the orientation and mechanics of failure. It is a particular problem here as the fault is large

compared to the recording distances and hence any small change in receiver position is likely to change the azimuth of the receiver with respect to the fault plane resulting in a change in the velocity field. It should be noted that the radiation pattern is much more azimuthaly independent, orthogonal to the fault plane and at close distances, for Model 2a (Figure A1b-6) than for Model 2b (Figure A1b-7). In Model 2b, the radiation pattern is more complex at close distances. We have tried to overcome the radiation pattern problem by using likely earthquake scenarios, and providing an array of hypothetical receivers at which detailed velocity records are obtained. It should also be noted that, although the velocity field changes in its exact nature, the approximate maximum amplitude that is likely to be recorded at any position around the fault varies little and is generally in the range 0.15–0.35 m/s for both Model 2a and 2b.

- **Free-surface effect.** This adds a second level of complexity to the exact nature of the velocity field, and produces significant differences in the maximum velocity field that is observed across the area of interest. By including a free surface above the fault, which is realistic as the repository is relatively shallow at 400–1,000 m depth, an amplification effect is observed. The surface introduces a focussing effect by confining the energy to the half space below it. This acts to double the amplitude of the velocity field in the near-surface region. The velocity field observed here depends on the depth of the fault, as the effect of the free surface reduces considerably as the fault is moved to larger depths, and is dependent on the radiation pattern emitted from the fault/earthquake orientation. It should be noted that, at the wavelengths and distances involved in the model, there is no separation of the P, S and surface waves into distinct phases. We have shown the differences between the two earthquake mechanisms on a vertical fault and have concluded that, in this case, the dip-slip earthquake generally produces the highest amplitude velocity field of the two. It is reasonable to assume that any change in the orientation of slip, from the vertical to the horizontal, is unlikely to provide a higher velocity field than this. What may increase the velocity field in this near-surface region, is a change in the orientation of the fault with respect to the free-surface. Figure A1b-11 shows a cross-section of the radiation pattern for the two mechanisms considered here if the free-surface is not included.

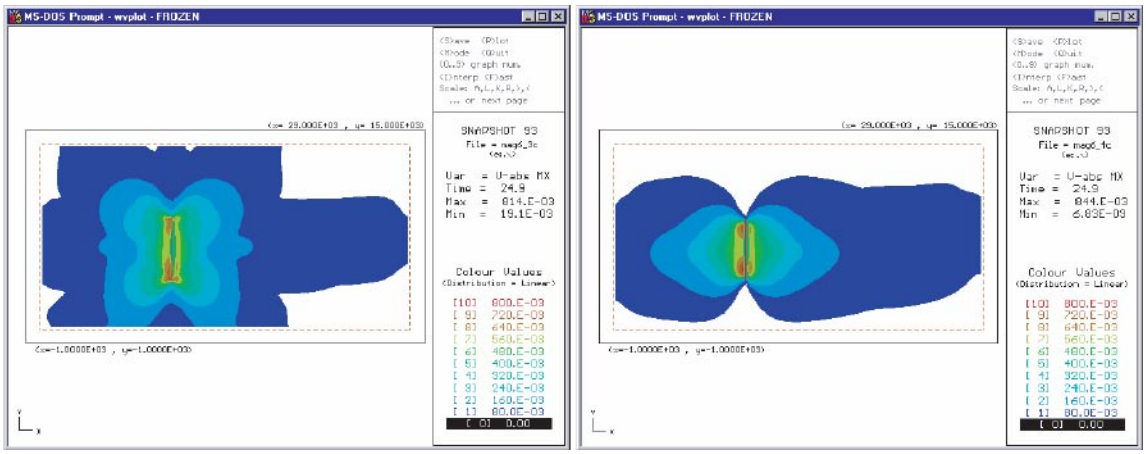

Figure A1b-11. *The velocity field resulting from Model 2 when no free surface is included. Left: Model 2a – Dip slip earthquake. Right: Model 2b – Strike slip earthquake. The plots show a cross section through the centre of the fault.*

It should be noted that there is also a complex out of plane radiation pattern. If the fault for the dip-slip earthquake is rotated from the vertical towards the horizontal, then the lobes in the radiation pattern will move with respect to a free-surface positioned just above the fault. This is likely to result in some regions of the model acquiring a higher amplitude velocity field, and some acquiring a lower amplitude velocity field, than that shown in Figure A1b-6 for Model 2a. Any increase in amplitude compared to this model is likely to be very localised and not considerably greater (less than an order of magnitude). For the strike-slip earthquake a change in orientation will produce a similar effect, but again one that should not result in a considerably higher velocity field than seen in Model 2a. For either mechanism, if the fault is re-orientated to a horizontal position (shallow-angle faulting is associated with thrusting at compressive plate boundaries), then the fault will have to be very shallow to produce an amplification effect considerably greater than that seen in Model 2a.

- **Fault geometry.** We have assumed an aspect ratio (length/width) for the fault of 2 and the fault as a planar feature. We consider this to be realistic for an earthquake of this size where the fault length is generally confined to the upper schizophere, and on one complete fault segment. In reality, for larger magnitude earthquakes, which occur on much larger faults, the fault geometry tends to become more complicated. This includes changing geometry, especially when the earthquake ruptures between multiple fault segments, and across the complete schizophere /e.g. Scholz, 1990/. In this case the aspect ratio will become larger as the rupture is bounded by the width of the schizophere. Such complexities in the fault geometry will change the exact nature of the velocity field. If a very high (or very low) aspect ratio is considered then this will cause the source of energy to be moved further towards the extremities of the models and will act to reduce the amplitude of the velocity field observed at any of the recording stations. The maximum amplitudes observed over the velocity field will occur when the aspect ratio approaches 1 (a square fault). Considering the measurements are all in the near field, a change in aspect ratio, from that assumed here, is unlikely to considerably increase the maximum amplitudes observed.

Anelastic attenuation. This is not considered in the modelling performed here, where the medium is assumed to be elastic, homogeneous and isotropic. Anelastic attenuation acts to reduce the amplitude of the velocity field and only becomes a problem where the ray path length, r, is long compared to the wavelength, λ. In seismology the near-field is generally defined as 10λ /Aki and Richards, 1980/. From the modelling, the dominant period at 10 km (e.g. Figure A1b-10) is 3.5 s, corresponding to an S-wave wavelength of 11 km. This period (and the general velocity amplitudes observed) is very similar to strong-ground motion records obtained from a real earthquake of a similar magnitude /e.g. Hanks and Brady, 1991/. As $r/\lambda \approx 1$, we are therefore in the near field. The effect of anelastic attenuation on the velocity records is therefore negligible.

- **Earthquake propagation.** There are a number of factors in the earthquake propagation model used here that may change the velocity field. I) The slip velocity has been defined as $0.7 \times V_s$, the velocity of shear waves in the rock. This is a realistic slip velocity /Scholz, 1990/. II) Slip rise time; the time taken for the stress drop to occur. We have performed tests that show, within reasonable limits, the rise time has little effect on the measured velocity field. We have used a realistic and computationally advantageous rise time (0.5 s) in the models. III) The earthquake ruptures from the centre of the fault (i.e. the earthquake hypocentre), however the hypocentre could be at any position on the fault plane. Moving the hypocentre will result in changes in the exact nature of the velocity field around the fault, especially at the near-field distances investigated. It is unlikely to change the maximum velocity amplitudes observed.

In conclusion, the exact nature of the velocity field is sensitive to the position at which the measurements are taken with respect to the position and orientation of the fault and the orientation of the earthquake's mechanism. A complication also arises due to reflections from the Earth's free surface. The velocity records supplied cannot, therefore, be an exact representation of what a repository would undergo in the event of a nearby earthquake as there are an infinite number of possible earthquake ruptures that could be modelled on an infinite number of differently orientated faults. However, the velocity records can be used as a representation of the velocity field from a realistic earthquake scenario, which is likely to produce some of the highest amplitude velocity measurements across the majority of the area of interest.

Table A1b-1. Rock mass properties used in all models described here.

Parameter	Description	Value	Notes
E	Youngs Modulus	75 GPa	Specified in advance.
v	Poissons Ratio	0.25	Specified in advance.
ρ	Density	2,700 gm^{-3}	Chosen value.
V_p	P-wave velocity	5,774 ms^{-1}	Calculated from elastic parameters.
V_s	S-wave velocity	3,333 ms^{-1}	Calculated from elastic parameters.

Table A1b-2. Description of the earthquake/fault parameters used in each of the four models.

Name	Parameter	Value
MODEL 1	Stress-drop, $\Delta\sigma$.	3 MPa
	Fault length (along strike).	12 km
	Fault width (down dip).	7 km
	Hypocentre depth.	4.5 km
	Slip rise-time.	0.5 seconds
MODEL 1a	Dip Slip mechanism.	
MODEL 1b	Strike-slip mechanism.	
MODEL 2	Stress-drop, $\Delta\sigma$.	15 MPa
	Fault length (along strike).	8 km
	Fault width (down dip).	4.6 km
	Hypocentre Depth.	3.3 km
	Slip rise-time.	0.5 seconds
MODEL 2a	Dip Slip mechanism.	
MODEL 2b	Strike-slip mechanism.	

A1b-7 References

Aki K, Richards P G, 1980. Quantitive Seismology: Theory and Methods. 1980, New York: W H Freeman and Co. ISBN.

Hanks T C, Brady A G, 1991. The Loma Prieta Earthquake, Ground Motion, and Damage in Oakland, Treasure Island and San Francisco. Bull. Seismol. Soc Am Vol 81(5): p 2019–2047.

Hildyard M W, Daehnke A, Cundall P A, 1995. WAVE, Version Proc of 35th U.S. Symp on Rock Mech, pp 519–524, 1995.

Appendix 2a

Flac3D analysis

Shear displacement on fractures due to seismic movements

Phase II

Calum Baker, Applied Seismology Consultants Ltd, UK

Mark Hildyard, Department of Earth Sciences, Liverpool University, UK

Mark Christianson, Itasca Consulting Group, Inc

A2a Executive summary

Several FLAC3D /ITASCA, 1997/ models were run to establish the amount of dislocation that may occur across a fracture during an earthquake. The applied motions were calculated to represent an earthquake with Richter 6.0 magnitude at distances of 2 km, 6 km, and 10 km from the fracture. The source fracture is a vertical fault with a dip slip motion. The motions were applied to models containing either a horizontal fracture or a fracture dipping at 45°. The 45° fracture model was run with the dip direction oriented both parallel and perpendicular to the vertical plane of the earthquake fault. The results of these runs were compared with the results from similar geometries that were run using the program WAVE /Hildyard et al. 1995/. The models included a matrix of three fracture orientations, three distances, several fracture strengths and three stress states. Table A2a-1 shows the maximum dislocations that occur during the earthquake for these runs. For most cases, the displacements were quite small. In addition, due to differences in the way the seismicity was modeled, the WAVE results show displacements that represent the static dislocation of the seismic source (while FLAC3D does not). This makes direct comparison difficult and is very significant for the near-field events studied. As distance increases, the static effects will diminish, and dynamic effects will dominate. It is also important to note that, for several of the stress states modeled, the fracture will slip under the static stress prior to applying the seismicity. While not specifically identified in this study, there exists a fracture strength value that could prevent this movement from taking place under the static load but could release this stored strain due to the seismicity. It is likely that releasing the stored strain would result in displacements that would exceed the displacements due to the seismicity alone.

In general, static displacements due to fault offset have a smaller distance of influence compared to seismic motions. However, the magnitudes of the static displacements seem to overshadow the seismic movements for the distances used in this study. The displacements due to seismicity for all distances seem to be relatively small for any cases that include friction. These results tend to affirm the assumptions of /LaPointe et al. 1997, 1999, 2000/ that a static analysis is useful for predicting displacements for near-field events. However, the displacements predicted by both FLAC3D and WAVE exceed the magnitudes of the displacements in the LaPointe study. It is unknown whether a 200-m fracture was present in the statistical sample used by LaPointe.

The results from both FLAC3D and WAVE indicate that friction on the joint surfaces significantly reduces the shear displacements due to the seismic event. In some cases the friction prevents movement. In other cases the friction causes shear strain to be stored which can be released by the seismic event. Friction also prevents recovery of the induced displacements. It is unknown if these displacements would accumulate due to multiple events

One of the purposes of this study was to determine the level of confidence in using a planar wave input to FLAC3D to simulate near-field events. For the case of planar wave input, it is not possible to simulate the static changes observed in the WAVE model. Also, a method of separating the dynamic and static portions of the WAVE results was not found, making comparison of the dynamic portions impossible. It is concluded that the FLAC3D results under-predict the motions from the seismic event (mainly due to the lack of the static portion) and are not conservative.

Table A2a-1. A Maximum Shear Displacement of Fracture for the Magnitude 6 Earthquake.

Model	Dist	Orientation	Stress	Phi	FLAC3D	Wave	Pre-Seis[1]
h2f0s0	2	H	0	0	0.580	1.66	
h6f0s0	6	H	0	0	0.380	0.32	
h10f0s0	10	H	0	0	0.160		
pp2f0s0	2	45 perp	0	0	0.180		
pp10f0s0	10	45 perp	0	0	0.070		
pl2f0s0	2	45 par	0	0	0.280		
pl10f0s0	10	45 par	0	0	0.080		
h2f1s1	2	H	I	15	0.017	0.29	
h2f1s2	2	H	II	15	0.208	0.67	
h2f2s1	2	H	I	30	0.017		
h2f2s2	2	H	II	30	0.133		
h6f1s1	6	H	I	15	0.013	0.14	
h6f1s2	6	H	II	15	0.013	0.14	
h10f1s1	10	H	I	15	0.006		
h10f1s2	10	H	II	15	0.005		
pp2f1s1	2	45 perp	I	15	0.099		0.823
pp2f1s2	2	45 perp	II	15	0.071		2.808
pp2f2s1	2	45 perp	I	30	0.009		
pp2f2s2	2	45 perp	II	30	0.125		1.118
pp10f1s1	10	45 perp	I	15	0.198		0.823
pp10f1s2	10	45 perp	II	15	0.171		2.808
pp10f2s1	10	45 perp	I	30	0.006		
pp10f2s2	10	45 perp	II	30	0.291		1.118
pl2f1s1	2	45 par	I	15	0.058		
pl2f1s2	2	45 par	II	15	0.202		0.527
pl2f2s1	2	45 par	I	30	0.014		
pl2f2s2	2	45 par	II	30	0.058		
pl10f1s1	10	45 par	I	15	0.059		
pl10f1s2	10	45 par	II	15	0.201		0.527
pl10f2s1	10	45 par	I	30	0.005		
pl10f2s2	10	45 par	II	30	0.082		

[1] All displacements are in cm. Pre-Seis are displacements that occur due to the static stress state prior to the seismic event.

Contents

A2a-1 Introduction

In a previous study (Appendix 1a), it was shown that FLAC3D predicts greater movements on target fractures then those predicted by /LaPointe et al. 1997/. That previous study looked only at frictionless fractures in an initially stress-free model. This study extends the range of conditions modeled to include frictional fractures and initial stress states. In addition, the study includes model runs from the computer program WAVE /Hildyard et al. 1995/. The results from the WAVE program will be compared to the FLAC3D results. Currently, the WAVE program can only be used to model horizontal and vertical fractures. The comparison is intended to test the effect of the plane- wave assumption used for input in FLAC3D. The results of the WAVE modeling are reported in Appendix 2b.

The study presented here looks at fracture displacements due to a 6 Richter magnitude earthquake at several distances from a 200 m^2 fracture. Several different target distances, as well as ranges in fracture strengths and initial stress conditions, were modeled.

The transmission of earthquake motions is difficult to model for nearby epicenters. Ideally, the wave motions would be described uniquely for each gridpoint on the model boundary. This approach is not employed in this study, and it is assumed that the earthquake is deep and distant enough that the motions can be described by a planar wave applied on the bottom of the model.

The motions applied in the model were calculated by Applied Seismology Consultants Ltd. (Appendix 1b). These data are the same as reported in the previous report (Appendix 1a). Of particular interest is the authors' recommendation that the most appropriate type of earthquake to be used in the study would be dip-slip. This is in contrast to the strike-slip assumption used in the study by LaPointe.

A2a-2 FLAC3D model

FLAC3D is a fully dynamic three-dimensional finite-difference code. The decision to use FLAC3D rather than a discontinuum code such as 3DEC was based on FLAC3D's ability to model a limited number of fractures and its free-field boundary. Viscous boundary conditions are used on the sides and the bottom of the FLAC3D model. The viscous boundaries absorb energy, thereby preventing reflections. The free-field boundary prevents the viscous boundaries on the sides of the models from absorbing incident energy that is moving parallel to the edge. This helps maintain the shape of the input seismic wave.

FLAC3D models were run to establish the amount of dislocation that may occur across a 200 m^2 fracture during an earthquake. The applied motions were calculated to represent a Richter 6.0 magnitude earthquake at distances of 2 km, 6 km and 10 km from the fracture. The motions were applied to models containing either a horizontal fracture or a fracture dipping at 45°. The 45° fracture model was run with the dip direction oriented both parallel and perpendicular to the vertical plane of the earthquake fault. Three friction values were used to model the strength of the fracture. In addition, three stress states were assumed.

Analysis of the frequencing spectrum in the earthquake data indicates that the maximum frequency is 1 Hz. The shear-wave velocity is 3.3 km/sec. Using Equation A2a-1, this gives a maximum zone length of 330 m:

$$\Delta l \leq \frac{f\, C_s}{10} \qquad \text{Equation A2a-1}$$

where Δl is the maximum zone dimension, f is the maximum frequency, and C_s is the shear-wave velocity. The zone sizes in the FLAC3D model are smaller than this value.

Figure A2a-1 shows the FLAC3D grid used to model the horizontal fracture orientations. The dimension of the entire model is 2,000 m × 2,000 m × 1,000 m. Figure A2a-2 shows the same model with the top removed to show the frictionless fracture (in red). Figure A2a-3 shows the FLAC3D grid used in the 45° orientation case. Figure A2a-4 shows the model with the top removed to show the frictionless fracture (in red). In all cases, the fracture is a 200-m square in the center of the model.

Viscous boundaries are applied on all sides and on the bottom. This prevents reflection of secondary seismic waves. The top surface is free and will reflect waves. The sides of the model also have a dynamic free-field boundary that prevents the absorption of the applied primary seismic wave.

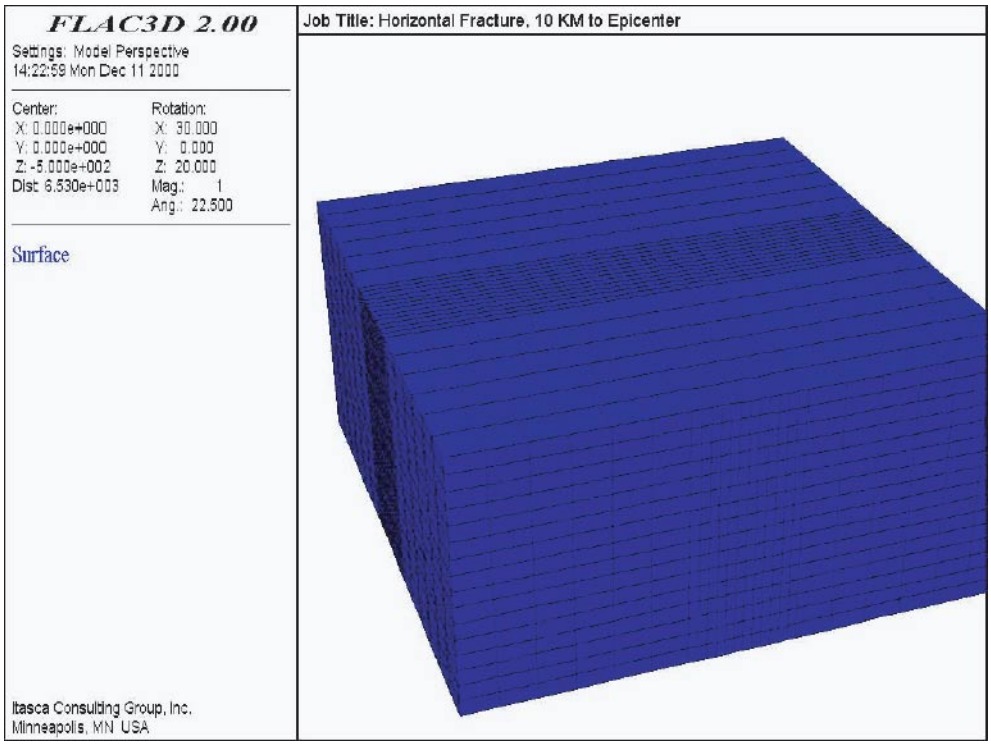

Figure A2a-1. *FLAC3D Grid for Horizontal Fracture Case.*

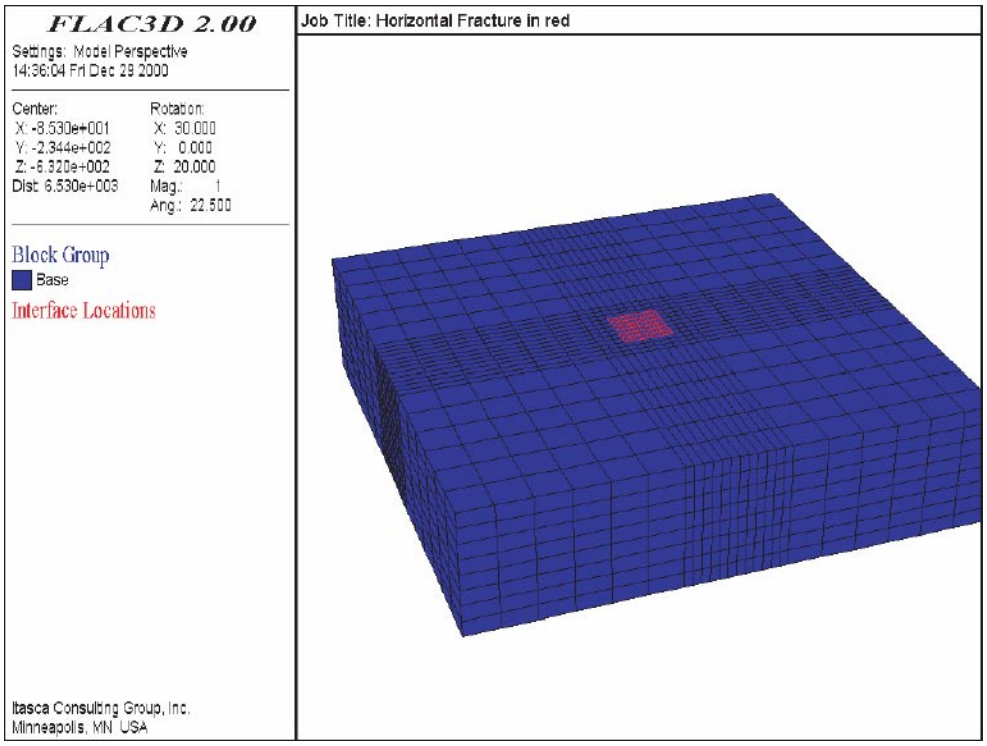

Figure A2a-2. *FLAC3D Grid for Horizontal Fracture Case. (The top is removed; the fracture is in red.)*

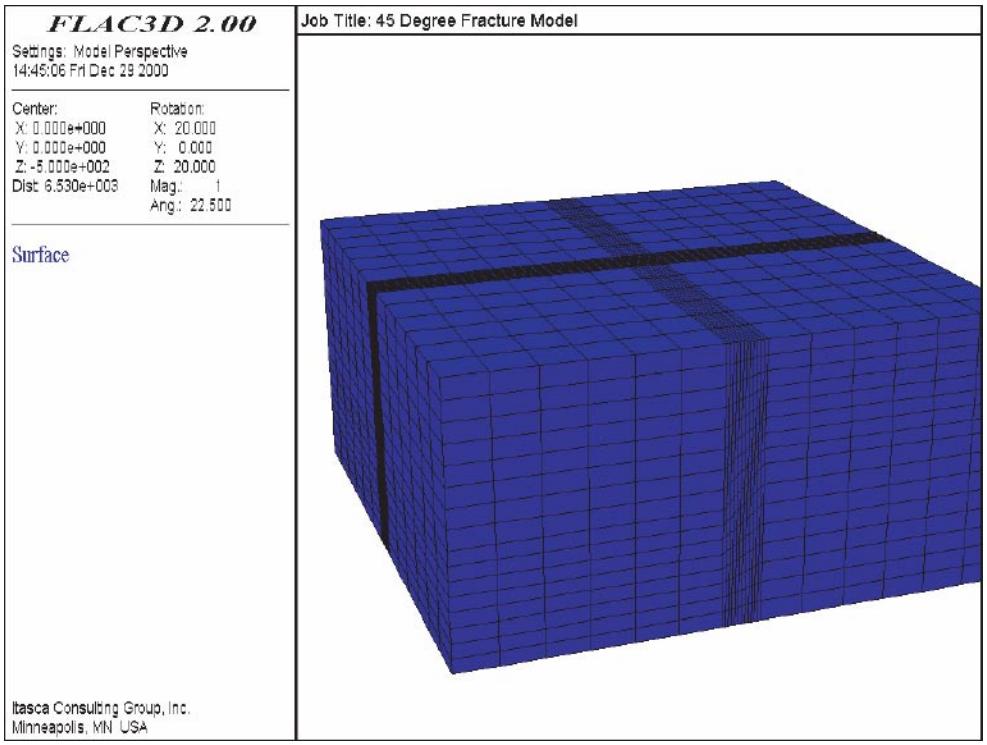

Figure A2a-3. *FLAC3D Grid for 45° Fracture Case.*

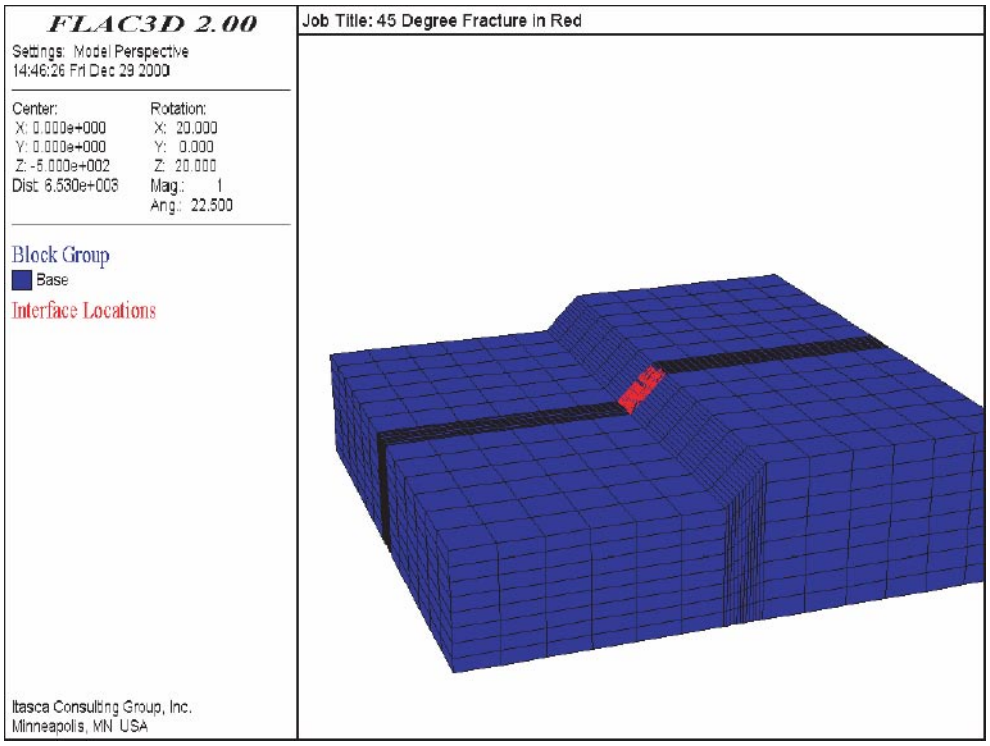

Figure A2a-4. *FLAC3D Grid for 45° Fracture Case. (The top is removed; the fracture is in red.)*

A2a-3 Properties

The rock mass is modeled as a homogeneous elastic mass with the following material properties:

Density	2,700 Kg/m^3
Young's Modulus	75 Gpa
Poisson's Ratio	0.25

The fracture has the following properties:

Friction	0, 15, 30 degrees
Cohesion	0.0
Tension	0.0
Normal Stiffness	10 GPa/m
Shear Stiffness	10 GPa/m

Table A2a-2. Stress States Considered in This Modeling Study.

	Stress State 0	Stress State I	Stress State II
σ_1 - horizontal	0 MPa	35 MPa	55 MPa
σ_2 - horizontal	0 MPa	20 MPa	20 MPa
σ_3 - vertical	0 MPa	13 MPa	7 MPa

A2a-4 Seismic input

Because there is a viscous boundary at the base of the model, it is not possible to define the seismic input as a velocity-vs.-time history, as is usual. In this case, a stress-vs.-time history is applied, in which the stress corresponds to the velocity according to the following relations:

$\Phi_n = 2V_n\,(\Delta C_p)$ Equation A2a-2

$\Phi_s = 2V_s\,(\Delta C_s)$ Equation A2a-3

where:

Φ_n = applied normal stress,
Φ_s = applied shear stress,
Δ = mass density,
Cp = speed of p-wave propagation,
Cs = speed of s-wave propagation,
V_n = normal particle velocity in the incident wave, and
V_s = shear particle velocity in the incident wave.

Following the recommendation from the seismology report (Appendix 1b), the input record of a dip-slip earthquake was used. Note that the dip-slip mechanism results in significant motions in only the vertical and x-planes. There is no relative motion in the plane parallel to the fault. Figure A2a-5 shows the conceptual geometry of the analysis. The fault is at a distance of 2 km, 6 km, or 10 km from the target fracture. In all cases, it is assumed that the motion at the base of the FLAC3D model is a plane wave and all base gridpoints move together. Figure A2a-6 shows the velocity-vs- time histories for the vertical and X-Y shear planes for the 2-km distance. The velocities for the 6 km and 10 km distances can be seen in Figure A2a-7 and Figure A2a-8. Figure A2a-9 through Figure A2a-11 show the same data converted to stress-vs.-time histories used as input to FLAC3D for the 2-km and 10-km cases, respectively.

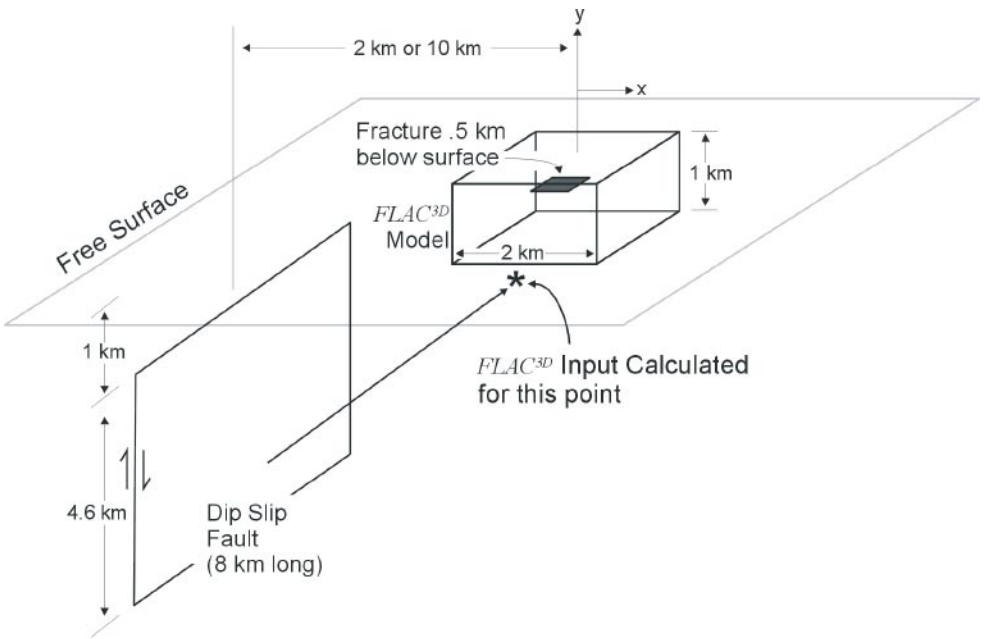

Figure A2a-5. *Conceptual Geometry.*

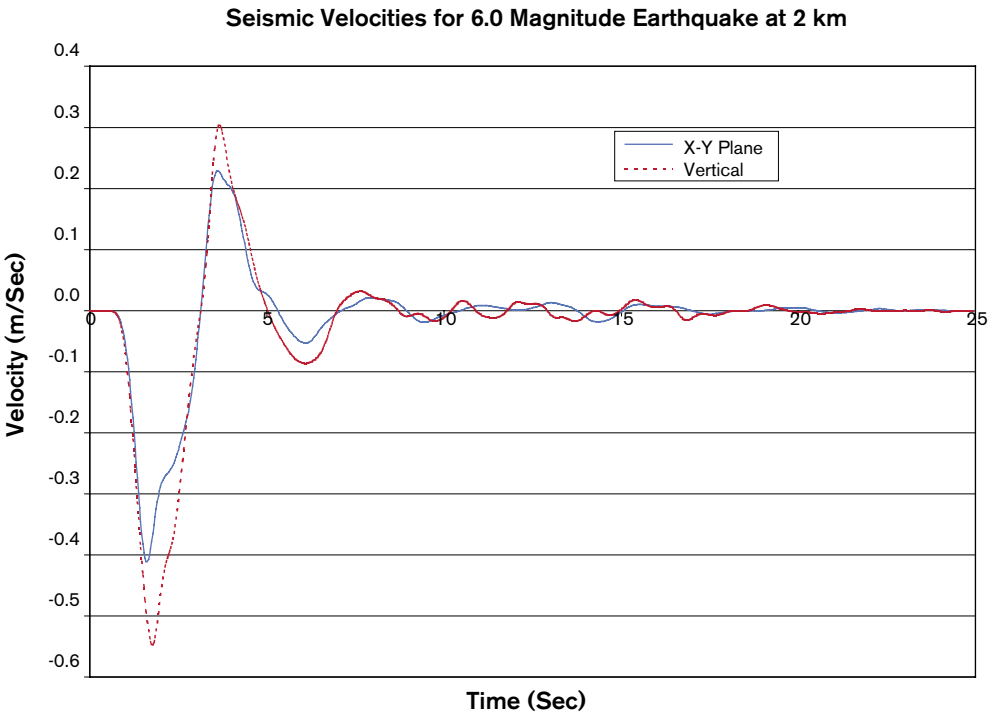

Figure A2a-6. *Velocity-Time Record for Magnitude 6.0 Earthquake at a Distance of 2 km.*

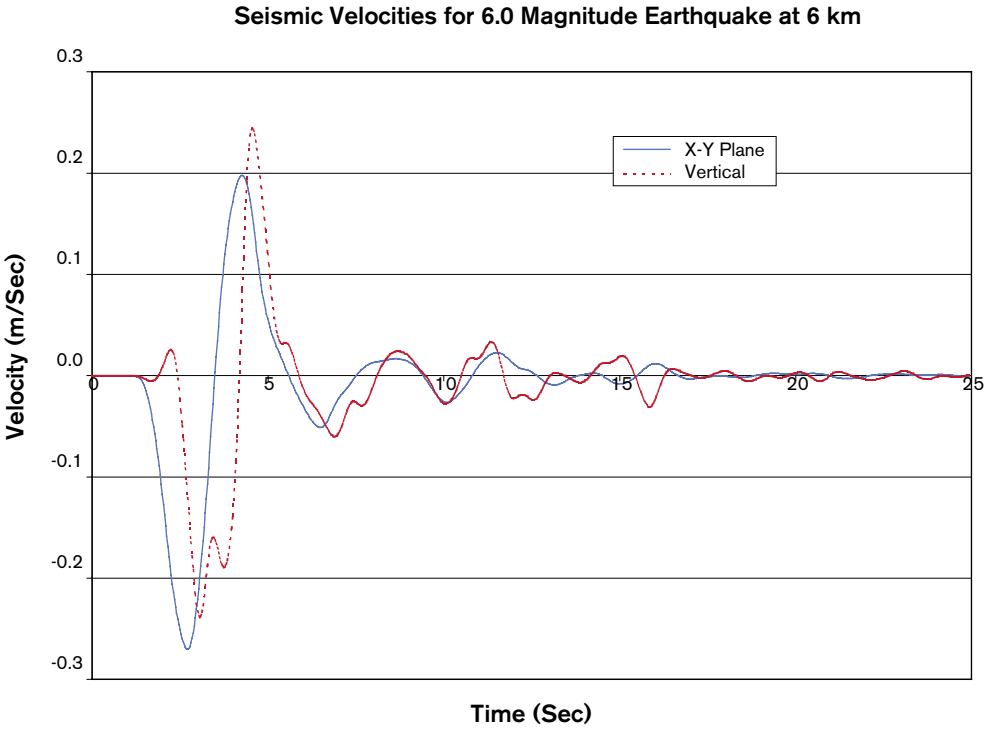

Figure A2a-7. *Velocity-Time Record for Magnitude 6.0 Earthquake at a Distance of 6 km.*

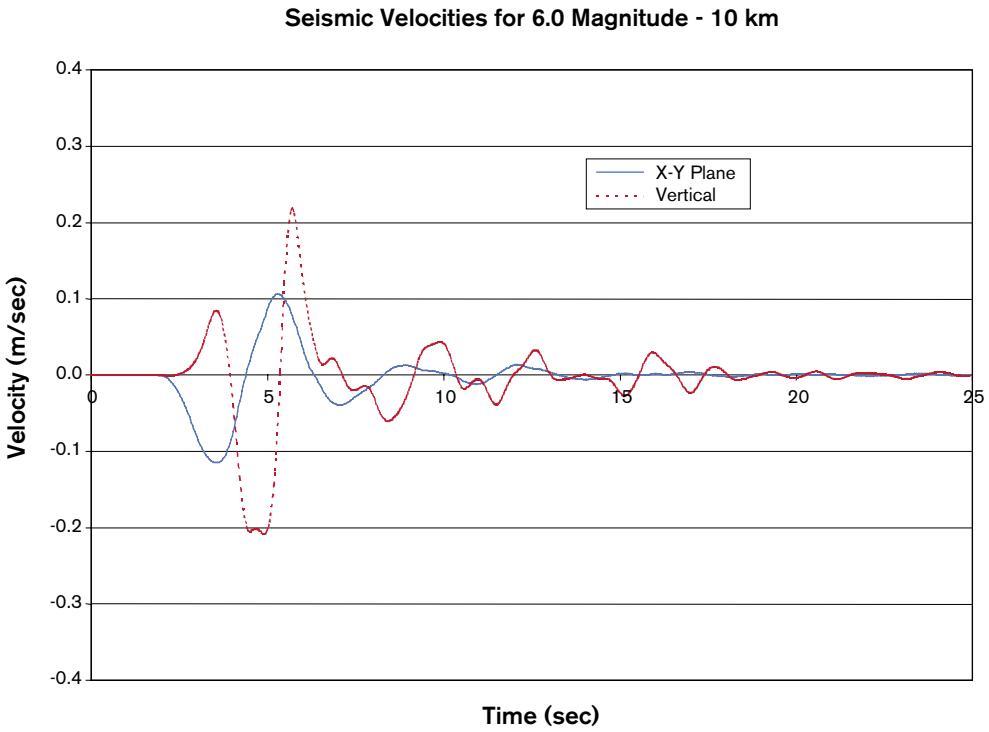

Figure A2a-8. *Velocity-Time Record for Magnitude 6.0 Earthquake at a Distance of 10 km.*

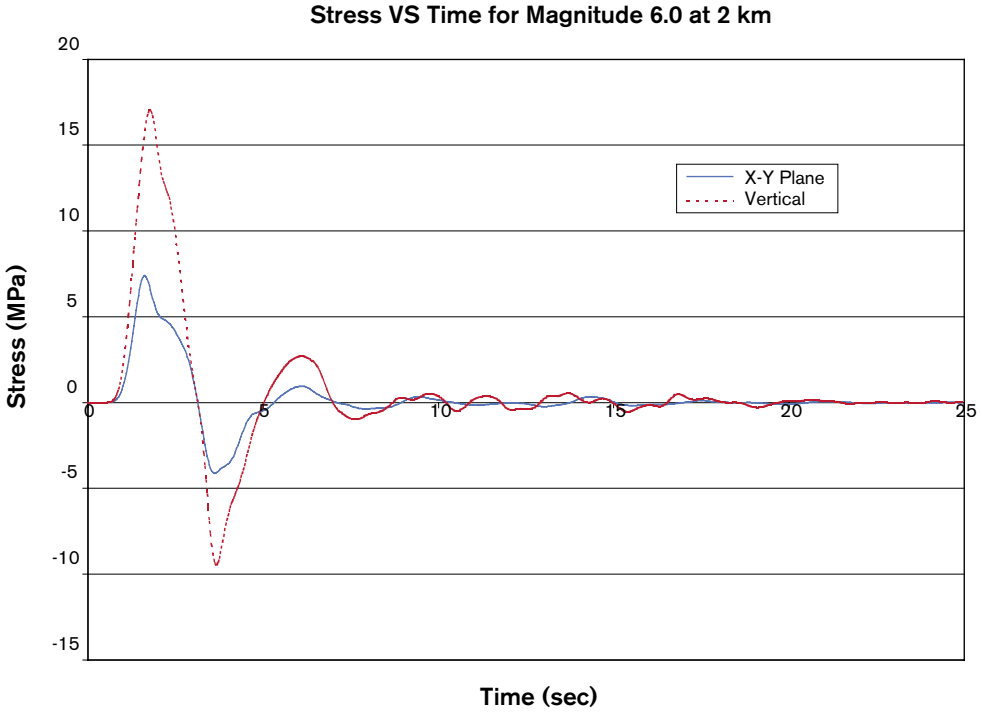

Figure A2a-9. *Stress-Time Record for Boundary Condition in FLAC3D. (Values are calculated from velocity record used in Equations A2a-2 and A2a-3. This record is for a Magnitude 6.0 earthquake at a distance of 2 km.)*

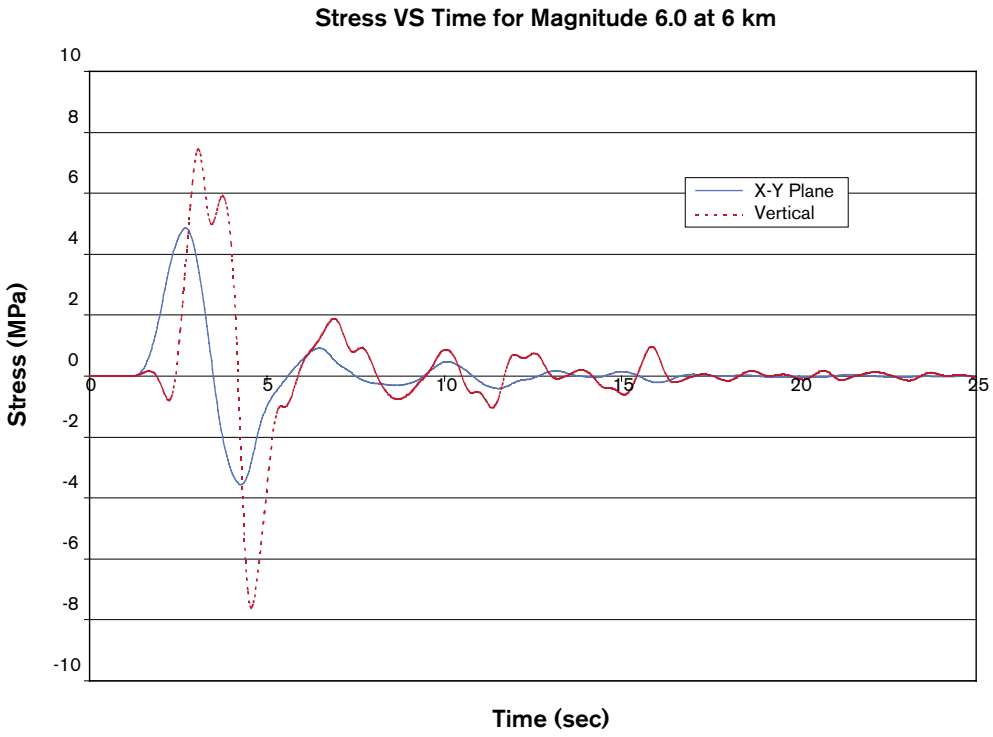

Figure A2a-10. *Stress-Time Record for Boundary Condition in FLAC3D. (Values are calculated from velocity record used in Equations A2a-2 and A2a-3. This record is for a Magnitude 6.0 earthquake at a distance of 6 km.)*

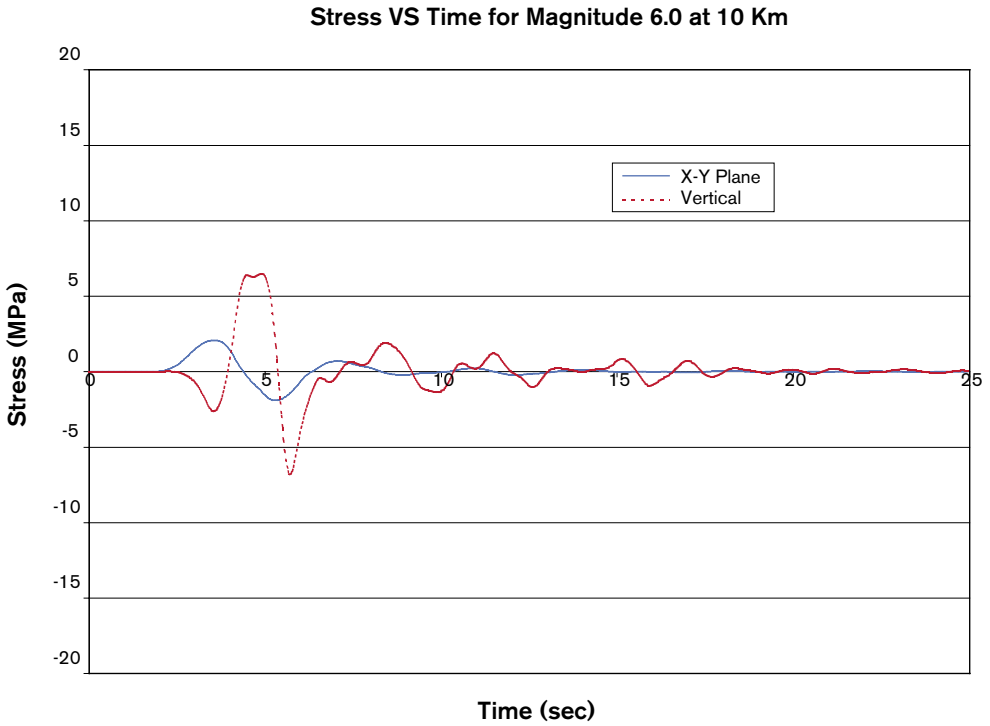

Figure A2a-11. *Stress-Time Record for Boundary Condition in FLAC3D. (Values are calculated from velocity record used in Equations A2a-2 and A2a-3. This record is for a Magnitude 6.0 earthquake at a distance of 10 km.)*

A2a-5 Results

Thirty-one (31) cases were analyzed. The horizontal fracture model was run with the input representing distances of 2 km, 6 km, and 10 km. The models with the 45° fracture were run with the data for 2 km and 10 km. In addition to these runs, the 45° model was also run for both distances, with the model rotated 90° so that the dip for the fracture was parallel to the earthquake fault. The shear displacements at the center of the fracture were calculated and saved as histories. All fractures were run with the stress states shown in Table A2a-2. Friction angles of 0°, 15°, and 30° were used. Some of the cases included here were also reported in the previous report (Appendix 1a). They are included here for comparison purposes. All displacements presented are the relative horizontal displacements across the target fracture. This represents the displacements that would impact a waste package in a vertical hole. The displacements are calculated at the center of the target fracture.

Figure A2a-12 shows the history of the shear displacements at a point in the center of the fracture for a horizontal fracture at a distance of 2-km from the epicenter. The maximum shear displacement in this case was 0.58 cm. This is approximately double the 0.3-cm maximum (0.1-cm mean) displacement reported by LaPointe for this distance and seismic magnitude. This displacement is approximately 30% of the combined static and dynamic displacement of the 1.66 cm calculated in WAVE. Figure A2a-13 shows the time histories for the same model but with the input from the 6-km distant earthquake. In this case the maximum displacement of 0.380 cm is greater then the maximum of 0.1 cm (0.05-cm mean) reported by LaPointe. This is approximately the same as the value calculated in WAVE (0.32-cm). Figure A2a-14 shows the time histories for the input from the10-km distant earthquake. Again, the maximum displacement of 0.16 cm is greater then the maximum of 0.07 cm (0.028-cm mean) reported by LaPointe.

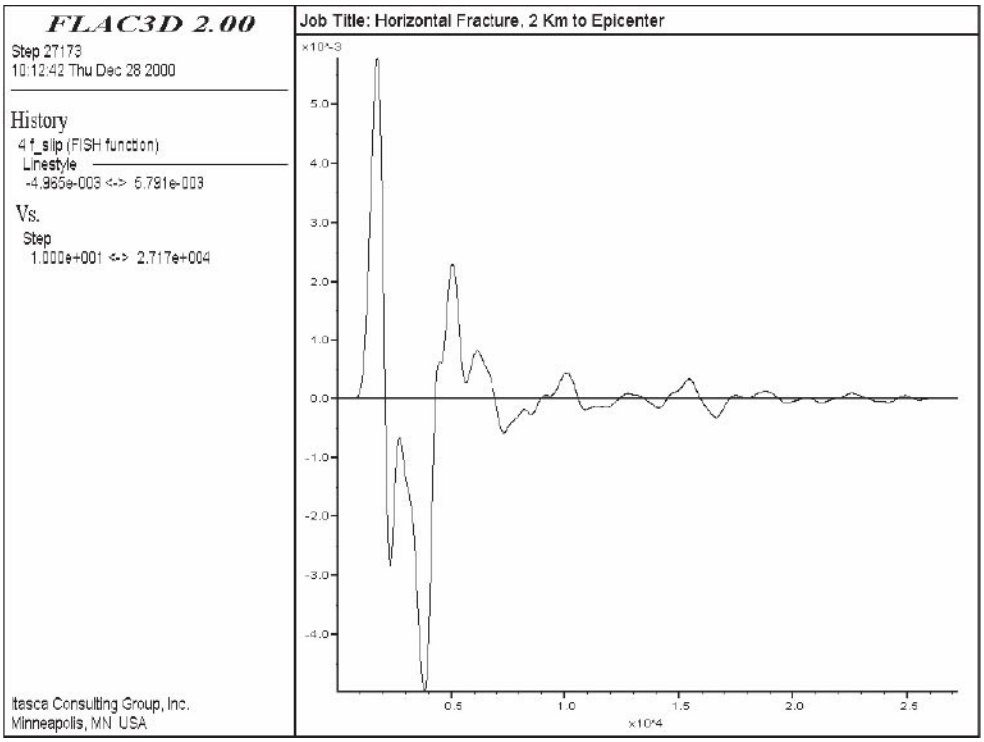

Figure A2a-12. *Shear Displacements at the Center of Fracture for a 6.0 Magnitude Earthquake at a Distance of 2 km (friction = 0°, stress state 0).*

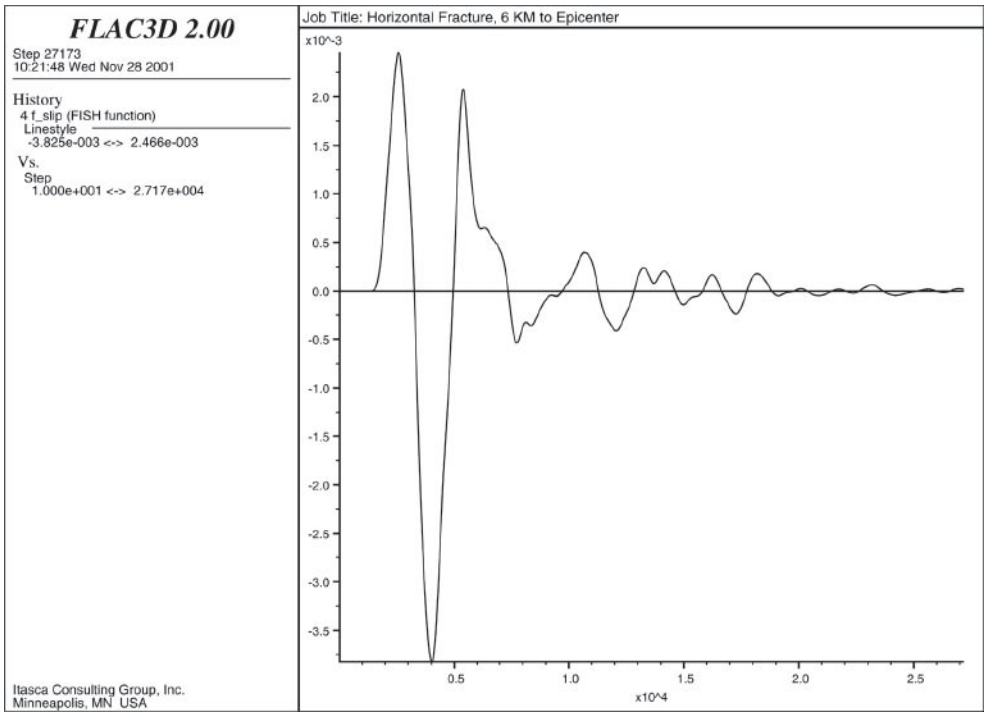

Figure A2a-13. *Shear Displacements at the Center of Fracture for a 6.0 Magnitude Earthquake at a Distance of 6 km (friction = 0°, stress state 0).*

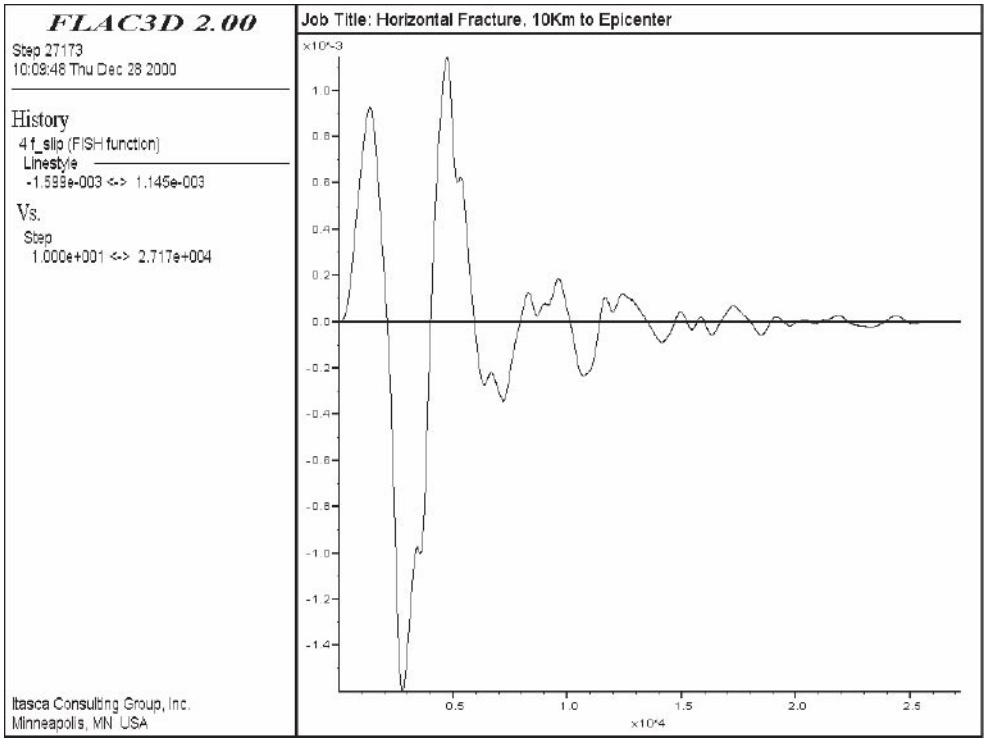

Figure A2a-14. *Shear Displacements at the Center of Fracture for a 6.0 Magnitude Earthquake at a Distance of 10 km (friction = 0°, stress state 0).*

Figure A2a-15 shows the maximum horizontal shear displacements for the case with a 45° fracture (dip direction perpendicular to the fault strike) at a distance of 2 km. The magnitude (0.18 cm) of the shear displacement is significantly smaller than the displacements of the horizontal fracture. For the 10-km distance, the shear displacement (0.07 cm), as shown in Figure A2a-16, is also smaller than that obtained for the horizontal fracture.

Figure A2a-17 and Figure A2a-18 show the shear displacements for the case in which the dip of the 45° fracture is parallel to the fault strike. For both distances (2 km and 10 km), the maximum shear displacements (0.28 cm and 0.08 cm) are similar to the case in which the dip direction is perpendicular to the fault strike.

Figure A2a-19 through Figure A2a-26 represent models of horizontal fractures in which the stress states and fracture strengths were varied. The displacements in most of these cases were very small and limited to elastic deformation of the fracture. In only two cases (both cases for stress state II at the 2 km distance) the fractures slipped in excess of the elastic deformation. Of these two, for the 15° friction case, the displacements calculated by WAVE were greater by a factor of three. In the other cases, where only elastic deformations took place, the total deformations where less than .02 cm. The WAVE results for the elastic deformation cases were 10 times greater.

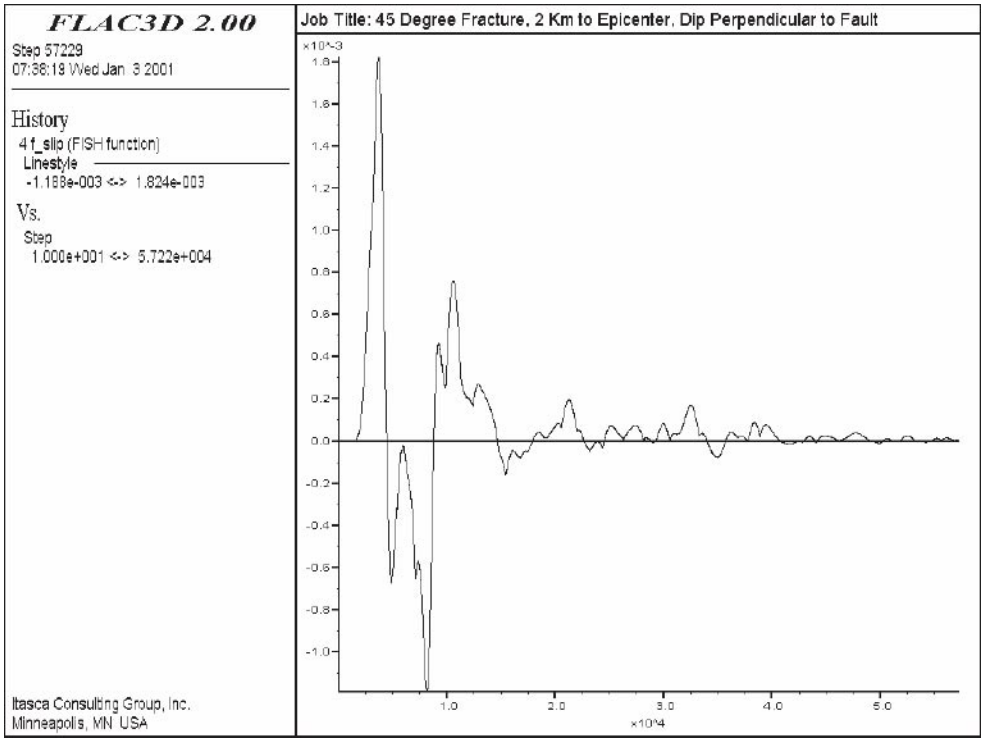

Figure A2a-15. *Shear Displacements at the Center of a 45° Fracture for 6.0 Magnitude Earthquake at a Distance of 2 km. (The dip direction of the fracture is perpendicular to the fault strike; friction = 0°, stress state 0.)*

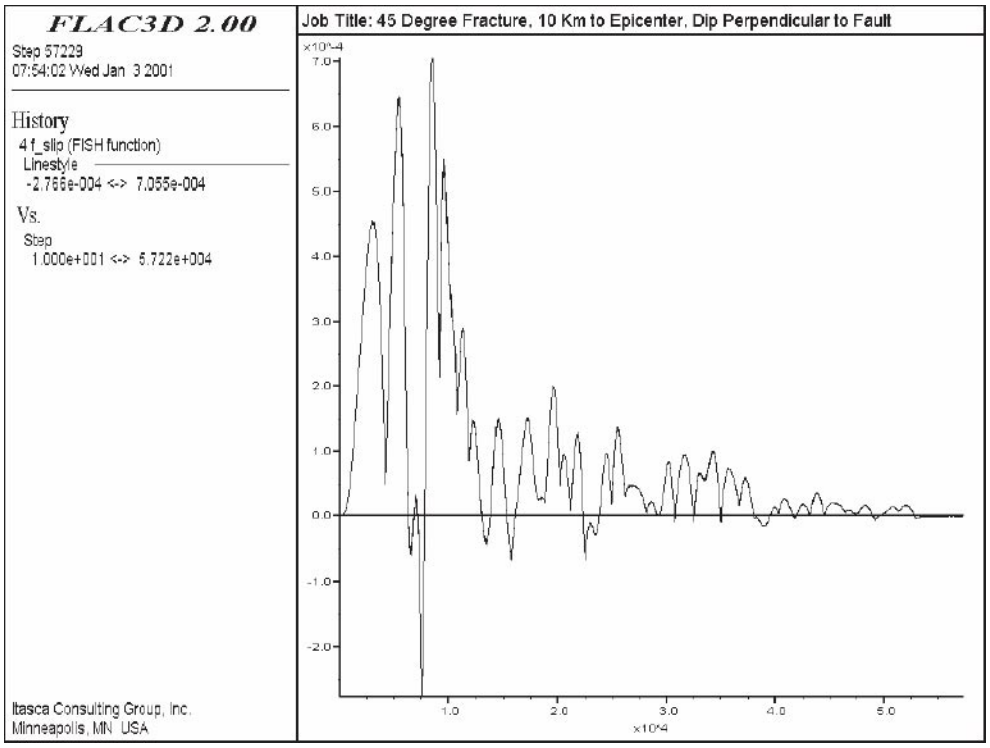

Figure A2a-16. *Shear Displacements at the Center of a 45° Fracture for a 6.0 Magnitude Earthquake at a Distance of 10 km. (The dip direction of the fracture is perpendicular to the fault strike; friction = 0°, stress state 0.)*

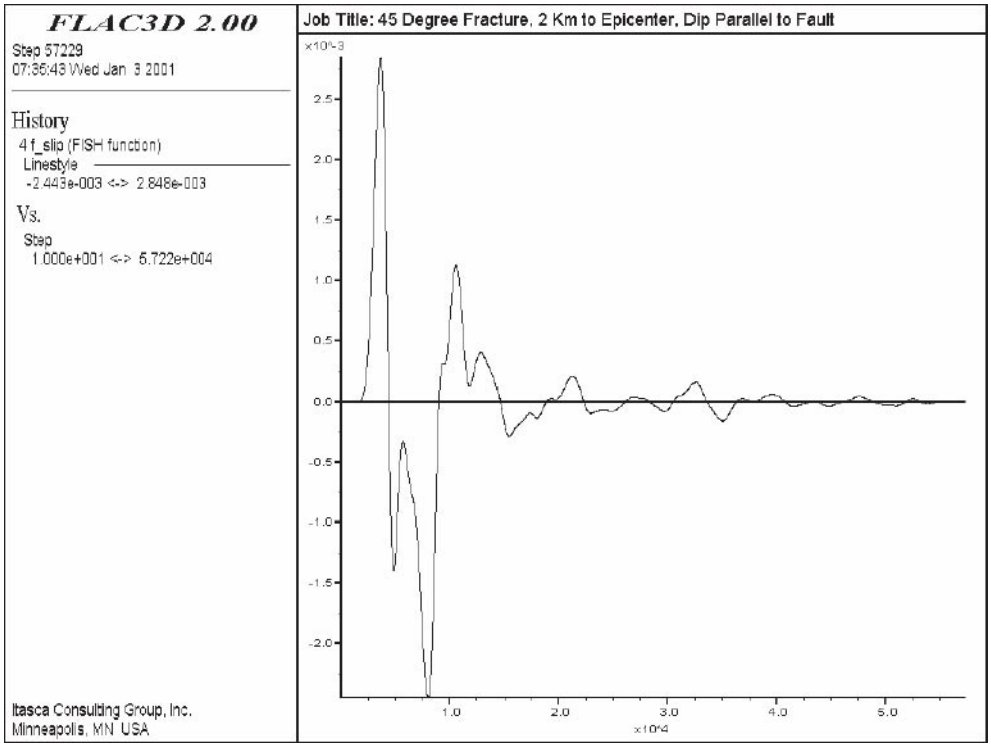

Figure A2a-17. *Shear Displacement at the Center of a 45° Fracture for a 6.0 Magnitude Earthquake at a distance of 2 km. (The dip direction of the fracture is parallel to the fault strike; friction = 0°, stress state 0.)*

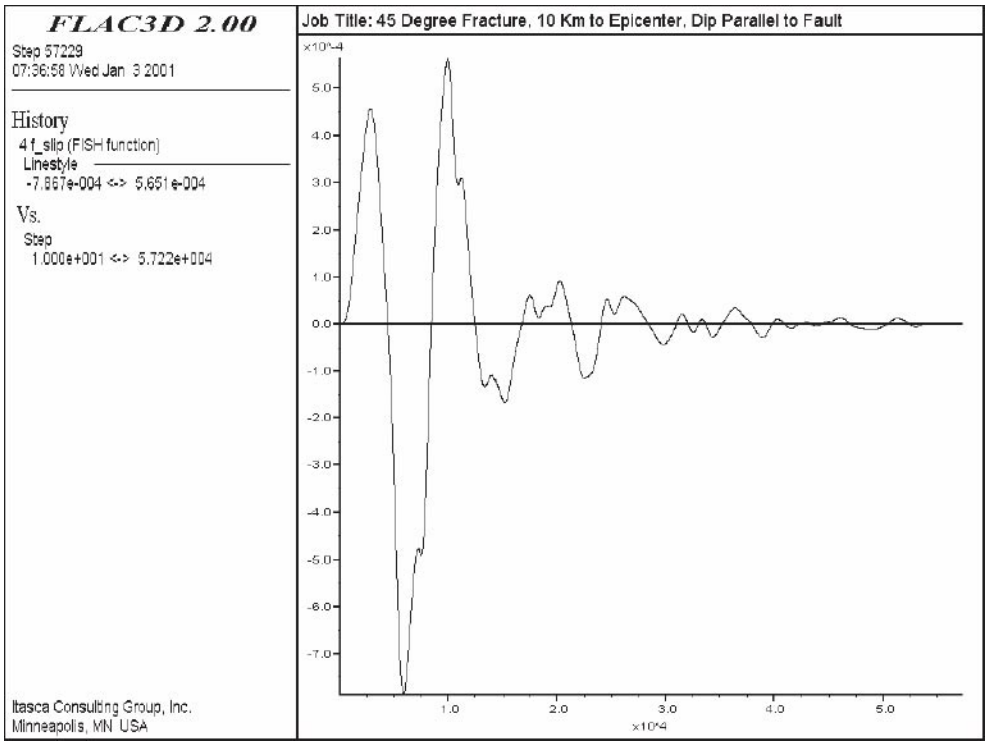

Figure A2a-18. *Shear Displacement at the Center of a 45° Fracture for a 6.0 Magnitude Earthquake at a Distance of 10 km. (The dip direction is parallel to the fault strike; friction = 0°, stress state 0.)*

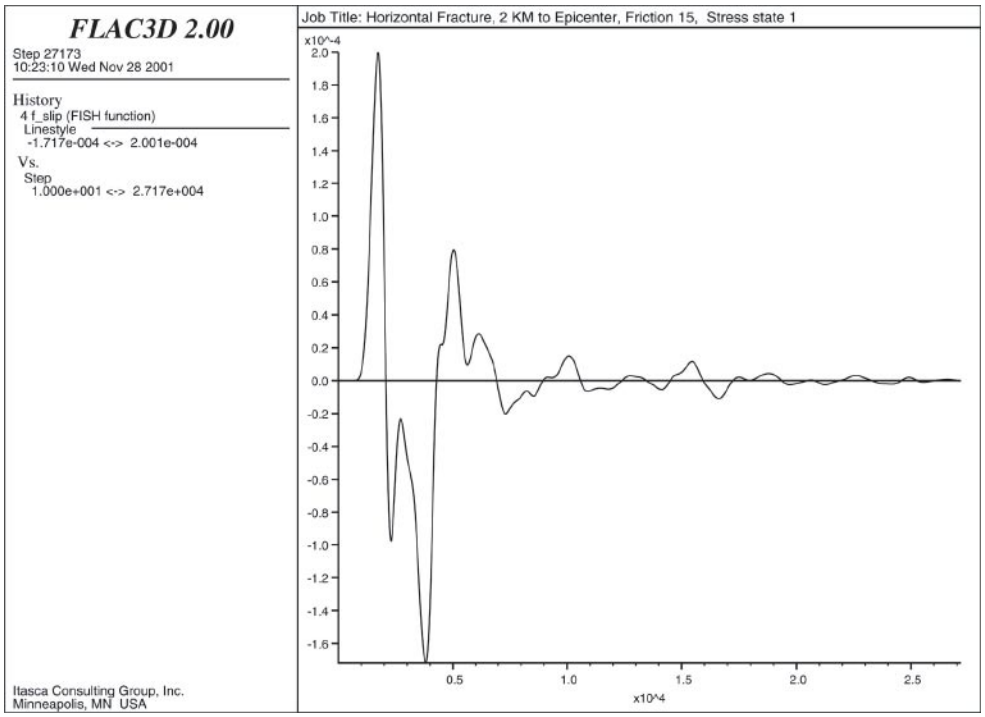

Figure A2a-19. *Shear Displacements at the Center of Fracture for a 6.0 Magnitude Earthquake at a Distance of 2 km (friction = 15°, stress state I).*

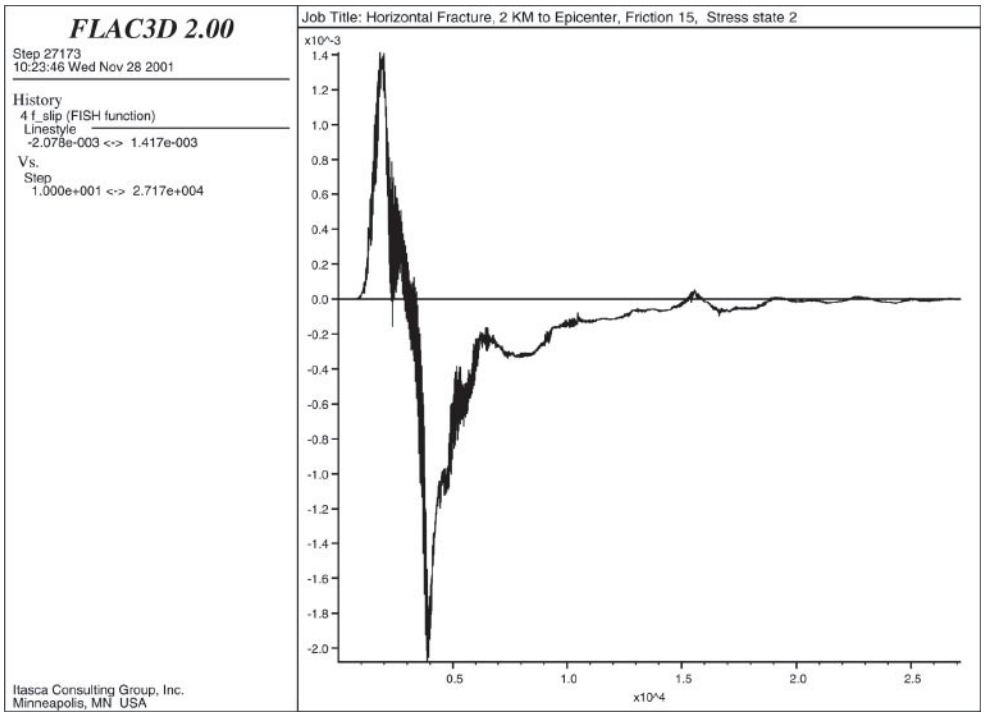

Figure A2a-20. *Shear Displacements at the Center of Fracture for a 6.0 Magnitude Earthquake at a Distance of 2 km (friction = 15°, stress state II).*

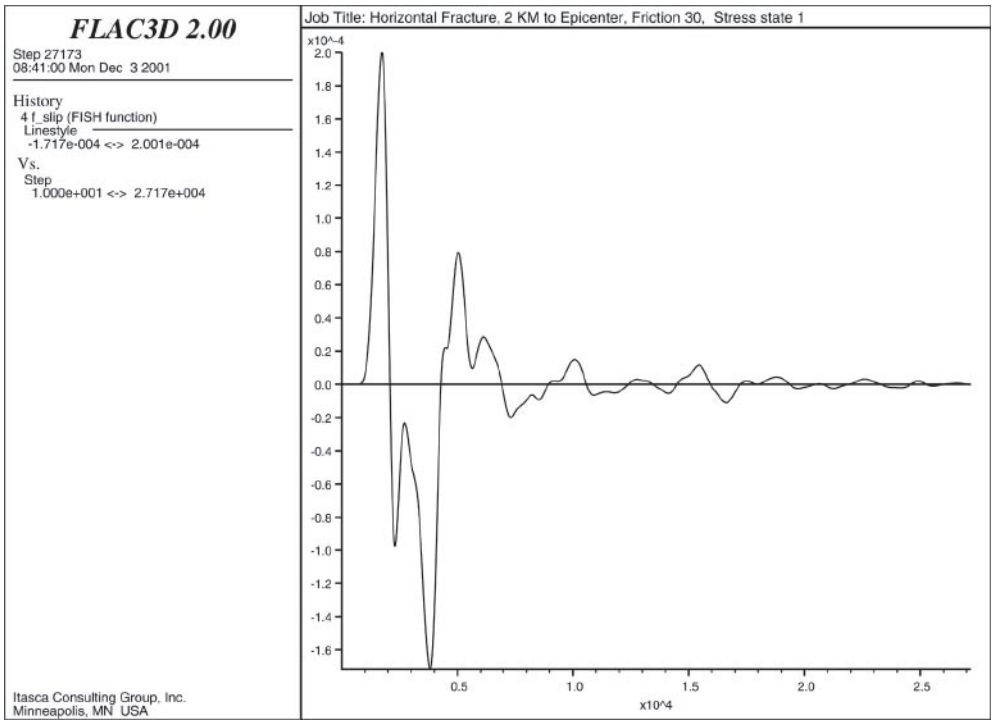

Figure A2a-21. *Shear Displacements at the Center of Fracture for a 6.0 Magnitude Earthquake at a Distance of 2 km (friction = 30°, stress state I).*

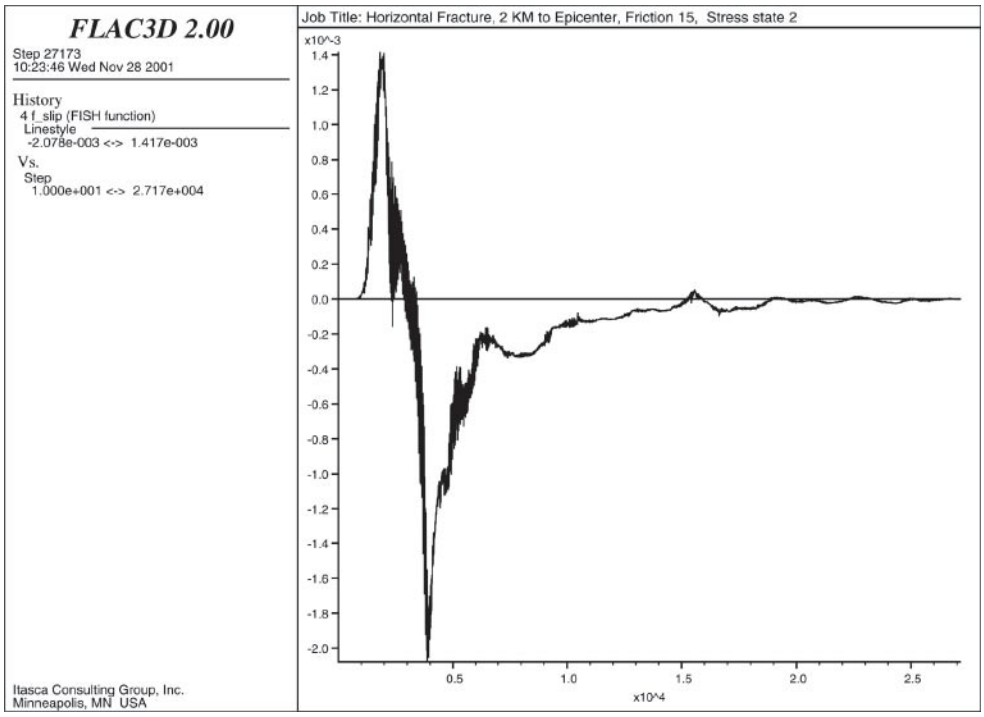

Figure A2a-22. *Shear Displacements at the Center of Fracture for a 6.0 Magnitude Earthquake at a Distance of 2 km (friction = 15°, stress state II).*

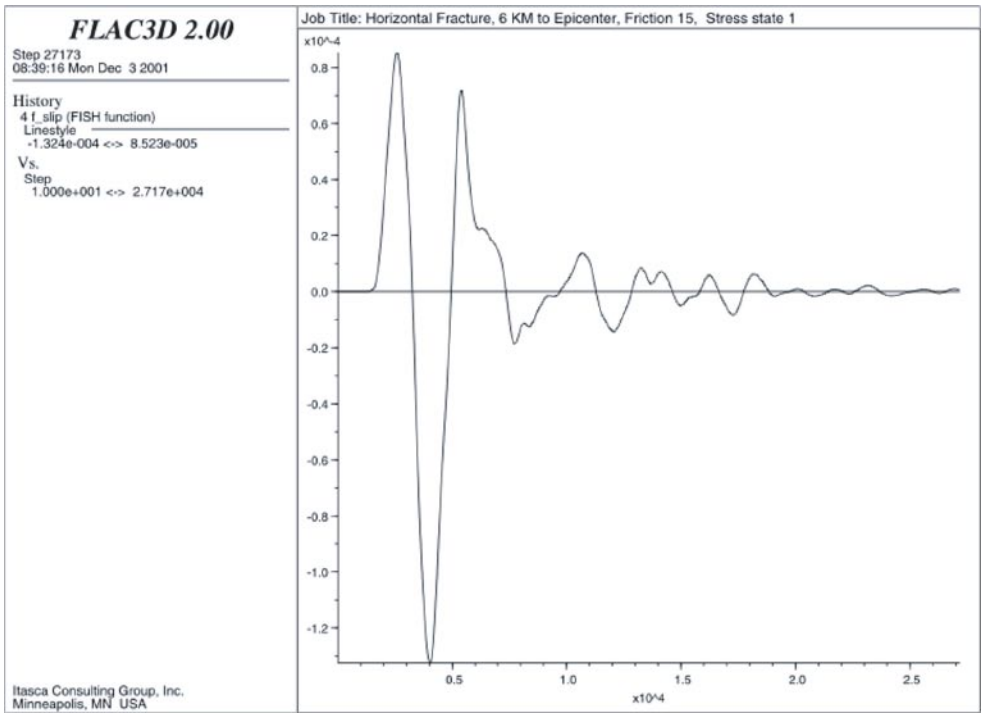

Figure A2a-23. *Shear Displacements at the Center of Fracture for a 6.0 Magnitude Earthquake at a Distance of 6 km (friction = 15°, stress state I).*

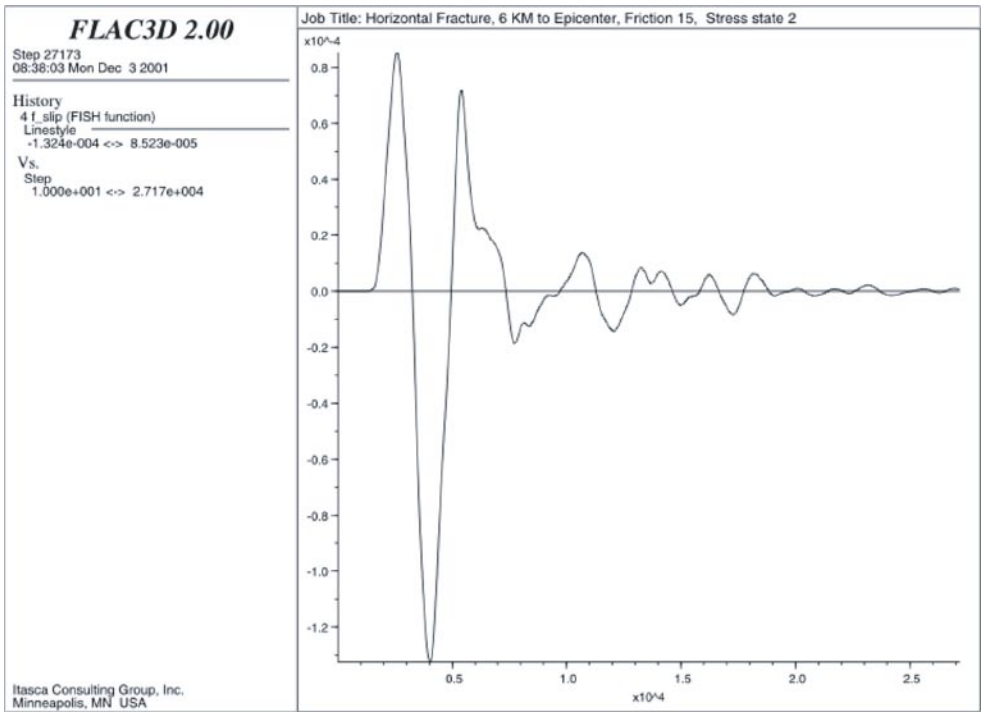

Figure A2a-24. *Shear Displacements at the Center of Fracture for a 6.0 Magnitude Earthquake at a Distance of 6 km (friction = 15°, stress state II).*

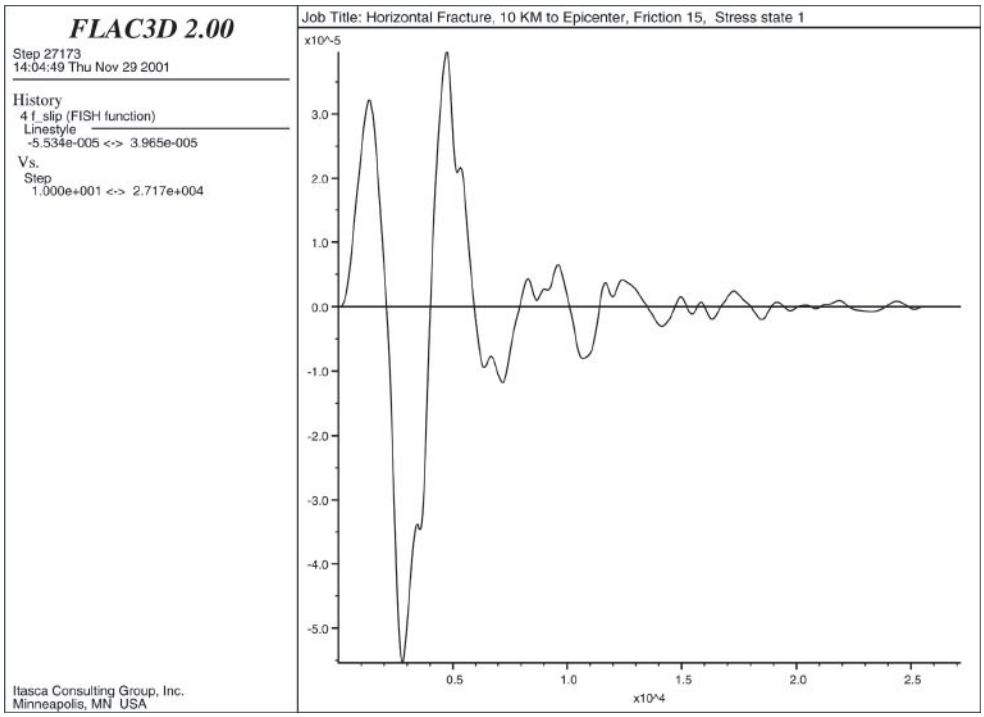

Figure A2a-25. *Shear Displacements at the Center of Fracture for a 6.0 Magnitude Earthquake at a Distance of 10 km (friction = 15°, stress state I).*

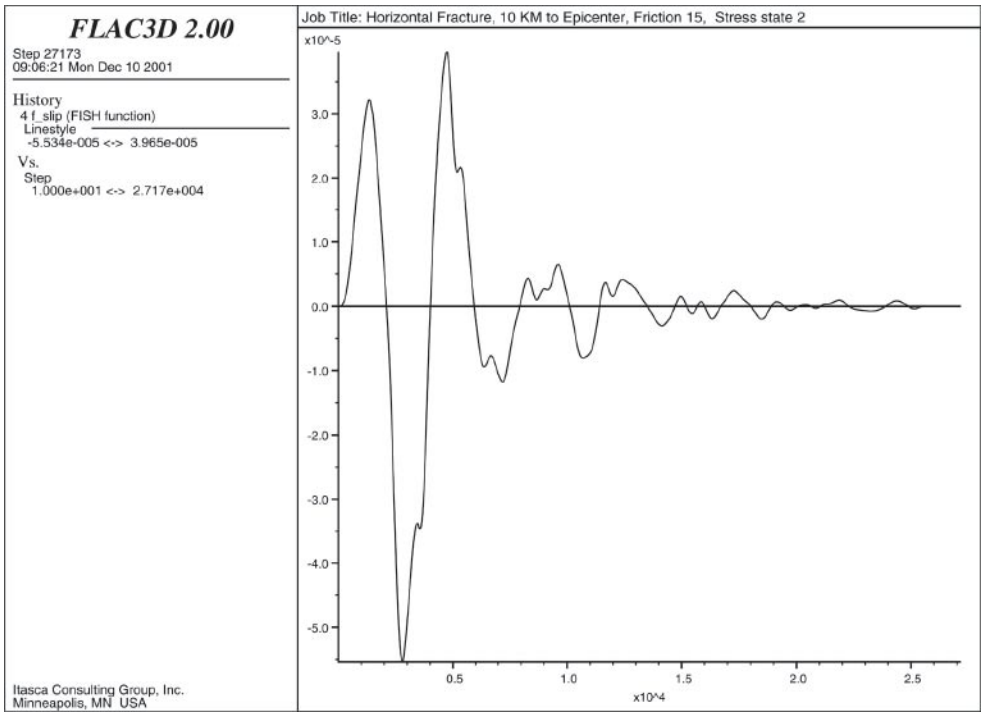

Figure A2a-26. *Shear Displacements at the Center of Fracture for a 6.0 Magnitude Earthquake at a Distance of 10 km (friction = 15°, stress state II).*

Figure A2a-27 through Figure A2a-42 represent the cases of the inclined fractures in which the friction and stress states were varied. In all cases, the displacements due to the seismic event were small. It is important to note the values of the pre-seismic displacements that occur as a result of the initial stresses (Table A2a-1). These static displacements are greater than any of the seismically induced displacements. The cases where displacements occurred prior to the seismic event also showed the greatest displacement during the seismic event. However, even in these cases, the maximum displacements were less that 0.3 cm. In the cases where pre-seismic displacements occurred, the seismic event resulted in permanent displacements. It is unknown if these displacements would accumulate as a result of multiple events

While it was not specifically determined in this study, there exists a stress-strength combination in which the fracture is just below the slip threshold (prior to the seismic event). A seismic event of the magnitude studied in this report could then cause a displacement of the order of 3.0 cm to occur.

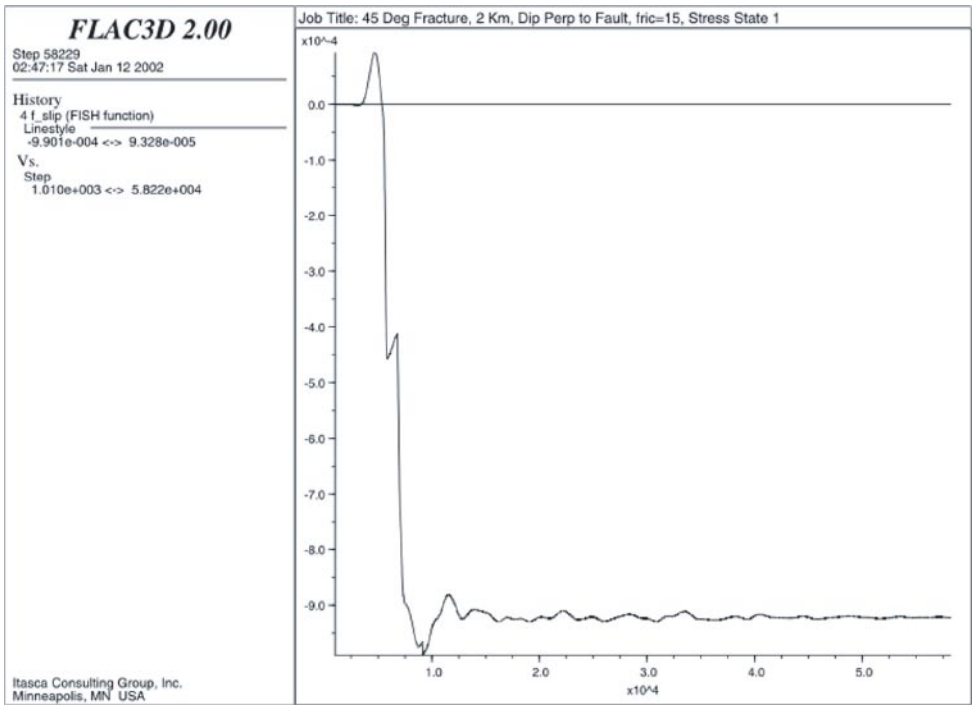

Figure A2a-27. *Shear Displacements at the Center of a 45° Fracture for 6.0 Magnitude Earthquake at a Distance of 2 km. (The dip direction of the fracture is perpendicular to the fault strike; friction = 15°, stress state I.)*

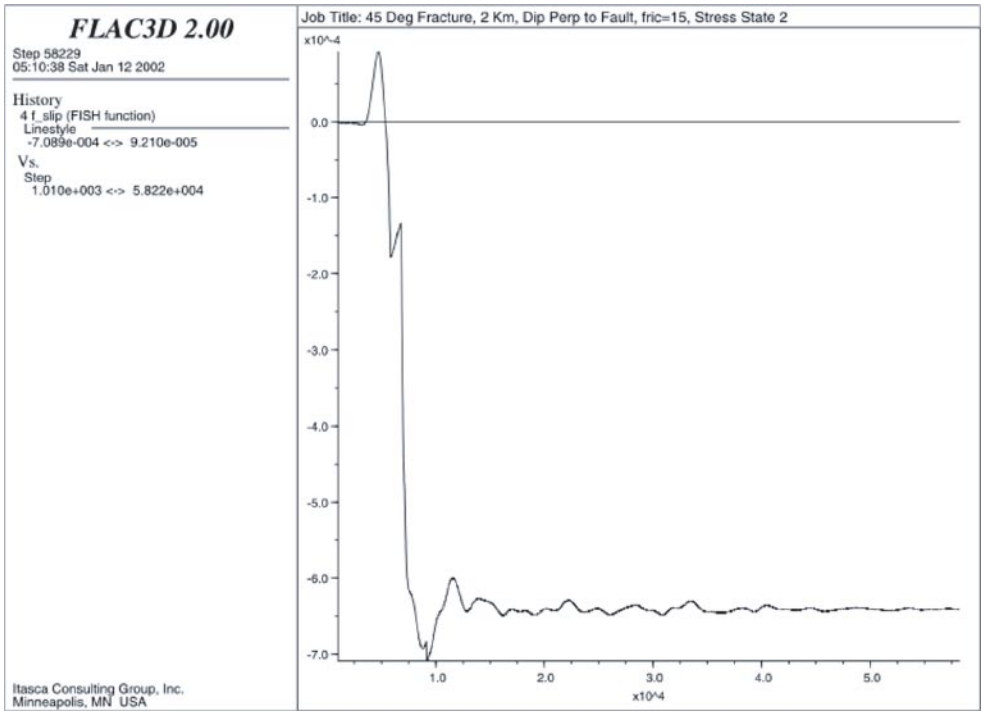

Figure A2a-28. *Shear Displacements at the Center of a 45° Fracture for 6.0 Magnitude Earthquake at a Distance of 2 km. (The dip direction of the fracture is perpendicular to the fault strike; friction = 15°, stress state II.)*

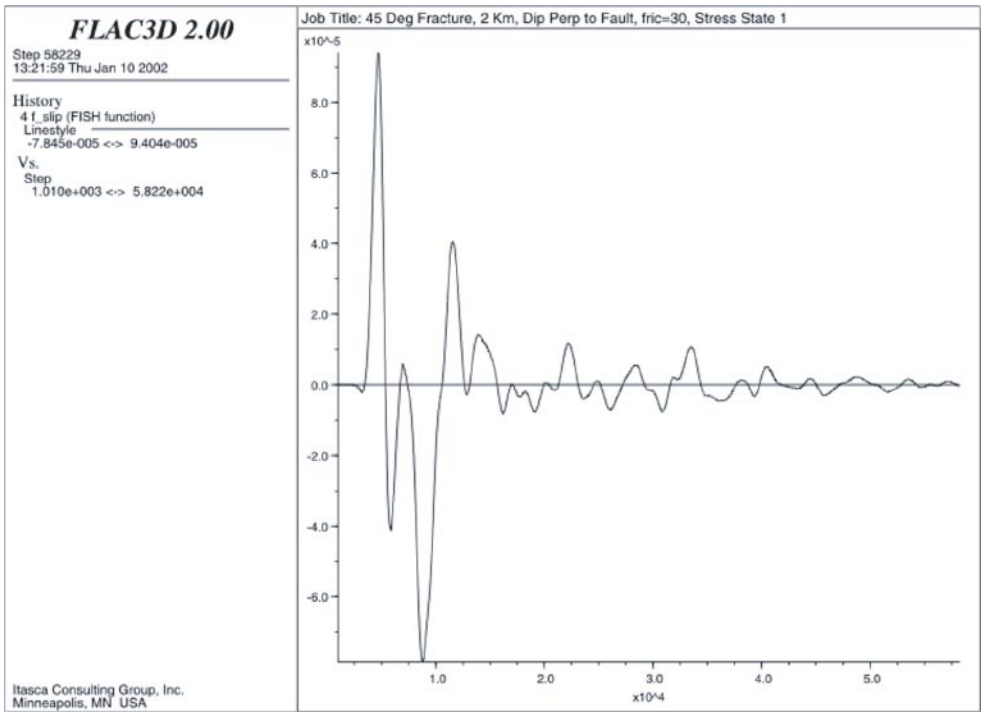

Figure A2a-29. *Shear Displacements at the Center of a 45° Fracture for 6.0 Magnitude Earthquake at a Distance of 2 km. (The dip direction of the fracture is perpendicular to the fault strike; friction = 30°, stress state I.)*

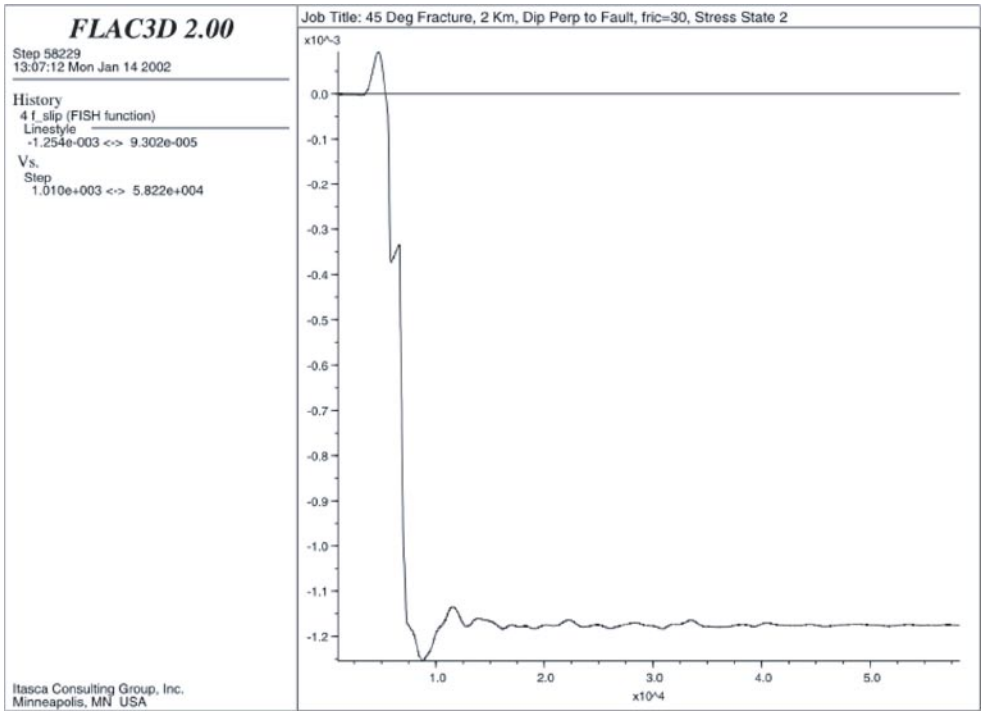

Figure A2a-30. *Shear Displacements at the Center of a 45° Fracture for 6.0 Magnitude Earthquake at a Distance of 2 km. (The dip direction of the fracture is perpendicular to the fault strike; friction = 30°, stress state II.)*

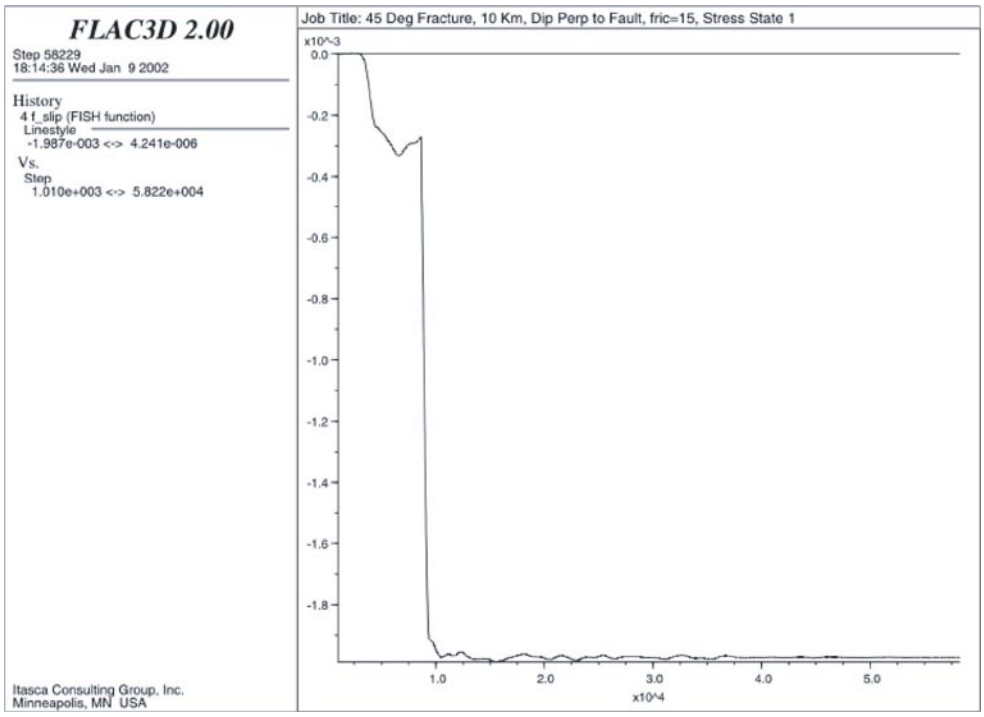

Figure A2a-31. *Shear Displacements at the Center of a 45° Fracture for 6.0 Magnitude Earthquake at a Distance of 10 km. (The dip direction of the fracture is perpendicular to the fault strike; friction = 15°, stress state I)*

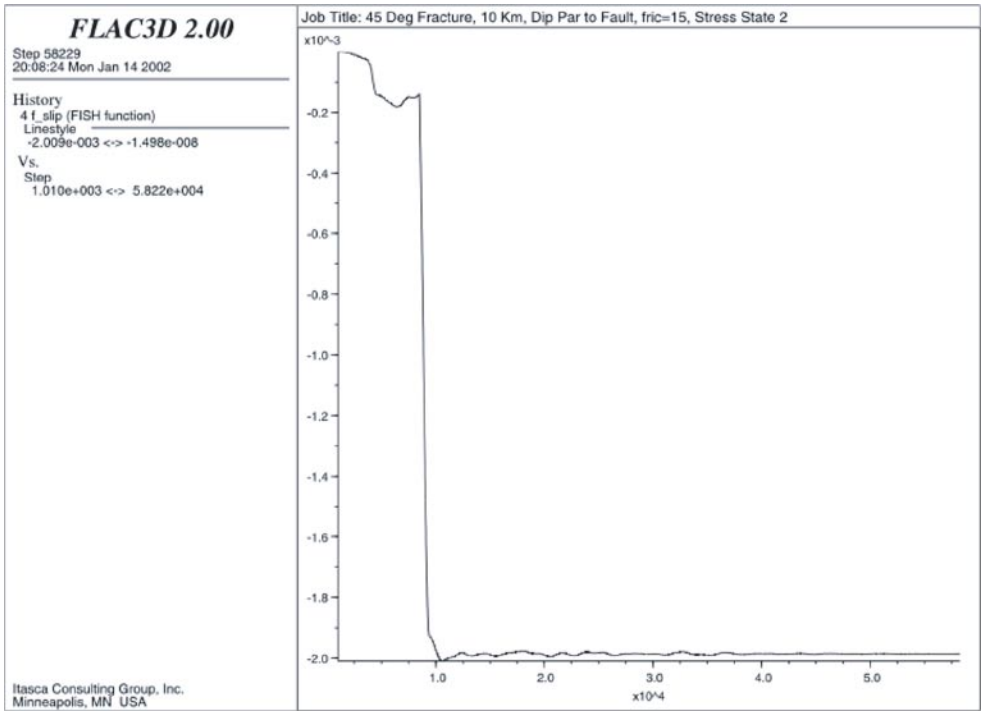

Figure A2a-32. *Shear Displacements at the Center of a 45° Fracture for 6.0 Magnitude Earthquake at a Distance of 10 km. (The dip direction of the fracture is perpendicular to the fault strike; friction = 15°, stress state II.)*

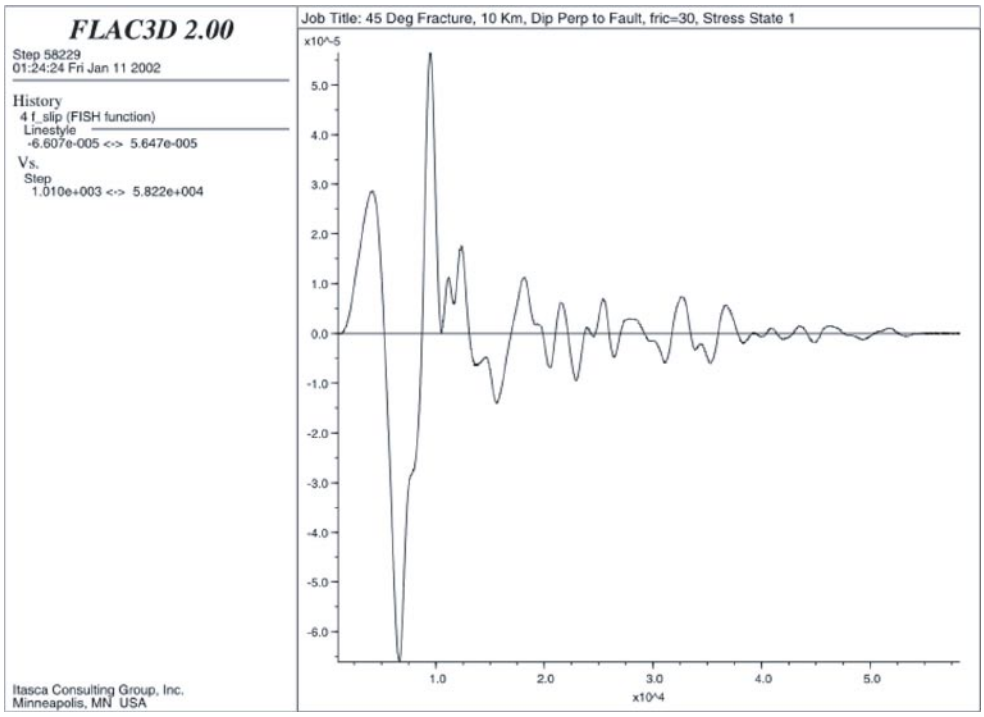

Figure A2a-33. *Shear Displacements at the Center of a 45° Fracture for 6.0 Magnitude Earthquake at a Distance of 10 km. (The dip direction of the fracture is perpendicular to the fault strike; friction = 30°, stress state I.)*

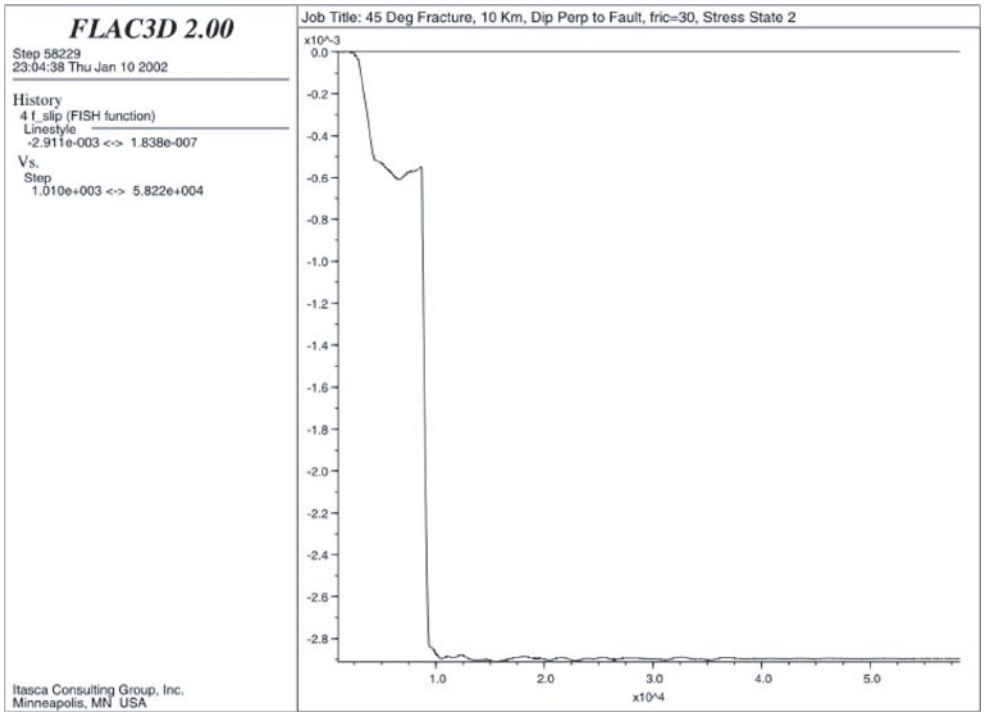

Figure A2a-34. *Shear Displacements at the Center of a 45° Fracture for 6.0 Magnitude Earthquake at a Distance of 10 km. (The dip direction of the fracture is perpendicular to the fault strike; friction = 30°, stress state II.)*

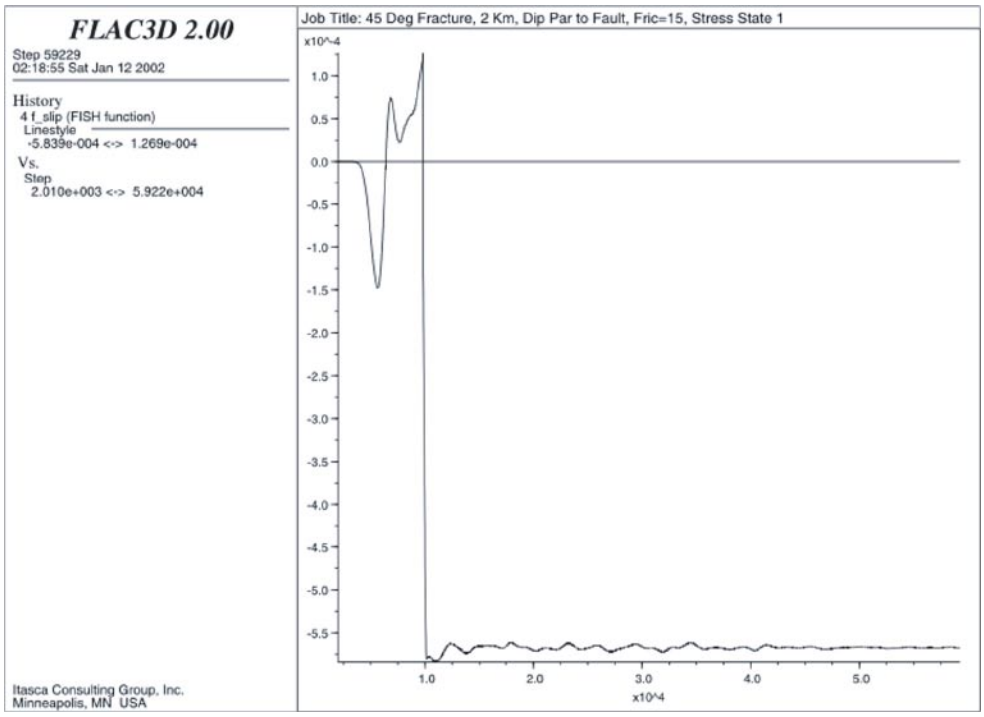

Figure A2a-35. *Shear Displacements at the Center of a 45° Fracture for 6.0 Magnitude Earthquake at a Distance of 2 km. (The dip direction of the fracture is parallel to the fault strike; friction = 15°, stress state I.)*

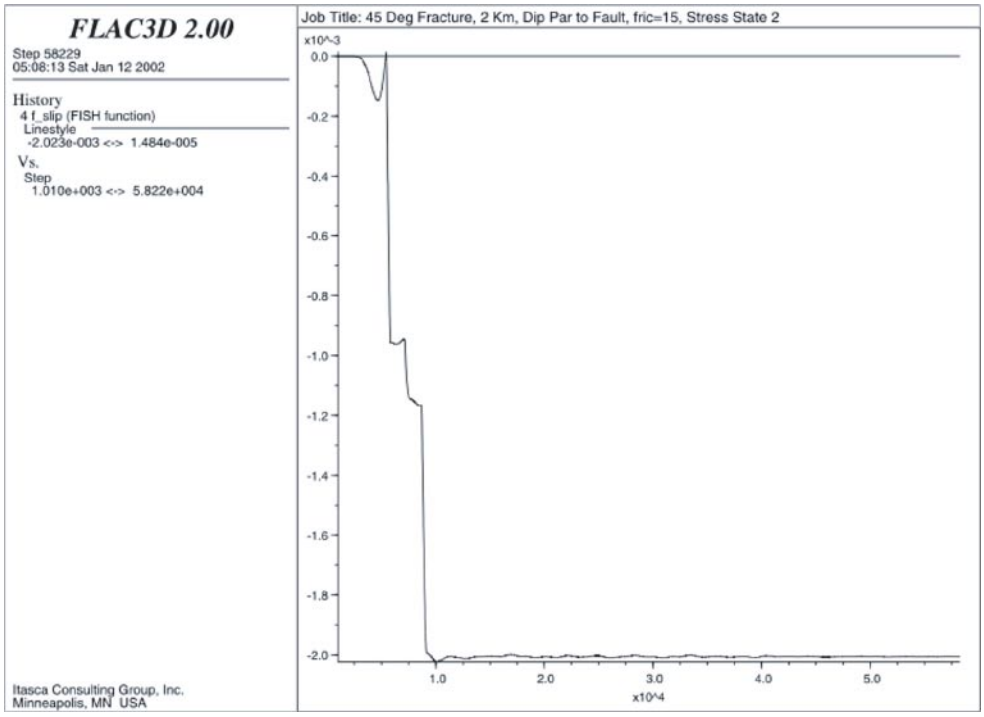

Figure A2a-36. *Shear Displacements at the Center of a 45° Fracture for 6.0 Magnitude Earthquake at a Distance of 2 km. (The dip direction of the fracture is parallel to the fault strike; friction = 15°, stress state II.)*

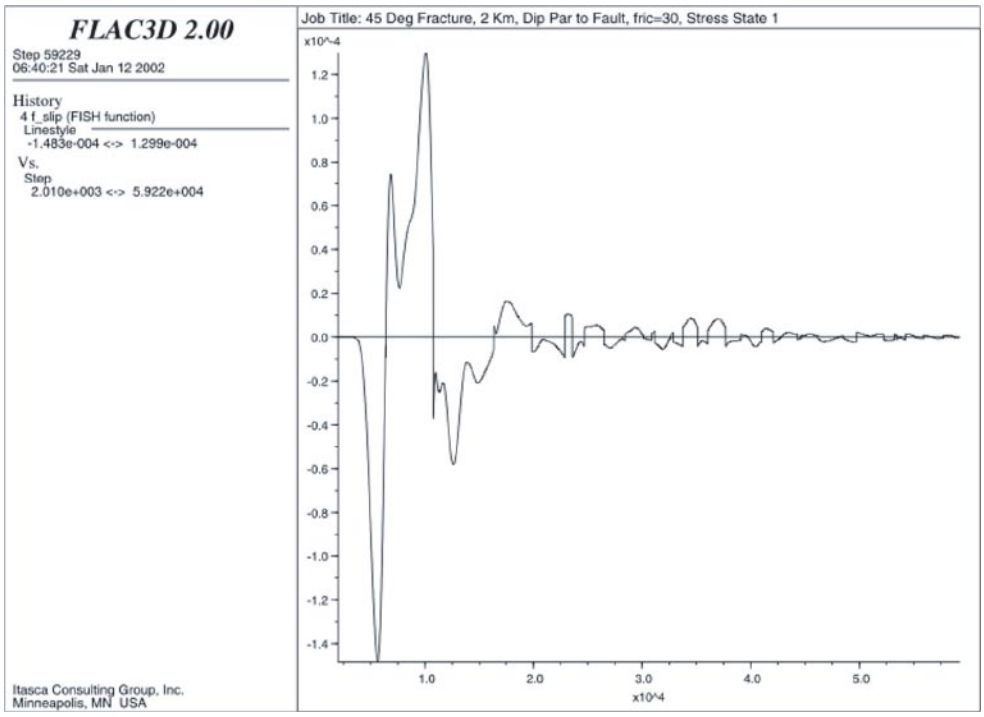

Figure A2a-37. *Shear Displacements at the Center of a 45° Fracture for 6.0 Magnitude Earthquake at a Distance of 2 km. (The dip direction of the fracture is parallel to the fault strike; friction = 30°, stress state I.)*

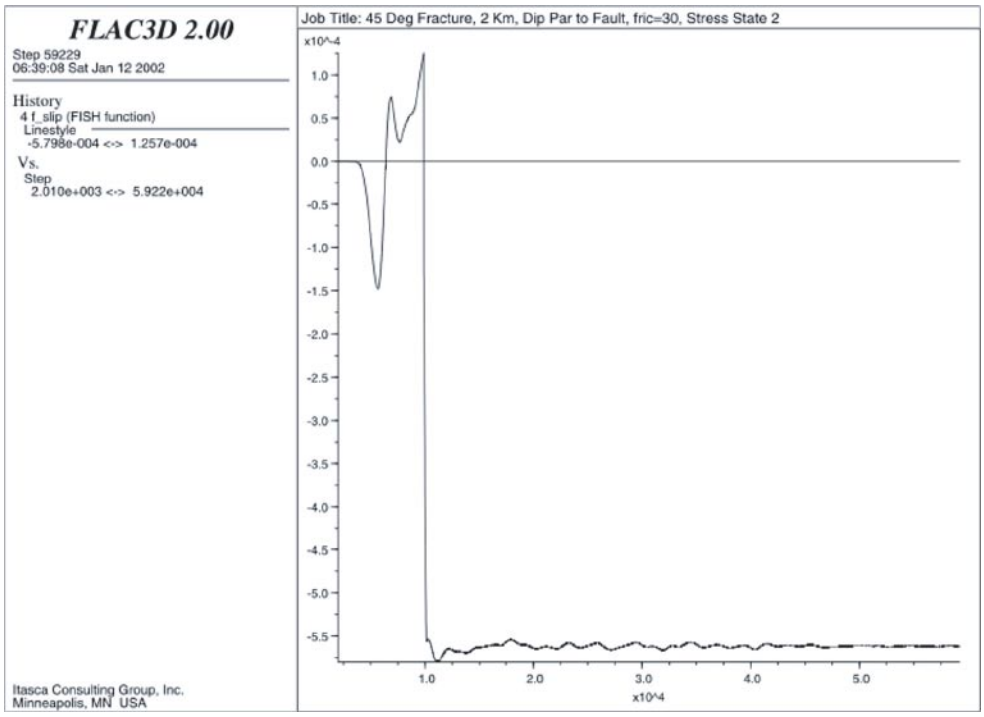

Figure A2a-38. *Shear Displacements at the Center of a 45° Fracture for 6.0 Magnitude Earthquake at a Distance of 2 km. (The dip direction of the fracture is parallel to the fault strike; friction = 30°, stress state II.)*

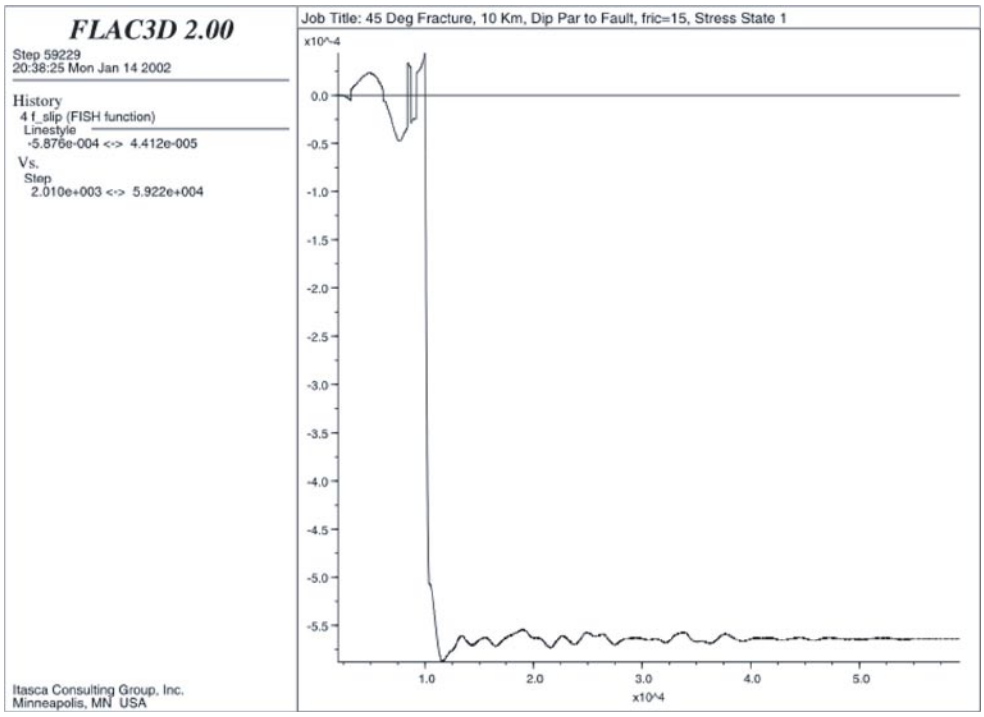

Figure A2a-39. *Shear Displacements at the Center of a 45° Fracture for 6.0 Magnitude Earthquake at a Distance of 10 km. (The dip direction of the fracture is parallel to the fault strike; friction = 15°, stress state I.)*

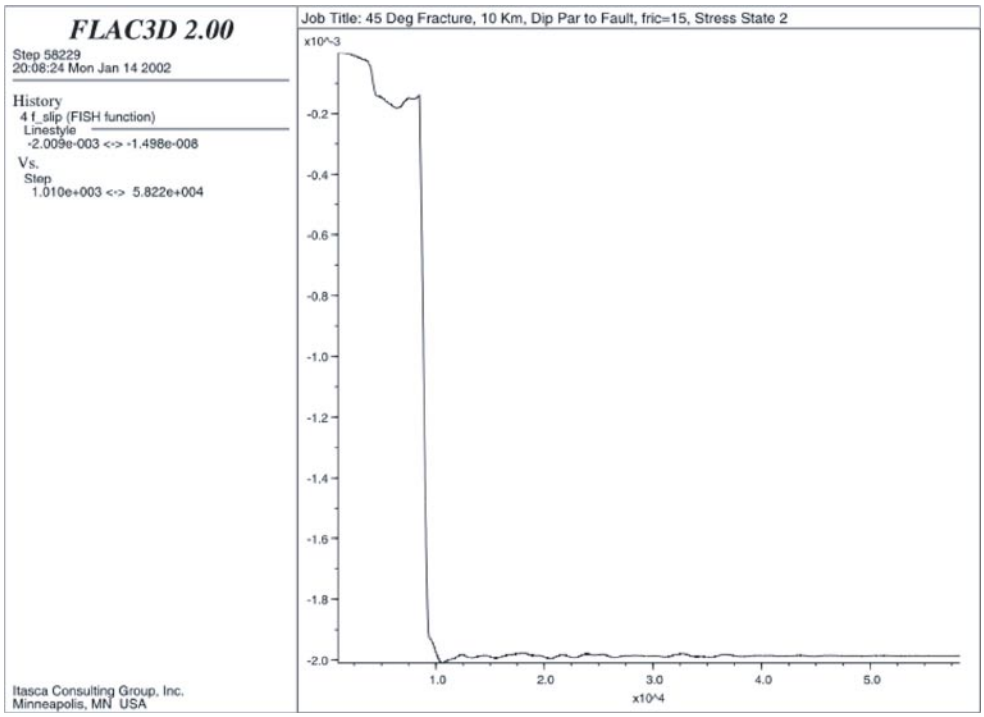

Figure A2a-40. *Shear Displacements at the Center of a 45° Fracture for 6.0 Magnitude Earthquake at a Distance of 10 km. (The dip direction of the fracture is parallel to the fault strike; friction = 15°, stress state II.)*

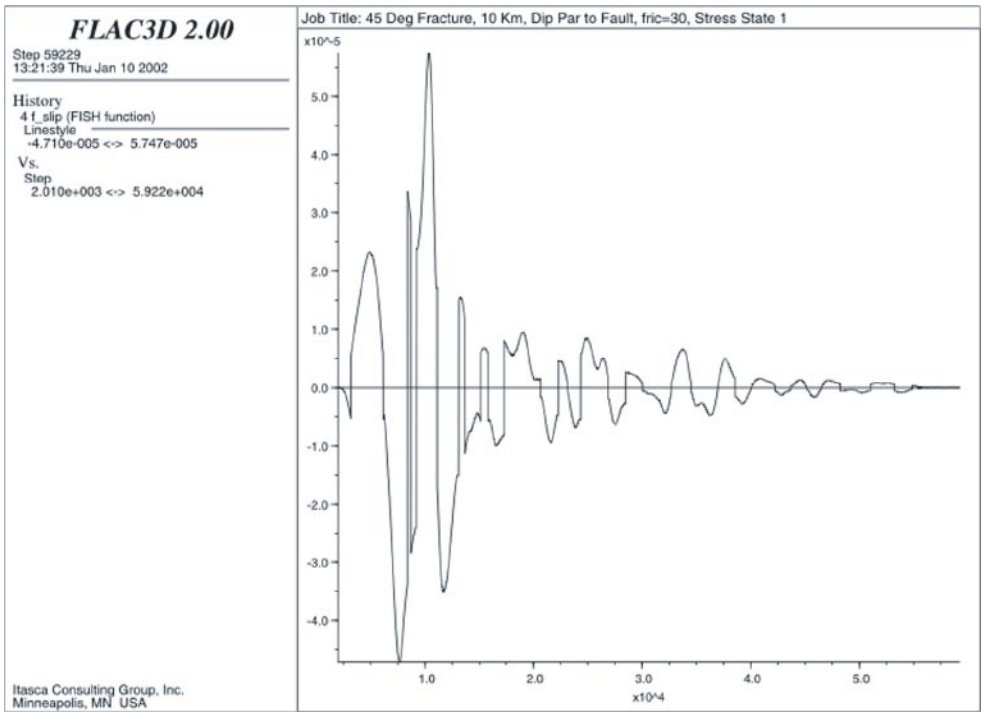

Figure A2a-41. *Shear Displacements at the Center of a 45° Fracture for 6.0 Magnitude Earthquake at a Distance of 10 km. (The dip direction of the fracture is parallel to the fault strike; friction = 30°, stress state I.)*

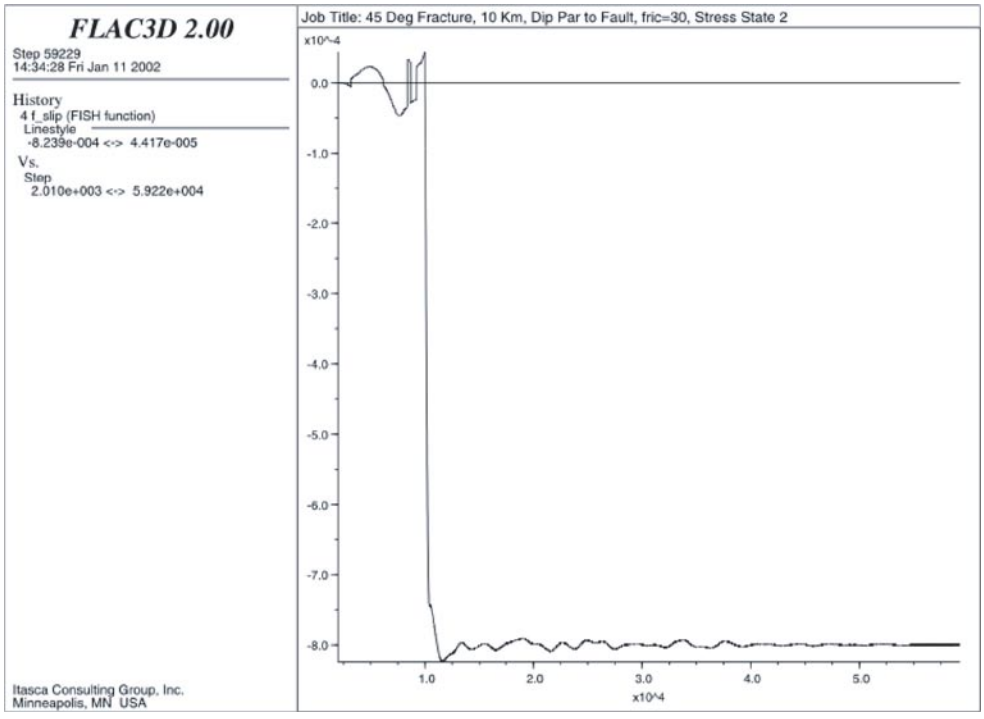

Figure A2a-42. *Shear Displacements at the Center of a 45° Fracture for 6.0 Magnitude Earthquake at a Distance of 10 km. (The dip direction of the fracture is parallel to the fault strike; friction = 30°, stress state II.)*

A2a-6 References

Hildyard M W, Daehnke A, Cundall P A, 1995. WAVE, Version Proc. of 35th U.S. Symp. on Rock Mech., pp 519-524, 1995.

ITASCA, 1997. FLAC3D, Fast Lagrangian Analysis of Continua in 3 Dimensions, Version 2.0,

LaPointe P, Wallmann P, Thomas A, Follin S, 1997. A methodology to estimate earthquake effects on fractures intersecting canister holes. SKB TR 97-07. Svensk Kärnbränslehantering AB.

LaPointe P R, Cladouhos T, Follin S, 1999. Calculation of displacements on fractures intersecting canisters induced by earthquakes: Aberg, Beberg and Ceberg examples. SKB TR-99-03. Svensk Kärnbränslehantering AB.

LaPointe P R, Cladouhos T T, Outters N, Follin S, 2000. Evaluation of the conservativeness of the methodology for estimating earthquake-induced movements of fractures intersecting canisters. SKB TR-00-08. Svensk Kärnbränslehantering AB.

Appendix 2b

WAVE analysis

WAVE Modeling Results

Numerical simulation of shear displacements on sub-surface fractures in response to dynamic loading from seismic waves

Calum Baker, Applied Seismology Consultants Ltd, UK

Mark Hildyard, Department of CSIR
Division of Mining Technology, South Africa

October 2001

Contents

A2b-1 Introduction

This report outlines the results obtained from simulating the effects of a large (M ~ 6) earthquake in the vicinity of a sub-surface fracture. Specifically, the objective was to estimate the amount of shear displacement on a horizontal fracture (referred to in the text as the 'target' fracture) under different *in situ* stress and friction states, at varying distances and azimuths from a fault. This report contributes to a wider study whose aim is to assess how shear displacements on fractures near a sub-surface waste repository may accumulate in response to repeat events and so assess the hazard associated with such events.

A2b-2 Methodology

The shear stress and relative fault displacement histories obtained in this report were calculated using *WAVE* /Hildyard et al.1995/, an explicit finite difference program developed by the CSIR division of Mining Technology to model elastodynamic movements within rock masses. The reader is referred to /Hildyard et al. 1995/ for further information and references on the formulation of the WAVE program.

A2b-3 Formulation of the model

The model geometry and input parameters were defined in advance following discussion with Mark Christianson (*Itasca Consulting Group*) and Harald Hökmark (*ClayTechnology*). In order to calculate the effect on the fracture of a nearby earthquake, we define a number of parameters for the model. These include:

1. The rock mass properties.
2. The source parameters of the earthquake (including stress drop, magnitude and source mechanism).
3. The relative locations (distance and azimuth) of the target fracture and the earthquake fault.
4. The properties of the target fracture (dimension, stiffness, friction angle and cohesion).
5. The in situ stresses acting on the target fracture.

The primary assumptions in the modelling are that the rock is elastic, linear and homogeneous. The rock mass properties defined in the model are those used in an earlier study of velocity time histories resulting from a magnitude 6 earthquake (Appendix 1b). In the previous study two stress-drop models (both with moment release equivalent to a magnitude 6 event) were compared. Of these two models the smaller dimension, higher stress-drop, model is used in the simulations described below. This choice was made for two reasons. The first is that a higher stress drop is close to the maximum that might be expected. The second is that it is consistent with values obtained for *intraplate* earthquakes /Scholz, 1990/, and in this study we are concerned with an intraplate environment. A summary of the input model parameters for the rock mass and the earthquake are given in Table A2b-1.

Table A2b-1. Rock mass and earthquake source parameters used for the modelling described in this report.

Parameter	Description	Value	Notes
Rock mass properties			
E	Young's Modulus	75 GPa	specified by user
v	Poisson's Ratio	0.25	specified by user
ρ	Density	2,700 kgm^{-3}	specified by user
V_p	P-wave velocity	5,774 ms^{-1}	calculated from elastic parameters
V_s	S-wave velocity	3,333 ms^{-1}	calculated from elastic parameters
Earthquake parameters			
$\Delta\sigma$	Stress Drop	15 MPa	specified by user
L	Fault Length (along strike)	8 km	calibrated to required moment
W	Fault width (down dip)	4.6 km	calibrated to required moment
H	Hypocentre depth	3.3 km	specified by user
t	Rise time	0.5	specified by user
	Event mechanism	Dip-slip (various)	different mechanisms tested as part of sensitivity study
Target fracture properties			
	Fracture orientation	horizontal	specified by user
	Depth to fracture	400 m	specifies by user
d	Target fracture diameter	200 m	specified by user
	Fracture shear stiffness	1 GPa/m	specified by user
	Fracture normal stiffness	100 GPa/m	specified by user

The fracture geometry and dimension is pre-defined within the grid – in *WAVE* any fault or fracture must be aligned with the grid. In the experiments carried out in this investigation, a horizontal fracture was specified. This is positioned at a depth of 400 m to simulate a realistic repository depth. Two different model geometries were investigated. These are shown in Figures A2b-1 and A2b-2. In each case a range of different model runs was performed. These are designed to investigate the sensitivity of the slip on the fracture to variations in stress state, distance and friction angle. The details of the model runs for each case are given in the tables in Figure A2b-1 and Figure A2b-2.

Target fracture at horizontal normal distance D1 from epicentre.

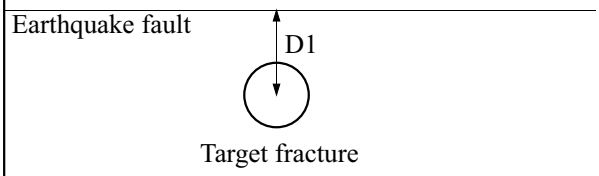

	Stress state #1				Stress state #2			
D1	200	800	2000	7000	200	800	2000	7000
φ=0 degr	√(1)	√(2)	√(3)	√(4)				
φ=15 degr	√(5)	√(6)	√(7)	√(8)	√(11)	√(12)	√(13)	√(14)
φ=30 degr		√(9)				√(15)		
φ=30 degr +1 MPa coh		√(10)				√(16)		

Figure A2b-1. *Geometry (plan view) of the position of the target fracture relative to the earthquake fault for Case 1. The target fracture is at a depth of 400 m. The table shows the different input parameters for which this model geometry was considered, investigating variations in stress state, horizontal distance (D1) and friction angle. The stress states are given in Table A2b-2. The model number is given in brackets and corresponds to those in Table A2b-4.*

Target fracture at horizontal normal distance D1 from epicentre.

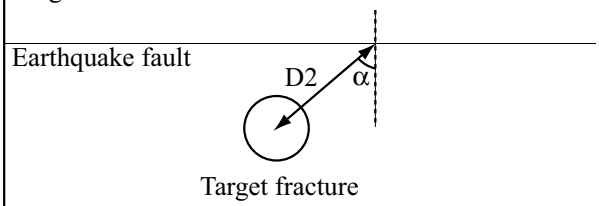

	Stress state #1				Stress state #2			
D1	200	800	2000	7000	200	800	2000	7000
φ=0 degr	√(1)	√(2)	√(3)	√(4)				
φ=15 degr	√(5)	√(6)	√(7)	√(8)	√(11)	√(12)	√(13)	√(14)
φ=30 degr		√(9)				√(15)		
φ=30 degr +1 MPa coh		√(10)				√(16)		

Figure A2b-2. *Geometry (plan view) of the position of the target fracture relative to the earthquake fault for Case 2. This case is only modelled using stress state 2 (Table A2b-2). The model number is given in brackets and corresponds to those in Table A2b-5.*

In the study we are interested in the total shear displacement arising on the target fracture as a result of the excess shear stress (ESS) caused by the earthquake. This ESS results from the passage of the seismic waves radiated by the earthquake. It can be defined as

$$ESS = (\sigma_{in\ situ} + \sigma_{dss}) - \tau_0$$

Where,

$\sigma_{in\ situ}$ is the in situ shear stress,

σ_{dss} is the 'dynamic' shear stress on the fracture arising from the earthquake waves

and τ_0 is the fracture strength defined as

$$\tau_0 = C + \mu\sigma_n$$

Here, C is the cohesion or inherent shear strength of the contact surface, σ_n is the normal stress acting across the fracture surface and μ is the coefficient of friction, with

$$\mu = \tan \varphi$$

(φ being equal to the *angle of friction*, see tables in Figure A2b-1 for values considered in this study.)

For the models in this study, the in situ stress field is orientated such that σ_3 is vertical and σ_1 and σ_2 are horizontal and in the plane of the target fracture. The normal stress on the target fracture therefore corresponds to the σ_3 value. As σ_1 and σ_2 are in the plane of the target fracture there is no resulting shear stress from the in situ stress field alone.

Slip is assumed to start instantaneously if the ESS > 0. In the cases where cohesion is considered, the cohesion is assumed to drop to zero as soon as the slip begins. This is realistic as cohesion on a fracture surface may be the result of an asperity, and once this asperity has failed the strength resulting from that asperity is lost. The slip will continue to develop according to the unbalanced forces, i.e. until the value of ESS drops to zero or less, at which point the slip stops. It is possible that the shear stress can end up being less than the initial limiting stress, in other words some 'overshoot' occurs. In this formulation, we assume that the coefficient of friction remains constant before, during and after slip. Experiments indicate that both static and dynamic values of μ could be considered. For example, the dynamic coefficient of friction, μ', is generally less than μ and varies with the velocity of sliding /for further discussions the reader is referred to Jaeger and Cook, 1979; Scholz, 1990/.

For the purposes of this study, we do not consider that these simplifications will significantly affect the results.

Table A2b-2. Stress states considered in this modelling study.

	Stress state #1	Stress state #2
σ_1 – horizontal	35 MPa	55 MPa
σ_2 – horizontal	20 MPa	20 MPa
σ_3 – vertical	13 MPa	7 MPa

Table A2b-3. Resulting normal, shear and resisting stresses used for the in situ stresses acting on the target fracture from stress state #1 and stress state #2. †The σshres value quoted is for the pre-failure state. Once the main earthquake has occurred, this value will change in response to the change in normal stresses that result.

Fracture stresses (Stress state 1)				
σ_1	σ_2	σ_3		
35	20	13		
			(max)	(resist)
fric	cohes	σ_n	σ_{sh}^{max}	σ_{sh}^{res}
0	0	13	0	0.000
15	0	13	0	3.483
30	0	13	0	7.506
30	1	13	0	8.506
Fracture stresses (Stress state 2)				
σ_1	σ_2	σ_3		
55	20	7		
			(max)	(resist)
fric	cohes	σ_n	σ_{sh}^{max}	σ_{sh}^{res}†
0	0	7	0	0.000
15	0	7	0	1.876
30	0	7	0	4.041
30	1	7	0	5.041

Table A2b-4. Parameters used for the model for Case 1 where target fracture centre is a horizontal distance D1 from the epicentre. Table gives the stress state, distance D1, friction angle and cohesion used for each model. The 'Name' corresponds to the 'File' label on the subsequent contour plots (Figure A2b-13). The right hand column shows the maximum relative displacement that was recorded for each model during the simulation (in cm). An asterisk (*) in this column indicates no actual slip failure occurred (see text for further discussion).

Model 1 cases							
#	**Name**	**Stress-state**	**D1**	**Fric**	**Coh**	**Final Rel. Disp (cm)**	**Max. Rel. Disp (cm)**
1	L1a_d1a	1	200	0	0	7.68	7.68
2	L1a_d2a	1	800	0	0	2.17	2.19
3	L1a_d3a	1	2,000	0	0	1.66	1.69
4	L1a_d4a	1	7,000	0	0	0.32	0.79
5	L1a_d1b	1	200	15	0	7.08	7.08
6	L1a_d2b	1	800	15	0	0.77	0.77
7	L1a_d3b	1	2,000	15	0	0.29*	0.30*
8	L1a_d4b	1	7,000	15	0	0.06*	0.14*
9	L1a_d2c	1	800	30	0	0.40*	0.40*
10	L1a_d2d	1	800	30	1	0.40*	0.40*
11	L1b_d1b	2	200	15	0	7.68	7.68
12	L1b_d2b	2	800	15	0	1.56	1.57
13	L1b_d3b	2	2,000	15	0	0.67	0.67
14	L1b_d4b	2	7,000	15	0	0.06*	0.14*
15	L1b_d2c	2	800	30	0	0.84	0.85
16	L1b_d2d	2	800	30	1	0.86	0.86

Table A2b-5. Parameters used for the model for Case 2 where target fracture centre is at horizontal distance D2 from the tip of the earthquake fault. Table gives distance D2, azimuth angle, friction angle and cohesion used for each model. The 'Name' corresponds to the 'File' label on the subsequent contour plots (Figure A2b-13). The right hand column shows the maximum relative displacement recorded for each model (in cm.)

Model 2 cases #	Name	Stress-state	D2	Angle	Fric	Coh	Final Rel. Disp (cm)	Max. Rel. Disp (cm)
17	L2b_d1a	2	200	0	0	0	2.38	2.48
18	L2b_d2a	2	200	30	0	0	2.30	2.35
19	L2b_d3a	2	200	60	0	0	2.28	2.29
20	L2b_d4a	2	200	90	0	0	2.24	2.24
21	L2b_d1b	2	200	0	15	0	1.91	1.96
22	L2b_d2b	2	200	30	15	0	1.76	1.80
23	L2b_d3b	2	200	60	15	0	1.67	1.67
24	L2b_d4b	2	200	90	15	0	1.40	1.40
25	L3b_d1a	2	800	0	0	0	1.85	1.97
26	L3b_d2a	2	800	30	0	0	1.45	1.67
27	L3b_d3a	2	800	60	0	0	1.01	1.27
28	L3b_d4a	2	800	90	0	0	0.99	1.06
29	L3b_d1b	2	800	0	15	0	1.13	1.15
30	L3b_d2b	2	800	30	15	0	0.78	0.82
31	L3b_d3b	2	800	60	15	0	0.46	0.50
32	L3b_d4b	2	800	90	15	0	0.18	0.19

A2b-4 Model sensitivity studies

In order to assess how sensitive the results from the modelling are to certain input parameters where assumptions are made, a series of comparative simulations were carried out in the initial phase of the work. These tests were undertaken to:

1. Assess the degree to which the source mechanism of the main earthquake leads to variations in the induced ESS on a target fracture. Specifically we investigate whether a dip-slip or a strike-slip mechanism for the main earthquake results in the larger induced ESS.
2. Investigate the sensitivity of the induced ESS to the orientation of the target fracture
3. Investigate the boundary effects resulting from using a boundary close to the target fracture.
4. Assess the resolution effects of a fine and coarse grid representation of the target fracture and different grid size elements of the rock-mass.

Tests (1) and (2) investigate the effects of variations in the actual physical model chosen for this study. Tests (3) and (4) investigate the effects of different parameterisations of this model, i.e. how the model is represented by *WAVE*. As in all numerical modelling routines, there is a trade off between model accuracy/resolution and computational expense. Tests (3) and (4) are carried out to optimise the model in this regard.

The results from these sensitivity studies are presented in Figure A2b-3 to Figure A2b-8. Note that in these, and all subsequent figures, the model is specified within a co-ordinate system with axes defined as X (+ve in East direction), Y (+ve upwards) and Z (+ve in South direction). The sense of slip modelled on the fault was chosen such that the induced shear stress on a horizontal fracture has a positive sense.

Figure A2b-3 shows a comparison of (a) velocity and (b) maximum *induced* ESS arising from the magnitude 6 earthquake for two different source mechanisms on a N-S striking vertical fault, namely strike-slip and dip-slip. The diagrams show a plan view of a horizontal slice at a depth of 1 km. The fault-line can be seen running parallel to the left-hand side of the model space. The upper diagrams compare the maximum velocity (see also Appendix 1b), and the lower row of diagrams shows a comparison of the maximum induced ESS. The dip-slip case shows the higher value of ESS (27.9 MPa compared with 6.54 MPa) so the dip-slip case was chosen for subsequent models, as this represents the 'less favourable case' for our models.

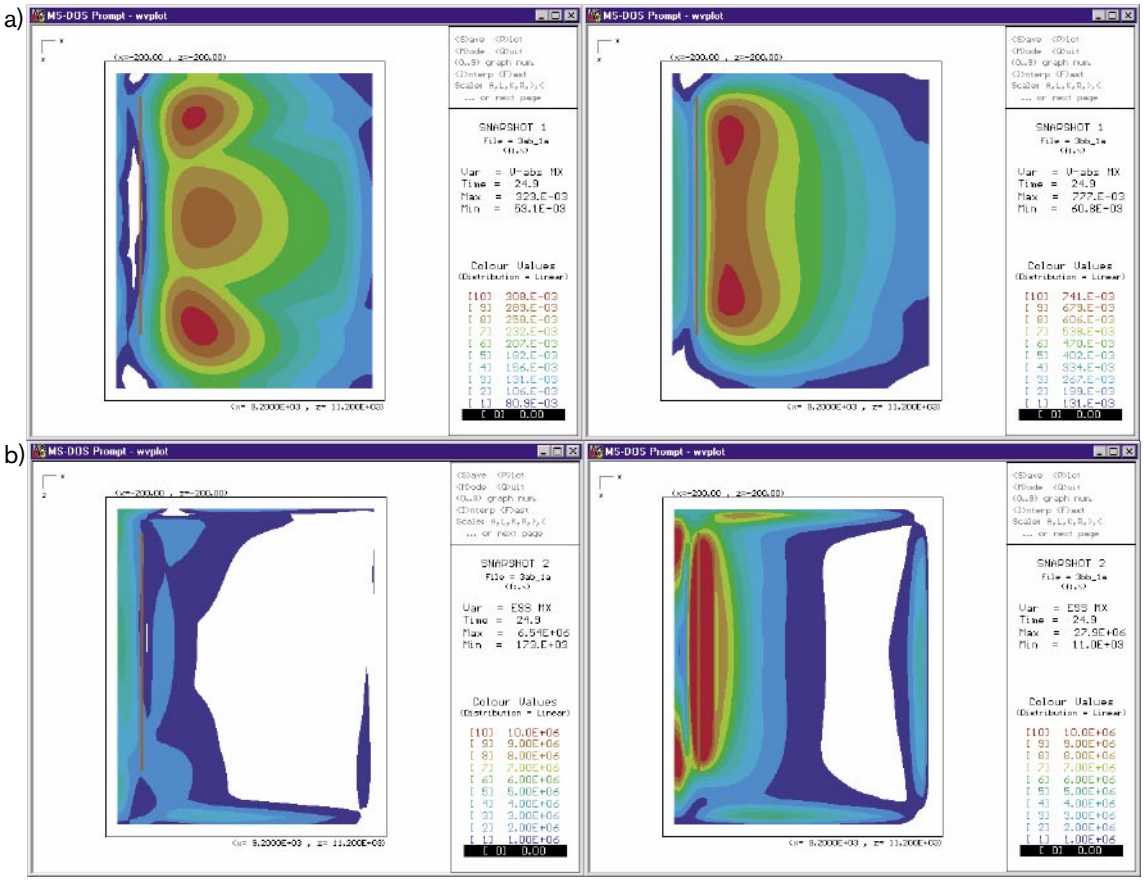

Figure A2b-3. *Comparison of maximum velocity (a) and maximum Excess Shear Stress (b) for a strike-slip (left side) and dip-slip (right side) faulting mechanism. Plan views in each case. The trace of the fault is the red line parallel to the left-hand side of each plot.*

Figure A2b-4 shows a comparison of the ESS obtained for 4 different orientations of target fracture; vertical, horizontal, 45 degrees and –45 degrees. This diagram shows only the induced ESS resulting from the earthquake and does not assume any in-situ stress on the target fracture. The diagram shows the resulting ESS on a target fracture of the specified orientation with an angle of friction φ = 30 degrees and with no cohesion. The diagram suggests that, very close to the earthquake fault, a horizontal target fracture experiences the largest ESS, but that other orientations show higher ESS values at greater distances than for the horizontal fault. As a horizontal fracture was specified for this study, it should be remembered that such a fracture *may not* represent the 'least favourable scenario' in terms of total slip at *all* distances. A more extensive analysis of the variation in induced ESS could be undertaken as part of a future study.

A series of models was run to investigate the effect of the model boundary on the results. All numerical models have artificial (compared to the real world) boundaries that can lead to numerical artefacts in the results. Wave is designed to have non-reflecting boundaries in response to plane waves. The results of this test are shown in Figure A2b-5. This diagram suggests that choosing a close boundary does have some effect on the final values of ESS (values around 10% more for close boundary compared to far boundary).

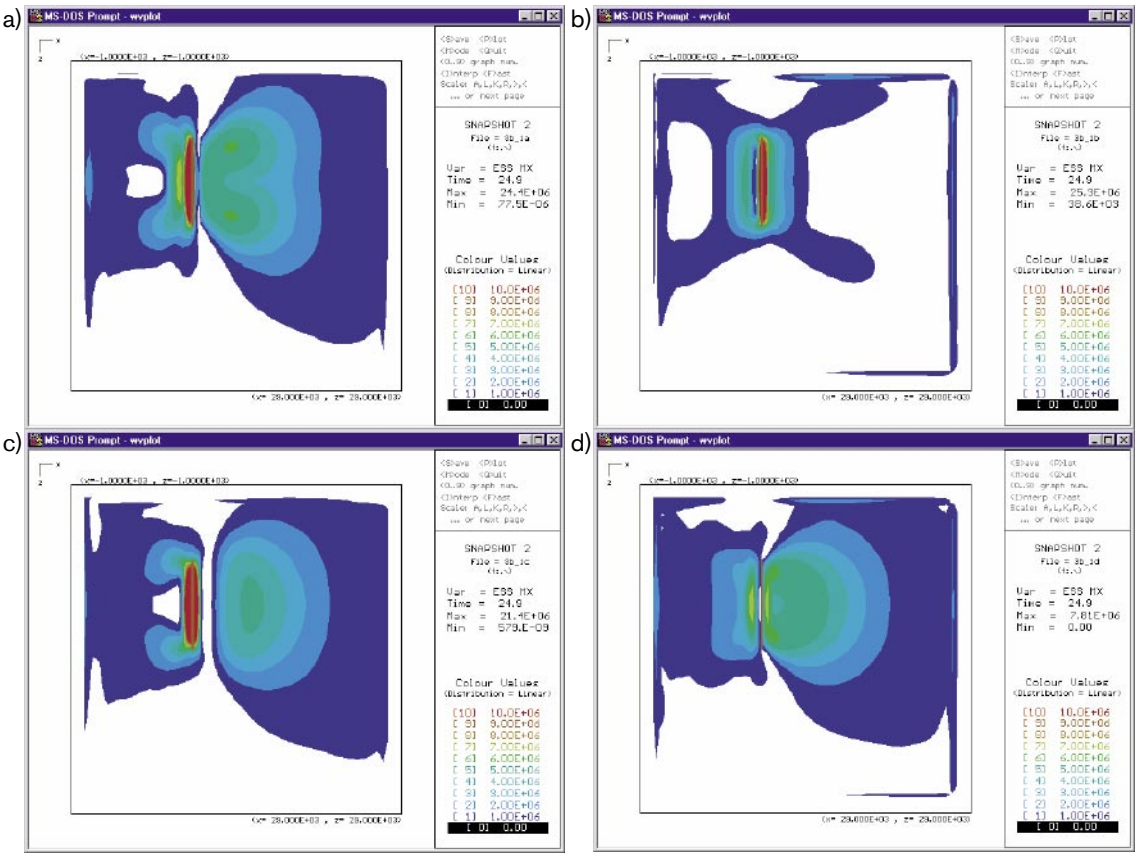

Figure A2b-4. *ESS on a fracture resulting from slip on dip-slip fault. Four different fracture orientations are considered with Friction angle 30 degrees, no cohesion – plan view, 400 m below surface, 4 different fracture angles: a) Vertical fracture, b) Horizontal fracture, c) 45 degree fracture (sloping toward fault), d) –45 degree fracture (sloping away from fault).*

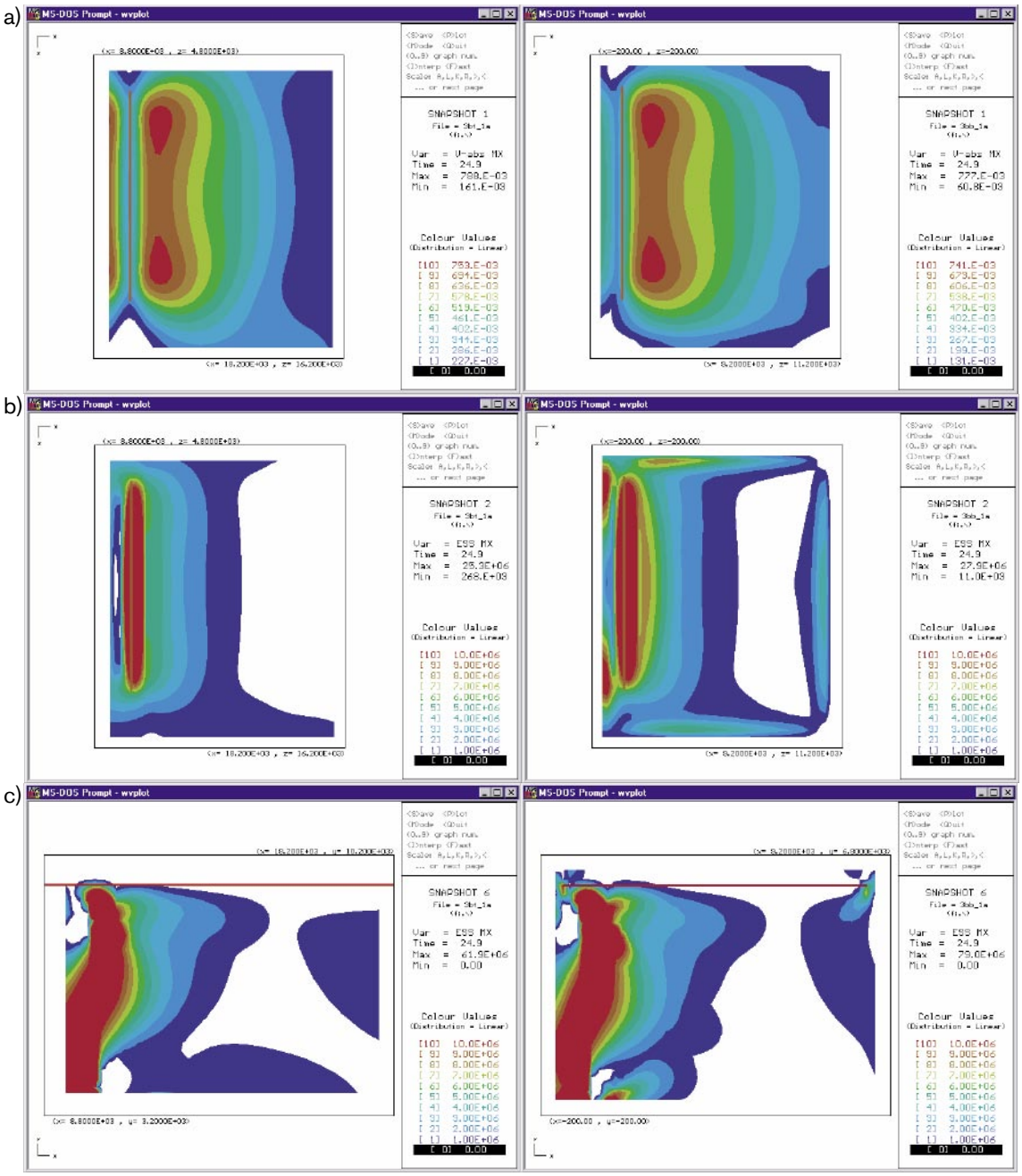

Figure A2b-5. *Plots of test to verify that using a very close boundary (right-hand column) has similar results to those of the original model boundaries (left-hand side). Each of the plots compares the same region (plane 400 m below surface). a) Velocity, b) ESS (plan view) – Horizontal fracture, 30 degree friction, no static stress, c) ESS (vertical slice) – Horizontal fracture, 30 degree friction, no static stress.*

Figure A2b-6 shows the variation in slip on a 1 km by 800 m horizontal fracture at different distances from the earthquake fault for far and very close boundaries. The important thing to note from this diagram is that the very close boundary leads to an *under-estimation* (compared to the standard distance) of the total slip. This amounts to 20% at 400 m and around 10% at greater distances. This is considered an acceptable margin of uncertainty for this study. Using a closer boundary means that the volume being modelled is smaller so a smaller element size can be used (better resolution) while maintaining computational efficiency.

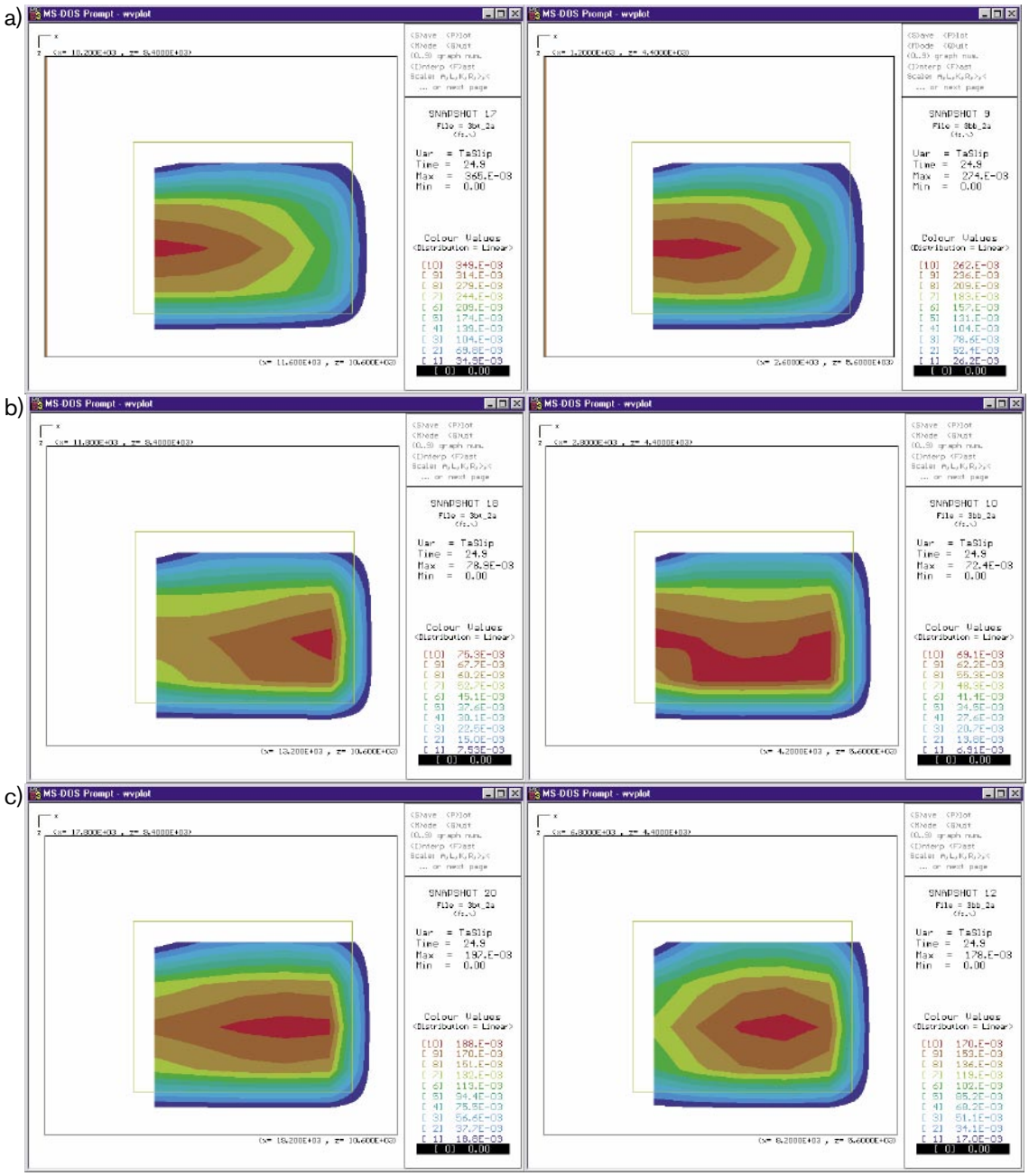

Figure A2b-6. *Plots showing the difference in total cumulative slip computed using the original boundary (left) and a very close boundary (right) for different distances between the target fracture and the fault. This demonstrates that using the close boundary provides similar (though smaller) values to the far boundary. The diagram compares the slip on a 1 km × 800 m (5×4 element) horizontal fracture, at 400 m (a), 2 km (b), 6 km (c).*

Results from tests aimed at testing the effect of model resolution are presented in Figure A2b-7 and Figure A2b-8. These figures show 3 different comparisons based on variations in the fracture resolution. Figure A2b-7a shows the variation in induced ESS computed for a fine model (50 m elements, left-hand side) and a coarse model (200 m elements, right hand side). In this case, the overall pattern of stress is similar for the two models and a difference of about 20% in the maximum ESS value is observed. Figure A2b-7b and Figure A2b-7c shows the total cumulative slip on a 1 km by 800 m horizontal fracture at 800 m depth and distances of 400 m and 6 km.

The left-hand column of diagrams shows the results when 50 m elements are used (i.e. fracture is represented by 20×16 elements) and the right-hand column when a 200 m element is used (i.e. fracture is represented by 5×4 elements). The pattern of slip shows better resolution when the finer element size is used, but the overall pattern of slip is similar and maximum values are about 20% larger for the coarse model. We opt to use an element size of 50 m for the main phase of the modelling. Figure A2b-8 shows the predicted slip on a 200 m × 200 m fracture at a depth of 400 m at 200 m and 7 km from the earthquake fault. The fracture is represented using 4×4, 3×3 and 5×5 elements respectively. This corresponds to element lengths of 50 m, 66.67 m and 40 m. The results show a small variation in the total cumulative slip and the pattern of the slip on the fracture surface.

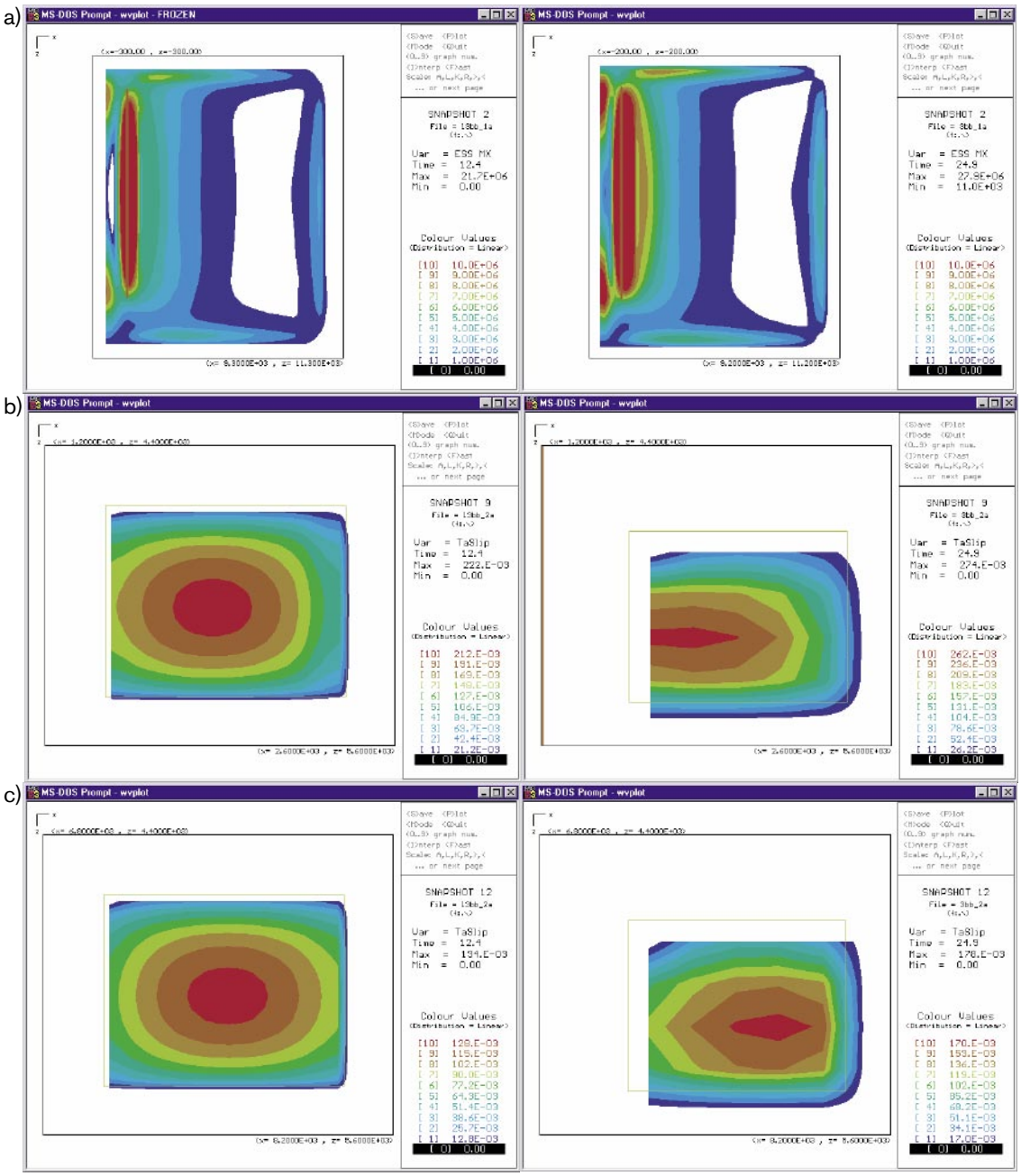

Figure A2b-7. *Compare results for large model 50 m elements (left), with the coarse model 200 m elements (right). (a) Induced ESS – Horizontal fracture, 30 degree friction, no static stress. b) Cumulative slip on a 1 km × 800 m fracture at 800 m depth (400 m to edge of fracture), c) Cumulative slip on a 1 km × 800 m fracture at 800 m depth, 6 km to edge of fracture.*

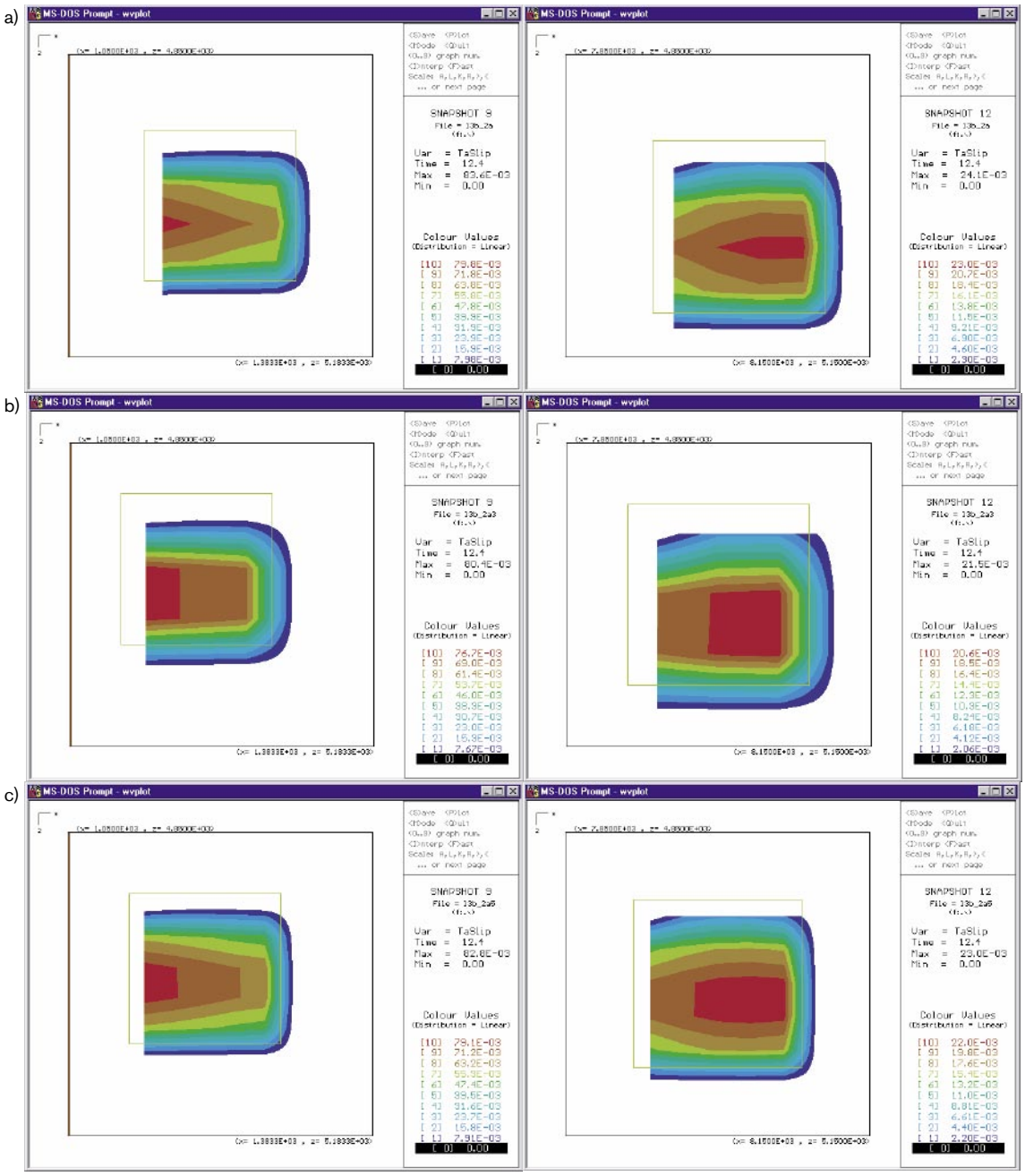

Figure A2b-8. *Diagram outlining results of analysis of variations in model resolution on resulting ESS and maximum cumulative slip values – see text for further discussion. Cumulative slip on a 200 m × 200 m fracture at 400 m depth, and at distances of 200 m and 7 km. (Modelled with 4×4, 3×3 and 5×5 element fracture, with element lengths of 50 m, 66.67 m and 40 m respectively). (a) 4×4 elements (left: fracture at 200 m); (right: fracture at 7 km), (b) 3×3 elements (left: fracture at 200 m); (right: fracture at 7 km), (c) 5×5 elements (left: fracture at 200 m); right: fracture at 7 km)*

A2b-5 Results from studies of displacement on target fractures

Following completion of the sensitivity tests described above, the main study to investigate the shear displacement on a target fracture at a depth of 400 m was undertaken. This consisted of two distinct case studies as outlined in Section 3. The first considers a tabular horizontal fracture at a normal distance, D1, from the earthquake fault and investigates the effect of variations in the in-situ stress state, distance to fracture and the nature of the friction on the target fracture (Figure A2b-1). In all, 16 different models are run for this geometry (see Table A2b-4). The second case considers a target fracture centred at a horizontal distance D2 from the tip of the earthquake fault (Figure A2b-2). In this case, 16 models are run as detailed in Table A2b-5.

The first task is to consider the in situ stress state and so calculate the corresponding normal (σ_n) and shear (σ_{sh}) stresses acting on the target fracture. In the cases considered here, we are dealing with a horizontal fracture and the σ_3 direction is vertical, so the σ_3 value corresponds to the normal stress acting on the fracture. As the σ_1 and σ_2 are horizontally orientated, there is no in situ shear stress acting on the target fracture for the models considered in this study. Details of the stresses used are shown in Table A2b-3.

The induced normal and shear stresses resulting from the earthquake are computed in response to the passage of seismic waves through the model space. These values are used to compute the resulting displacement on the fracture. The variation of induced normal and shear stress with time has been computed for a point at the centre of the target fracture for each model and these are shown in Figure A2b-9 to Figure A2b-12.

The results (in terms of final relative shear displacement on the target fracture) for each of the models are shown in Figure A2b-13 to Figure A2b-18. One contour plot is shown for each model, showing a 'snapshot' of the distribution of the final displacement on the target fracture at the end of the simulation. The value of the largest final displacement is listed under each figure and in Table A2b-4 and Table A2b-5. The maximum total relative displacement for each model is also given in Table A2b-4 and Table A2b-5 (right-hand column, shaded). This maximum value represents the largest displacement on the target fracture that occurred at any time during the simulation. In some cases (e.g. model 4) this is larger than the final displacement because of the dynamic effects of the seismic waves and the resulting variations in shear and normal stresses (see Figure A2b-9 to Figure A2b-12). It should be noted that the shear displacement includes a component of failure slip and a component due to the elastic stiffness of the crack. In 'zero friction' cases this elastic stiffness component is zero so that total displacement is equal to the failure slip. In some cases, where friction and cohesion is sufficiently high, no slip failure displacement takes place (the shear strength is not exceeded), although a small component of displacement arising from the elastic stiffness may be present. Such cases are marked with a '*' in Table A2b-4 and Table A2b-5 and in Figure A2b-13 to Figure A2b-18.

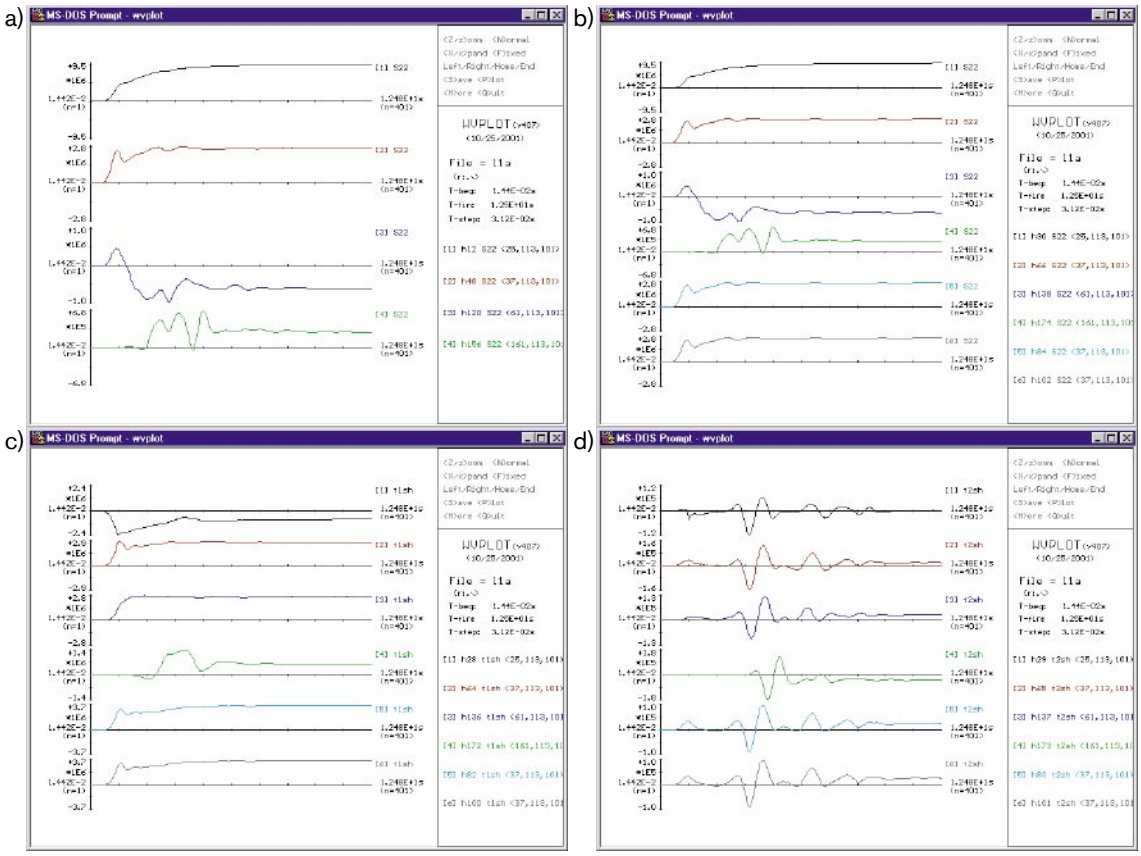

Figure A2b-9. *Plots showing time histories of induced normal and shear (s12 and s23) stresses on target fracture following earthquake on main fault. Vertical axis is the value of the stress component in Pa (scale range varies depending on the model). Horizontal axis is time from 0 to 12.5 seconds. Note that for models 1–4, 17–20 and 25–28 there is no induced shear stress sustained on the fracture as the friction angle is zero. (a) Models 1–4 – induced normal stress, (b) Models 5–10 – induced normal stress, (c) Models 5–10 – shear stress shT1 (s12), (d) Models 5–10 – shear stress shT2 (s23).*

Figure A2b-10. *(a) Models 11–16 – induced normal stress, (b) Models 11–16 – shear stress shT1 (s12), (c) Models 11–16 – shear stress shT2 (s23).*

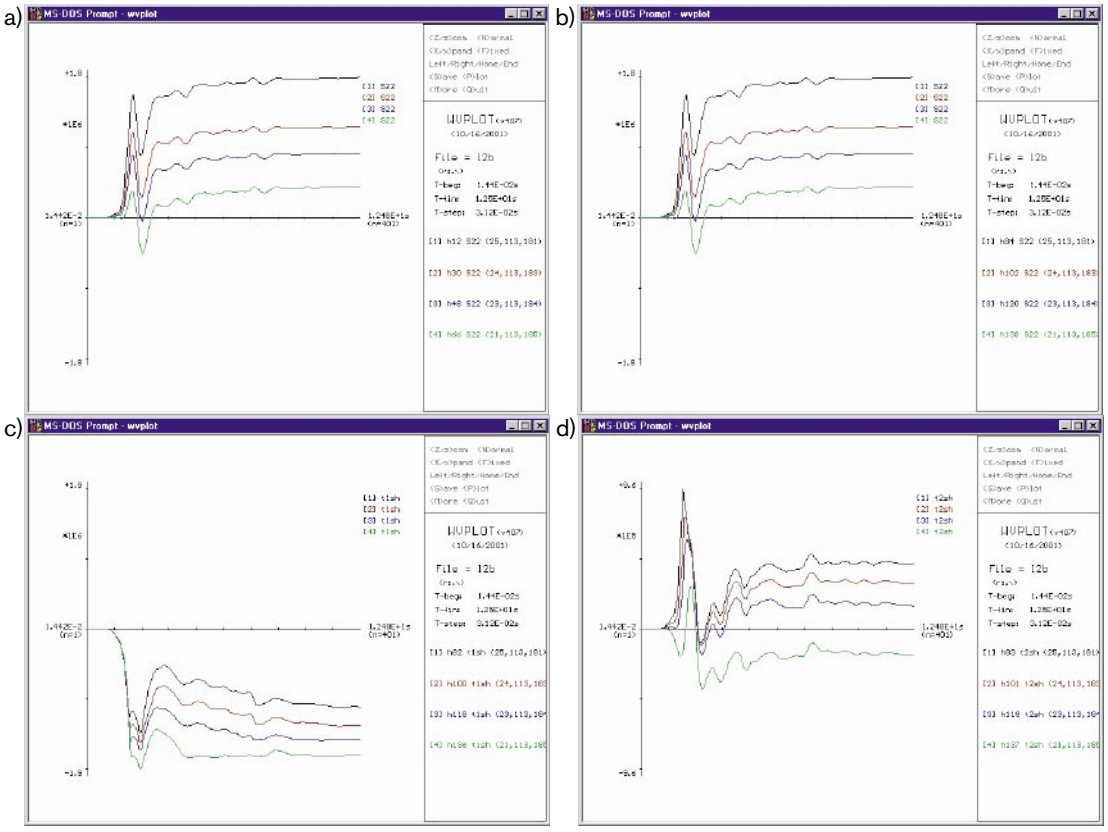

Figure A2b-11. *(a) Models 17–20 – induced normal stress, (b) Models 21–24 – induced normal stress, (c) Models 21–24 – shear stress shT1 (s12), (d) Models 21–24 – shear stress shT2 (s23).*

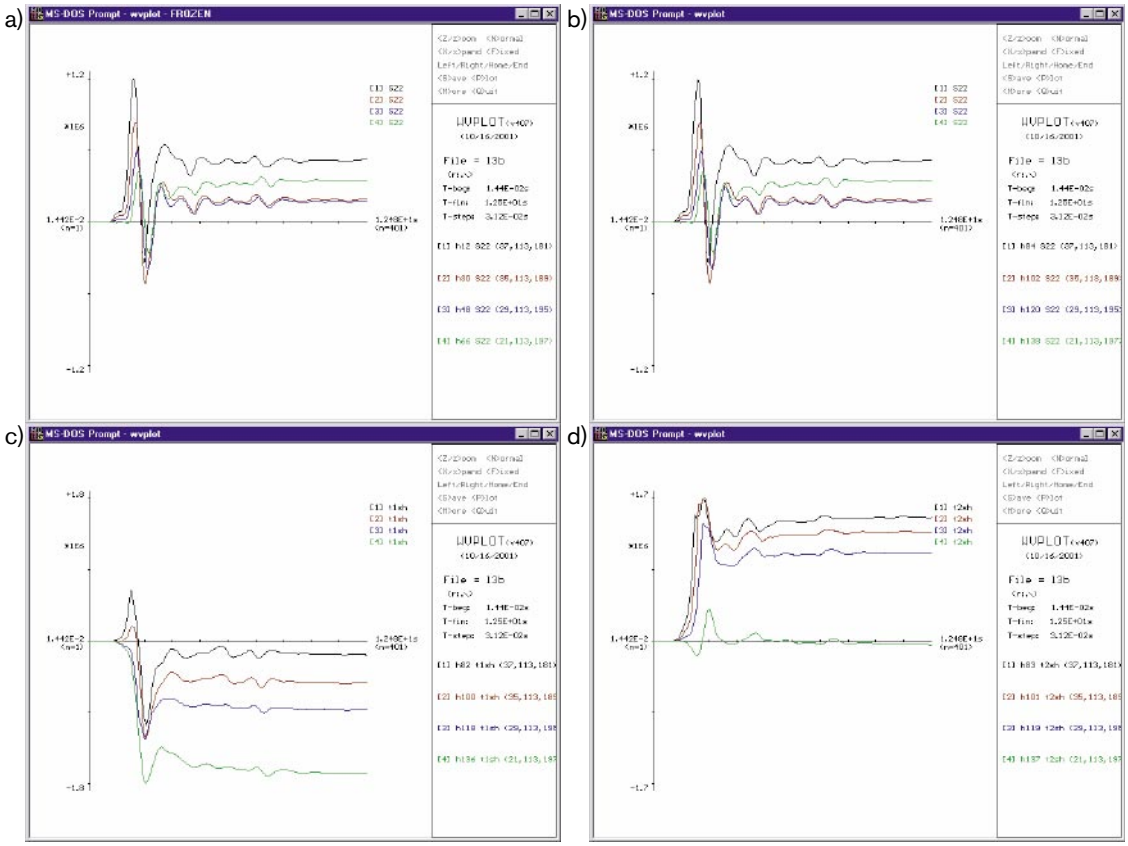

Figure A2b-12. *(a) Models 25–28 – induced normal stress, (b) Models 29–32 – induced normal stress, (c) Models 29–32 – shear stress shT1 (s12), (d) Models 29–32 – shear stress shT2 (s23).*

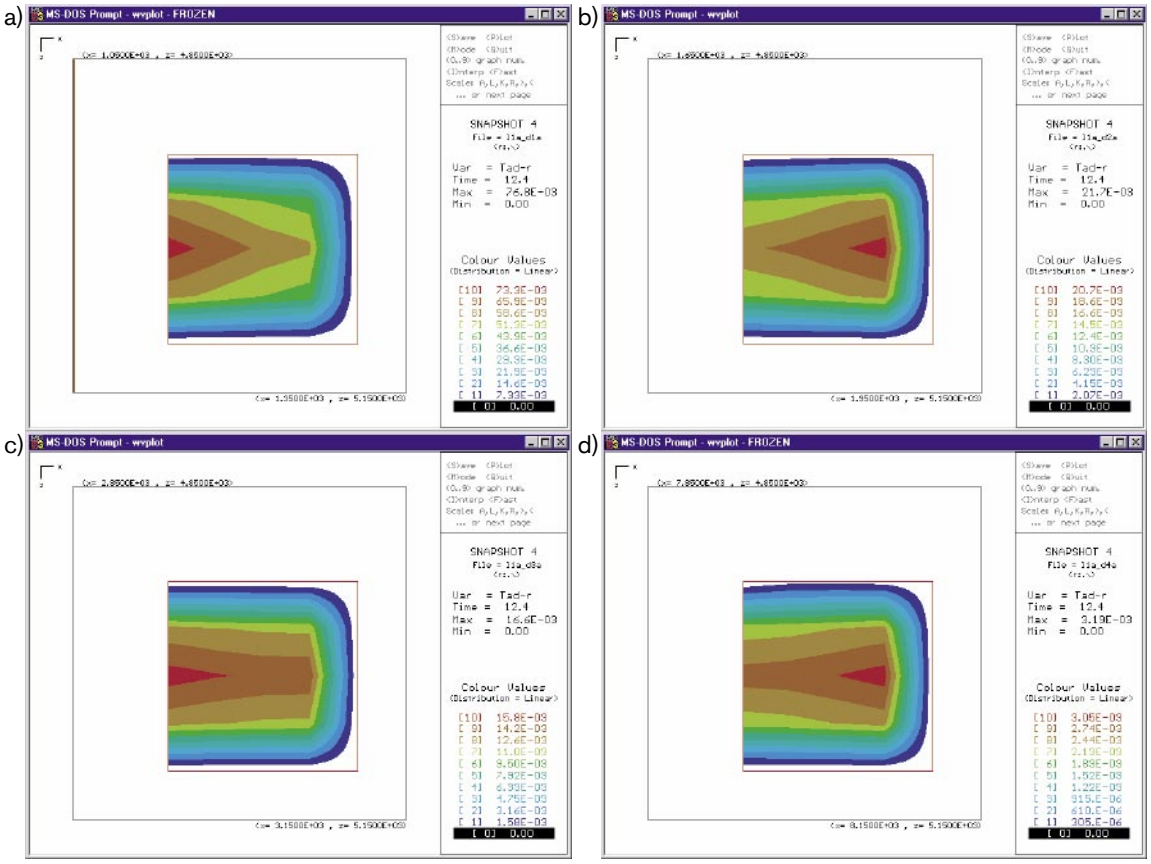

Figure A2b-13. *Diagrams on this and subsequent pages show distribution of resulting relative displacement on target fracture in response to Magnitude 6 event. Each diagram shows a contour plot of the distribution of displacement across the fracture surface (plan view). Note that the scales are not the same for all diagrams. The relative displacement (in metres) is given in the right hand margin of each diagram (Max =). This value (converted to cms) is also shown in Table A2b-4 and Table A2b-5 for the corresponding model and file name. Where the slip is marked with a '*' no actual 'slip' has taken place and the displacement is purely 'elastic'.*
a) Model 1: L1a_dla (Max disp = 7.68 cm), b) Model 2: L1a_d2a (Max disp = 2.17 cm),
c) Model 3: L1a_d3a (Max disp = 1.66 cm), d) Model 4: L1a_d4a (Max disp = 0.32 cm).

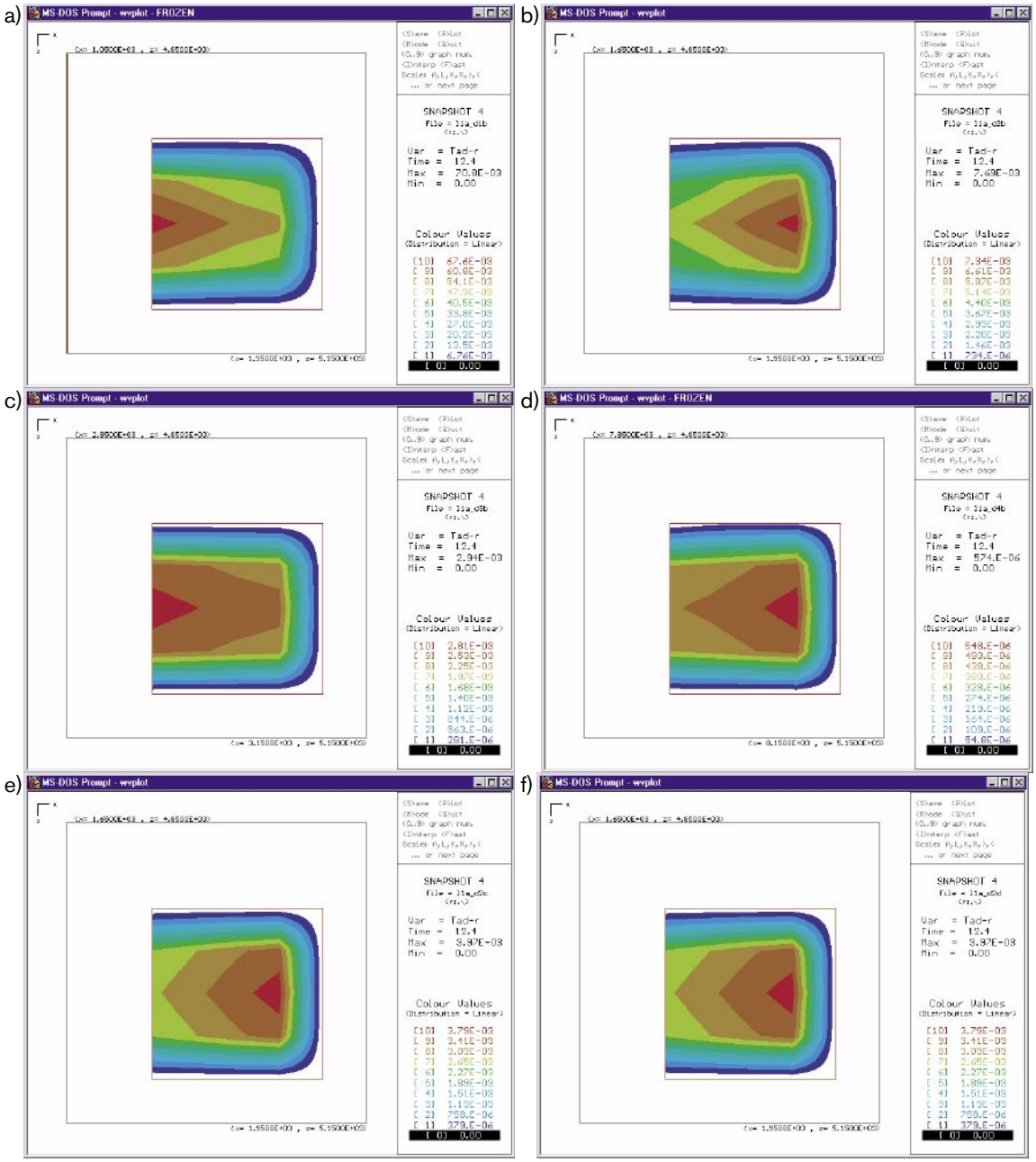

Figure A2b-14. *a) Model 5: L1a_dlb (Max disp = 7.08 cm), b) Model 6: L1a_d2b (Max disp = 0.77 cm), c) Model 7: L1a_d3b (Max disp = 0.29* cm), d) Model 8: L1a_d4b (Max disp = 0.06* cm), e) Model 9: L1a_d2c (Max disp = 0.4*cm), f) Model 10: L1a_d2d (Max disp =0.4*cm).*

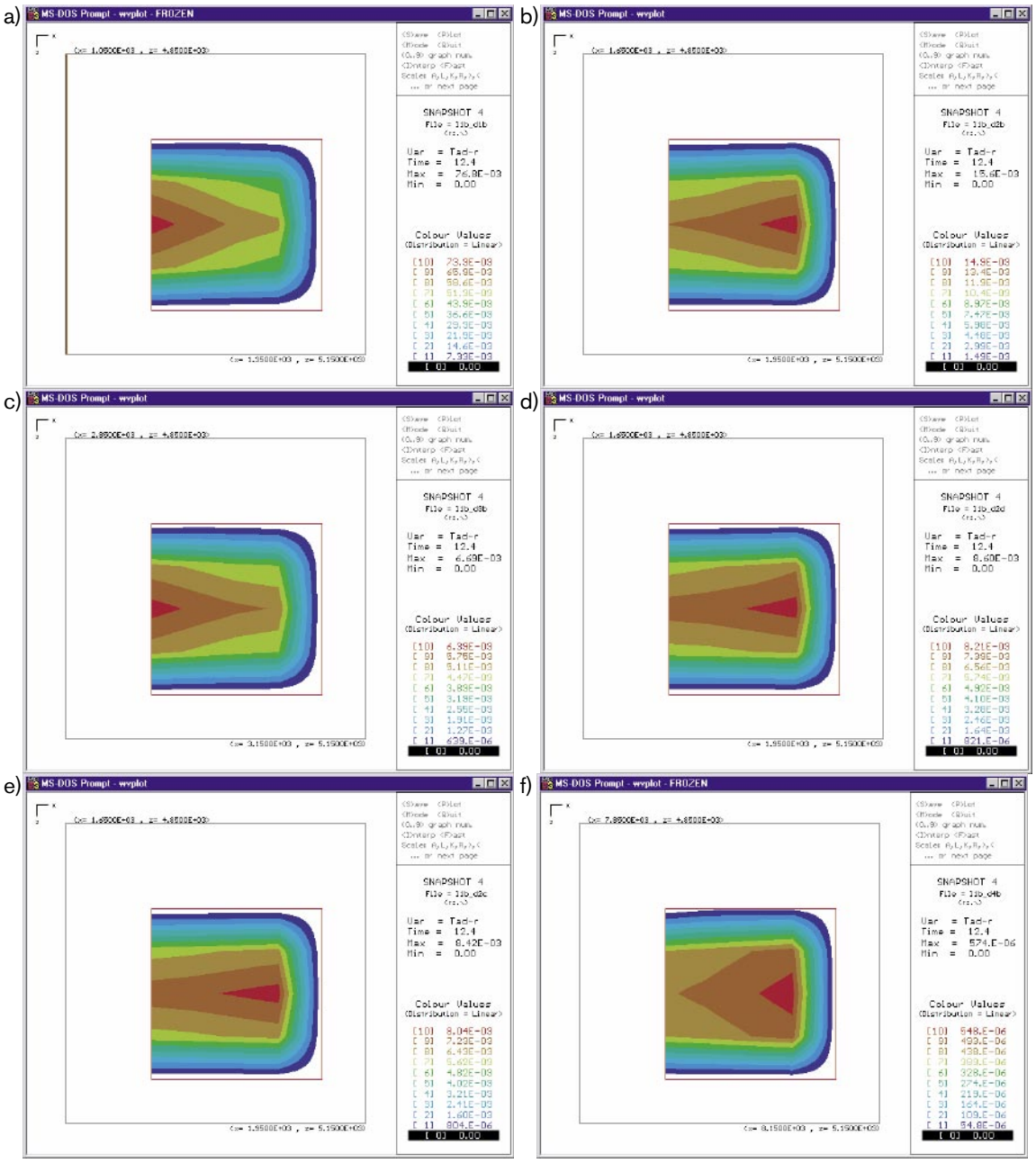

Figure A2b-15. *a) Model 11: L1b_d1b (Max disp = 7.68 cm), b) Model 12: L1b_d2b (Max disp = 1.56 cm), m), c) Model 13: L1b_d3b (Max disp = 0.67 cm), d) Model 14: L1b_d4b (Max disp = 0.06*cm), e) Model 15: L1b_d2c (Max disp = 0.84 cm), f) Model 16: L1b_d2d (Max disp = 0.86 cm).*

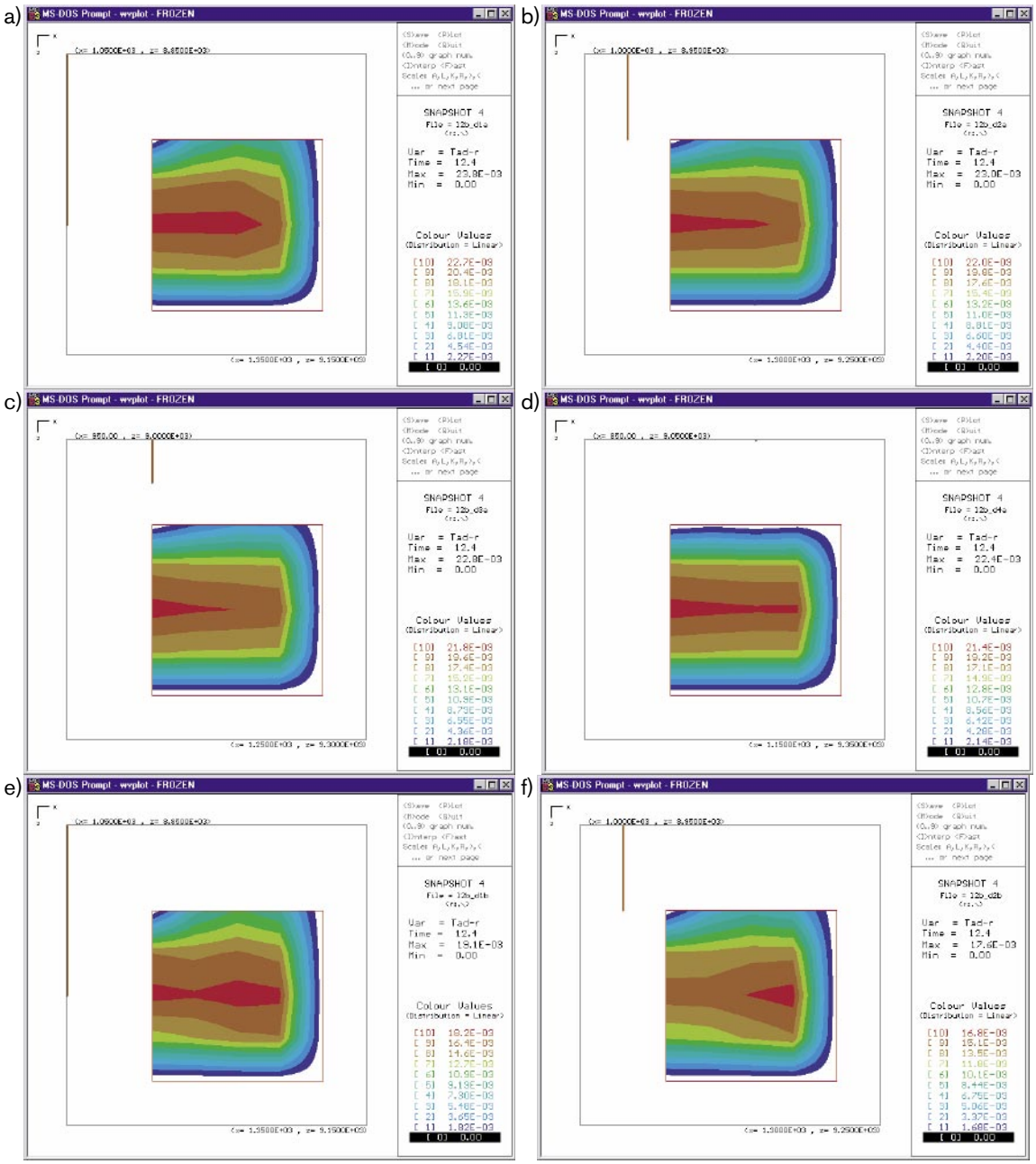

Figure A2b-16. *a) Model 17: L2b_d1a (Max disp = 2.38 cm), b) Model 18: L2b_d2a (Max disp = 2.30 cm), c) Model 19: L2b_d3a (Max disp = 2.28 cm), d) Model 20: L2b_d4a (Max disp = 2.24 cm), e) Model 21: L2b_d1b (Max disp = 1.91 cm), f) Model 22: L2b_d2b (Max disp = 1.76 cm).*

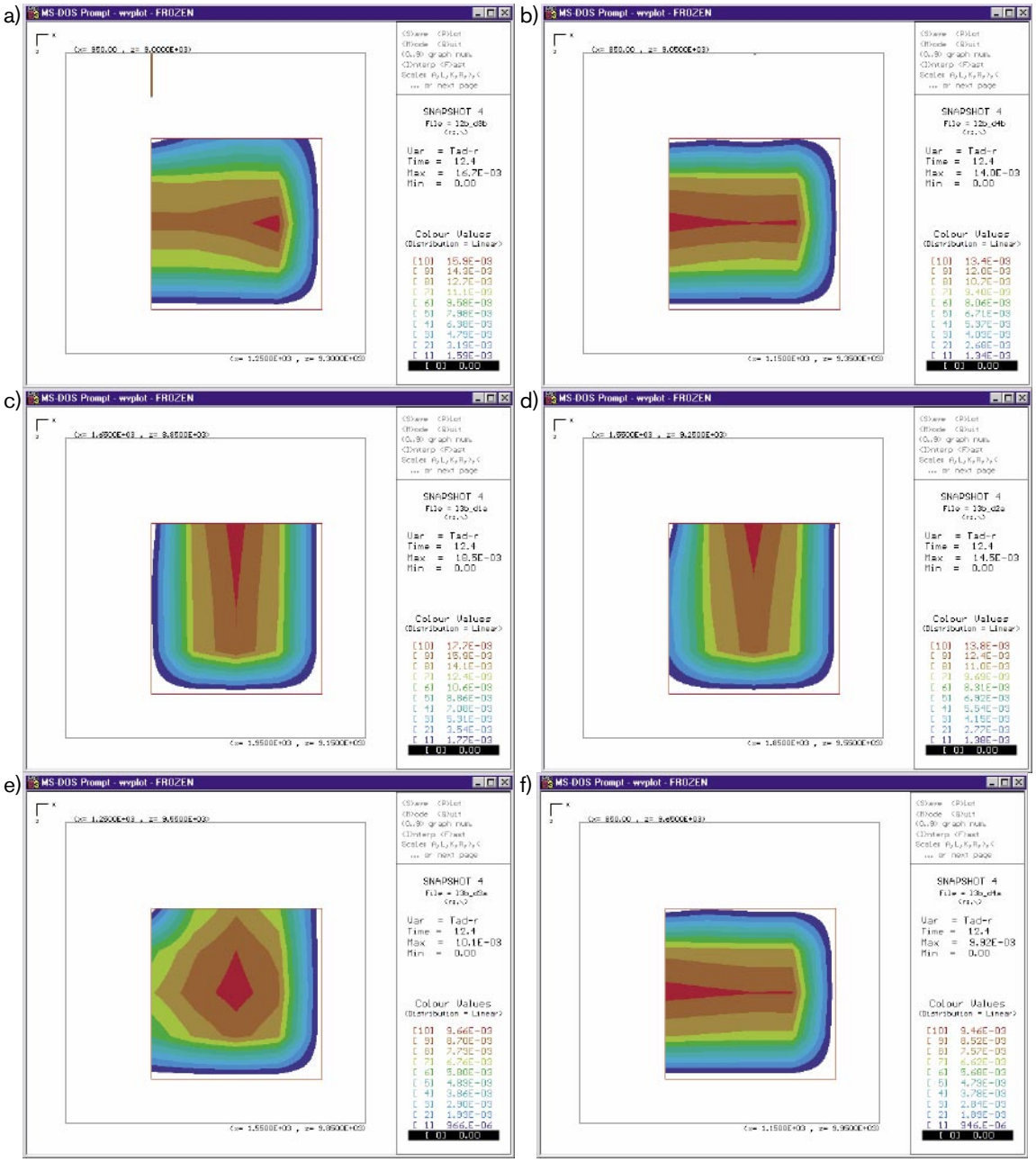

Figure A2b-17. *a) Model 23: L2b_d3b (Max disp = 1.67 cm), b) Model 24: L2b_d4b (Max disp = 1.40 cm), c) Model 25: L3b_d1a (Max disp = 1.85 cm), d) Model 26: L3b_d2a (Max disp = 1.45 cm), e) Model 27: L3b_d3a (Max disp = 1.01 cm), f) Model 28: L3b_d4a (Max disp = 0.92 cm).*

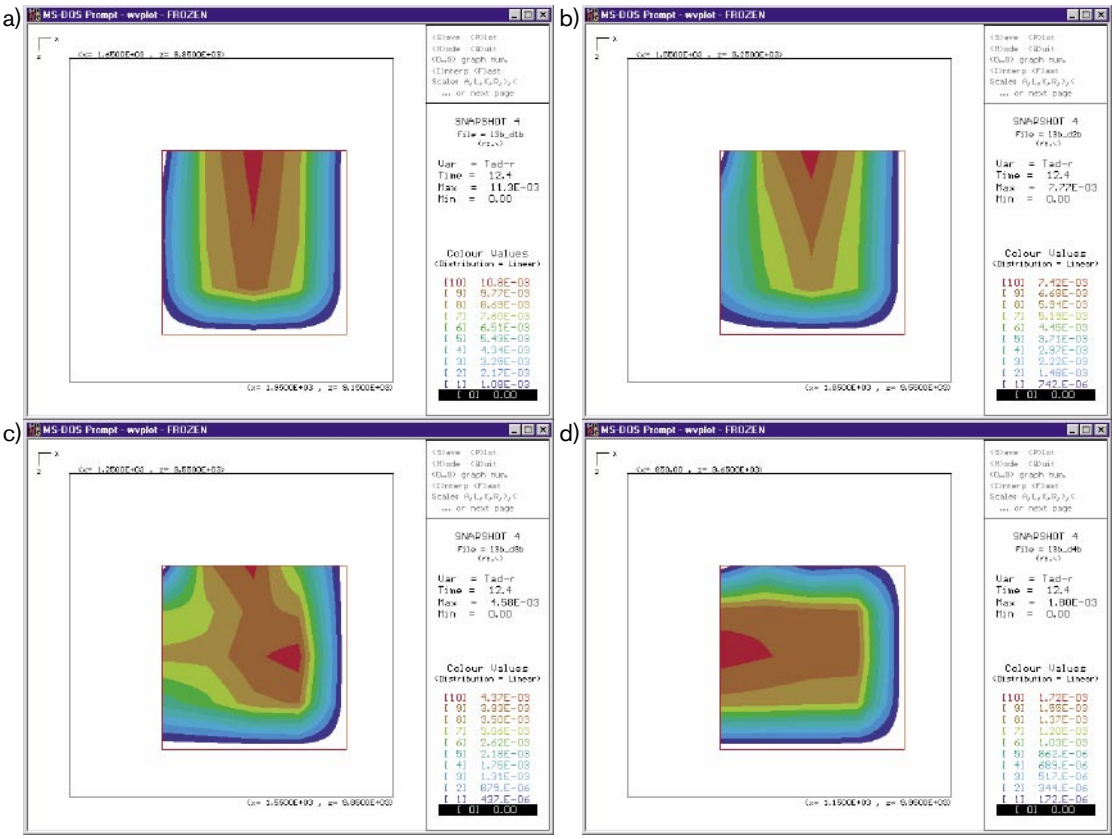

Figure A2b-18. *a) Model 29: L3b_d1b (Max disp = 1.13 cm), b) Model 30: L3b_d2b (Max disp = 0.78 cm), c) Model 31: L3b_d3b (Max disp = 0.46 cm), d) Model 32: L3b_d4b (Max disp = 0.18 cm).*

For several of the models, the variation in target fracture displacement and shear velocity with time have been computed for a point at the centre of the target fracture. These allow an assessment to be made of how these values develop following the earthquake. The plots for these measurements are shown in Figure A2b-19 to Figure A2b-21.

A2b-6 Discussion

The plots in Figure A2b-9 to Figure A2b-12 show how the induced normal and shear stress values vary in time. For models where the angle of friction is '0' there is no induced shear stress measured as this cannot be sustained by the fracture surface. In the cases where friction and cohesion are not zero, the shear stress is plotted for both the s_{12} and s_{23} components. Figure A2b-9 and Figure A2b-10 show the induced stress histories for models 1 to 16. For these cases the induced stress histories appear to be primarily a function of the distance of the target fracture from the earthquake and the strength of the target fracture. Thus, models 1, 5 and 11, where the distance of the target fracture from the earthquake is 200 m, show the same induced normal stress history. Similarly, the normal stress histories for models 2, 6, 12, 15 and 16 show the same pattern as all these models are for target fractures at 800 m and show some failure slip. Models 9 and 10, which are also at a distance of 800 m, do not show failure slip and the peak value of shear stress (s12) is greater than for the cases where slip does occur (e.g. model 5). The plots in Figure A2b-11 and Figure A2b-12 show the variation in induced stress for models 17 to 32. Here the effects of the radiation pattern from the earthquake are clear – the induced stress varies with angle of the target fracture from the fault.

The contour plots of the final relative shear displacement on the target fracture for each modelled case are shown in Figure A2b-13 to Figure A2b-18. Each diagram shows the distribution of displacement on the fracture surface. The largest value for the final relative displacement is shown in Table A2b-4 and Table A2b-5. The maximum displacement for each model is listed in the far right hand column of Table A2b-4 and Table A2b-5. The largest displacement seen on any of the examples tested is 7.68 cm for model '11'. This corresponds to a case where the target fracture is very close to the earthquake source and the target fracture has low strength. Model '11' has a low resisting shear strength due to the relatively small σ_n value and coefficient of friction. It is possible to compute the approximate seismic moment released by displacement of this magnitude on a fault of this dimension using the relationship

$$M_0 = \mu \bar{\Delta u} A$$

where M_o is the seismic moment, μ is the shear modulus and Δu is the mean slip vector averaged over the fault area. Taking the average value of slip over the fault area to be 5 cm (estimated from inspection of the contour plot of displacement for Model 11 in Figure A2b-13 to Figure A2b-18), then the moment released by the event 'induced' following the earthquake is 6×10^{13} Nm. Then, using the relationship between seismic moment and moment magnitude, M_w, where

$$M_w = 2/3 \log_{10} M_o - 6.07$$

this corresponds to an event of magnitude ~ 3. Such an event would be perceptible to personnel nearby, but would be indistinguishable from the effects of the main-shock, which would be strongly felt at this distance. All other cases studied in this report show smaller induced events than this.

Figure A2b-19 to Figure A2b-21 show the time histories of relative displacements and shear velocities for selected models. These plots illustrate how these values vary at a point in the centre of the target fracture for 12.5 seconds after the earthquake. Although the time scale of the graphs suggest slip occurs effectively instantaneously, in most cases the rise takes place over more than a second (> 200 model time steps). Figure A2b-19a and Figure A2b-19b compares models 1 to 4. In this case, where the fracture has no friction, the drop in displacement with increasing distance is clear. This can be directly related to the decreasing relative velocities with distance. On comparing Figure A2b-19a and Figure A2b-19c, we can see the effects of the friction on the target fracture. In models 5 to 8, no failure slip occurs on the target fracture due to the increased fault strength at distances of 2,000 m or more. For models 11 to 16, for which the normal stress acting on the target fracture is less than in models 1–10, failure slip is produced for the target fracture at a distance of 2,000 m from the earthquake. For the models where the target fracture is at greater distances or where the fracture has higher strength due to greater friction and/or cohesion, only a small component of elastic displacement is produced.

For the cases of models 17 to 32, where the lower of the two σ_3 stress values is used, all the models show some failure slip, varying with distance and angle form the main earthquake.

Figure A2b-22 shows the variation in maximum total displacement versus distance for models 1–16. This clearly shows that the displacement on the target fracture falls away quickly with distance from the earthquake. Above a distance of about 1 km, failure slip is observed only for the zero friction case. Figure A2b-23 shows the variation in displacement with azimuth for models 17–32.

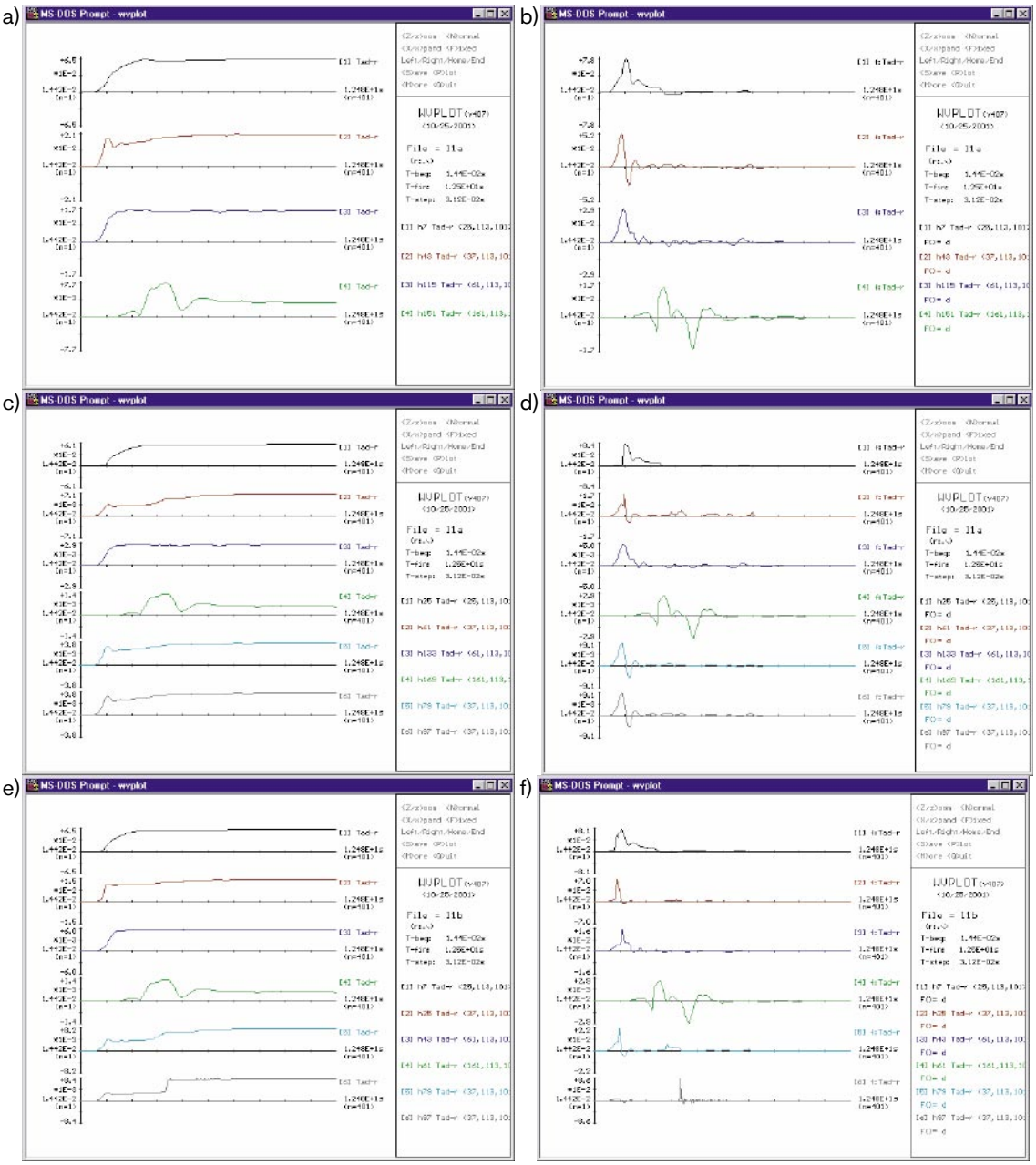

Figure A2b-19. *Plots showing relative shear displacement and relative shear velocity versus time at a point at the centre of the target fracture for selected models. Displacement values are in metres. Velocity values are in ms–1. The total time shown covers a 12.5 second time window following the earthquake on the main fault. Each plot has the same starting T0. a) Models 1–4: Relative displacement, b) Total relative velocity, c) Models 5–10: Relative displacement, d) Total relative velocity, e) Models 11–16: Relative displacement, f) Total relative velocity.*

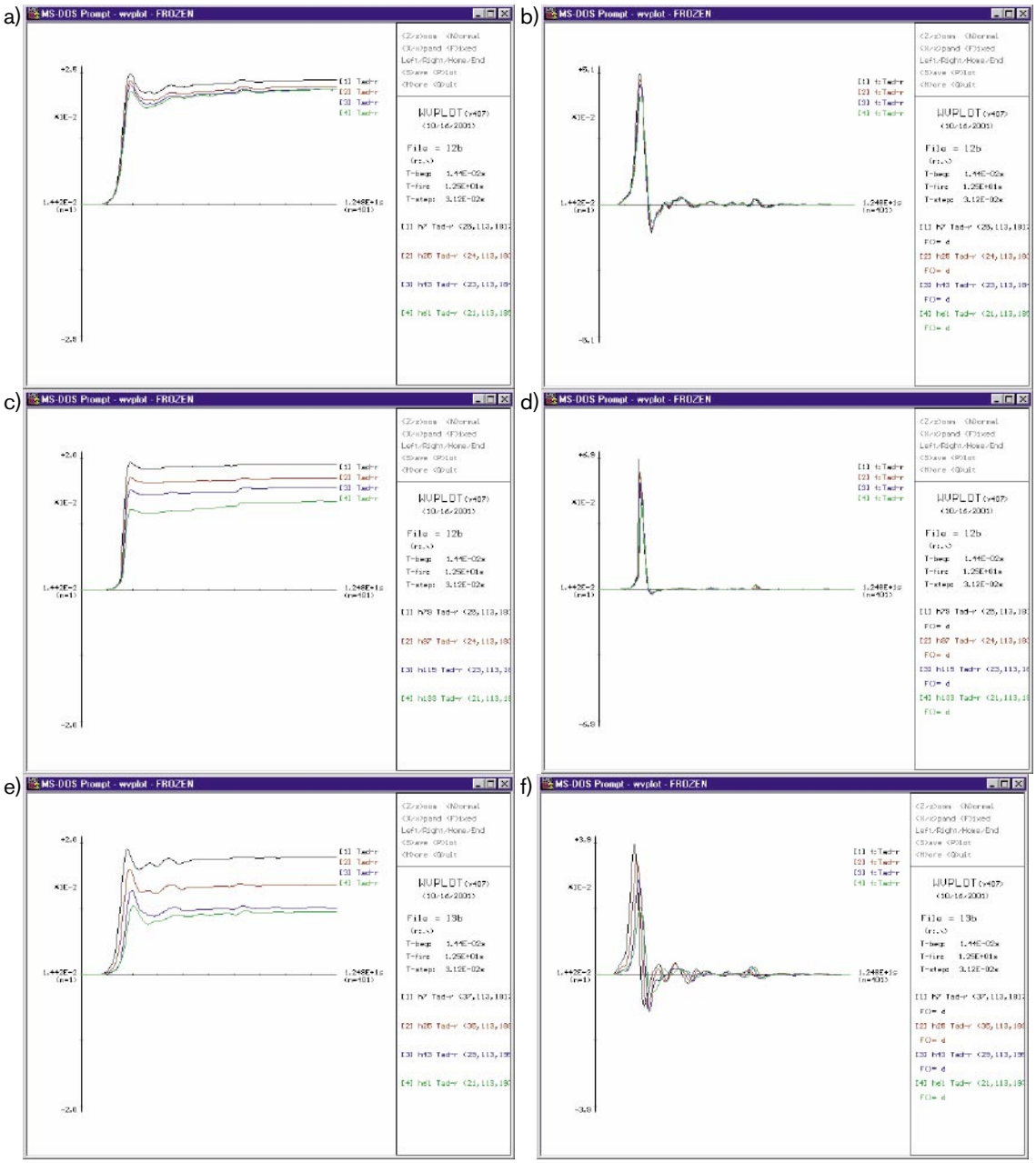

Figure A2b-20. *a) Models 17–20: Relative displacement, b) Total relative velocity, c) Models 21–24: Relative displacement, d) Total relative velocity, e) Models 25–28: Relative displacement, f) Total relative velocity.*

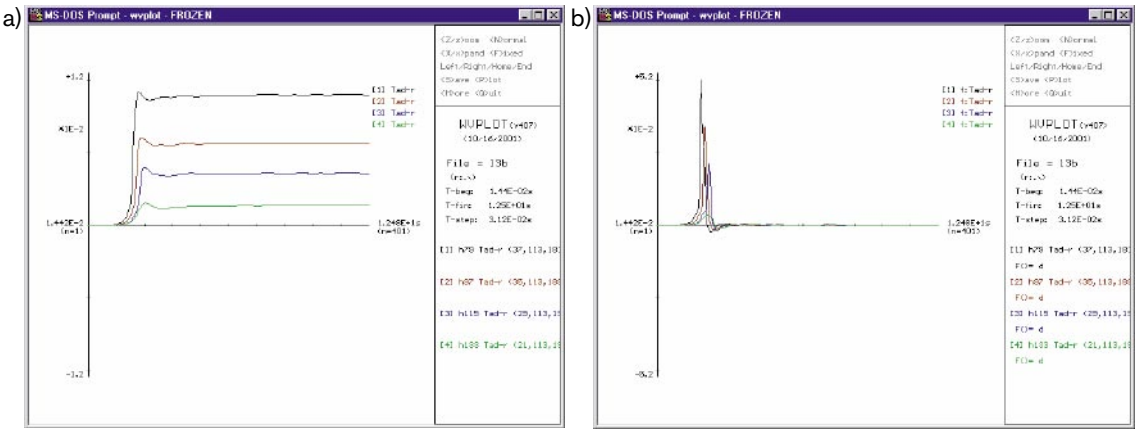

Figure A2b-21. *a) Models 29–32: Relative displacement, b) Total relative velocity.*

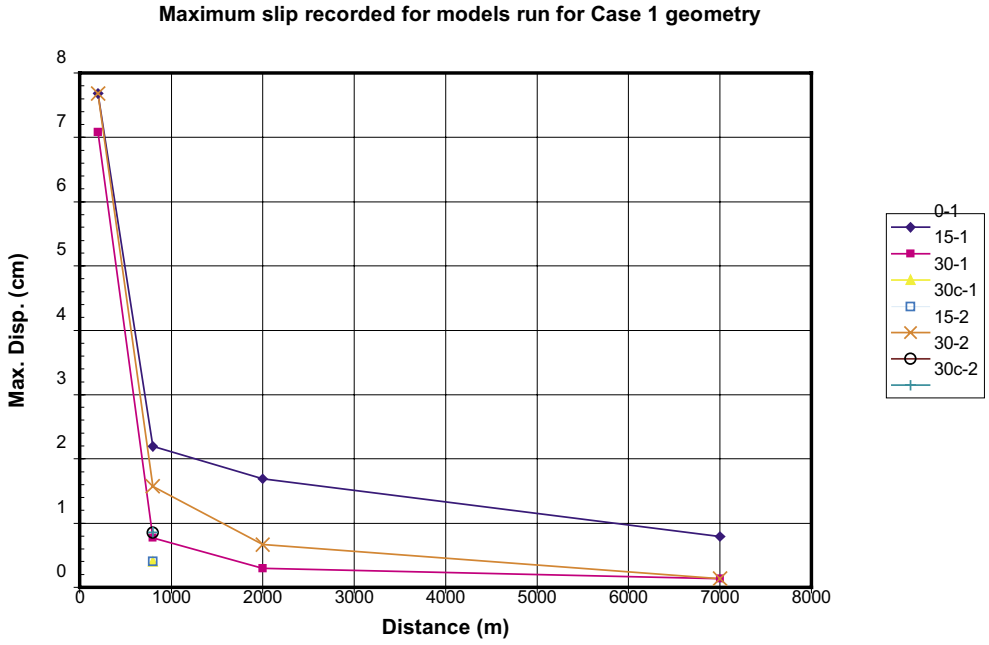

Figure A2b-22. *Variation of maximum relative displacement (cm) with distance (m) for the models run for the case 1 geometry (Models 1–16). The symbols are named according to the convention 'x–y' where x is the angle of friction and y is the stress state. 'c' signifies cohesion. Note that each data set is connected by a line for clarity – a linear relationship may not exist.*

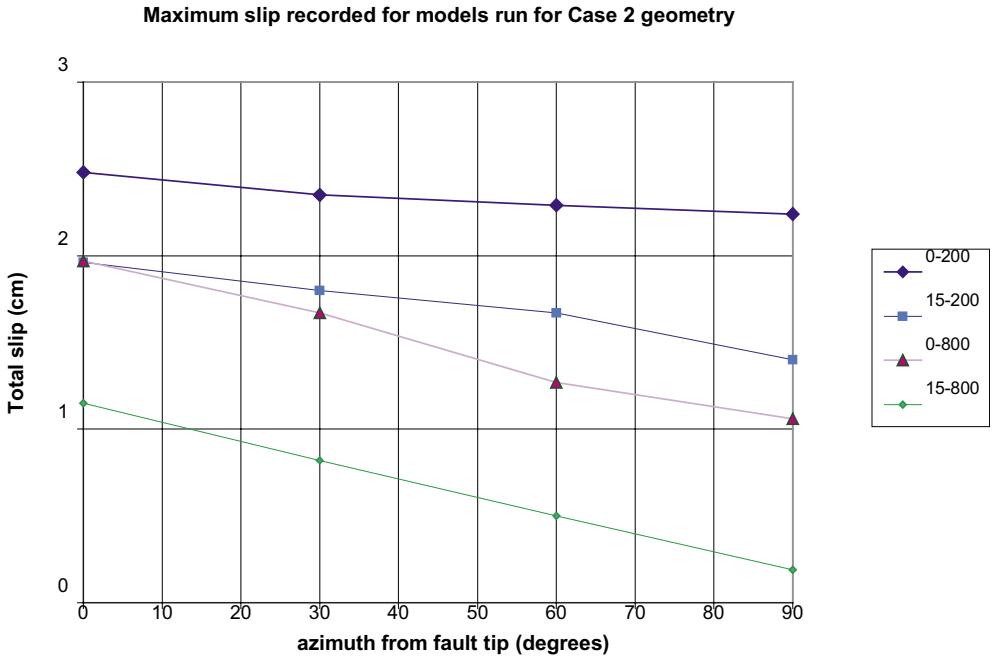

Figure A2b-23. *Variation of maximum relative displacement (cm) with azimuth (degrees) from fault tip for the models run for the case 2 geometry (Models 17–32). The symbols are named according to the convention 'x–y' where x is the angle of friction and y is the distance from the fault tip to the centre of the target fracture. Note that each data set is connected by a line for clarity – a linear relationship may not exist due to the complexity in the radiation pattern of the earthquake.*

A2b-7 Conclusions

In this study, an investigation of the displacement arising on a horizontal fracture of dimension 200 m by 200 m in response to a magnitude 6 earthquake at distances between 200 m and 7 km has been made. The position of the target fracture relative to the fault on which the earthquake occurred has been varied and two in-situ stress states have been considered.

A series of initial simulations suggested a dip-slip faulting mechanism for the main earthquake represented the 'worst case scenario'. Other sensitivity tests were carried out to optimise the model boundaries and model element size.

Once the model parameters were selected, 32 models were run to investigate the differences in relative displacement arising on the target fracture for different model geometries, stress states, distances and the values of friction and cohesion on the target fracture. For each model the Excess Shear Stress (ESS) resulting from the dynamic stresses arising from the earthquake waves is calculated and compared to the strength of the fault. These values are then used to determine the resulting displacement on the target fracture. The results indicate:

- Maximum relative displacement values ranging from ~ 0 to 7.68 cm were obtained.
- For some models the maximum relative displacement attained on the target fracture during the simulation is higher than the final displacement
- For the models tested, distance has the largest effect on the resulting displacement on the target fault. Only for zero friction or low strength cases is any significant displacement seen at distances greater than 1 km.

- Higher friction angles (~ higher coefficients of friction) show smaller total slips for the same in-situ stress and distance/geometry. In some cases, no failure slip takes place, as the shear stress does not overcome the strength of the target fracture.
- An analysis of the excess shear stress on target fractures of different orientations suggests that the horizontal fracture specified for this study is not the worst case for generating slip in response to an earthquake fault of the chosen orientation. A more detailed study of the variation of ESS and slip for different target fracture orientations could be undertaken as part of a future study.

A2b-8 References

Hildyard M W, Daehnke A, Cundall P A, 1995. WAVE, Version Proc of 35th U.S. Symp on Rock Mech., pp 519–524, 1995.

Jaeger J C, Cook N G W, 1979. Fundamentals of rock mechanics. Third ed. 1979: Science Paperbacks/Chapman and Hall London UK. ISBN.

Scholz C H, 1990. The mechanics of earthquakes and faulting. 1990, USA: Cambridge University Press USA. ISBN.

Appendix 3

Review of postglacial faulting

Current understanding and directions for future studies

Raymond Munier, SKB

Clark Fenton, URS Corporation, Oakland, CA, USA

December 2004

Abstract

This paper presents the results of an investigation into the current state of research on postglacial faulting and summarizes SKB's current understanding of postglacial faulting and the mechanisms that trigger faulting in the postglacial environment. This study is based on the review of published literature and discussions with leading researchers in the fields of postglacial faulting and intraplate tectonics. The focus of this investigation has been to explore the characteristics of postglacial faults and associated seismically-triggered deformation.

Since the concept of glacio-isostacy was first presented almost 140 years ago, there has been a wealth of empirical data accumulated that shows that major ice sheet advances and retreats are associated with crustal deformation. In particular, the data from raised marine and lacustrine shorelines, and uplift data from recent GPS measurements, used to test models of Earth rheology, indicate that glacio-isostatic recovery involves both elastic lithospheric flexure and viscous mantle flow over large areas. Recently, the role of (seismogenic) brittle failure resulting from glacio-isostacy in the upper crust has gained more attention. These investigations have shown that postglacial rebound is associated with the triggering of brittle faulting and the generation of earthquakes. Repeated growth and decay of ice sheets results in changes in the vertical crustal loading, shallow crustal fluid pressure and the strain field in formerly glaciated regions. This influences both the nature and rate of deformation in these regions. Recent rheological models have greatly advanced the understanding of postglacial crustal deformation, including when and where fault instability (and earthquakes) will occur.

Investigations of postglacial faulting are still very much in their infancy and the geographic extent of investigations is still limited. Despite this, great progress has been made in the last couple of decades. Field investigations have shown that the timing of fault movement is related to deglaciation and glacio-isostatic rebound. Studies have also shown the temporal association between fault ruptures and seismically-triggered landslides and liquefaction, indicating the seismogenic nature of glacio-isostatic faulting.

The uncertainty in determining whether or not certain deformation features are indeed true glacio-isostatic fault highlights the need to adopt a wide-ranging, multi-disciplinary approach to postglacial fault investigations. Only by careful, objective investigations, can we be sure that what we are observing in the field are seismogenic, postglacial faults.

Foreword

As this report is essentially a summary of current knowledge, we have relied heavily on the work of others. Over the years, many researchers have been generous with both their time and data. Though they do not necessarily agree on our conclusions, we wish to express our special gratitude to:

John Adams, Peter Basham, Doug Grant, Bill Shilts, Linda Dredge, Art Dyke, Tom James, Allison Bent, John Cassidy, and Maurice Lamontagne (Geological Survey of Canada); Stuart Haszeldine, Iain Allison, and Colin Davenport (Strathclyde/Glasgow University); Phil Ringrose (Statoil); Doug Peacock and Frank May (British Geological Survey); Colin Ballantyne (University of St. Andrews); Geoff Boulton (University of Edinburgh);

Iain Stewart and Callum Firth (Brunel University); Alex Mohajer, Nick Eyles, and Constantin Rogojina (University of Toronto); Joe Wallach (AECB); Anton Brown (AECL); Robert Muir Wood (RMS); Nils-Axel Mörner (University of Stockholm); Robert Lageräck (Geological Survey of Sweden); Chris Talbot (University of Uppsala); Odliev Olesen (Geological Survey of Norway); Arch Johnston (CERI, Memphis); David Greene (Denison University); Ronald Arvidsson (University of Uppsala); Björn Lund (University of Uppsala).

Sammanfattning

I föreliggande rapport presenteras resultatet av en utredning med syftet att sammanställa aktuellt kunskapsläge avseende postglaciala förkastningar och de mekanismer som kan generera förkastningar i en postglacial miljö. Utredningen baseras på en genomgång av publicerad litteratur och diskussioner med ledande forskare specialiserade på postglaciala förkastningar och intrakontinental tektonik. Utredningen har fokuserat på de postglaciala förkastningarnas karakteristik och med dessa associerade, seismiskt inducerade, deformationer.

Alltsedan landhöjning lanserades som begrepp för nära 140 år sedan, har det ackumulerats en stor mängd empiriska data som tydligt visar att istäcken som ömsom ryckt fram och dragit sig tillbaka är kopplade till deformationer i jordskorpan. I synnerhet pekar data från kustlinjer vid såväl sjöar som hav, och GPS mätningar av landhöjningen, vilka använts för att testa modeller av Jordens reologi, på att landhöjningen omfattar såväl elastisk litosfärisk flexur som visköst mantelflöde över stora områden. På senare tid har spröd deformation som orsakats av landhöjningen rönt ökande intresse. Forskningsinsatser i området har visat att landhöjningen är kopplad till jordskalv och spröd deformation. Upprepad tillväxt och avsmältning av inlandsisar resulterar i förändringar av belastningsfältet och vattentrycket i områden som varit nedisade. Detta påverkar både omfattningen och typen av deformation i sådana områden. På senare tid har stora framsteg i reologisk modellering väsentligen ökat förståelsen av postglacial deformation bland annat avseende när och var förkastningsinstabilitet inträffar och med detta associerade jordskalv.

Forskningen kring postglaciala förkastningar är fortfarande i sin linda och den geografiska utbredningen av undersökningarna är begränsad. Trots detta, har stora forskningsframsteg gjorts de senaste decennierna. Fältstudier har visat att tidpunkten för rörelser längs förkastningar är kopplad till inlandsisen avsmältning och den resulterande landhöjningen. Studier har också visat ett tidssamband mellan förkastningar och seismiskt inducerad jordskred och flytbildning (liquefaction) vilket ytterligare pekar på en seismogenisk förklaring till glacio-isostatiska förkastningar.

Osäkerheten i att bedöma huruvida en viss deformation verkligen är orsakad av glacio-isostatiska förkastningsmekanismer belyser nödvändigheten av ett brett, multidisciplinärt angreppssätt vid undersökningarna. Det är endast medelst noggranna, objektiva undersökningar som vi kan bli säkra på att de fenomen vi observerar verkligen är seismogeniska, postglaciala förkastningar.

Contents

A3-1 Introduction

Glacio-isostatic faulting, commonly referred to as “postglacial faulting”, occurs in regions of glacial advance, in response to changes in the glacial load: either as a result of deglaciation (crustal unloading) or glacial advance (crustal loading). Postglacial faulting has been reported from northwest Europe (Norway, Sweden, Finland, Russia, Eire, and Scotland) and North America (eastern Canada, New England, and possibly California and Montana). To date, all examples of postglacial faulting have been recorded in regions of low to moderate seismicity, namely passive margin, failed rift, or intraplate/craton environments. With the notable exception of the 1989 M 6.1 Ungava surface rupture /Adams et al. 1991/, postglacial faults are unique in that they occur in regions where there is no evidence of surface rupture during historical time. In addition, these regions have no historical record of seismicity that approaches the magnitude thresholds for generating surface faulting. To date, all examples of postglacial faulting have involved reactivation of existing faults and fractures.

Postglacial faulting poses a number of problems for seismic hazard assessment. Namely, how do we incorporate faults that only appear to move under specific climatic/tectonic conditions into hazard assessments and how do we determine which faults are likely to be capable structures during the design life of specific structures? The latter concern is highlighted by the occurrence of the 1989 M 6.1 Ungava, Canada, surface rupture. This fault ruptured along a Proterozoic ductile shear zone that showed no evidence for having experienced brittle failure during the Phanerozoic. How do we handle faults that have apparent repeat times on the order of hundreds of millions of years? And as a consequence, how do we identify potentially active structures in regions that are dissected by numerous generations of faults?

With these and other questions in mind, this study was conceived in order to summarize SKB’s current understanding of postglacial faulting and the mechanisms that give rise to such activity. In addition, this investigation also looked into the methods that are utilized for addressing postglacial faulting in seismic hazard assessments.

A3-1.1 Scope of report

This report summarizes the current knowledge of postglacial faulting at SKB and is structured as follows:

An introductory section defines the problem, records the geographic limitations of the study (A3-1.2) and the data sources used (A3-1.3). A nomenclature is proposed in section A3-2. Section A3-3 reviews studies of postglacial faulting in Fennoscandia, and evaluates both the claims made for postglacial faulting and the techniques used in their study. This section also includes comparisons from similar studies in eastern North America. Section A3-4 concerns the characteristics of postglacial faults and the methods used to identify such structures. Techniques to investigate postglacial faults are presented in section A3-5. We propose formal set of criteria for the recognition of postglacial faults in section A3-6. Section A3-7 concerns the conditions that give rise to postglacial faulting. We conclude this review in section A3-8.

This report does not include an extensive discussion of the seismotectonic setting of Fennoscandia, however readers are encouraged to refer to /Muir Wood, 1993, 1995/ for comprehensive summaries of the seismotectonics and e.g. /Lindström et al. 2000/ for tectonic history of Sweden.

A3-1.2 Geographic scope

The primary concern of this report is the understanding of postglacial faulting in Fennoscandia (Sweden, Norway and Finland). In this light the main topics of discussion are focused on research that has been carried out in this region. In addition, for the purposes of completeness and comparison, this report also includes discussion of postglacial faulting research in North America (Canada and the United States) and other northern European countries (United Kingdom and Eire).

A3-1.3 Data sources

This report has been produced by summarizing published research on postglacial faulting and intraplate seismotectonics. These published sources include peer-reviewed journals, SKB Reports, Geological Survey Open-File Reports, and published reports from other public agencies (NRC in the United States; AECL and AECB in Canada). In addition, information has also been included from discussions with researchers in the various fields concerned with postglacial faulting and intraplate neotectonics. A3-ll data sources are referenced in the text of the report and full citations for each source are given in the reference list at the end of this report.

A3-1.4 Data quality

Much of the research on postglacial faults has been as a result of the search for long-term storage sites for medium- and high-grade nuclear waste. Such activities, naturally stir up strong emotions and they are not often considered in a perfectly objective light. As such, some of this work has been driven by political prejudice rather than carried out in an objectively scientific manner. Thus, some claims for postglacial faulting and intraplate neotectonic activity may be questionable. With this in mind, and following the examples set by previous reviews of postglacial faulting /Muir Wood, 1993; Fenton, 1994c, 1999; Olesen et al. 2000/, all claims for postglacial faulting are evaluated against a set of qualitative criteria (see Section A3-3). Thus, claims for postglacial faulting and neotectonic activity can be considered in a more objective manner.

A3-2 Definitions

The term *postglacial faulting* contains inference to both the timing and genesis of such faulting. Firstly, it implies faulting occurring after the disappearance of glacial ice cover. It also implies faulting that *occurs as a result of the disappearance* of glacial ice cover.

/Matthew, 1894b/ first used the term postglacial faulting to describe faulting that offset glacially-scoured surfaces at St. John, New Brunswick, in eastern Canada. The use of this term has been perpetuated by numerous authors /e.g. Hobbs, 1921/ to describe similar fault offsets in the northeastern United States. /Fenton, 1994b/, describing intraplate faulting from eastern Canada and northeastern United States, considered the term “postglacial” unsatisfactory, stating that it merely implied a temporal constraint and did not consider the genesis of these faults. Equally unsatisfactory, is that the postglacial period differs

markedly in duration in different regions. In this respect, it is preferable to use a term that is reflective of the process that triggers these faults, thus the terms *glacio-isostatic faulting or glacial rebound faulting* are considered more suitable. However, since the term postglacial faulting has become established in the published literature as a synonym for glacio-isostatic faulting, it will be used in this report to denote faulting that results from glacial loading/unloading. A more broad definition, adopted herein, is that postglacial faulting is any faulting that occurs after glacial maximum and during the time that glacial ice volumes decline from that maximum. This faulting is triggered by crustal rebound resulting from crustal adjustments arising as a result of decreasing ice volume and consequent crustal unloading.

Glaciotectonics, on the other hand, is the process by which glacial movement results in the deformation of underlying substrate, including shallow bedrock as well as unconsolidated deposits. The majority of glaciotectonic deformation is the result of ice-push at the leading edge of advancing ice fronts /Croot, 1988/. The dominant style of deformation is contraction, resulting in the formation of folds and thrust faults /e.g. Croot, 1987/. However, like tectonic thrust systems, glaciotectonic deformation can also form extensional features as a result of bending moment stresses or stress relaxation /Adams et al. 1993a/. Another form of deformation resulting from ice movement is basal drag. Underlying substrate or shallow rock can become frozen to the base of the ice mass and dragged along. Like ice-push deformation, this results in contractional deformation at the leading edge, however, the trailing edges of areas that have undergone basal drag commonly display extensional deformation /Schroeder et al. 1986/. /Broster and Burke, 1990/ also used the term ‘glacigenic’ to describe faults that they considered the result of glacial movement. This term is considered redundant, and the term glaciotectonic will be used to denote any deformation resulting from ice movement.

A3-3 History of investigations

Although postglacial faulting was first reported in the mid-nineteenth century /Mather, 1843/, there has been little concerted effort in this field of research until comparatively recently. Initial examples of postglacial faulting were described by researchers that were almost always investigating some other late or postglacial geomorphic features, including shorelines and glaciated pavements.

Targeted research on postglacial faulting boosted as Johnston published his paper in Nature, /Johnston, 1987/ where he noted that the interiors of the two continental scale glaciations, Antarctica and Greenland, are virtually aseismic (Figure A3-1). He used the lack of contemporary seismicity beneath the Antarctic and Greenland ice sheets to argue that pore fluid pressures are insignificant and suggested that the weight of the ice sheets alone act to suppress brittle failure in compressional intraplate environments. The sudden release of stored stresses has ever since been used as explanation for the triggering of postglacial faults.

In the following paragraphs, a brief history of the progress in discovery of postglacial faulting in several geographic regions is presented.

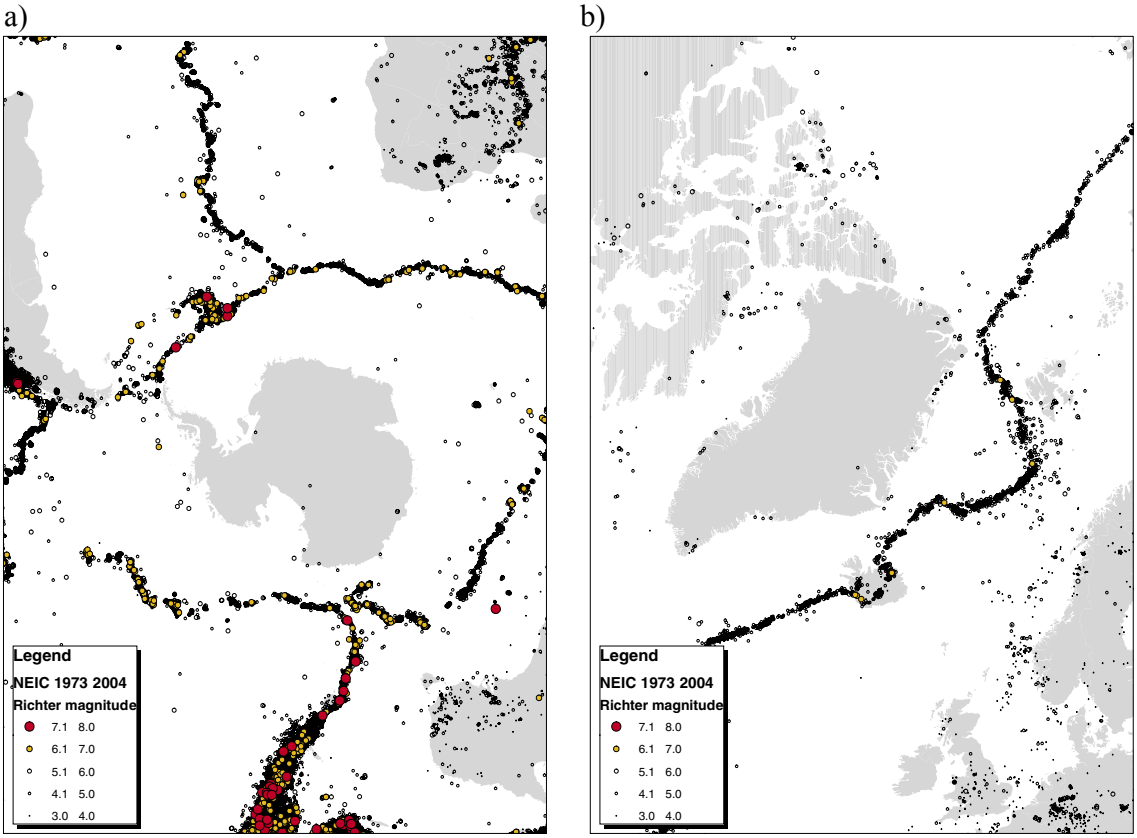

Figure A3-1. *Recent seismicity under a) Antarctica and b) Greenland /earthquake data from NEIC, 2004/.*

A3-3.1 Fennoscandia

Although the Pärvie postglacial fault (Figure A3-2) had been long been recognized as a prominent geomorphic feature by Laplanders, postglacial faulting was not reported in Europe until comparatively recently /Tanner, 1930; Kujansuu, 1964/. Tanner reported dislocation and warping of the postglacial marine limit in northern Finland. In particular, a 10 m down-to-the-northeast step in the shoreline profiles on the Fiskarhalvön Peninsula (part of present days Kola peninsula, Russia) appeared to suggest postglacial fault activity. /Kujansuu, 1964/ subsequently reported a number of postglacial faults in Finnish Lapland. However, until /Lundqvist and Lagerbäck, 1976/ reported the existence of the 200-km-long Pärvie fault in northern Sweden, the work of both /Tanner, 1930/ and /Kujansuu, 1964/ languished in relatively obscure and hard-to-get literature sources. Subsequent to the work of /Lundqvist and Lagerbäck, 1976/ several other, equally spectacular examples of postglacial faulting were discovered in northern Sweden /e.g. Lagerbäck, 1979; Lagerbäck, 1988/. Meanwhile, in Finnmark, northern Norway, the Stuoragurra fault had been discovered and shown to be postglacial in age using a combination of geophysical and geologic techniques /Olesen et al. 1989, 1992a,b/. In Finland, the Pasmajärvi and several other faults were the subject of intensive investigation /Kuivamäki, 1986; Paananen, 1987; Vuorela et al. 1987/. The search for a hard rock radioactive waste repository site by the Swedish Nuclear Fuel and Waste Management Company (SKB), spurred further work on postglacial faulting in Sweden using a wide variety of geological and geophysical techniques /e.g. Bäckblom and Stanfors, 1989/. In particular, fault trenching and detailed age-dating investigations demonstrated that fault displacement had occurred in a single

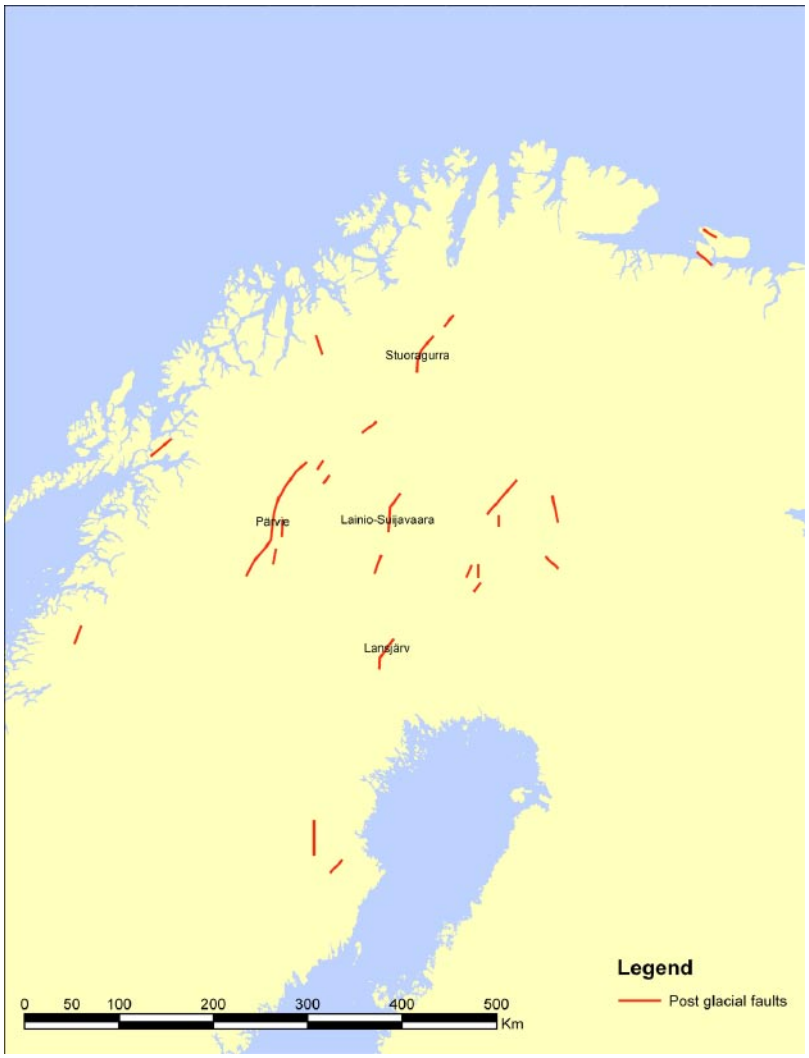

Figure A3-2. *Confirmed post glacial faults in Fennoscandia of which only the most well known are named for clarity.*

event following deglaciation /Lagerbäck, 1992/. The spatial association with low-angle landslides and extensive liquefaction demonstrated that fault movement was seismogenic /Lagerbäck, 1991/ which together with the physical characteristics of observed faulting and the strong statistical correlation with recent seismicity further strengthened the conclusion /Arvidsson, 1996/.

To date, the spectacular postglacial faults in northern Sweden are the most convincing examples of glacio-isostatic faulting. Although there have been numerous claims of postglacial faulting in southern Sweden /Mörner, 1989; 2003/, many appear to be questionable /SKB, 1990; Carlsten and Stråhle, 2000; Wänstedt, 2000/. /Muir Wood, 1993/, evaluated claims for neotectonic activity throughout Fennoscandia. Only the postglacial faults of Lapland were considered unequivocally the result of neotectonic activity. Although investigations in southern Sweden have yet to describe a convincing example of postglacial faulting, recent investigations by Mörner and his co-workers /Mörner and Tröften, 1993; Tröften and Mörner, 1997; Mörner et al. 2000/ have described widespread, contemporaneous soft-sediment deformation in varved sequences that appear to have been triggered by strong seismic shaking during the late- or post-glacial period.

/Kuivamäki et al. 1998/ summarized the evidence for postglacial faulting in Finland and Russian Karelia. Much of this work had never been published in English and thus, had not been readily available. In addition to the demonstrably postglacial ruptures in northern Finland and a number of minor offsets of glaciated pavements in southern Finland near the Gulf of Finland, /Kuivamäki et al. 1998/ also present some circumstantial evidence for postglacial faulting in Russian Karelia. These examples are not well documented and the case for the Russian postglacial faults is not strong.

An initiative by Norges Geologiske Undersøkelse (NGU) to investigate neotectonics in Norway (NEONOR-Olesen et al. 2000) led to extensive investigations for postglacial faulting both onshore and offshore Norway. As part of this effort, /Olesen et al. 2000/ evaluated suspected neotectonic features in Norway in a manner similar to that of /Muir Wood, 1993/. Only the Stuoragurra and Nordmannvikdalen faults in Finmark and Troms, respectively, were unequivocally considered to be tectonic faults of postglacial age. The Båsmoen fault in Nordland also appears a strong candidate for having a postglacial faulting origin, however, field evidence is not conclusive /Hicks et al. 2000a,b/. In all other examples postglacial faulting was either unproven or the features were shown to be the result of nontectonic processes such as gravity-induced slope movement /Olesen et al. 2000/.

A3-3.2 North America

The first example of postglacial faulting was first described by /Mather, 1843/ at Copake, in New York State, where:

"masses of slate had been shifted a few inches in a vertical direction by a slight fault, so that the grooves and scratches on the lower part that had been elevated; and on the upper mass, the same grooves that had once been continuous, were prolonged in their former direction, with the same breadth and depth. This shift of position, or slight fault may have been subsequent to the period when the scratches were made."

This description predated the general acceptance of Agassiz's theory of global glacial episodes /Agassiz, 1863, 1864a,b, 1872; Agassiz et al. 1872/, and the "grooves and scratches" described by /Mather, 1843/ are in fact glacial striations. Several other examples of postglacial faulting where glacial deposits and glacial striae were offset were reported from the north-eastern United States and eastern Canada around the turn of the century /Matthew, 1894a,b; Chalmers, 1897; Hitchcock, 1905; Woodworth, 1905; Hobbs, 1907; Woodworth, 1907; Miller, 1913/. Almost all of these examples involved small-scale faults in slates and phyllites where numerous small faults with throws of only a few millimetres were exposed on glacially-polished rock pavements. Several notable examples, including the Aspy fault on Cape Breton Island, Canada /Grant, 1990/, have experienced considerably larger offsets. /Hobbs, 1926/ proposed that postglacial rebound was responsible for this faulting and the generation of earthquakes in north-eastern Canada. Numerous other examples of postglacial faulting have been described throughout eastern Canada and the New England states throughout the twentieth century. Much of this work was carried out under the auspices of the Nuclear Regulatory Commission (NRC). /Adams, 1981/ compiled a bibliography of neotectonic features, including postglacial faults and stress relief features in eastern North America. This was updated by /Fenton, 1994a/, who also evaluated each claim for neotectonic faulting using similar criteria to /Muir Wood, 1993/. Like Sweden, much of the work on postglacial faulting has been driven by the need to site new, or re-evaluate existing, nuclear power facilities. Thus, some of the claims for postglacial faulting and neotectonic activity are speculative /Mohajer et al. 1992; Adams et al. 1993a/.

Until comparatively recently, no examples of postglacial faulting had been reported from the west of the Rockies. /Greene, 1996/ described a spectacular fault scarp with suspected postglacial movement from the eastern Sierra Nevada, California, and /Hinz et al. 1997/ describe postglacial offsets in Archean basement rocks in Montana.

/Thorson, 1996/ and /James et al. 2000/ show that glacial loading and unloading in the Puget Sound region in the Pacific Northwest may have controlled the timing of movement on crustal faults, namely the Seattle fault, situated above the Cascadia subduction zone. Similarly, /Sauber et al. 2000/ also show that glacial loading and unloading may control the release of seismic strain in the eastern Chugach Mountains of Alaska, and consequently control uplift /Meigs and Sauber, 2000/.

The modelling work of /Grollimund and Zoback, 2001/ has shown that the influence of the Laurentide ice-sheet may have extended for a considerable distance beyond its margins, indicating that deglaciation may have acted as a trigger for elevated seismotectonic activity in the New Madrid region during the Holocene. /Kenner and Segall, 2000/ echo the possibility that the historical seismicity observed in the New Madrid region may be the result of far-field ice sheet loading and unloading.

A3-3.3 United Kingdom

The first examples of glacio-isostatic tectonism were revealed by delevelled shorelines along the Firth of Forth in eastern central Scotland /Sissons, 1972/. Subsequently, other investigations of postglacial and late-glacial shorelines in Scotland indicated that postglacial rebound had not been uniform and had involved dislocation along existing faults /e.g. Gray, 1974a,b/. The work of Brian Sissons in Glen Roy was probably the most important in highlighting the role of postglacial faulting in Scotland /Sissons and Cornish, 1982a,b/. The shorelines of the glacially-dammed lake that had occupied Glen Roy during the latest Pleistocene showed significant displacement. The first systematic investigation of postglacial tectonism in the UK was carried out by Phil Ringrose at the University of Strathclyde /Ringrose, 1987, 1989a,b; Ringrose et al. 1991/. This work showed that a number of fault offsets were spatially and temporally associated with seismically-induced deformation features, including liquefied sediments and landslides. This work has been gradually expanded upon /e.g. Fenton, 1991b, 1992a,b/ with the identification of a number of postglacial faults in the western Highlands of Scotland. Recent investigations by /Stewart et al. 1999, 2000/ in the northwest Highlands has questioned some of the findings of earlier workers. They conclude that rather than discrete fault displacements, postglacial faulting in Scotland occurred as distributed displacement across broad zone of faulting. They argue that postglacial rebound is accommodated on smaller faults with smaller displacements. These faults parallel the glaciated valleys, but are subsidiary to larger faults buried beneath valley floors and lochs (lakes).

A3-3.4 Other regions

There have been comparatively few investigations of postglacial faulting elsewhere in Europe. /Mohr, 1986/ described a number of potential postglacial fault scarps in the west of Ireland. To date, these features have only been subject to geomorphic analysis. /Knight, 1999/ described a number of features from Northern Ireland that appear to be more likely glaciotectonic in origin, i.e. resulting from either ice-push or basal shear during ice-sheet movement.

/Lukashov, 1995/ described a number of faults from Russian Karelia that are suspected of having postglacial movement. These descriptions lack detail and the true nature of the features described is not known.

/Jackli, 1965/ describes ice deformation features from the Swiss Alps that may be related to gravitational instability rather than tectonic faulting. Several examples of geologically recent fault displacements have been reported from elsewhere in the intraplate region of northwest Europe /e.g. Gregersen et al. 1996; Vanneste et al. 1999/. However, these appear to be the result of intraplate tectonics (i.e. rifting) rather than glacio-isostatic rebound.

Postglacial faulting has not been actively investigated in other regions. /Jones, 1996/ described three small faults showing recent movement in South Victoria Land, Antarctica. Although these faults are located at the margin of the Antarctic ice sheet, apparent sinistral strike-slip displacements indicates that they are more likely the result of regional tectonism rather than postglacial rebound. A potential postglacial fault scarp has also been reported from southwest Greenland, within granitic rocks of the Isua Complex /Greene, 2000/. As both Antarctica and Greenland are the largest current ice-caps, these regions probably warrant further investigation for postglacial faulting. /Ivins and James, 1999/ investigated the crustal response to Holocene and recent ice mass fluctuations in Patagonia. Recently established initiatives to investigate the rebound and tectonics of Antarctica may yield further information /James, 2002/.

In Iceland, the time of deglaciation is associated with an increase in volcanic activity and the production of volcanic ashes /Einarsson, 1978; Jull and McKenzie, 1996/. Whether a major difference in volcanic activity occurred across glacial/interglacial periods has not been specifically investigated. However, the presence of hyaloclastic deposits in much of the Pleistocene succession in Iceland indicates subglacial eruption. If this interpretation is valid, then it does suggest that depression of the surface by the ice load induced an increase in magma production. /Sigmundsson and Einarsson, 1992/ showed that volume changes in the Vatnajökull ice cap during the last 1,000 years have resulted in land level changes. Although short-term loading changes have been shown to effect historical land levels, no fault movement has been attributed to icecap loading.

A3-4 Characteristics

Postglacial faults and similar-looking landforms have been described almost exclusively in terms of their geomorphic (surficial) expression. This level of investigation, has unfortunately led to a less-than-complete understanding of the processes involved. In addition, many landforms created by non-tectonic processes (glaciation, periglaciation, and landsliding) have also been mistakenly attributed to postglacial fault activity /SKB, 1990; Muir Wood, 1993/.

Postglacial faults are best described using a number of criteria, from regional seismotectonic setting, through local geologic setting, and finally detailed geometric and geomorphic features (Table A3-1). These criteria are discussed in the following sections.

A3-4.1 Regional context

A3-4.1.1 Physiographic setting

Postglacial faults, by definition, occur in formerly glaciated regions (Figure A3-3) that have been subject to glacio-isostatic adjustment. The nature of the last glaciation determines the physiography of the region; areas subject to ice-cap or continental-scale glaciation (e.g. north-western Europe and Canada) invariably comprise broad regions of predominantly subdued topography, whereas regions subject to valley or Alpine glaciation, (e.g. UK, Norway) are more dissected, leading to high relief (1,000 m+), with oversteepened slopes. Common to both areas is the presence of glacial deposits (tills, eskers, drumlins, etc) and glacially polished/scoured bedrock (striated pavements, rôche moutonées, flutes, etc). In some instances, if ice retreat was lateral, rather than purely by downwasting (the latter, however, is more common in areas of ice-cap glaciation), many of these features are further modified by glaciofluvial processes or can be entirely buried by outwash deposits. Thus, the topographic/physiographic characteristics of regions containing postglacial faulting vary from broad open regions with subdued relief to areas of extremely steep, dissected Alpine topography.

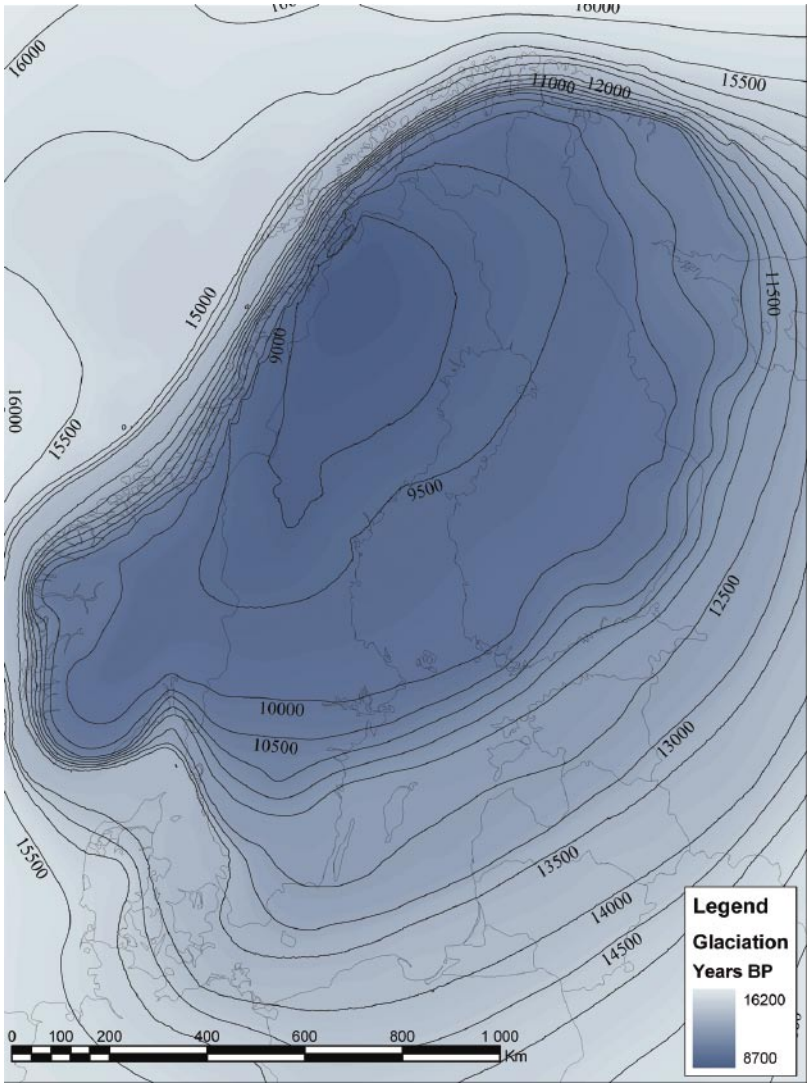

Figure A3-3. *Extent of the Weichselian glaciation /redrawn from data in Påsse, 2001/.*

A3-4.1.2 Plate tectonic setting

The regions where postglacial faulting has been observed are exclusively intraplate craton regions (e.g. eastern Canada, Sweden), passive margin settings (e.g. Scotland, Norway), and failed rifts (e.g. the St. Lawrence rift zone, eastern Canada). Although some of the intraplate regions may have been subject to tectonic activity as recently as the early Cenozoic, as shown by igneous activity /Muir Wood, 1989b/ and sedimentation in the basins formed in the arms of failed rifts, they are essentially regions of contemporary tectonic quiescence. These regions are similar to the 'stable continental regions' (SCRs) defined by /Johnston et al. 1994/. These are regions of continental crust, including extended crust, that have not been subject to post-Cretaceous orogenic activity, and have not been the subject of post-Paleogene extension. These regions exhibit low levels of seismicity and surface faulting is very rare /Johnston et al. 1994/.

The geophysical characteristics of both passive margins and cratonic settings for postglacial faulting are similar. Each is a region of presently low to moderate heat flow, with low to moderate, diffuse seismicity. Strain rates are low, approximately 10^{-9} to 10^{-10} (yrs^{-1}) for passive margins and at least two orders of magnitude less for cratons. Craton areas are generally regions of over-thickened silicic crust. Heat flow at passive margins may be marginally higher than cratons (57 mWm^{-2} as opposed to 38 mWm^{-2}, /Bott, 1982/) on account of relatively recent rifting and magmatic activity (e.g. the last rifting/magmatic episode in the UK was during the Paleogene-Eocene, with some minor activity continuing into the Oligocene, /Muir Wood, 1989b/). Seismically, these regions are characterised by low to moderate rates of seismic strain release.

A3-4.1.3 Glacio-isostacy

The most visible characteristic of regions undergoing glacio-isostatic rebound is the presence of both uplifted (more common) and submerged marine shorelines /Firth, 1989; Dyke et al. 1991/ all depending of the size of the centra,l downloaded bulge, and distance from the centre. The stresses acting on the uplifted and submerged parts are different. Extension is expected within the uplift region whereas compression is expected at the outer rim /e.g. Stein et al. 1989/. Postglacial faulting has only been described from areas within the regions undergoing glacio-isostatic uplift, i.e. within the rebound dome. Although some researchers have proposed that the far-field effects of glacial unloading may have triggered faulting out with the forebulge /Kenner and Segall, 2000; Grollimund and Zoback, 2001/, the role of glacio-isostacy in triggering such fault movement is as yet unproven.

In Fennoscandia (Figure A3-4), the uplift dome encompasses a northeast-southwest elongate dome covering the majority of the landmass, with a maximum postglacial uplift of approximately 850 m from the time of maximum subsidence /Ekman, 1996; Gudmundsson, 1999/. The major postglacial faults in Lapland are all within the uplift dome, close to the centre of maximum uplift. The Båsmoen fault in northern Norway may be in the transition zone between uplift dome and peripheral bulge /Hicks et al. 2000a,b/. Though most known postglacial faults in eastern North America lie within the margins of the Laurentian uplift dome /Andrews, 1991; Dyke and Peltier, 2000/ Wu and Johnston argue that the New Madrid faulting was not influenced by glaciation /Wu and Johnston, 2000/.

Measurements of raised shorelines have traditionally been used to infer uniform or concomitant uplift of broad crustal regions, with minor perturbations in the elevation data assumed to be the result of measurement inaccuracies /Andrews, 1991/. More recently, these discontinuities in elevation data have become understood as indications of non-uniform behaviour of the crust during glacio-isostatic rebound /Tanner, 1930; Sissons, 1972; Sissons and Cornish, 1982a,b; Dyke et al. 1991; Dyke and Peltier, 2000/.

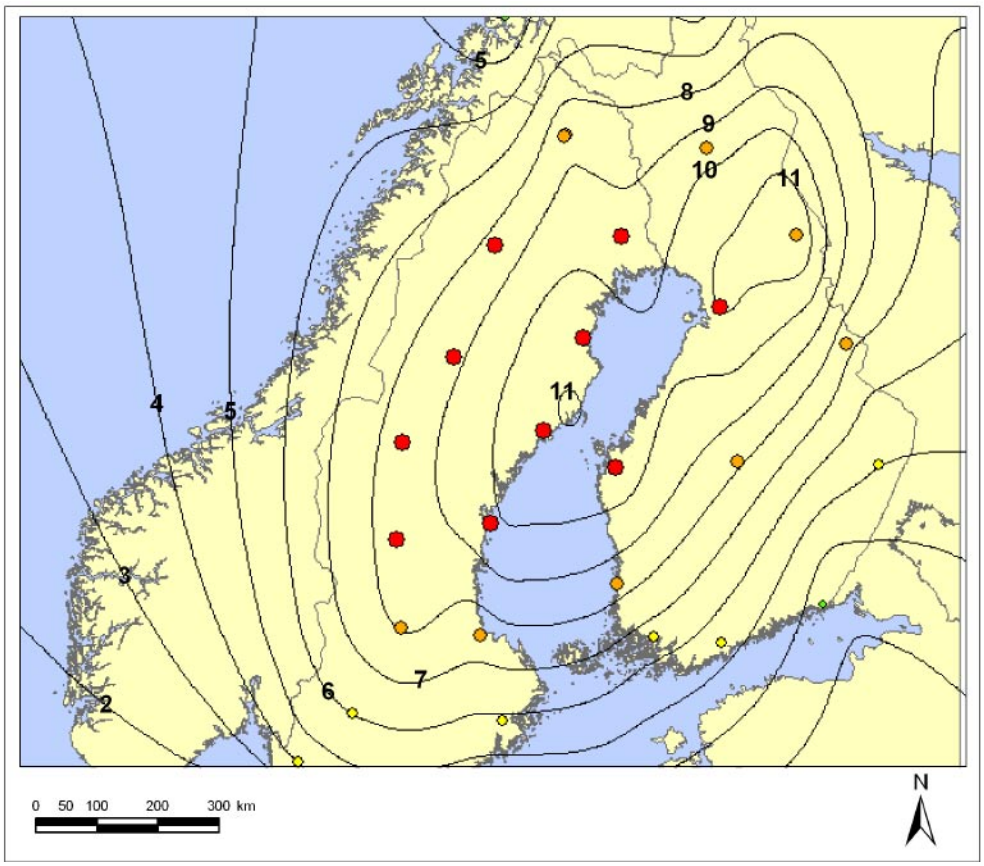

Figure A3-4. *Contours of recent vertical motion (mm/y). Bifrost GPS observations from the period 1993–2001 were kindly provided by Scherneck /pers. comm. See also Scherneck et al. 2002/. The best fit model was obtained from /Milne et al. 2001/.*

In addition, where there is good age-control on these shorelines and when there is well constrained elevation data, differential depression of shoreline elevations can be noted during ice-advance stages /e.g. Firth, 1986; Koteff et al. 1993/. The well constrained age of uplifted shorelines around the Gulf of Bothnia, Sweden, and the west coast of Scotland in particular, provide ideal time markers with which to date the movement on postglacial faults /e.g. Lagerbäck, 1992/. The Aspy fault on Cape Breton Island, Nova Scotia is observed to displace the 125 ka late Sangamon rock-cut platform by 15 m /Grant, 1990/. Several smaller shoreline offsets are also recorded along the north coast of Cape Breton Island, Nova Scotia /Neale, 1963a,b, 1964/.

A3-4.1.4 Summary

At a regional scale, postglacial faults occur in formerly glaciated (recently deglaciated) craton, failed rift, and passive margins settings that are undergoing or have recently undergone glacio-isostatic rebound. These regions are characterized by relative tectonic quiescence with low to moderate levels of seismicity, and low to moderate heat flow. Topography is generally subdued in regions of former ice-cap glaciation or can be extremely dissected in areas of valley or alpine glaciation.

A3-4.2 Local geologic context

Postglacial faults are found in areas of relative contemporary tectonic quiescence. This includes highly deformed cratons, Phanerozoic (Paleozoic) fold belts and Mesozoic-Cenozoic rifted margins. On a local scale, with the exception of minor (millimetre scale) faults in eastern Canada expressed in fissile slates and phyllites adams /Grant, 1980; Adams, 1981, 1989a; Fenton, 1994b/, there appears to be no lithologic control on faulting. Structural control of faulting, however, is important. To date, all examples of postglacial faulting involve rupture of pre-existing faults /e.g. Eliasson et al. 1991; Munier, 1993/. Note, no postglacial faults have been reported from platform regions /Hancock et al. 1984/ that have undergone relatively little deformation. In addition, at a local scale postglacial faults do not appear to be constrained to any particular geophysical characteristics, merely that they tend to follow pre-existing faults and fractures /Fenton, 1991b/. This is in line with observed, current intraplate seismicity which concentrates at old deformation zones /Sykes, 1971; Arvidsson et al. 1987/.

A3-4.2.1 Association with contemporary seismicity

Regional seismicity studies show a gross association between areas of postglacial faulting and elevated levels of seismicity /Hasegawa and Basham, 1989/. /Bungum and Lindholm, 1997/ show that seismicity in Fennoscandia defined a series of north- and northeast-trending belts that approximately correlate with the postglacial fault domains (Figure A3-6). Most seismicity is confined to the upper 15 km of the crust and is located to the SE of the fault traces, indicating a SE-dipping fault geometry /Bungum and Lindholm, 1997; Kuivamäki et al. 1998/. Though Wahlström /Wahlström et al. 1987, 1989/ could not demonstrate any significant spatial correlation between contemporary seismicity and postglacial faults, a recent study by /Arvidsson, 1996/, using improved locations of microearthquakes at the Lansjärv PGF, showed that the microseismic activity in the Lansjärv region is correlated to the Lansjärv fault. This has later been further elaborated /Arvidsson, 2001/ using Mohr-Coulomb calculations that implies that micro-earthquake locations that deviates from the fault surface is the result of the state of stress on the fault. This is presently observed in aftershocks locations from recent earthquakes. It should be noted that the Lansjärv fault was chosen for special study by SKB. /Arvidsson, 2001/ also demonstrated that the correlation between seismicity and PGFs was statistically significant on larger scales. Most earthquakes appear to have been located to the eastern downdip side of the largest fault scarps / Arvidsson, 1996/. Similarly, /Bungum and Lindholm, 1997/ showed that there was a diffuse linear trend of seismicity associated to the down-dip projection of the Stuoragurra fault.

/Hicks et al. 2000a,b/ investigated the Rana region in northern Norway, the location of the largest known earthquake in Fennoscandia during historic time (the M_s 5.8–6.2 earthquake of 1819). This is a region with a high postglacial rebound gradient and has experienced relatively elevated levels of seismicity during historic time. This is also the locus of the Båsmoen fault, a fault that has possibly experienced 0.3–0.4 m of postglacial movement.

/Fjeldskaar et al. 2000/ note that the highest rates of seismicity in Fennoscandia are in a NE-SW oriented belt off the west coast of Norway (Figure A3-6), in a region that, according to uplift models, corresponds to the glacio-isostatic forebulge.

The region of greatest postglacial rebound in the western Highlands of Scotland is also associated with elevated levels of seismicity /Fenton, 1991a,b; Stewart et al. 2000/.

Elsewhere, in most intraplate settings, the quality of the source of local earthquakes are too poor to be convincingly associated with large-scale fault structures. In addition, the location errors, especially for depth control are usually larger than the inferred earthquake source dimensions /Muir Wood, 1993/.

For reference, the current world seismicity is shown on Figure A3-5.

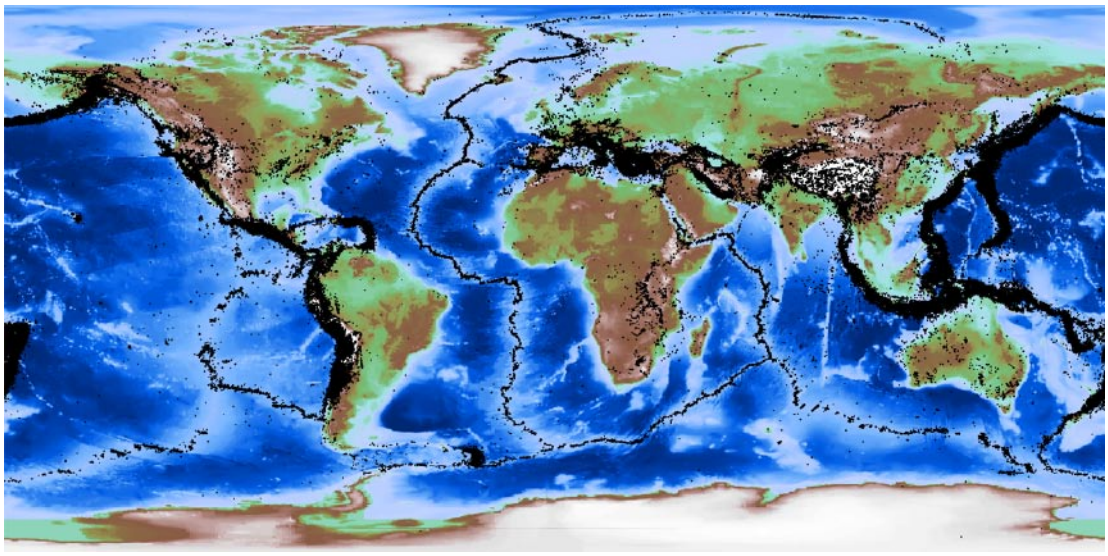

Figure A3-5. *World seismicity (M > 3) recorded during the last 30 years /earthquake data from NEIC, 2004; bathymetry data from NGDC, 2004/.*

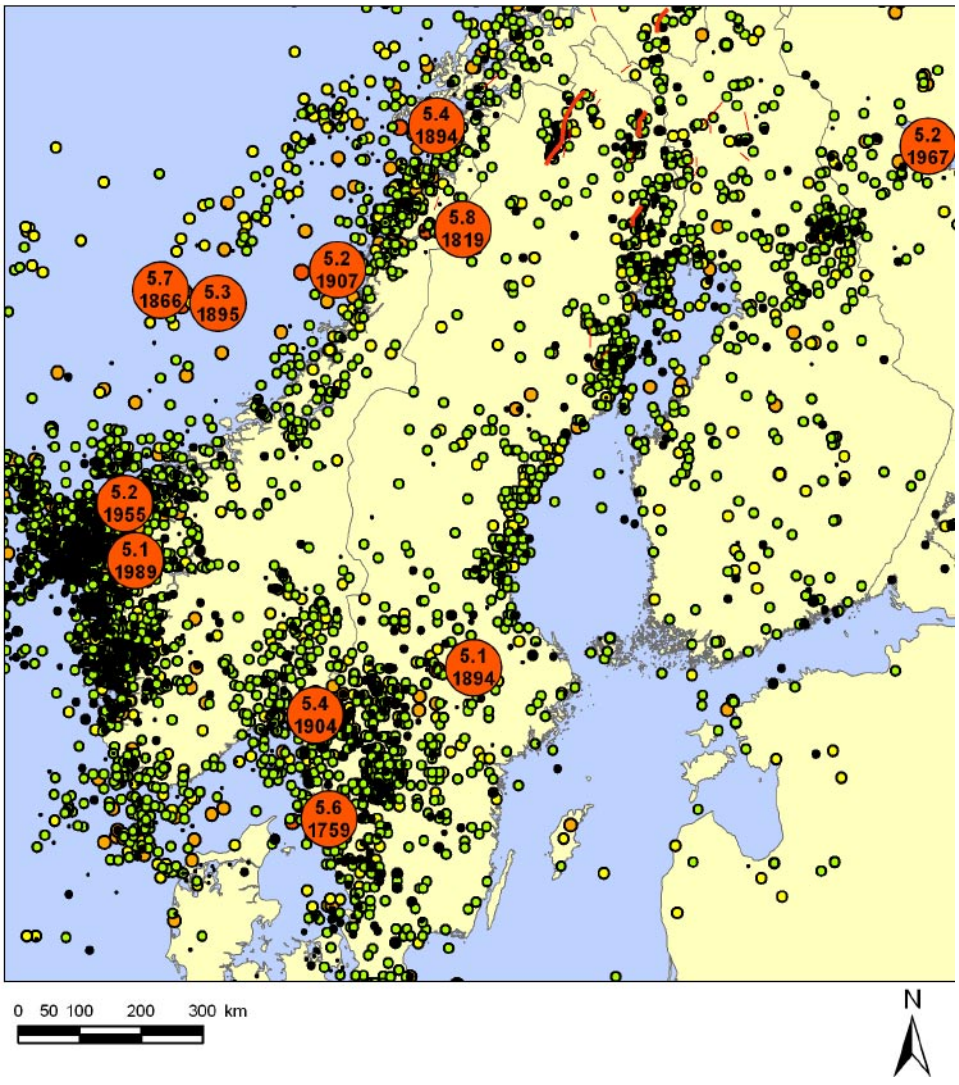

Figure A3-6. *Historic and recent earthquake epicentres 1375–1996. Data from /Arvidsson, personal communication 2001/ and the University of Helsinki. Magnitudes larger than 5 are indicated in red with event dates.*

A3-4.2.2 Seismites and landslides

The seismogenic nature of the postglacial faulting process itself, is highlighted by the spatial association of the fault scarps with seismically-induced liquefaction features (Figure A3-7) and seismically-triggered landsliding /Ringrose, 1989b; Lagerbäck, 1990/.

Although soft-sediment deformation is often considered synonymous with seismicity, there are a number of mechanisms that can result in either gravitational instability or the creation of cyclic pore pressure and the loss of bearing strength that produce similar liquefaction features /Ringrose, 1987/. Therefore, it is important that we exercise a degree of caution when investigating and interpreting soft-sediment deformation.

/Sims, 1975/ developed a series of criteria to describe true seismites. By rigorous application of these criteria we will reduce the risk of mistakenly attributing non-seismic soft-sediment deformation to paleoseismic activity. Only by being aware of the structure and style of known seismites from seismically active areas, can we make reasoned determinations concerning the origins of paleoliquefaction features in intraplate settings.

The majority of liquefaction features described from formerly glaciated regions are found in varved lacustrine deposits /Adams, 1982; Ringrose, 1989b; Mörner et al. 2000/. These include injection and involution structures, slumps, micro-faulting, fissuring, and other features commonly caused by seismically-induced liquefaction /Sims, 1975/. /Davenport and Ringrose, 1987/ report a particularly extensive liquefaction event(s?) in a sequence of glacial outwash sands in eastern Scotland. /Lagerbäck, 1991/ describes extensive liquefaction in glacio-fluvial and glacio-deltaic sequences in the Lansjärv region in northern Sweden.

Figure A3-7. *Sand vent at Rowmari, India, resulting from the Assam M=8.7 earthquake, June 12, 1897 /Photopgraphy by La Touche, 1897/.*

One unusual, and as yet unique potential liquefaction feature reported from northern Sweden is the 'graded tills' in the Lansjärv region described by /Lagerbäck, 1991/. In these sequences, instead of being a typically poorly sorted, diamict till, these deposits are well sorted and show a distinct fining upwards texture. These graded sequences are found in the hanging wall of the Lansjärv fault and are associated with surface depressions. It is argued that violent seismic shaking liquefies these tills, allowing the coarser materials to settle out first. As these types of deposits have as yet, not been described from any tectonically-active region, a seismic shaking mechanism for their genesis must therefore be viewed with a certain degree of scepticism.

Landsliding is ubiquitous in almost all environments where there is a slope and suitably weak materials. Seismic triggering for landsliding is notoriously difficult to prove. However, a spatial and temporal association of landsliding and postglacial faulting has been demonstrated in northern Sweden /Lagerbäck, 1988; 1992/. These landslides occur on particularly low-angle slip planes and in areas of subdued relief. /Ringrose, 1987/ and /Fenton, 1991a/ showed that landslides in the area of Glens Roy and Gloy, Scotland, were synchronous and contemporaneous with liquefaction features in lacustrine varves and a faulted offset of a late-glacial ice-damed lake shoreline. /Aylesworth et al. 2000/ used the contemporaneous nature of landsliding over a large region of the Ottawa Valley, eastern Canada, to infer paleoseismic activity.

A3-4.2.3 Groundwater

At a local scale there appears to be no consistent association of postglacial faults with hydrologic conditions. Expulsion of groundwater was noted along the scarp of the Lainio fault during a field visit in 1991 (Fenton, *unpublished field notes*). Also, /Lagerbäck, 1988/, noted groundwater expulsion features in trenches excavated along the Lansjärv fault. Elevated fracture water pressure may be important in the triggering of postglacial faults /Fenton, 1991a, 1992b; Muir Wood, 1993/.

/Gudmundsson, 1999/ argues that postglacial doming is sufficient to generate tensile stresses that may be as high as 30 MPa at the surface. This is an order of magnitude greater than the typical tensile stress, thus doming may be sufficient to generate new tensile fractures, which in turn should increase the hydraulic conductivity of crystalline bedrock. Enhanced production of groundwater wells in many areas of Norway within regions of high postglacial uplift are cited as support /Gudmundsson, 1999/.

To date, there appears to be no consistent regional association between groundwater and postglacial faults.

A3-4.3 Physical characteristics

A3-4.3.1 Surface expression

From the study of postglacial faulting around the world, a number of characteristics appear to be common to all postglacial fault scarps. The faults are generally reverse and have reactivated precursor deformation zones or faults. However, larger faults, for example the Pärvie and Lansjärv faults in northern Sweden do partly break along new paths over short sections in order to join a number of pre-existing faults. The scarps typically displace striated or polished pavements or landforms. Faults covered by glacial or postglacial materials are more difficult to identify due to the mechanical instability of these materials in the postglacial environment /Lagerbäck, 1990/. The geometry of postglacial fault scarps are roughly continuous, linear to slightly arcuate reverse fault scarps. Some trace length and offset statistics are tabulated in Table A3-1.

Table A3-1. Observed Fennoscandian postglacial fault scarps.

Fault	Length (km)	Average scarp height (m)	Reference
Pärvie	150	10	/Lagerbäck, 1979/
Lainio-Suijavaara I	50	15	/Lagerbäck, 1979/
Merasjärvi	10	12	/Lagerbäck, 1979/
Lansjärv	40	10	/Lagerbäck, 1979/
Skellefteå I	40	10	/Lagerbäck, 1979/
Skellefteå II	30	10	/Lagerbäck, 1979/
Stuoragurra	80	7	/Olesen et al. 1989/
Nordmannvik	3	1	/Dehls et al. 2000/
Suasselkä	48	5	/Kujansuu, 1964/
Pasmajärvi –Venejärvi	15	12	/Kujansuu, 1964/
Vaalajärvi	6	2	/Kujansuu, 1964/

A3-4.3.2 Scale and aspect ratio

The scale of postglacial fault scarps range from features that can only be traced for a few millimetres to the 150-km-long Pärvie fault. Shorter fault lengths may be a consequence of relatively poorly exposed faults in areas with considerable glacial deposits. Smaller faults generally occur in large groups in areas of slaty or phylitic rocks, where up to several hundred faults, each with a throw of only a few millimetres, may occur over an outcrop width of a few tens of meters /Oliver et al. 1970; Adams, 1981; Fenton, 1994a/. Larger faults are almost exclusively single scarps with few or no branch faults, splays or secondary deformation. A notable exception is the 'big bend' region of the Pärvie fault where a shallow thrust ramp is associated with secondary normal faulting that accommodates bending moment stresses /Muir Wood, 1989a, 1993/. A similar low-angle thrust 'flake' is observed along the Lansjärv fault and does not appear to be associated with any pre-existing brittle structure /Lagerbäck, 1988/. The aspect ratio (scarp height to fault scarp length) for postglacial faults is often less than 1:10,000, i.e. less than that for most tectonic reverse faults /Scholz, 1990/ but still within the range of offsets. The slip also scales well within the scaling laws of large earthquakes /Kanamori and Anderson, 1977/. /Arvidsson, 1996/ suggested the large slip to be due to the thickness of the brittle seismogenic crust. A small aspect ratio can be an indication of relatively strong crust (allowing large strains at the ends of a fault), a long repeat time between successive faulting events, or a relatively immature fault that has not reached an equilibrium displacement profile /Cowie and Roberts, 2001/. The scarp heights range from a few millimetres to possibly several tens of meters. As stated above, the sense of deformation is almost exclusively reverse faulting, however, small components of strike-slip faulting and normal faulting have been reported /Muir Wood, 1989a/. These almost exclusively accommodate geometric complexities, namely bending moment stresses, in the fault trajectories. Strike-slip displacement previously reported on postglacial faults in Scotland /Ringrose, 1987; Fenton, 1991a/ are now considered spurious /Stewart et al. 2000/.

A3-4.3.3 Paleoseismology

Where paleoseismic trench data is available, the offsets on postglacial faults are observed to be the result of single events /Lagerbäck, 1988, 1990/. Trenching studies in Sweden (Figure A3-8), Scotland, and Canada have so far not shown any conclusive evidence for repeated movement on these structures following deglaciation. In some cases, this means that fault motions have involved up to 15 m of vertical displacement /Muir Wood, 1989a/. However, Lagerbäck reports that the Lainio fault (northern Sweden) having a 30-m-high scarp, could have been formed by repeated reactivations (Lagerbäck, personal communication). Degradation of the Lainio bedrock scarp has, however, not allowed any assessment of the number of faulting events that resulted in its formation.

Figure A3-8. *The Lansjärv fault scarp exposed by trenching.*

A3-4.3.4 Depth

The crustal extent of most postglacial faults is unknown except from indications of present seismicity. /Arvidsson, 1996/ points out that seismic faulting is generally initiated at the base of the seismogenic crust which would indicate that faults stretch down to 30–40 km below surface, which also fits well with models for fault width and maximum fault slip. The large faults in Fennoscandia, exemplified by the Pärvie scarp, with tracelengths of hundreds of kilometers and offsets of up to 15 m per-event, extend to seismogenic depths and have been inferred to continue through the entire (40 km) thickness of the brittle lithosphere /Muir Wood, 1989a; Arvidsson, 1996/. These fault dimensions (40×200 km) have been used to infer paleoevents as large as M_w 8.5 for the Fennoscandian faults /Muir Wood, 1989a; Arvidsson and Wahlström, 1993/, though restrictions posed from recent seismological data gives a more modest M_w=8.2 /Arvidsson, 1996/ and a minimum fault length of the Pärvie fault of 150 km.

A3-4.3.5 Relationship to local stress field

A final local characteristic of postglacial faults is their relationship to the contemporary stress field. Although many minor or small faults show no apparent relationship to the stress field /e.g. Fenton, 1991a,b/, larger faults are almost always oriented perpendicular to the direction of maximum horizontal compression /Muir Wood, 1993/. Also related to the stress field or rather the strain rate (the release of stress) is the spacing between postglacial faults. In Fennoscandia and western Scotland, two areas where postglacial faults have been studied in considerable detail over a broad region, there appears to be a self-similar relationship between fault size (length) and interfault spacing. In Fennoscandia, where the faults are several tens to hundreds of kilometres long, the spacing between faults is of the order of about 100 km. In Scotland, where the mapped faults range in length from a few km to several tens of km, the spacing between faults is about 10 km. The offset along these faults scales in a similar manner, with the average being 10 m and 1 m for Fennoscandia and Scotland, respectively. The reasons for this behaviour are not clear. The main difference between Scotland and Fennoscandia is that the former was subject to valley glaciation with an ice thickness of ~ 1 km, while Fennoscandia was covered by a 2–2.5-km-thick ice-cap during the last glaciation.

A3-4.4 Fault timing and recurrence

From age-dating, stratigraphic and geomorphic relationships, faulting has been demonstrated to occur during or immediately following deglaciation. Many faults in eastern Canada displace glacial striae but the bedrock fault scarps show no glacial modification /Adams, 1981; Fenton, 1994b/). In northern Sweden, the post glacial faults moved very close in time to the occurrence of the local deglaciation. The Pärvie fault reactivated while some of the fault trace was still covered with ice /Lagerbäck and Witshard, 1983/. The Lansjärv fault reactivated within a few years of deglaciation, at the time of the highest postglacial sea level /Lagerbäck, 1988/. In northern Norway, the Stuoragurra fault offsets glaciofluvial deposits indicating Holocene or postglacial movement /Dehls et al. 2000; Olesen et al. 2000/. In Scotland, the displacement of lateglacial and postglacial shorelines clearly demonstrates the postglacial timing of fault movement /Ringrose, 1987/.

In northern Sweden, where the timing of fault movement is best constrained, it is clear that the lowland faults, i.e. those closest to the ice margins, moved first as ice retreated away from the Gulf of Bothnia and into the upland areas /Muir Wood, 1993/. The relative timing of individual faults among the lowland faults is, however, not known.

In Norway, the Stuoragurra fault displaces late and postglacial deposits /Olesen et al. 1989/. Similarly, the Nordmannvikdalen fault is marked by a scarp in late-glacial and postglacial deposits /Sollid et al. 1988/. Investigations carried out under the NEONOR program showed that faulting on the Båsmoen fault occurred following deglaciation /Hicks et al. 2000a,b/.

In Scotland, the timing of movement on the Glen Roy fault appears to be related to more localized loading and unloading /Fenton, 1991a; Ringrose et al. 1991/. In this case, fluctuations in ice volume and in local crustal loading as the glacially-dammed lake rose and fell were sufficient to trigger several paleoseismic events. The Glen Roy paleoseismic record also provides the only circumstantial evidence for repeated fault movement during deglaciation. Where paleoseismic trenching has been carried out, the stratigraphic relationships observed indicate that faulting occurred as "one-off" events.

In Canada, to date, there have been no detailed age-dating investigations of postglacial faults /Adams, 1996/. The postglacial age of faults is based on the displacement of glacial striations and other late-glacial and postglacial landforms and deposits.

A3-4.5 Unproven paleoseismic indicators

/Muir Wood, 1993/ highlighted a number of features that have been used to infer paleoseismic activity in Sweden. The main argument against using these features as diagnostic indicators of paleoseismic activity is the fact that there is no documentation of them being associated with historical seismic activity. Similar situations have arisen in eastern Canada /Adams et al. 1993a/.

In particular, the association of boulder caves (Figure A3-9) with paleoseismic activity /Sjöberg, 1994/ is peculiar to Sweden. Similarly, other features such as 'boulder trains', seismic morraines, and seismic varves /e.g. Mörner, 2003/ must also be considered suspect.

a) b)

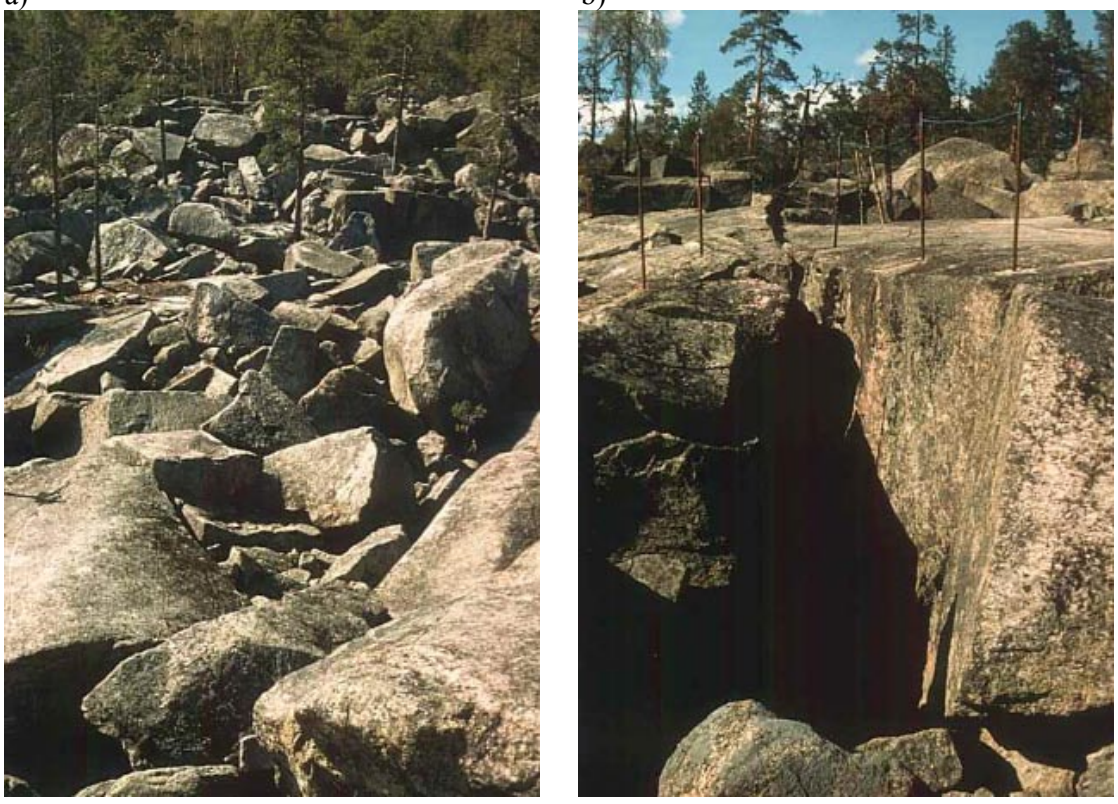

Figure A3-9. *a) Overview from the top of the Boda cave area, looking west. b) One of the entrances to the cave system /both pictures from Wänstedt, 2000/.*

The formation of such features are not known from any other seismically-active region in the World. Therefore, caution must be exercised when using such features to indicate past earthquake activity.

A common argument for recency of faulting has been the ‘fresh’ nature of bedrock scarps /Lukashov, 1995; Mörner, 2003/. Without accompanying evidence, such as offset of late and postglacial deposits and landforms, such claims must also be called into question. A number of mechanisms, including glacial plucking and endglacial freeze-thaw action can also produce scarps that appear to be ‘fresh’.

A3-5 Investigative techniques

Postglacial faulting has been investigated using numerous techniques, from basic geologic and geomorphic mapping to advanced geophysical techniques. In the following section various investigative techniques that have been used, with varying degrees of success, to investigate postglacial faulting are briefly described. Each technique is evaluated in terms of its usefulness in identifying and understanding postglacial faults and their environment. The pros and cons of each technique are also discussed. In addition, suitable techniques used in investigating active faults elsewhere in the World are also discussed if considered useful for the study of postglacial faulting. This discussion is not intended to be exhaustive, but is used to illustrate how no one technique is sufficient for fault investigations.

A3-5.1 Remote sensing

Remote sensing incorporates all airborne and satellite-based spectral imaging techniques, including stereoscopic aerial photography and satellite imaging.

A3-5.1.1 Satellite Imagery

Satellite imaging includes a broad range of imaging techniques utilizing various wavelengths of electromagnetic radiation. Using limited or multiple spectral ranges to enhance various land surface features, satellite imaging has been used extensively to map large scale geologic and geomorphic features. In addition, more recent developments including radar imaging have been used to identify large-scale crustal structures. /Ringrose, 1987/ made extensive use of Thematic Mapper satellite imagery for investigating recent faulting in Scotland.

Although not used specifically for the investigation of postglacial faulting, high-resolution SPOT imagery has proved especially useful for investigating faults in active tectonic regimes /e.g. Bellier and Sebrier, 1994/.

Synthetic Aperture Radar Interferrometry (InSAR) has recently proven to be an extremely useful technique for investigating contemporary fault movement /Baer et al. 1999/ and land level changes /Amelung et al. 1999/. Although most useful for post earthquake analysis of land surface changes, InSAR campaigns could prove fruitful in exposing some of the local heterogeneities in postglacial rebound that cannot be resolved using conventional land based survey and space geodetic techniques.

A3-5.1.2 Aerial photography

To date the most successful techniques in searching for postglacial faulting has been the analysis of stereoscopic aerial photographs. Much of the shield regions of Fennoscandia and North America are comparatively remote. Region wide mapping using aerial photographs allows rapid analysis of large swaths of terrain. Using such an approach to aerial photographic analysis allows textural anomalies, such as fault displacements, landslides, and potentially areas that have undergone liquefaction to be easily identified. Even if it is not a truly diagnostic technique with which to determine the age and origin of tectonic features, aerial photographic analysis allows the rapid identification of 'target sites' for future field reconnaissance. Aerial photography is one of the techniques currently used in SKB's site investigation programme /Lagerbäck and Sundh, 2003; SKB, 2004a/.

A3-5.1.3 Digital terrain data

The examination of landforms for evidence for neotectonic deformation has been greatly aided by the use of digital elevation data. Using 3-D visualisation software can be used to enhance landform irregularities by topographic exaggeration and altering illumination angles and direction. Such digital manipulation can assist in the identification of subtle fault scarps /Henkel, 1987; Dehls et al. 2000/ or the identification of uplifted and dissected surfaces /Ringrose and Migon, 1997/. /Dehls et al. 2000/ used detailed digital terrain modeling to investigate the possible geometry of the Nordmannvikdalen fault in northern Norway. /Ringrose and Migon, 1997/ investigated the deformation of planation surfaces in Scotland using regional scale DEM data. Similarly, Tirén et al. /Tirén et al. 1987; Tirén and Beckholmen, 1988/ demonstrated vertical block movements in the Simpevarp area using the sub-cambrian peneplane as marker.

Digital elevation data allows rapid analysis of geomorphic surface, particularly at a regional scale. Using observational scaling, large-scale deformation, such as tilting of peneplain surfaces, and more localised fault displacement can be quantified.

A3-5.2 Mapping

Detailed field mapping has been the most useful technique for the investigation of postglacial faulting. As with any neotectonic investigations regardless of the tectonic setting, without a detailed understanding of regional and local stratigraphy and geomorphic development, it is impossible to make determinations of the age of faults or other deformation features. Detailed geomorphic mapping in northern Sweden has helped determine the age of faulting and shown the synchroneity between faulting and other seismically-triggered deformation /Lagerbäck, 1992/. Much of the dubiety over claims for postglacial faulting in Scotland are the result of a poor understanding of late- and post-glacial stratigraphy /Stewart et al. 2000/.

Additionally, any indication of post-glacial faulting using other techniques should be followed up by a detailed mapping of the suspected structures. For instance, during the Forsmark site investigation, suspected postglacial faults were after exhumation (Figure A3-10) and detailed mapping shown to be the result of surficial glacial processes /SKB, 2004a/, presumably hydraulic jacking.

Figure A3-10. *Detailed investigation of a locality with offset glacial striae a potential expression of postglacial faulting. Underlying subhorisontal, sediment dykes assumed to be created by hydraulic jacking, enabled rotation/tilting of blocks on a wide range of scales. The effect is locally enhanced by repeated freeze-thaw effects.*

A3-5.3 Geophysics

Postglacial faults and related deformation features have been investigated by a number of geophysical techniques. Most of these techniques cannot provide a definitive answer with regards to the timing and origins of the faults, however, they nonetheless provide important information concerning subsurface fault geometry.

A3-5.3.1 Aeromagnetics

Aeromagnetics, along with most other airborne geophysical techniques has been used to provide regional images of bedrock structure /Henkel and Wållberg, 1987/. Nisca /Nisca, 1987; Nisca and Triumf, 1989/ used aeromagnetics as part of a suite of geophysical techniques in the Simpevarp area of southeast Sweden. Similar investigations in Finland /Kuivamäki et al. 1998/, and Canada /Seeber and Armbruster, 1993/ have been used to interpret bedrock structure. As with most regional geophysical techniques, aeromagnetics does not have the ability to discern between ancient and potentially active structures. Unfortunately, this has not prevented some researchers using geophysically-defined lineaments to infer the presence of active tectonic structures /e.g. Mohajer et al. 1992/.

A3-5.3.2 Gravity

Airborne and land-based gravity measurements have been used extensively to measure and delineate regions of postglacial rebound. Asthenospheric movement of materials creates gravity anomalies. This technique cannot, however be used as a general tool to search for PGFs.

A3-5.3.3 Seismic reflection

Seismic reflection is probably the most commonly used subsurface investigative technique. It has been used to investigate both structure and stratigraphy at various scales. State-of-the-art techniques, including 3- and 4-D surveys allow extremely detailed images of the subsurface. However, these techniques are limited by the wavelength of the structure. Identification of faults requires high-frequency seismics which restricts depth penetration. Thus, parts of the fault in the middle and lower crust cannot be resolved unless large offsets have occurred in geologic history. However, the technique can be important for sounding fault traces in the upper crust.

A3-5.3.4 GPR

Ground Probing Radar (GPR) is a relatively new technique for investigating faults. Although GPR has been used with success in some studies /Smith and Jol, 1995/, the technique is hampered by reduced penetration, poor signal quality and a lack of acoustic contrast in clay-rich and waterlogged soils. However, investigations of the Stuoragurra fault in Finnmark, northern Norway by /Olesen et al. 1992a/ have successfully used GPR to image the fault plane down to depths of approximately 20 m. Although GPR can be used successfully to investigate known faults, it does not provide a means to discriminate between faults and other non-tectonic structures /Dehls et al. 2000/. The method can however not be used for analysing structures deeper than about a kilometre.

Where shallow ground conditions permit, GPR has the potential to provide useful information on the shallow structure of faults. If used in conjunction with shallow drilling (see below), it may be used in place of extensive fault trenching in order to reveal the recent history of fault activity. GPR is one of the techniques currently used in SKB's site investigations /Nissen, 2003/.

A3-5.3.5 Sonar profiling

In many formerly glaciated intraplate environments, there is a paucity of recent deposits. The absence of recent deposits means that there is very little opportunity for paleoseismic activity to be recorded. Because of the paucity of active faults in eastern Canada, researchers have concentrated on investigating the sedimentary evidence for paleoseismicity. Sonar profiling of lakes has revealed a number of lake-bottom features that are interpreted as being the result of seismic shaking /Shilts, 1984; Doig, 1986, 1990, 1991, 1998; Shilts and Clague, 1992; Shilts et al. 1992, 1993/. Using such high-frequency seismic reflection techniques, researchers can identify relatively small disturbances in the surface and shallow subsurface of lake-bottom sediments. This technique is limited by the depth of penetration of the sonar signal.

A3-5.3.6 GPS

Global Positioning System (GPS) is a very efficient tool for measuring ongoing deformation within a plate such as an active tectonic region or the current postglacial uplift of Fennoscandia /Milne et al. 2004; Johansson et al. 2002/. An analysis of the accuracy of GPS measurements can be found in /Scherneck et al. 1996/ and /Scherneck et al. 2002/ where it is argued that for small motions, a few mm/year, around ten years of data acquisition is needed due to different error sources e.g. climatological variations, instrument drift etc. It should be noted, additionally, that faults can be locked during considerable time periods during which the surrounding rock deforms elastically. Therefore, under unfavourable conditions, GPS campaign must be run for very long periods in order to positively demonstrate motions along a fault.

A3-5.4 Drilling

Drilling investigations have been almost exclusively carried out in Scandinavia. Drilling investigations on the Stuoragurra fault /Olesen et al. 1992a, 1992b/ and the Lansjärv fault /Bäckblom and Stanfors, 1989/ aimed to reveal the shallow subsurface geometry of the fault planes and the mechanical and chemical composition of the fault zones themselves. The dip of the Lansjärv fault is, however, still poorly constrained despite efforts. A recent drilling investigation was carried out to test competing tectonic and glacigenic origins for the Rouge River faults near Toronto, eastern Canada (J.Adams, Geological Survey of Canada, personal communication, 2000). Claims /Mörner et al. 2000; Mörner, 2003/ that postglacial faulting at Boda, Sweden, had shattered the bedrock to several hundred meters of depth, was counter proven by a geophysics campaign and subsequent drilling using borehole TV /Carlsten and Stråhle, 2000; Wänstedt, 2000/.

Drilling is a useful tool for investigating the characteristics of the shallow parts of a fault zone. With good recovery (never guaranteed within the broken materials of a fault or shear zone), drilling has the potential to provide information on the geometric characteristics of the fault zone (dip, width, degree of shearing) and potentially on the stratigraphic offsets across the fault. Drilling is best used when the fault is well located and the approximate subsurface geometry has already been investigated using GPR, seismic reflection, or some other shallow geophysical technique.

The problem with drilling within or close to a fault zone is recovery of material. Shearing and brecciation adjacent to the fault plane makes core recovery difficult. Without supporting shallow geophysical data, it can also be difficult to correlate stratigraphy in what is often a very heterogeneous environment. As a technique on its own, it is unlikely that drilling operations will ever be able to provide unequivocal answers to the timing or origin of faulting. However, when used as part of a multidisciplinary investigation, drilling can impart a wealth of pertinent information.

A3-5.5 Trenching

Fault trenching is by far the most commonly-used technique employed in contemporary active fault investigations /McCalpin, 1996/. Investigation of the recent stratigraphic offsets across a fault gives us information on the timing of movement, the style of faulting. To date, fault trenching has been utilized on a limited basis in postglacial faulting investigations. A combination of the level of investigation (often preliminary or reconnaissance level) and/or the relative inaccessibility of the faults play a part in the lack of paleoseismic trenching.

The Lansjärv fault /Lagerbäck, 1988/, the Stuoragurra fault /Dehls et al. 2000/ and the Båsmoen fault /Olesen et al. 2000/ have all been subject to detailed paleoseismic trenching investigation. Limited fault trenching has been carried out across the Kinloch Hourn fault /Ringrose, 1987/, Scardroy (Loch Maree), Glen Gloy, and Beinn Tharsuinn faults in western Scotland /Fenton, 1991b/, and a small postglacial fault near Cobalt, Ontario, eastern Canada (Fenton, unpublished field notes).

The trenching investigations on postglacial faulting in northern Norway and northern Sweden have been successful in providing information on the local dip of the fault and the timing of faulting /Bäckblom and Stanfors, 1989/. The fault trenching investigations in Scotland were used to obtain materials for age-dating, primarily fault gouge, or peat deposits into which fault gouge had been injected /Ringrose, 1989a; Grün and Fenton, 1990/.

Fault trenching remains the most reliable method by which to obtain accurate and meaningful age-dates for fault movement. Without well a documented fault zone stratigraphy, age-dating of fault movement can be almost meaningless.

Figure A3-11. *A trench, machine-cut during the Forsmark site investigations, Sweden, is studied for seismically induced liquefaction. The trench is c 80 m long, located on the eastern flank of the Börstilåsen Esker site investigations.*

A3-5.6 Age-dating

The presumed late Quaternary age for a number of postglacial faults is based mainly on the fresh appearance of the fault scarps in areas of glacially-smoothed terrain /Lagerbäck, 1992/. It is assumed that such delicate morphotectonic features would not have survived the erosive effects of continental glaciation. Additionally, these faults often displace late-glacial geomorphic features including eskers and meltwater channels. However, investigations in northern Sweden have shown that many glacial landforms are a product of an Early Weichselian glaciation and were mostly unaffected by later glacial cycles /Lagerbäck, 1988/. The fact that geomorphic features from previous glacial cycles can survive subsequent glacial periods must be a caveat when using landforms to date the age of fault movement. Thus, more conclusive evidence than merely geomorphic offsets may be desirable in regions where late-glacial geomorphic features cannot be unequivocally attributed to the most recent glacial cycle. However, ^{14}C has been used to determine age of landslides triggered by earthquake motion as well as earthquake that occurred at time between recession of ice and uplift of land below highest coastline /Lagerbäck, 1990/.

The dating of the Lansjärv fault showing washed sediments from the short time the fault was under water, before it was raised due to uplift, gives a fairly good indication of the age of faulting, about 8,500 y BP.

Although a number of age-dating techniques have been used in postglacial fault studies /Fenton, 1991b/, to date the most widely used method is radiocarbon (^{14}C and AMS). Where carbonaceous deposits (peat, gjitia, wood or charcoal fragments) are present, radiocarbon age-dating can be accomplished. Secondary age-dating techniques including thermoluminescence (TL), electron spin resonance (ESR), and optically-stimulated light (OSL) have been used to a much lesser degree. Most age-dating utilized in fault studies is indirect, that is; the age-dating is carried out to date strata offset by the fault. Direct techniques, including ESR and fault gouge quartz grain morphology are used to a much lesser extent /Grün and Fenton, 1990; Fenton, 1991b/. These methods attempt to date the materials created by the fault process, namely fault gouge. To date, these techniques have met with little success. The confining pressures in surface and near surface localities are insufficient to overprint the age-dates from previous reactivation episodes /Grün, 1992/.

The problems of age dating postglacial fault movements are similar to those faced by fault investigations in other environments. For the pros and cons of various age-dating techniques in relation to determining the timing of faulting, the reader is referred to the compilations by /Noller et al. 2000/, /Sowers et al. 1998/ and /Tullborg et al. 2001/. These publications provide great detail on the application and limitation of various age dating methods and their application in paleoseismic investigations.

A3-5.7 Surveying and geodetics

Recent land level changes have been measured in formerly glaciated environments by geodetic surveys including repeated levelling surveys, tide gauge observations, and satellite geodesy.

Earlier evidence for vertical movement is based primarily on tide gauge records and strand line age-dating. The precision of tide gauge records is approximately 1 mm/yr using records of 50 years or more /Scherneck et al. 1996/. Long records are required to remove the effects of air pressure, wind, water/air temperature, and salinity, all of which can affect the tide gauge readings. Often, there is a lack of tide gauges that have long enough records to remove the effects of atmospheric and climatic factors. In addition, the spatial distribution of suitable sites is often not uniform.

Land-based precision levelling can also be used to determine uplift patterns. Successive campaigns of re-levelling can determine short-term uplift rates. Sweden, Norway, and Finland have each carried out three re-levelling campaigns /Scherneck et al. 1996/.

These terrestrial techniques measure land levels with respect to a reference datum, most commonly sea level, or its geodetic derivative, the geoid. As sea level varies with time, these measurements determine apparent land uplift or land emergence.

In contrast, satellite-based surveying techniques (e.g. GPS) are capable of determining absolute elevations without such references. They also have the advantage of allowing either continuous (monument) or rapid repeated (campaign) surveys of land level that would otherwise be both expensive and time consuming using conventional terrestrial survey techniques. Space-based survey techniques such as GPS also have the advantage of being able to detect very small horizontal displacement.

The SWEPOS GPS network has recently been used by the BIFROST research group to determine both vertical uplift and horizontal deformation in Fennoscandia /Milne et al. 2004; Johansson et al. 2002/. A rather precise uplift pattern has now emerged with the maximum movements being of the order of 11–12 mm/year around Umeå (Figure A3-4).

A3-5.7.1 Finland

In Finland, in addition to the precise levelling network of the Geodetic Institute (FGI) there are additional, more dense levelling networks established by the National Land Survey (NLSF). These additional networks cover the areas within the precise leveling loops. Along with other levelling loops from the Central Board of Public Roads and Waterways and the Hydrographic Bureau, this amounts to a comprehensive network of observation points.

The FGI has carried out two precise levellings, in 1892–1910 and 1935–1955/1953–1975 /Chen, 1992; Johansson et al. 1993; Chen and Kakkuri, 1994; Poutanen and Ollikainen, 1995/. These data has been used to search for postglacial faults; where changes in land uplift differences exceeded three times the standard deviation, the differences were classified as exceptional. Additional measurements were carried out at these sites and 13 were identified for further investigation.

In the 1970s the NLSF remeasured its levelling network to ascertain the location and magnitude of contemporary irregularities in the uplift rate. The investigation did not show that the rebound had been elastic and uniform. Bedrock movements seemed to concentrate on certain fracture zones /Paananen, 1987; Vuorela et al. 1987/. A series of new levelling profiles were constructed to cross these zones. A number of these profiles have been measured repeatedly. Of 53 profiles, 27 underwent significant local elevation and 7 showed significant deviation from the predicted elastic uplift model.

Horizontal movements have been measured by Kakkuri and Chen /Kakkuri and Chen, 1992; Chen and Kakkuri, 1993/ using a first order triangulation network that cover the entire country. Over the country as a whole, NW-SE compression is clearly visible. In central Lapland the NW-SE compression is accompanied by significant extension in a NE-SW direction. Kakkuri and Chen /Kakkuri and Chen, 1992; Chen and Kakkuri, 1993/ also demonstrated significant movement between certain tectonic blocks. Significant correlation was found between areas of dilation and areas of anomalously low land uplift.

FGI established a permanent GPS network in 1993–1995. Measurements at the Nuottavaara fault zone, located near the Pasmajärvi postglacial fault, have not detected any movement on this old fault /Poutanen and Ollikainen, 1995/. Similarly, GPS measurements across the Pasmajärvi postglacial fault have not detected any contemporary movement /Paananen, 1987; Vuorela et al. 1987/.

A3-5.7.2 Sweden

/Ekman, 1996/ produced a map of recent postglacial rebound for Fennoscandia using sea-level records, lake-level records, and repeated high-precision land levellings to show a present-day uplift dome centred over the Gulf of Bothnia, with a maximum uplift rate of 9 ± 0.2 mm/yr. The uplift dome is elongate in a NNE-SSW direction, with the 0 mm/yr contour essentially encompassing the Fennoscandian landmass. The pattern of present day uplift is similar to that revealed by uplifted shorelines of the Litornia Sea. The ratio between past (since 7,000 BP) and present (1892 to 1991) uplift rate increases towards the uplift centre and the uplift centre appears to have migrated approximately 300 km towards the NNE.

The recent SWEPOS GPS network /Scherneck et al. 1996, 2002; Johansson et al. 2002/ has after ten years of operation given a high quality picture of the present rebound. The BIFROST research group has used these data to deliver a high quality uplift model including both horizontal and vertical motions, which was not possible with previous techniques /Milne et al. 2004; Johansson et al. 2002/.

A3-6 Criteria for recognition of postglacial faults

Potential methods for differentiating between postglacial faults, tectonic faults and other landforms/structures can be divided into geological, geomorphic, structural, and associated criteria. /Mohr, 1986/ first proposed a list of criteria to differentiate postglacial fault scarps from glacially-plucked features in western Ireland. These criteria were modified and added to by Fenton /Fenton, 1994a,b,c, 1999; Fenton and Olig, 1994/ using additional data from Scotland, Sweden, and Canada. These criteria are:

1. Faults should have demonstrable movement since the disappearance of the last ice sheet within the area of concern.
2. The fault should offset glacial and late-glacial deposits, glacial surfaces or other glacial geomorphic features. Preferably, it should be demonstrated that the fault displaces immediately postglacial stratigraphy and/or geomorphic features, though it need not cut younger features.
3. Fault scarp faces and rupture planes expressed in bedrock should show no signs of glacial modification, such as striations or ice-plucking. Limited glacial modification, however, may be present on scarps that are late-glacial or inter-glacial in age.
4. Surface ruptures must be continuous over a distance of at least 1 km, with consistent slip and a displacement/length ration (D/L) of less than 0.001.
5. Scarps in superficial material must be shown to be the result of faulting and not due to the effects of differential compaction, collapse due to ice melt, or deposition over pre-existing scarps.
6. Care must be taken with bedrock scarps controlled by banding, bedding, or schistosity to show that they are not the result of differential erosion, ice plucking, or meltwater erosion.
7. In areas of moderate to high relief, the possibility of scarps being the result of having been created by deep-seated slumping driven by gravitational instability must be disproved.

With the exception of the fourth criterion, /Fenton, 1994c/ applied these criteria in ranking claims for postglacial faulting in eastern North America. The criterion of a rupture length of greater than 1 km was given less weight in discerning postglacial faulting origins in eastern Canada and the north-eastern U.S. This criterion was originally proposed for the

study of faulting in Scotland and Fennoscandia, where postglacial faults are found almost exclusively in crystalline basement rock. The mechanical behaviour of slates and phyllites, within which many smaller postglacial faults are found in eastern North America, may not promote the formation of a large, through-going rupture. Indeed, some sites with multiple small displacements at the surface may be represented by a single, larger fault at some depth. On the other hand, such small displacements may be the manifestation of the pervasive release of shallow rebound stresses.

/Muir Wood, 1993/ put forward a list of "neotectonic diagnostics" to grade claims for neotectonic activity (not merely postglacial fault activity) in formerly glaciated regions. These criteria were:

1. The surface or material that appears to be offset has to have originally formed as a continuous, unbroken unit. Can the surface be dated? Is it the same age?
2. Can the apparent evidence of an offset be shown to be related directly to a fault?
3. Is the ratio of displacement to overall length of the feature less that 1/1,000? For most faults this ratio, a function of the strength of the rock prior to fault rupture, is between 1/10,000 and 1/100,000 /Scholz, 1990/.
4. Is the displacement reasonably consistent along the length of the feature?
5. Can the movement be shown to be synchronous along its entire length?

Similar criteria have been adopted by the Norwegian Geological Survey (O. Olesen, Norwegian Geological Survey, *written communication*, 1996). From the author's experience in eastern Canada, the criteria of /Muir Wood, 1993/ proved particularly useful for differentiating between glaciotectonic deformation and postglacial faulting.

As stated previously, the main aim of this appendix is to present criteria for recognizing postglacial faulting. If we look at the physical characteristics of postglacial faulting, tectonic faulting and glaciotectonic deformation, we see that no single criterion is unique to any type of faulting (Table A3-2).

Table A3-2. Fault scarp characteristics.

	Postglacial Faults	(Reverse) Tectonic Faults	Glaciotectonic Deformation
Length	10 m to 100's km	> 10 km	m to km (< 3 km)
Continuity	Generally Continuous	Continuous to Discontinuous	Discontinuous
No. Scarps	Single	Single to Multiple	Generally Multiple
Sense/Style	Predominantly Reverse	All	Reverse (and normal)
Plan	Linear, Angular	Linear, Arcuate	Irregular
Scarp Height	mm to 10s m	Up to km	Up to several m
Displacement History	Single Event	Repeated	Continuous
Secondary Deformation	Minor Faulting	Faulting and Folding	Faulting and Folding
Relationship to Ice Cover	Within Area of Former Ice Cover	No Relation	Margins of Former Ice Cover
Timing	Postglacial	No Constraint	Syn-glacial

Faults can be described in terms of their geologic (stratigraphic), geomorphic, and structural expression. In addition, their spatial association with secondary, or off-fault, deformation, such as liquefaction and land sliding, can provide clues as to whether the deformation is seismogenic. The usefulness of these characteristics in providing criteria with which to determine the origin of faulting will be discussed in the following sections.

A3-6.1 Geologic and stratigraphic criteria

By definition postglacial faults occur in recently deglaciated regions. The areas that had significant late Quaternary ice cover are predominantly intraplate/craton, passive margin, and failed rift environments. Although postglacial faults do not appear to be constrained by rock type, they are controlled by pre-existing structure, nearly always following existing faults, shear zones, or fractures. Determining a postglacial faulting genesis for a fault structure has more than just academic interest. Since postglacial faulting appears to occur almost exclusively in the immediate postglacial period, while the transient glacial unloading stresses are sufficient to trigger faulting, it is important to differentiate between 'one-off' postglacial faults and tectonic faults with long recurrence intervals in order to evaluate seismic hazards.

In order to assess whether postglacial faulting is seismogenic or not, we have to assess whether movement has been episodic or continuous. Stratigraphic evidence for slow, continuous deformation will preclude seismogenic surface-rupturing, even if continuous movement is the result of tectonic creep. Episodic movement could also be the result of non-seismic processes. The following criteria are intended to address the questions of episodicity of displacement and seismogenic versus non-seismic processes.

A3-6.1.1 Evidence for continuous deformation vs episodic deformation

In order to assess whether scarps in formerly glaciated environments are tectonic or non-tectonic, we have to discern whether they are the result of continuous deformation or by discrete and/or episodic events. Structural or stratigraphic evidence for continuous deformation would indicate that the scarp would not have formed co-seismically. However, 'event scarps' could also have been produced by non-tectonic, hence non-seismic, mechanisms. The following criteria are discussed in an attempt to differentiate between postglacial faults and glaciotectonic or other non-tectonic processes.

To date, there have been very few trench excavations across postglacial faults. The most notable exception is the Lansjärv fault in northern Sweden /Lagerbäck, 1988/. Each trench exposure indicates that there has been only one faulting event during the postglacial period. Like tectonic faults, the fault movement history is determined by stratigraphic offsets, upward terminations of fault strands, and colluvial wedge stratigraphy. It is clearly observed that each trench exposure contains only one colluvial wedge and that the trench stratigraphy shows uniform offset, regardless of age. Were these scarps to have formed by a continuous process, whether it be tectonic creep or some non-tectonic mechanism, we would observe continuous onlap within the trench stratigraphy, with increasing offset with age within the faulted units. Thus, for the few Fennoscandian faults, and one example each from Scotland and eastern Canada, it appears that the development of colluvial wedge stratigraphy indicates that these scarps were produced by discrete, one-off events. Glaciotectonic features, in contrast, are the result of continuous deformation and, although they may result from pulses or surges of glacial movement, they do not produce the stratigraphic and structural relationships that are indicative of sudden co-seismic offsets.

The deformation observed in trenches across postglacial faulting is entirely steeply dipping, reverse faulting. Glaciotectonic faulting, on the other hand, is much more variable, showing a wide range of dips from near vertical to subhorisontal, often along the one fault plane. Many examples of glaciotectonism show shallow decollement, often at stratigraphic contacts (e.g. till-bedrock contact). In addition, glaciotectonism often displays both compressional and extensional deformation within the same outcrop /Adams et al. 1993a/. Compressional glaciotectonic deformation often involves the formation of folds. Folding has not been reported to be associated with reverse postglacial faulting, even where expressed in unconsolidated sediment.

Thus, stratigraphic relationships that show discrete, one-off displacements can be used to distinguish postglacial faulting from glaciotectonic deformation. Folding and combined extensional and compressive deformation on the other hand are more typical of glaciotectonic deformation.

A3-6.1.2 Timing of faulting

By definition, postglacial glacio-isostatic faulting occurs following the disappearance of ice cover within the region of concern. Glaciotectonic deformation, however, can only occur while ice is present and actively advancing or retreating. Establishing the timing of faulting, therefore, should prove useful in distinguishing between postglacial and glaciotectonic faulting /Lagerbäck, 1992/.

A3-6.2 Geomorphic criteria

Tectonic faulting and glaciotectonic deformation can both produce geomorphic scarps. In areas of high relief, gravitational slope movements can also produces scarps that can be mistaken for tectonic faulting. Glacial action, in particular plucking at the base of the ice-sheet/glacier along pre-existing faults, fractures, or bedding/schistosity planes, can result in bedrock steps that may be misidentified as fault scarps. The following criteria are an attempt to differentiate between these differing scarp-forming mechanisms.

A3-6.2.1 General geomorphology

If we ignore the small displacements of glaciated pavements by movement along steeply-dipping cleavage planes in slaty horizons in north-eastern North America, postglacial faults are generally a kilometre or more in length, with a roughly continuous surface trace. Postglacial faults expressed entirely in bedrock show displacement of glacial geomorphic features such as flutes and striations /see description of Mather, 1843/. By definition, postglacial faults scarps should show no evidence of glacial modification such as moulding or plucking of the scarp face. Although a number of postglacial fault scarps may have suffered periglacial degradation, such as freeze-thaw frost heave (e.g. the Lainio fault scarp in northern Sweden), they show no evidence for glacial modification.

By their morphology alone, the large postglacial faults of northern Sweden can be clearly identified as the surface rupture of major faults /Muir Wood, 1993/. Postglacial fault ruptures resemble tectonic surface faults, in particular in their along strike continuity and consistency of sense and amount of throw. Many postglacial faults that are expressed in bedrock rather than unconsolidated materials display “elementary textbook” thrust fault geometry, having very dramatic, steeply-dipping planar fault planes, with little or no modification of the fault scarp. Postglacial fault zones appear to relatively simple, often comprising a single fault plane, with no other evidence of surface deformation. Overall the fault trace is often planar, with only minor local geometric complexities. These local geometric complexities often arise from postglacial faulting utilizing pre-existing fault and fracture sets.

In contrast, glaciotectonic deformation is often localized and irregular, representing the position of the ice front during periods of glacial advance. There is no along strike continuity in either orientation, sense of displacement or amount of offset.

In areas of high relief, such as the West Highlands of Scotland and Norway, several large landslide scarps have been misidentified as fault scarps /Fenton, 1991c; Muir Wood, 1993/.

Differentiating between landslide scarps and faults scarps in areas of high relief is a global problem not merely confined to recently deglaciated regions /McCalpin, 1999/. Slope failure scarps often parallel slope contours and show considerable along-strike differences in both amount and sense of throw. Slope failures often create multiple subparallel scarps, whereas postglacial faults are generally simple, single scarps.

Postglacial faults have much simpler morphologies than either glaciotectonic and slope failure scarps. They have consistent throw and sense of throw (reverse) along strike. In addition, their geomorphic expression is continuous along strike. They displace glacial deposits and glacial bedrock geomorphology, and they are not controlled by either slope morphology or the position of the former ice front.

A3-6.2.2 Scarp aspect ratio

When we compare the surface traces of postglacial faults with recent continental reverse faults, the larger Fennoscandian postglacial faults have scarp height to rupture length ratios similar to those of tectonic faults. Shorter faults, however, have much larger scarp heights (displacements) than tectonic faults of comparable length, i.e. “short, fat faults”. This may result from incomplete mapping of the surface fault trace, the mechanism of fault rupture differs from ‘normal’ tectonic faults, possible involving deep crustal rupture in thick, cold cratonic crust, or that the relatively strong crust in these regions requires higher levels of angular strain before the rupture threshold is exceeded. Regardless, for the majority of postglacial faults, it appears that they have higher displacement to length ratios than similarly sized tectonic faults.

By comparison to reverse faults from stable intraplate/craton environments, postglacial faults are up to four times longer. In this context, earthquakes on postglacial faults have characteristics similar to reverse faulting on subduction zones. The only other large intraplate earthquake of similar size, the New Madrid earthquakes of 1811–1812, occurred on a fault of comparable length to the Pärvie fault, but the net displacement is obscured by large sedimentary cover /Johnston, 1989b; 1996/.

A3-6.3 Structural criteria

Postglacial faults almost all have reverse offsets. In addition, all reported postglacial faults have reactivated pre-existing faults, fractures, or shear zones /e.g. Eliasson et al. 1991/. The morphology of postglacial faults is very similar to that of tectonic reverse faults. There are a number of structural characteristics that can be used to differentiate between postglacial faults, non-tectonic deformation, and shallow stress-relief features. The latter, which include pop-ups and offset boreholes, have often been misinterpreted as postglacial or tectonic faults /Fenton, 1994a/).

A3-6.3.1 Dip of fault plane and depth of deformation

The style of glaciotectonic deformation differs significantly from that of postglacial faulting in that glaciotectonic deformation is a shallow phenomenon /Dredge and Grant, 1987/, which although it may involve bedrock deformation, faults tends to shallow with depth, sometimes dying out in a shallow decollement /Adams et al. 1993a,b/. Postglacial faulting on the other hand, appears to steepen with depth /Muir Wood, 1993/ and, at least for larger faults, involves rupture of the entire brittle crust /Muir Wood, 1989a, 1993; Arvidsson, 1996/. Shallowing of the fault planes in the near surface may be a result of increased density of rebound fractures that are oriented subparallel to the ground surface and the relative ease

of movement along these fractures in the presence of postglacial crustal fluid overpressuring /Fenton, 1991c/, Although some larger postglacial faults show sections that have relatively low angle dips /Lagerbäck, 1988; Muir Wood, 1993/, overall, the fault planes dip at steep angles. Stress relief pop-ups /Wallach et al. 1993/, when observed in section, die out into shallow decollements /Wilson, 1902; Fenton, 1994c/.

A3-6.3.2 Orientation with respect to the contemporary tectonic stress Field

The majority of postglacial faults, being thrust faults, are oriented orthogonal to the direction of maximum horizontal compressive stress (Figure A3-12) whereas some smaller postglacial faults may not show any relationship to the tectonic stress field. Shallow stress relief features such as pop-ups are expected to show the same orientation /Adams, 1989a/. Glaciotectonic deformation, however, is expected to be oriented parallel to the former ice front, and therefore, is unlikely to show any consistent relationship to the ambient stress field. Though these statements seem generally valid elsewhere, in Northern Sweden (cf Figure A3-12 and Figure A3-4) the directions of maximum horizontal stress happens to, locally, be perpendicular to the direction of the ice front and also perpendicular to many postglacial faults. Furthermore the pattern of stress vectors can be rather heterogeneous, locally, and the orientation of PGFs with respect to contemporary tectonic stress must, unless demonstrated differently, be regarded as a rather weak indicator.

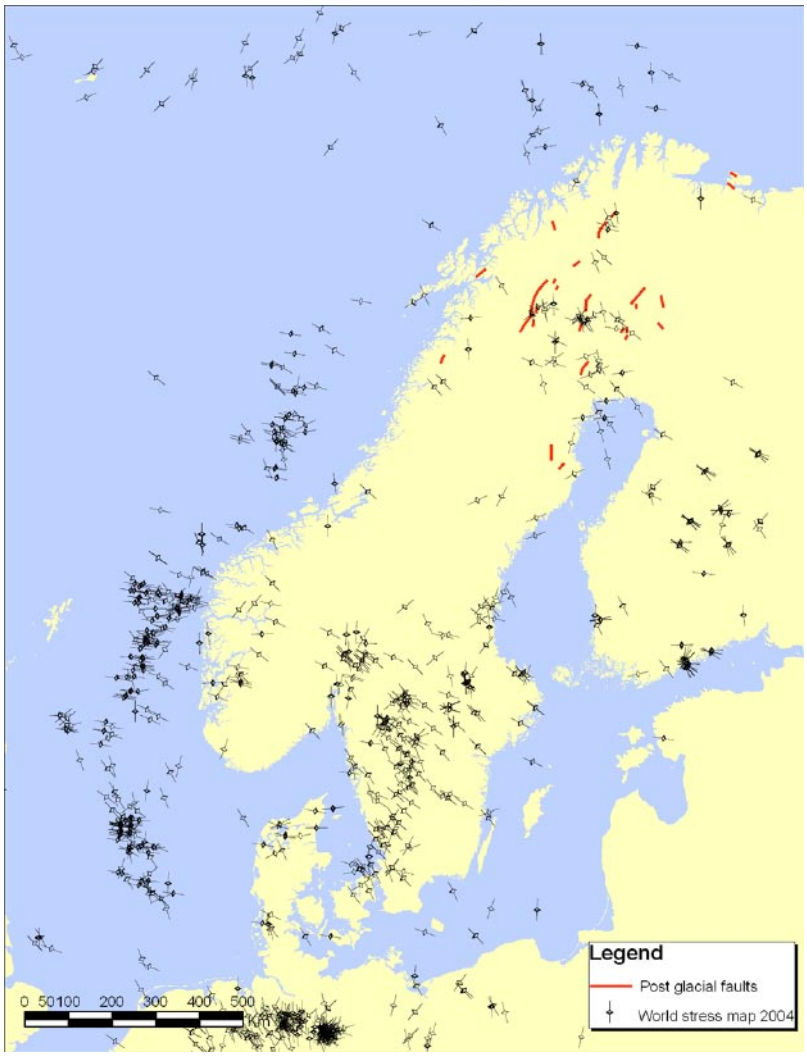

Figure A3-12. *Contemporary tectonic stress field /data from Reinecker et al. 2004/ in relation to known postglacial faults.*

A3-6.3.3 Association with contemporary seismicity

A spatial association with contemporary seismicity is a common criteria used to define active faults. Postglacial faults occur in seismically quiet regions. Despite a relatively low seismicity, several studies has indicated a spatial correlation between PGFs and microearthquakes /Arvidsson, 1996; Bungum and Lindholm, 1997/. Areas with recognized postglacial faults, however, are almost always in areas where there is insufficient seismograph coverage to accurately locate microseismic activity. Thus, without further data, it may appear that association with contemporary seismicity cannot be used as a criterion for recognizing postglacial faulting. However, the study of /Arvidsson, 1996/ shows that even this type of datasets can be used even though the accuracy prohibits finding the fault plane at depth.

The recently employed SKB sponsored seismic network in northern Sweden (Figure A3-13) will hopefully provide valuable information in this sense.

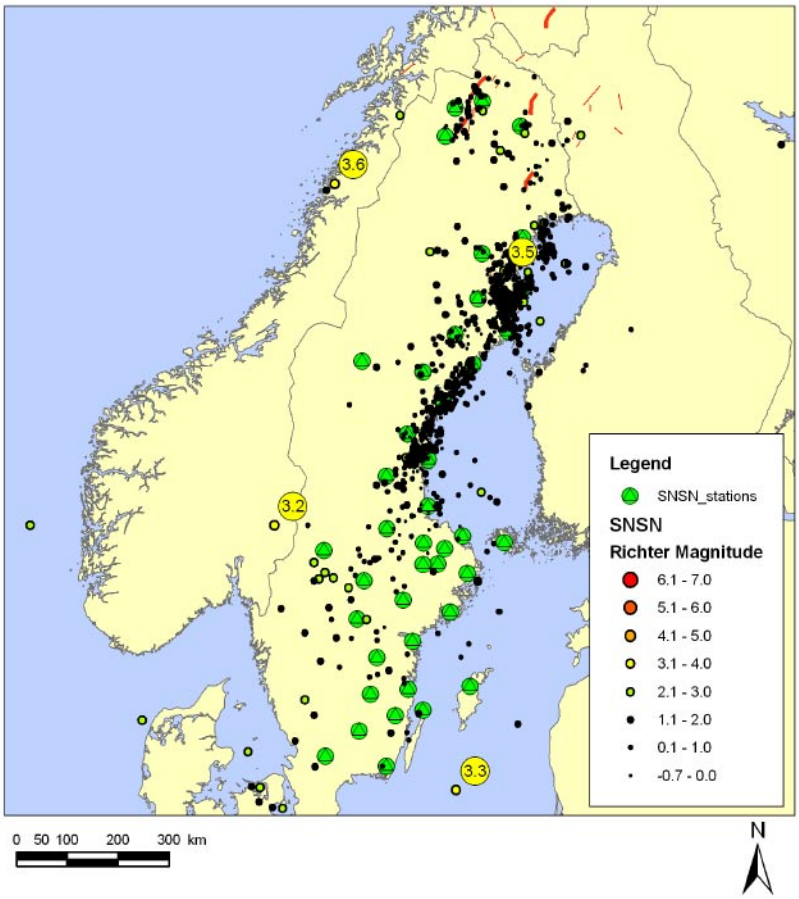

Figure A3-13. *Earthquake activity in Sweden recorded by the Swedish National Seismic Network /data from Bödvarsson, 2001, 2002a,b, 2003a,b,c, 2004a,b/ since 2001.*

A3-6.3.4 Spatial association with areas of high rates of glacio-isostatic uplift

By definition, postglacial faults occur in regions that have undergone recent deglaciation. It follows, therefore, that postglacial faults will be found in regions that have or are undergoing significant glacio-isostatic rebound. Evidence from uplifted shorelines /e.g. Gray, 1974a,b, 1978; Påsse, 1996, 2001; Morén and Påsse, 2001/, geodetic measurements /e.g. Saari, 1992; Milne et al. 2004; Johansson et al. 2002; Scherneck et al. 2002/, and gravity measurements, can all be used to identify areas of glacio-isostatic uplift.

It is obvious that the icesheet thickness is one of/or the paramaters that directly determine the scope and extent of the deformations and thus of the PGF faulting. Currently, the present ice-sheet model is under the work of being improved (Lambeck, Näslund, personal communication).

A3-6.3.5 Rupture complexity and secondary deformation

Postglacial faulting utilizes pre-existing faults, fractures, and shear zones, many of which could have been inactive for considerable periods of time /Eliasson et al. 1991/. Most postglacial faulting involves single fault planes, with relatively simple fault geometries. Larger faults like the Pärvie and Länsjarv, however, do display more complexities, at least on a local scale /Lagerbäck, 1988; Muir Wood, 1993/. These complexities are a function of the geometry of pre-existing faults and fractures. Thus, fault bends and changes in orientation tend to be angular in nature. These fault bends result in secondary accommodation features, most commonly in the hangingwall, namely subparallel normal faults above extensional bends, and thrust faults above compressional fault bends. Complexities in the rupture planes, since they are expressed in brittle bedrock are manifest as secondary faults. Movement of a relatively simple fault beneath an area with multiple fault/fracture sets can lead to chaotic looking rupture patterns /Fenton, 1991c/. Despite this localized heterogeneity, overall, the sense of displacement is consistent along the entire fault length.

Glaciotectonism conversely results in more heterogeneous deformation /Croot, 1988/. The main difference being the lack of consistency in the sense and amount of throw along strike. Even when involving bedrock, glaciotectonic deformation results in broader deformation zones comprising multiple fault planes, with both normal and reverse offsets. In the cases where glaciotectonic deformation shows large throws of say 1 m one might expect that the fracturing is very shallow, otherwise it must be associated with substantial fault movement stretching into deeper parts of the upper crust.

When postglacial faulting involves both bedrock and unconsolidated materials, the zone of deformation remains a discrete fault plane in both materials /e.g. Lagerbäck, 1988/. In glaciotectonic deformation, faults often do not propagate up from bedrock into overlying unconsolidated deposits as discrete planes. It is more common for this deformation to be expressed as folding within these deposits /Adams et al. 1993a/.

A3-6.3.6 Contemporaneous association with seismically-induced features

Many postglacial faults are confined to bedrock outcrops; therefore it is difficult to determine whether they have formed as a result of discrete movement episodes or are the result of creep. At smaller scales, e.g. the millimetre-scale offsets of glaciated pavements on slate outcrops in eastern North America, the mechanism of formation becomes a point for academic debate, since, by their size alone, these are clearly not potentially

seismogenic structures. However, at larger scales, and also if there are numerous small offsets, possibly representing a larger, through-going structure at depth, the size of the scarps and the continuity of these structures suggests that they may be seismogenic. In order to show that these structures are tectonic (seismogenic) in origin, we need to demonstrate contemporaneous association with off-fault seismogenic deformation. The most common seismically-induced deformations are liquefaction and landsliding. Unfortunately, landsliding and liquefaction are common products of climatic and groundwater conditions in the postglacial environment. Landsliding results from gravitational instabilities on oversteepened glaciated slopes and oversaturation of unconsolidated materials as a result of melting permafrost. Liquefaction occurs spontaneously in saturated glacio-fluvial outwash deposits and also occurs as a result of the expulsion of permafrost meltwater. In addition, freeze-thaw can produce involutions in unconsolidated sediments that resemble seismically-induced liquefaction features. It is therefore important to discount non-seismic mechanisms for triggering landsliding and liquefaction /Davenport and Ringrose, 1987/.

In order to show coseismal genesis for liquefaction and landsliding, the criteria of /Sims, 1975/ provides a useful guide, i.e. these deformation features must have a spatial and temporal association with the suspected seismic source. A spatial and temporal association between liquefaction, landsliding and faulting, however, will only show that the faulting is seismogenic, it will not allow us to differentiate between postglacial faulting and tectonic faulting *sensu stricto*. In formerly glaciated regions, however, the uncertainty is usually over whether the surface deformation observed is the result of (seismogenic) faulting or glacial or periglacial processes. Therefore, a spatial and temporal association with landsliding, liquefaction, or any other seismically-induced deformation, may be a useful criterion in identifying tectonic faults *sensu lato* in recently deglaciated regions /Ringrose, 1987, 1989a; Fenton, 1991c; Lagerbäck, 1991/.

A3-6.4 Summary of criteria

From the preceding discussions, it is clear that no single criterion enables unambiguous identification of postglacial faulting. Rather, several criteria can be used to distinguish between postglacial faulting and nontectonic deformation. Differentiating between postglacial faulting and tectonic faulting *sensu stricto* proves to be more difficult.

Initially, it must be demonstrated that the observed faulting occurs within the former ice limits of the region in question and that the observed scarp or stratigraphic offset post-dates the disappearance of ice cover. Displacement must be shown to have occurred as a discrete event(s) and be continuous in terms of both amount and sense of throw along the fault length. A spatial and temporal association with liquefaction and/or landsliding may indicate that postglacial faulting is seismogenic.

Required studies to differentiate between postglacial faulting and nontectonic deformation include:

- detailed geomorphic mapping,
- exploratory trenching (where possible) and accurate age-dating,
- detailed structural analysis and,
- mapping of contemporaneous deformation features.

A3-7 Seismotectonics

A3-7.1 Rebound and tectonic setting

Glacial rebound is the process by which the surface of the Earth recovers from the state of isostatic disequilibrium induced by loading by continental ice sheets (Figure A3-14). This was early recognised by /e.g. Daly, 1934, 1974/, who, in his classic book *Changing World of the Ice Age*, proposed two models for glacio-isostatic rebound. The first model postulated that recovery from the ice load is accommodated by the inward migration of material at great depths. His second hypothesis includes a zone of vertical faults that were reactivated during deglaciation.

Glacial rebound is commonly quantified from observations of uplifted and warped shorelines /e.g. Morén and Påsse, 2001/, and presently from high-resolution GPS observations in Fennoscandia /Milne et al. 2004/. Postglacial uplift curves are calculated from shoreline emergence profiles, based on age-dating beach terrace deposits, combined with eustatic sea level curves. The maximum recorded postglacial change in relative sea level is slightly above 300 m on the east side of Hudson Bay /Andrews, 1991/. In Fennoscandia the maximum raise of shore lines are of the order of 260 m /Lambeck et al. 1998/. Extensive areas in the southeast and northwest of the Laurentide ice sheet have recovered at least 200 m since deglaciation. In Greenland, delevelling is less, partly due to the presence of a smaller ice load and the continued existence of the Greenland ice cap throughout the Holocene. In Iceland, a much smaller ice cap caused substantial depression of the crust /Andrews, 1991/. This is primarily because of the substantially thinner lithosphere beneath the island compared to the other regions that are located in intraplate regions.

The rate of relative sea level change associated with ice unloading has been measured by ^{14}C dating of raised marine deposits. The resulting time/elevation plots indicate that initial rate of sea level change exceeded 100 $mmyr^{-1}$ /Andrews, 1991/. The rates drop exponentially with time, and the highest contemporary rates are estimated to be 10 to 20 $mmyr^{-1}$ in southwest Hudson Bay /Weber, 1975/. Tide gauge and geodetic levelling data indicate contemporary vertical motions.

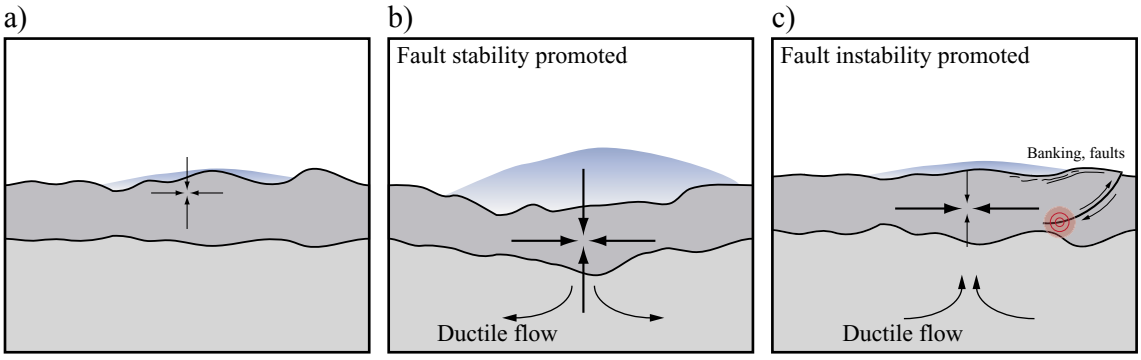

Figure A3-14. *Schematic cartoon illustrating how the stress field changes during the pre (a) syn (b) and c) post glacial times. During the growth of the glacier, horizontal tectonic stresses accumulate while differential compressibility promotes fault stability. Mantle material flows, relatively slowly, from beneath the glacier. When the glacier retreats, differential stresses promotes fault instability, in particular on gently dipping faults oriented perpendicular to σ_1. Mantle material flows back, and the crust is slowly regaining its state of equilibrium.*

Differential crustal uplift from ice loading causes former shorelines to be tilted towards the zones of maximum crustal rebound. The rate of tilting has decreased nonlinearly since deglaciation, but average tilts vary between 10 and 100 nanoradians yr^{-1} /Andrews, 1991/. The projection of the tilt of these former shorelines towards former ice centres has delimited several domes of postglacial uplift /Andrews, 1991/.

Our understanding of crustal deformation resulting from glacial rebound has largely been limited to vertical motions. However, observations of postglacial faulting do allow some understanding of the state of stress and amount of shortening involved in glacial rebound. Emerging space geodetic data are gradually increasing our knowledge of horizontal deformation in formerly glaciated regions. /James and Morgan, 1990/ showed that mm/yr horizontal rebound velocities are plausible in North America. Within the area of former glaciation and immediately peripheral to it, the vector of motion is directed towards the former centre of glaciation because of the return flow off sub-lithospheric mantle flow dragging the over-riding lithosphere. According to /James and Morgan, 1990/ the maximum rate of change of horizontal motions occurs in the region of the glacier edge. This is, however, in contrast to results from measurements by the SWEPOS GPS network. In papers by /Scherneck et al. 1996/, /Milne et al. 2001/ and /Johansson et al. 2002/ a precise uplift has been revealed, including horizontal motions, which are extensional and of the order of up to 1/3 of vertical motions, and largest at the centre of uplift /Milne et al. 2004; Johansson et al. 2002/.

A3-7.2 Stress and the strain field

The importance of postglacial rebound in the generation of the stress field in formerly glaciated regions has been debated for quite some time. Several researchers note that the stress measured in boreholes or inferred from earthquake focal mechanisms bears little resemblance to that expected from postglacial rebound /Müller et al. 1992/. Rather, the stress field in Fennoscandia, like that in Scotland, eastern Canada, and the northeastern United States appears to be consistent with that expected from north Atlantic plate motions /Adams, 1989b; Becker and Davenport, 2001/. In contrast to these results, /Clauss et al. 1989/ filtered data from the world stress map project to exclude observations of doubtful or poor quality and concluded that stresses in Fennoscandia are distributed in a much more scattered fashion than observed in continental Europe. /Clauss et al. 1989/ conclude that the heterogeneous stress field of Fennoscandia should be a consequence of several mechanisms, not only plate tectonics. Likewise, the dominant contributor to the strain field in formerly glaciated regions is also a subject of debate. The occurrence of postglacial faults, paleoseismic deformation features, and contemporary seismicity are all evidence of past and ongoing deformation within regions undergoing glacio-isostatic adjustment.

/James and Bent, 1994/ computed strain-rates of the order of 10^{-9} yr^{-1} within and for 300 to 400 km beyond the former region of glaciation using a simple Laurentide glacial loading model. For eastern Canada and the eastern United States, this is 1–3 orders of magnitude greater than the estimated average seismic strain-rate /Anderson, 1986/, and about an order of magnitude greater than the predicted erosional strain-rate. At distances of 500 km and greater the rebound strain-rate decreases to values similar to that from erosion. /James and Bent, 1994/ concluded that glacial rebound should be considered as a potential mechanism for triggering seismicity not just within the formerly glaciated region, but also for several hundred kilometres beyond. However, the average rate at which strain energy is released seismically in eastern North America within a few hundred kilometres of the former glacial limits is only 0.1 to 1.0% of the rate at which elastic strain energy in the lithosphere is changing due to post-glacial deformation /James and Bent, 1994/. This may be a result of the directions and magnitudes of glacial rebound strain-rates not being

oriented in such a way as to augment the observed deviatoric stress field. Given the large difference between glacial rebound strain-rates and the observed seismic strain-rates, this indicates that the lithosphere exhibit elastic deformation since non-seismic deformation would indicate plastic deformation. Up to date, current plastic deformation has not been observed in the old Archean rocks. The cyclic nature of glacial loading and the relatively short time over which glacial strains are applied may also be important, because if large strain-rates are present over long periods of time then the lithosphere would eventually be driven to failure.

A3-7.3 Rebound models and fault triggering

Past investigations assumed that the state of stress in formerly glaciated regions was due to glacial loading/unloading stresses alone /James and Bent, 1994/. However, /Quinlan, 1984/ cautioned that ambient tectonic stress was also important and should not be discounted. A fundamental question in the study of intraplate seismicity in formerly glaciated regions is the relative importance of tectonic and rebound stresses in earthquake generation.

There are geologic and geophysical evidence to support postglacial rebound as the dominant cause of such intraplate earthquakes. However, there is other evidence that favour tectonic stress as the dominant cause. The spatial distribution of recent earthquakes in eastern Canada and northern Europe shows little correlation with the centre of postglacial rebound. Seismicity in eastern Canada predominantly lies along failed rift arms /Adams and Basham, 1989/, while most of the larger ($M > 4$) earthquakes in northern Europe are distributed along coastal regions while the interior is relatively aseismic /Slunga et al. 1984; Wahlström, 1988; Bungum, 1989; Slunga, 1991; Wahlström, 1995; Byrkjeland et al. 2000/. Additionally, the orientation of the contemporary stress field appears to show little influence from the effects of past glaciation. The maximum horizontal stress (σ_{Hmax}) in eastern Canada and Fennoscandia are ENE-NE and NW, respectively, in agreement with the direction of North Atlantic ridge-push. Thus, rebound stress appears to have little influence on contemporary seismotectonics, indicating that the dominant stress is tectonic.

On the other hand, the timing of faulting and paleoseismicity in eastern Canada and Fennoscandia correlates well with the end of deglaciation, indicating that rebound stresses may have played a more important role in earthquake generation during early postglacial time. All the postglacial faults reported from Eastern Canada and Northern Europe show reverse displacement, consistent with the fault mechanism predicted by postglacial rebound. The orientation of these faults indicates that the paleostress field was predominantly NW-SE, perpendicular to the ice margin, in eastern Canada. This is almost perpendicular to the contemporary σ_{Hmax} direction. The situation in Fennoscandia is less clear, with NNE-striking faults indicating a paleostress field that is sub-parallel to the current ridge-push stress direction. Several authors have reported spatial correlation between maximum curvature of postglacial uplift or steep gradients of uplift contours and contemporary seismicity /Basham et al. 1977; Ekman, 1988; Hasegawa and Basham, 1989/. However, seismicity is not found in association with all areas with steep uplift gradients. All modern, major earthquakes in Fennoscandia are strike-slip /Slunga, 1991/ and indicate that the contemporary stress regime is controlled by more than rebound stress alone. In fact, /Wu, 1998b/ proposes that both tectonic and rebound stresses are required to explain contemporary seismotectonics. Paleotectonics are responsible for creating the pre-weakened tectonic zones and North Atlantic ridge-push brings these faults close to failure. The stress induced by glacial unloading, although not large enough to dictate the location and style of new faults /Quinlan, 1984/, is sufficient to reactivate those existing faults that are favourably oriented with respect to the ambient stress field.

Glacial unloading stresses decrease with time and as a result at a certain time, not known, the tectonic stress dominates the stress orientation. However, this point in time is depending upon whether stored elastic strain has been released or not and on the magnitude of respective strain mechanism. GPS measurements show that the prevailing strain in the central part of the Fennoscandian uplift is extensional and generally caused by postglacial uplift (Scherneck, personal communication). Rebound stress is still of sufficient magnitude to trigger intraplate earthquakes, and is still responsible for most of the seismicity in eastern Canada and at least some of the earthquake activity in northern Europe /Wu, 1998b/.

/Wu, 1997/, /Johnston et al. 1998/, /Johnston and Lambeck, 1999/, and /Wu and Johnston 2000/ have used finite element modelling to describe the spatio-temporal distributions of stress and changes in fault stability in Eastern Canada and Fennoscandia. These studies differ from previous investigations /e.g. Walcott, 1970, 1972; Quinlan, 1984; Spada et al. 1991; James and Bent, 1994/ in that they include a viscoelastic mantle and therefore can accommodate the migration of stress associated with viscoelastic relaxation. These models also include more realistic ice sheet decay histories and sawtooth cycles of loading and unloading. The calculation of the total stress field includes contributions from rebound stress, tectonic stresses, and overburden stresses. Deviatoric stress and mean stress are used to calculate fault reactivation potential /cf Johnston, 1987; 1989a/, where a factor dFSM (change in time of the Fault Stability Margin, where FSM is the shortest distance between the Mohr circle and the failure envelope) describes the relative stability of the crust. The model considered is a compressible, stratified flat earth that contains an elastic lithosphere over isotropic, viscoelastic layers in the mantle that, in turn overlie an viscid fluid core /Wu, 1998b/. Variations in the elastic structure and viscosity profiles are considered. Lithospheric thicknesses of 100 km and 80 km are considered for North America and northern Europe, respectively. /Wu, 1998b/ demonstrates that the modelling results are not affected by the lithospheric thickness. The initial state of the Earth is assumed deglaciated, with only time-independent tectonic and loading stresses acting. Loading and unloading of the ice sheets, in addition to eustatic loading/unloading off the ocean floor are also included using the ICE3G model of Tushingham and Peltier /Peltier, 1991; Tushingham and Peltier, 1991, 1992/. Thirty glacial cycles are included before final deglaciation that began around 19 kyr BP. These glacial cycles are assumed to have a saw-tooth profile, with a slow build up of 90 kyr and a rapid decay time of 10 kyr /Wu, 1997/.

/Wu, 1998a,b/ considers two Earth models: a uniform viscosity mantle and a high viscosity lower mantle. dFSM is calculated at depths of 12.5 km. For the uniform viscosity (1×10^{21} Pa–s) mantle maximum fault stability of 14 MPa and 8 MPa for Laurentia and Fennoscandia, respectively, is promoted beneath the ice load and in the surrounding areas at the glacial maximum about 18 kyr BP. At 9 kyr BP stability is still promoted beneath the existing ice and around the peripheral bulge in Laurentia. Instabity is promoted in the deglaciated areas. In Fennoscandia at 9 kyr BP, instability is promoted beneath the remaining 300–500 m of ice cover while stability is promoted in the surrounding peripheral bulge. The early promotion of instability before the onset of complete deglaciation is a consequence of the amplification of stress as the wavelength of the load approaches the thickness of the elastic lithosphere /Johnston et al. 1998/. At present, minor fault instability is promoted in the centre of rebound in eastern Canada and northern Europe. The magnitude of this instability is probably too low to cause fracturing, but it is large enough to reactivate optimally oriented faults /Wu, 1998a,b/. The magnitude of instability calculated by /Wu, 1997, 1998a,b/ for Fennoscandia is at least twice as large as that for Laurentia. If the values of fault instability are an indicator of the magnitude of rebound stress available to trigger seismicity, then this large magnitude dFSM may explain the large throw of faults in Fennoscandia /Wu, 1998a,b/.

Their results predict a pulse of seismicity following deglaciation, with the predicted timing agreeing with that from geologic investigations in south-eastern Canada. In addition, the predicted mode of failure broadly agrees with the observed mode of thrust faulting in eastern Canada.

/Grollimund and Zoback, 2001/ used a three-dimensional finite element model to incorporate more realistic lithospheric rheologies and to explore the coupled interaction between large-scale plate forces, the stress perturbations resulting from deglaciation, and lithospheric heterogeneity. This showed that the removal of the Laurentide ice sheet changed the stress field in the vicinity of New Madrid and caused seismic strain rates to increase by approximately three orders of magnitude. Their modeling also predicts that the elevated rate seismic energy release observed during the late Holocene is likely to remain for the next few thousand years.

A3-8 Conclusions and recommendations

SKB is currently pursuing site investigations at two sites: Forsmark and Oskarshamn. Naturally, understanding of how postglacial faults form, and how they can be recognised is important so that eventual remnants of such faults can be properly detected at our sites. Furthermore, understanding of their mechanics enables us to account for such structures and design the repository accordingly.

There are numerous claims of post-glacial faults in the literature many of which have been questioned. We believe that the criteria argued for in section A3-6 provide a useful tool that should be used to recognise post-glacial faults during the site investigations. Even if we fail to detect any postglacial faults at our sites, it does not necessarily mean that such do not exist or that such cannot occur within the time frame of our interest, the next million years.

It appears increasingly clear that the size, form and temporal length of the ice sheet are the parameters that mostly determine the strain in underlying rock. There are indications that the ice was extremely thick in the northern Fennoscandia, which might influence the formation of the PGFs (Lambeck, personal communication). This could possibly explain why PGFs have only been observed in northern Fennoscandia and not in the south where the ice cover was thinner.

There are some unknown or uncertain factors that have to be regarded. For instance:

- Is it at all possible, using the latest climate and glaciation models, to produce stress fields at our site such that faulting is likely to occur during deglaciation? If so, what are the prerequisites for reactivation of faults? Ongoing modelling within the framework of SKB's safety assessment /SKB, 2004b, Section 10.1.6/ is targeting these particular questions. Using codes such as Abaqus /HKS, 2004/ and 3DEC /ITASCA, 1997/ the following analyses are planned:
  - **Basic investigations to understand the physical relationships:** 2D simulations of the response of rheologically different Earth models to simple ice load models. The influence of factors such as crustal thickness, crustal and lithospheric rheology, material failure criteria, pore pressure and initial stress state on the resulting state of stress will be analyzed. The response of the models to surface and Moho topography and inclusion of weak zones will also be tested.

- **2D simulation of northern Scandinavia:** Construction of a realistic 2D Earth model based on data from northern Scandinavia. Investigations of the importance of ice sheet geometry and evolution, failure criteria and pore pressure on the formation of postglacial faults. Sensitivity tests and validation against available stress and surface displacement data.
- **3D simulation of northern Scandinavia:** Similar to the 2D simulation but in 3D in order to model the strong 3D effects in the loading and unloading of the ice sheet.
- **Site-specific 3D simulations:** Site-specific data, such as mapped faults and rock stresses will be used together with realistic ice models to investigate the local evolution of the crustal stress field and its implications for the occurrence of postglacial faulting.

- How likely is it that extensive fracturing occurs in pristine rock? Ongoing modelling within the framework of SKB's safety assessment /SKB, 2004b, Section 10.2/ is addressing this issue.
- Can the dynamics of post glacial earthquakes be compared to contemporary earthquakes? If so, what knowledge of contemporary earthquakes can be directly applied on postglacial faults (e.g. known effects on underground constructions)?
- The geometry of known PGFs with depth is poorly constrained. Ongoing monitoring of micro-seismicity /e.g. Bödvarsson, 2004b/ might provide additional information.

A3-9 References

Adams J, 1981. Postglacial faulting: A literature survey of occurrences in Eastern Canada and comparable glaciated areas. AECL TR-142, Aecl.

Adams J, 1982. Deformed lake sediments record prehistoric earthquakes during the deglaciation of the Canadian shield. EOS, Transactions of the American Geophysical Union. Vol 63: p 436.

Adams J, Basham P W, 1989. Implications of the 1988 Saguenay earthquake for seismic hazard zoning of southeastern Canada, in Abstracts of the 84th annual meeting of the Seismological Society of America, Johnston Arch C, Editor. 1989, Seismological Society of America, Eastern Section: [El Cerrito, CA], United States. p 19.

Adams J, 1989a. Postglacial faulting in Eastern Canada; nature, origin and seismic hazard implications, in Paleoseismicity and neotectonics. Morner N A and Adams J, Editors. 1989a, Elsevier: Amsterdam, Netherlands. p 323–331.

Adams J E, 1989b. A Paleozoic-Mesozoic rift framework for earthquake hazard estimates in Eastern Canada – Incidence des fosses d'effondrement Paleozoiques et Mesozoiques sur l'estimation des dangers de seismes dans l'Est Canadien, in Geological Survey of Canada; current activities forum; program with abstracts – Commission geologique du Canada; forum des travaux en cours; programme et resumes. 1989b, Geological Survey of Canada: Ottawa ON, Canada. p 3.

Adams J, Wetmiller R J, Drysdale J, Hasegawa H S, 1991. The first surface rupture from an earthquake in eastern North America,. Current Research, Geological Survey of Canada. Vol 91-1C: p 9–15.

Adams J, Dredge L, Fenton C, Grant D R, Shilts W W, 1993a. Late Quaternary faulting in the Rouge River Valley, southern Ontario: seismotectonic or glaciotectonic? Geological Survey of Canada. Vol. Open File 2652: p 60pp.

Adams J, Dredge L A, Fenton C, Grant D R, Shilts W W, 1993b. Neotectonic faulting in metropolitan Toronto; implications for earthquake hazard assessment in the Lake Ontario region: Comment. Geology (Boulder). Vol. 21(9): p 863.

Adams J, 1996. Paeoseismology in Canada: a dozen years of progress. Journal of Geophysical Research. Vol 101: p 6193–6207.

Agassiz L, 1863. The formation of glaciers. The Atlantic Monthly. Vol 12: p 568–576.

Agassiz L, 1864a. Ice period in America. The Atlantic Monthly. Vol 14: p 86–93.

Agassiz L, 1864b. Glacial period. The Atlantic Monthly. Vol: p 224–232.

Agassiz L, 1872. On the extent of the glacial sheet. Proceedings of the Boston Society of Natural History. Vol 14: p 386.

Agassiz L, Shaler N S, Jackson C T, 1872. On glacial phenomena of the southern hemisphere compared with those of the north.

Amelung F, Galloway D L, Bell J W, Zebker H A, Laczniak R J, 1999. Sensing the ups and downs of Las Vegas: InSAR reveals structural controls of land subsidence and aquifer-system deformation. Geology. Vol 27: p 483–486.

Anderson J G, 1986. Seismic strain in the central and eastern United States. Bulletin of the Seismological Society of America. Vol 76: p 273–290.

Andrews J T, 1991. Late Quaternary glacial isostatic recovery of North America, Greenland and Iceland; a neotectonics perspective, in Neotectonics in North America, Slemmons D B, Engdahl E R, Zoback M D, and Blackwell D D, Editors. 1991, Geological Scoiety of America Decade Map: Boulder, Colorado. p 473–486.

Arvidsson R, Wahlström R, Kulhanek O, 1987. Earthquakes in northern Europe, in particular in southern Sweden and Denmark. p 10 pp, Seismological Department, Uppsala University.

Arvidsson R, Wahlström R, 1993. A review of the seismotectonics of Sweden. Svensk Kärnbränslehantering AB.

Arvidsson R, 1996. Fennoscandian earthquakes; whole crustal rupturing related to postglacial rebound. Science. Vol 274(5288): p 744–746.

Arvidsson R, 2001. Mechanics of large postglacial earthquakes caused by deglaciation. in Ten years of Paleoseismology in the ILP: progress and prospects. 2001. Kaikoura, New Zealand.

Arvidsson, pers. comm. 2001.

Aylesworth J M, Lawrence D E, Guertin J, 2000. Did two massive earthquakes in the Holocene induce widespread landsliding and near-surface deformation in part of the Ottawa Valley, Canada? Geology. Vol 28: p 903–906.

Baer G, Sandwell D, Williams S, Bock Y, Shamir G, 1999. Coseismic deformation associated with the November 1995, Mw=7.1 Nuweiba earthquake, Gulf of Elat (Aqaba), detected by synthetic aperture radar interferometry. Journal of Geophysical Research. Vol 104: p 25221–25232.

Basham P W, Forsyth D A, Wetmiller R J, 1977. The seismicity of northern Canada. Canadian Journal of Earth Sciences = Journal Canadien des Sciences de la Terre. Vol 14(7): p 1646–1667.

Becker A, Davenport C A, 2001. Contemporary in situ stress determinations at three sites in Scotland and northern England. Journal of Structural Geology. Vol v 23: p 407–419.

Bellier O, Sebrier M, 1994. Relationship between tectonism and volcanism along the Great Sumatran fault zone deduced by SPOT image analysis. Tectonophysics. Vol 233: p 215–231.

Bott M H P, 1982. The Interior of the Earth. 1982, London: Edward Arnold. p 403. ISBN.

Broster B E, Burke K B S, 1990. Glacigenic postglacial faulting at Saint John, New Brunswick. Atlantic Geology. Vol 26(2): p 125–138.

Bungum H, 1989. Earthquake occurrence and seismotectonics in Norway and surrounding areas, in Earthquakes at North-Atlantic passive margins; neotectonics and postglacial rebound, Gregersen S. and Basham P W, Editors. 1989, D Reidel Publishing Company: Dordrecht-Boston, International. p 501–519.

Bungum H, Lindholm C, 1997. Seismo- and neotectonics in Finnmark, Kola and the southern Barents Sea; Part 2, Seismological analysis and seismotectonics. Tectonophysics. Vol 270(1–2): p 15–28.

Byrkjeland U, Bungum H, Eldholm O, 2000. Seismotectonics of the Norwegian continental margin. Journal of Geophysical Research. Vol 105: p 6,221–6,236.

Bäckblom G, Stanfors R, 1989. Interdisciplinary study of post-glacial faulting in the Lansjärv area Northern Sweden 1986–1988. SKB TR 89-31, Svensk Kärnbränslehantering AB.

Bödvarsson R, 2001. Djupförvarsteknik. Swedish National Seismic Network (SNSN). A short report on recorded earthquakes during year 2001. SKB TD-02-06, Svensk Kärnbränslehantering AB.

Bödvarsson R, 2002a. Djupförvarsteknik. Swedish National Seismic Network (SNSN). A short report on recorded earthquakes during the second quarter of the year 2002. SKB TD-02-16, Svensk Kärnbränslehantering AB.

Bödvarsson R, 2002b. Swedish National Seismic Network (SNSN). A short report on recorded earthquakes during the third quarter of the year 2002. SKB P-02-04, Svensk Kärnbränslehantering AB.

Bödvarsson R, 2003a. Swedish National Seismic Network (SNSN). A short report on recorded earthquakes during the fourth quarter of the year 2002. SKB P-03-02, Svensk Kärnbränslehantering AB.

Bödvarsson R, 2003b. Swedish National Seismic Network (SNSN). A short report on recorded earthquakes during the first quarter of the year 2003. SKB P-03-37, Svensk Kärnbränslehantering AB.

Bödvarsson R, 2003c. Swedish National Seismic Network (SNSN). A short report on recorded earthquakes during the second quarter of the year 2003. SKB P-03-79, Svensk Kärnbränslehantering AB.

Bödvarsson R, 2004a. Swedish National Seismic Network (SNSN). A short report on recorded earthquakes during the first quarter of the year 2004. SKB P-04-73, Svensk Kärnbränslehantering AB.

Bödvarsson R, 2004b. Swedish National Seismic Network (SNSN). A short report on recorded earthquakes during the fourth quarter of the year 2003. SKB P-04-24, Svensk Kärnbränslehantering AB.

Carlsten S, Stråhle A, 2000. Borehole radar and BIPS investigations in boreholes at the Boda area. SKB TR-01-02, Svensk Kärnbränslehantering AB.

Chalmers R, 1897. Report on the surface geology of auriferous deposits of south-eastern Quebec. Annual Report Annual Report X, Part J, Geological Survey of Canada.

Chen R, 1992. Processing of the 1991 GPS campaigns in central Finland for crustal deformation studies. Suomen Geodeettisen Laitoksen Tiedonantoja = Reports of the Finnish Geodetic Institute. Vol 92–3. 1992, Helsinki, Finland: Suomen Geodeettinen Laitos. p 16. ISBN.

Chen R, Kakkuri J, 1993. Horizontal crustal deformations in Finland; a result from analysis of the Finnish first order triangulation, in Long-term observation of the geological environment; needs and techniques; proceedings of an NEA workshop, Anonymous, Editor. 1993, Nuclear Energy Agency: Paris, France | OECDFrance. p 171–176.

Chen R, Kakkuri J, 1994. Feasibility study and technical proposal for long-term observations of bedrock stability with GPS. Raportti – Voimayhtioiden Ydinjatetoimikunta = Report – Nuclear Waste Commission of Finnish Power Companies = Rapport – Finska Kraftbolagens Kommission for Radioaktiv Avfall. 1994, Helsinki, Finland: Imatran Voima. p 33. ISBN.

Clauss B, Marquardt G, Fuchs K, 1989. Stress orientations in the north sea and Fennoscandia, A comparison to the Central European stress field, in Earthquakes at North-Atlantic passive margins: Neotectonics and postglacial rebound, Gregersen S and Basham P, Editors. 1989, Kluwer: Dordrecht. p 277–287.

Cowie P A, Roberts G P, 2001. Constraining slip rates and spacings for active normal faults. Journal of Structural Geology. Vol 23: p 1901–1915.

Croot D G, 1987. Glacio-tectonic structures: A mesoscale model of thin-skinned thrust sheets? Journal of Structural Geology. Vol 9: p 797–808.

Croot D G, 1988. Glaciotectonics: Forms and Processes. 1988, Rotterdam: Balkema. p 212. ISBN.

Daly R A, 1934. The Changing World of the Ice Age. 1934, New York: Hafner. ISBN.

Daly R A, 1974. The Changing World of the Ice Age, in Glacial Isostasy, Early Work. 1974. p 111–121.

Davenport C A, Ringrose P S, 1987. Deformation of Scottish Quaternary sediment sequences by strong earthquake motions, in Deformation of sediments and sedimentary rocks, Jones M E and Preston M F, Editors. 1987, Geological Society of London: London, United Kingdom. p 299–314.

Dehls J F, Olesen O, Olsen L, Blikra L H, 2000. Neotectonic faulting in northern Norway: the Stuoragurra and Nordmannvikdalen postglacial faults. Quaternary Science Reviews. Vol 19: p 1,447–1,460.

Doig R, 1986. A method of determining the frequency of large-magnitude earthquakes using lake sediments. Canadian Journal of Earth Sciences. Vol 23: p 930–937.

Doig R, 1990. 2300yr history of seismicity from silting events in Lake Tadoussac, Charlevoix, Quebec. Geology. Vol 18: p 820–823.

Doig R, 1991. Effects of strong seismic shaking in lake sediments, and earthquake recurrence interval, Temiscaming, Quebec. Canadian Journal of Earth Sciences = Journal Canadien des Sciences de la Terre. Vol 28(9): p 1349–1352.

Doig R, 1998. 3000-year paleoseismological record from the region of the 1988 Saguenay, Quebec, earthquake. Bulletin of the Seismological Society of America. Vol 88: p 1198–1203.

Dredge L A, Grant D R, 1987. Glacial deformation of bedrock and sediment, Magdalen Islands and Nova Scotia, Canada: evidence for a regional grounded ice sheet, in Glaciotectonics, Tills A A and van der Meer J J M, Editors. 1987, Balkema: Rotterdam. p 183–195.

Dyke A S, Morris T F, Green D E C, 1991. Postglacial tectonic and sea level history of the central Canadian Arctic. Bulletin 397 p 49, Geological Survey of Canada.

Dyke A S, Peltier W R, 2000. Forms, response times and variability of relative sea-level curves, glaciated North America, Geomorphology. Vol 32: p 315–333.

Einarsson P, 1978. Seismological evidence for a magma chamber under Krafla central volcano and horizontal magma intrusion along the Krafla fault swarm in NE Iceland, in 1978 International symposium on the Rio Grande Rift; program and abstracts, Olsen Kenneth H and Chapin Charles E, Editors. 1978, Los Alamos Scientific Laboratory: Los Alamos, NM, United States. p 32–35.

Ekman M, 1988. Gaussian curvature of postglacial rebound and the discovery of caves created by major earthquakes in Fennoscandia. Geophysica. Vol 24: p 47–56.

Ekman M, 1996. A consistent map of the postglacial uplift of Fennoscandia. Terra Nova. Vol 8: p 158–165.

Eliasson T, Smellie J, Tullborg E-L, 1991. Mineralogical studies of the “post-glacial” fault exposed at Molberget, Lansjärv area, Northern Sweden. SKB AR 91-14, Svensk Kärnbränslehantering AB.

Fenton C, 1991a. Postglacial faulting and paleoseismic activity in North West Scotland, in Geological Society of America, 1991 annual meeting, Anonymous, Editor. 1991a, Geological Society of America (GSA): Boulder, CO, United States. p 90–91.

Fenton C, 1991b. Neotectonics and Palaeoseismicity in North West Scotland. Ph.D. University of Glasgow.

Fenton C H, 1991c. Postglacial faulting and paleoseismic activity in North West Scotland, in Geological Society of America, 1991 annual meeting, Anonymous, Editor. 1991c, Geological Society of America (GSA): Boulder, CO, United States. p 90–91.

Fenton C, 1992a. The effects of ice-cap loading on crustal stress patterns and the consequences for seismotectonic activity in the postglacial environment. Annales Geophysicae Supplement. Vol 10: p 113.

Fenton C, 1992b. Late Quaternary fault activity in north west Scotland, in Neotectonics – Recent Advances, Mörner N-A, Owen L A, Stewart I and Vita-Finzi C, Editors. 1992b, Quaternary Research Association. p 21.

Fenton C H, Olig S S, 1994. Length-displacement profiles and rates of displacement decay on surface rupturing Basin and Range normal faults; evidence for characteristic earthquakes? in Proceedings of the workshop on Paleoseismology, Prentice C S, Schwartz D P, and Yeats R S, Editors. 1994, U. S. Geological Survey: Reston, VA, United States. p 62.

Fenton C, 1994a. Paleoseismology in northwestern Europe; investigations of postglacial intraplate faulting, in Proceedings of the workshop on Paleoseismology, Prentice C S, Schwartz D P and Yeats R S, Editors. 1994a, U.S. Geological Survey: Reston, VA, United States. p 63–65.

Fenton C, 1994b. Postglacial faulting in Eastern Canada. Open-File Report – Geological Survey of Canada. 1994b, Calgary, AB, Canada: Geological Survey of Canada. p 99. ISBN.

Fenton C, 1994c. An annotated bibliography of postglacial faulting in eastern north America: the first 150 years. Bulletin of the INQUA Neotectonics Commission. Vol 17: p 61–62.

Fenton C, 1999. Glacio-isostatic (postglacial) faulting: Criteria for recognition, in Identifying Faults and Determining Their Origins, Hanson K L, Kelson K I, Angell M A and Lettis W R, Editors. 1999, U.S. Nuclear Regulatory Commission. p A-51–A-99.

Firth C R, 1986. Isostatic depression during the Loch Lomond Stadial: preliminary evidence from the Great Glen, Northern Scotland. Quaternary Newsletter. Vol. 48: p 1–9.

Firth C R, 1989. Late Devensian raised shorelines and ice limits in the inner Moray Firth area, northern Scotland. Boreas. Vol 18(1): p 5–21.

Fjeldskaar W, Lindholm C, Dehls J F, Fjeldskaar I, 2000. Postglacial uplift, neotectonics and seismicity in Fennoscandia. Quaternary Science Reviews. Vol 19: p 1413–1422.

Grant D R, 1980. Quaternary stratigraphy of southwestern Nova Scotia: glacial events and sea-level changes, Guidebook to excursion 9 p 63, Geological Association of Canada.

Grant D R, 1990. Late Quaternary movement of Aspy Fault, Nova Scotia. Canadian Journal of Earth Sciences. Vol 27: p 984–987.

Gray J M, 1974a. Lateglacial and postglacial shorelines in western Scotland. Boreas. Vol 3: p 129–138.

Gray J M, 1974b. The main rock platform of the Firth of Lorn, western Scotland. 61 p 81–99, Transactions of the Institute of British Geographers.

Gray J M, 1978. Low-level shore platforms in the south-west Scottish Highlands: altitude, age and correlation. 3 p 151–164, Transactions of the Institute of British Geographers.

Greene D, 2000. Pers comm 2000, Denison University.

Greene D C, 1996. Quaternary reactivation of the Lost Lakes fault, a brittle fault zone containing pseudotachylite in the Tuolumne intrusive suite, Sierra Nevada, California. Abstracts with Program, 28 p 70, Geological Society of America.

Gregersen S, Leth J, Lind G, Lykke-Andersen H, 1996. Earthquake activity and its relationship with geologically recent motion in Denmark. Tectonophysics. Vol 254: p 265–273.

Grollimund B, Zoback M D, 2001. Did deglaciation trigger intraplate seismicity in the New Madrid seismic zone? Geology. Vol 29: p 175–178.

Grün R, Fenton C, 1990. An ESR study of fault gouge from Holocene fault systems in Scotland. in 6th Int. Specialist Seminar on T.L. & E.S.R. Dating. 1990: Clermont-Ferrand.

Grün R, 1992. Some remarks on ESR dating of fault movements. Journal of the Geological Society of London. Vol 149: p 261–264.

Gudmundsson A, 1999. Postglacial crustal doming, stresses and fracture formation with application to Norway. Tectonophysics. Vol 307: p 407–419.

Hancock P L, Al Kadhi A, Sha'at N A, 1984. Regional joint sets in the Arabian Platform as indicators of intraplate processes. Tectonics. Vol 3: p 27–43.

Hasegawa H S, Basham P W, 1989. Spatial correlation between seismicity and postglacial rebound in Eastern Canada, in Earthquakes at North-Atlantic passive margins; neotectonics and postglacial rebound, Gregersen S, Basham P W, Editors. 1989, D Reidel Publishing Company: Dordrecht-Boston, International. p 483–500.

Henkel H, 1987. Tectonic studies in the Lansjärv region. Svensk Kärnbränslehantering AB.

Henkel H, Wållberg B, 1987. The post-glacial faults at Lansjärv. Ground geophysical measurements and interpretations in a 40x20 km surrounding area. SKB AR 88-05, Svensk Kärnbränslehantering AB.

Hicks E C, Bungum H, Lindholm C D, 2000a. Seismic activity, inferred crustal stresses and seismotectonics in the Rana region, northern Norway. Quaternary Science Reviews. Vol 19: p 1423–1436.

Hicks E C, Bungum H, Lindholm C D, Olesen O, Dehls J, 2000b. Neotectonics in Nordland, northern Norway in Neotectonics in Norway. Final Report 2000.002 p 24–32, NGU.

Hinz N H, Carson R J, Gardner T W, McKenna K, 1997. Late Quaternary deglaciation, flooding, and tectonism (?), upper Clarks Fork Valley, Park County, Wyoming. Abstracts with Program v 29 p 15, Geological Society of America.

Hitchcock C H, 1905. The geology of Littleton, New Hampshire, in History of Littleton. 1905. p 28–29.

HKS, 2004. ABAQUS, Version Hibbit, Karlsson & Sorensen, Inc. 1080 main street, Rhode island 02860-4847.

Hobbs W H, 1907. Earthquakes. 1907, New York: Appleton & Co. ISBN.

Hobbs W H, 1921. Postglacial faulting in the French River District of Ontario. American Journal of Science. Vol 1: p 507–509.

Hobbs W H, 1926. The cause of earthquakes. Annual Report p 257–277, Smithsonian Institute.

ITASCA, 1997. 3DEC, Version Itasca Geomekanik AB, Box 17, Hummelgatan 14, S-781-21 Borlänge.

Ivins E R, James T S, 1999. Simple models for late Holocene and present-day Patagonian glacier fluctuations and predictions of geodetically detectable isostatic response. Geophysical Journal International. Vol 138: p 601–624.

Jackli H C A, 1965. Pleistocene glaciation of the Swiss Alps and signs of postglacial differential uplift. Geological Society of America Special Paper. Vol 84: p 153–157.

James T, Morgan W J, 1990. Horizontal motions due to postglacial rebound. Geophysical Research Letters. Vol 17: p 957–960.

James T S, Bent A L, 1994. A comparison of eastern North American seismic strain-rates to glacial rebound strain-rates. Geophysical Research Letters. Vol 21: p 2127–2130.

James T S, Clague J J, Wang K, Hutchinson I, 2000. Postglacial rebound at the northern Cascadia subduction zone. Quaternary Science Reviews. Vol 19: p 1527–1541.

James T, 2002. Pers comm, Geological Survey of Canada.

Johansson J M, Ronnang B O, Carlsson T R, Carlsson T M, Elgered G, Jaldehag R T K, Jarlemark P O J, Nilsson B I, Scherneck H G, 1993. VLBI and GPS measurements of the Fennoscandian uplift, in Proceedings of the 9th working meeting on European VLBI for geodesy and astrometry, Campbell J and Nothnagel A, Editors. 1993, Geodaetisches Institut der Universitaet Bonn: Bonn, Federal Republic of Germany. p 49–55.

Johansson J M, Davis J L, Scherneck H G, Milne G A, Vermeer M, Mitrovica J X, Bennet R A, Ekman M, Elgered G, Elosegui P, Koivula H, Poutanen M, Rönnäng B O, Shapiro I I, 2002. Continuous GPS measurements of postglacial adjustment in Fennoscandia, 1. Geodetic results. J. Geophys. Res Vol 106 in press.

Johnston A C, 1987. Suppression of earthquakes by large continental ice sheets. Nature. Vol 303: p 467–469.

Johnston A C, 1989a. The effect of large ice sheets on earthquake genesis, in Earthquakes at North-Atlantic passive margins; neotectonics and postglacial rebound, Gregersen S and Basham Peter W, Editors. 1989a, D Reidel Publishing Company: Dordrecht-Boston, International. p 581–599.

Johnston A C, 1989b. The size of the 1811–12 New Madrid earthquakes; a reappraisal, in Geological Society of America, 1989 annual meeting, Anonymous, Editor. 1989b, Geological Society of America (GSA): Boulder, CO, United States. p 186.

Johnston A C, Coppersmith K J, Kanter L R, Cornell C A, 1994. The earthquakes of stable continental regions, Volume 1: Assessment of large earthquake potential. Technical Report TR-102261-V1 p 368, Electric Power Research Institute.

Johnston A C, 1996. Seismic movement assessment of earthquakes in stable continental regions; III, New Madrid 1811–1812, Charleston 1886 and Lisbon 1755. Geophysical Journal International. Vol 126(2): p 314–344.

Johnston P, Wu P, Lambeck K, 1998. Dependence of horizontal stress magnitude on load dimension in glacial rebound models. Geophysical Journal International. Vol 132(1): p 41–60.

Johnston P, Lambeck K, 1999. Postglacial rebound and sea level contributions to changes in the geoid and the Earth's rotation axis. Geophysical Journal International. Vol 136(3): p 537–558.

Jones S, 1996. Late Quaternary faulting and neotectonics. South Victoria Land, Antarctica. Journal of the Geological Society of London. Vol 153: p 645–653.

Jull M, McKenzie D, 1996. The effect of deglaciation on mantle melting beneath Iceland. Journal of Geophysical Research, B, Solid Earth and Planets. Vol 101: p 21815–21828.

Kakkuri J, Chen R, 1992. On horizontal crustal strain in Finland. Bulletin Geodesique. Vol 66(1): p 12–20.

Kanamori H, Anderson D, 1977. Theoretical basis of some empirical relations in seismology. Bull. Seismol Soc Am. Vol 65: p 1073–1095.

Kenner S J, Segall P, 2000. A mechanical model for intraplate earthquakes: Application to the New Madrid seismic zone. Science. Vol 289: p 2329–2332.

Knight J, 1999. Geological evidence for neotectonic activity during deglaciation of the southern Sperrin Mountains, Northern Ireland. Journal of Quaternary Science. Vol 14: p 45–57.

Koteff C, Robinson G R, Goldsmith R, Thompson W B, 1993. Delayed posglacial uplift and synglacial sea levels in coastal central New England. Quaternary Research. Vol 40: p 46–54.

Kuivamäki A, 1986. Havaintoja Venejarven ja Ruosterjarven postglasiaalisista siirroksista Translated Title: Observations on the Venejarvi and Ruostejarvi postglacial faults. Tiedonanto YST. 1986, Espoo, Finland: Geologian Tutkimuskeskus, Ydinjatteiden Sijoitustutkimukset. p 20. ISBN.

Kuivamäki A, Vuorela P, Paananen M, 1998. Indications of postglacial and recent bedrock movements in Finland and Russian Karelia. Report YST-99, Geological Survey of Finland Nuclear Waste Disposal Research Espoo Finland.

Kujansuu R, 1964. Nuorista siirroksista Lapissa. (Recent Faulting in Lapland). Geologi Vsk. Vol 16: p 30–36.

La Touche T D, 1897. India Geological Survey

Lagerbäck R, 1979. Neotectonic structures in northern Sweden, In: Geologiska Föreningens i Stockholm Förhandlingar Vol 100(1978) Pt. 3 pp 263–269: Sveriges geologiska undersökning, Uppsala, Sweden.

Lagerbäck R, Witshard F, 1983. Neotectonics in northern Sweden – geological investigations. SKBF/KBS TR 83-58, Skbf/Kbs.

Lagerbäck R, 1988. Postglacial faulting and paleoseismicity in the Landsjärv area, northern Sweden. SKB TR 88-25, Svensk Kärnbränslehantering AB.

Lagerbäck R, 1990. Late Quaternary faulting and paleoseismicity in northern Fennoscandia, with particular reference to the Lansjaerv area, northern Sweden. Geologiska Föreningen i Stockholm Förhandlingar. Vol. 112(Part 4): p 333–354.

Lagerbäck R, 1991. Seismically deformed sediments in the Lansjärv area, Northern Sweden. SKB TR 91-17, Svensk Kärnbränslehantering AB.

Lagerbäck R, 1992. Dating of Late Quaternary faulting in northern Sweden. Journal of the Geological Society of London. Vol 149: p 285–291.

Lagerbäck R, Sundh M, 2003. Forsmark site investigation. Searching for evidence of late- or post-glacial faulting in the Forsmark region. Results from 2002. SKB P-03-76, Svensk Kärnbränslehantering AB.

Lambeck K, Smither C, Ekman M, 1998. Tests of glacial rebound models for Fennoscandia based on instrumental sea and lake level records. Geophys. J. Int. Vol 135: p 375–387.

Lindström M, Lundqvist J, Lundqvist T, 2000. Sveriges geologi från urtid till nutid, 2:a uppl 2000, Sweden: Studentlitteratur Lund. ISBN.

Lukashov A D, 1995. Paleoseismotectonics in the northern part of Lake Onega (Zaonezhskij peninsula, Russian Karelia). Report YST-90, Geological Survey of Finland Nuclear Waste Disposal Research Espoo Finland.

Lundqvist J, Lagerbäck R, 1976. The Pärve Fault: A late-glacial fault in the Precambrian of Swedish Lapland. GFF. Vol 98(1): p 45–51.

Mather W W, 1843. Geology of New York, Part 1, comprising geology of the first geological district. 1843. p 653. ISBN.

Matthew G F, 1894a. Postglacial faults at Saint John, N. B. American Journal of Science. Vol 48: p 501–503.

Matthew G F, 1894b. Movements of the earth's crust at Saint John, N B, in postglacial times.

McCalpin J P, 1996. Using GIS to predict zones of earthquake-induced landsliding in Seattle, Washington, in Geological Society of America, 28th annual meeting, Anonymous, Editor. 1996, Geological Society of America (GSA): Boulder, CO, United States. p 526.

McCalpin J, 1999. Criteria for determining the seismic significance of sackungen and other scarplike landforms in mountainous regions, in Identifying Faults and Determining Their Origins, Hanson K L, Kelson K I, Angell M A and Lettis W R, Editors. 1999, U.S. Nuclear Regulatory Commission. p A-120–A-142.

Meigs A, Sauber J, 2000. Southern Alaska as an example of long-term consequences of mountain building under the inluence of glaciers. Quaternary Science Reviews. Vol. 19: p 1543–1562.

Miller W G, 1913. The cobalt-nickel arsenides and silver deposits of Temiskaming (Cobalt and adjacent areas). Annual Report – Ontario Department of Mines. 1913, Toronto, ON, Canada: Ontario Department of Mines. p 279. ISBN.

Milne G A, Davis J L, Mitrovica J X, Scherneck H-G, Johansson J M, Vermeer M, 2001. A of 3-D crustal deformation in Fennoscandia emerges from a network of GPS measurements. Science Vol 291: p 2382–2385.

Milne G A, Mitrovica J X, Scherneck H-G, Davis J L, Johansson J M, Koivula H, Vermeer M, 2004. Continuous GPS measurements of postglacial adjustment in Fennoscandia: 2. Modeling results. J Geophys Res Vol 109.

Mohajer A, Eyles N, Rogojina C, 1992. Neotectonic faulting in metropolitan Toronto; implications for earthquake hazard assessment in the Lake Ontario region. Geology (Boulder). Vol 20(11): p 1003–1006.

Mohr P, 1986. Possible Late Pleistocene faulting in Iar (west) Connacht, Ireland, Geological Magazine. Vol 123: p 545–552.

Morén L, Påsse T, 2001. Climate and shoreline in Sweden during Weichsel and the next 150,000 years. SKB TR-01-19, Svensk Kärnbränslehantering AB.

Muir Wood R, 1989a. Extraordinary deglaciation reverse faulting in northern Fennoscandia, in Earthquakes at North-Atlantic passive margins; neotectonics and postglacial rebound, Gregersen S and Basham P W, Editors. 1989a, D Reidel Publishing Company: Dordrecht-Boston, International. p 141–173.

Muir Wood R, 1989b. Fifty million years of "passive margin" deformation in North west Europe, in Earthquakes at North-Atlantic passive margins; neotectonics and postglacial rebound, Gregersen S and Basham Peter W, Editors. 1989b, D Reidel Publishing Company: Dordrecht-Boston, International. p 7–36.

Muir Wood R. 1993. A review of the seismotectonics of Sweden. SKB TR 93-13, Svensk Kärnbränslehantering AB.

Muir Wood R, 1995. Reconstructing the tectonic history of Fennoscandia from its margins: The past 100 million years. SKB TR 95-36, Svensk Kärnbränslehantering AB.

Munier R, 1993. Segmentation, fragmentation and jostling of the Baltic shield with time. Doctoral thesis. Uppsala University.

Müller B, Zoback M-L, Fuchs K, Mastin L, Gregersen S, Pavoni N, Stephansson O, Ljungren C, 1992. Regional patterns of Tectonic stress in Europe, J Geoph Res Vol 97(B8): p 11783–11803.

Mörner N-A, 1989. Postglacial faults and fractures on Äspö. SKB HRL Progress report 25-89-24, Svensk Kärnbränslehantering AB.

Mörner N-A, Tröften P-E, 1993. Palaeoseismotectonics in glaciated cratonal Sweden, In: Zeitschrift für Geomorphologie N F. Suppl -Bd. 94 pp 107–117

Mörner N-A, Tröften P E, Sjöberg R, Grant D, Dawson S, Bronge C, Kvamsdal O, Sidèn A, 2000. Deglacial paleoseismicity in Sweden: the 9663 BP Iggesund event. Quaternary Science Reviews. Vol 19: p 1461–1468.

Mörner N-A, 2003. Paleoseismicity of Sweden – a novel paradigm. 2003. ISBN 91-631-4072-1.

Neale E R W, 1963a. Geology, Dingwall, Cape Breton Island, Nova Scotia. Map 119A, Geological Survey of Canada.

Neale E RW, 1963b. Geology, Pleasant Bay, Nova Scotia. Map 1124A, Geological Survey of Canada.

Neale E R W, 1964. Geology, Cape North, Nova Scotia. Map 1150A, Geological Survey of Canada.

NEIC, 2004. Earthquake search. USGS National Earthquake Information Center. http://wwwneic.cr.usgs.gov/.

NGDC, 2004. National Geophysical Data Center. NOAA, Mail Code E/GC, 325 Broadway, Boulder, CO, 80305-3328, USA ngdc.info@noaa.gov.

Nisca D H, 1987. Aeromagnetic interpretation. SKB HRL Progress report 25-87-23, Svensk Kärnbränslehantering AB.

Nisca D H, Triumf C-A, 1989. Detailed geomagnetic and geoelectric mapping of Äspö. SKB HRL Progress report 25-89-01, Svensk Kärnbränslehantering AB.

Nissen J, 2003. Forsmark site investigation. Ground penetrating radar and resistivity measurements for overburden investigations. SKB P-03-43, Svensk Kärnbränslehantering AB.

Noller J S, Sowers J M, Lettis W R, 2000. Quaternary Geochronology: Methods and Applications. p 582, American Geophysical Union.

Olesen O, Lile O B, Henkel H, Ronning J S, Dalsegg E, 1989. Geophysical investigations of the postglacial Stuoragurra Fault, Finnmark, northern Norway, in 17th meeting of the Nordic Association for Applied Geophysics, Anonymous, Editor. 1989, Elsevier: Amsterdam, Netherlands. p 62–63.

Olesen O, Dehls J, Bungum H, Riis F, Hicks E, Lindholm C, Blikra L H, Fjeldskaar W, Olsen L, Longva O, Faleide J I, Bockmann L, Rise L, Roberts D, Braathen A, Brekke H, 2000. Neotectonics in Norway. Final report, 2000.02, Geological Survey of Norway.

Olesen O, Henkel H, Lile O B, Mauring E, Ronning, J S, 1992a. Geophysical investigations of the Stuoragurra postglacial fault, Finnmark, northern Norway. Journal of Applied Geophysics. Vol 29(2): p 95–118.

Olesen O, Henkel H, Lile O B, Mauring E, Ronning J S, Torsvik T H, 1992b. Neotectonics in the Precambrian of Finnmark, northern Norway, in Post-Cretaceous uplift and sedimentation along the western Fennoscandian Shield, Jensen L N, Riis F, and Boyd R, Editors. 1992b, Universitetsforlaget: Oslo, Norway. p 301–306.

Oliver J, Johnson T, Dorman J, 1970. Postglacial faulting and seismicity in New York and Quebec, in Symposium on recent crustal movements. 1970, National Research Council of Canada: Ottawa, ON, Canada. p 579–590.

Paananen M, 1987. Geophysical studies of the Venejärvi, Ruostejärvi, Suasselkä and Pasmajärvi postglacial faults in northern Finland. YST-59, Geological Survey of Finland Nuclear Waste Disposal Research Espoo.

Peltier W R, 1991. The ICE-3G model of late Pleistocene deglaciation; construction, verification and applications, in Glacial isostasy, sea-level and mantle rheology, Sabodini R, Lambeck K and Boschi E, Editors. 1991, D Reidel Publishing Company: Dordrecht-Boston, International. p 95–119.

Poutanen M, Ollikainen M, 1995. GPS measurements at the Nuottavaara post glacial fault. Suomen Geodeettisen Laitoksen Tiedonantoja = Reports of the Finnish Geodetic Institute. Vol 95:6. 1995, Helsinki, Finland: Suomen Geodeettinen Laitos. p 24. ISBN.

Påsse T, 1996. Lake-tilting investigations in southern Sweden. SKB TR 96-10, Svensk Kärnbränslehantering AB.

Påsse T, 2001. An empirical model of glacio-isostatic movements and shore-level displacement in Fennoscandia. SKB Rapport R-01-41, Svensk Kärnbränslehantering AB.

Quinlan G M, 1984. Postglacial rebound and the focal mechanisms of eastern Canadian earthquakes. Canadian Journal of Earth Sciences = Journal Canadien des Sciences de la Terre. Vol 21(9): p 1018–1023.

Reinecker J, Heidbach O, Tingay M, Connolly P, Müller B, 2004. The 2004 release of the World Stress Map. www.world-stress-map.org.

Ringrose P S, 1987. Fault activity and palaeoseismicity during Quaternary time in Scotland. Ph.D. University of Strathclyde.

Ringrose P S, 1989a. Recent fault movement and palaeoseismicity in western Scotland, in Paleoseismicity and neotectonics, Morner Nils A and Adams J, Editors. 1989a, Elsevier: Amsterdam, Netherlands. p 305–314.

Ringrose P S, 1989b. Palaeoseismic (?) liquefaction event in late Quaternary lake sediments at Glen Roy, Scotland, Terra Nova. Vol 1: p 57–62.

Ringrose P S, Hancock P, Fenton C, Davenport C A, 1991. Quaternary tectonic activity in Scotland, in Proceedings of the 25th annual conference of the Engineering Group of the Geological Society; Quaternary engineering geology, Forster A, Culshaw M G, Cripps J C, Little J A and Moon C F, Editors. 1991, Geological Society of London: London, United Kingdom. p 679–686.

Ringrose P S, Migon P, 1997. Analysis of digital elevation data from the Scottish Highlands and recognition of pre-Quaternary elevated surfaces, in Palaeosurfaces; recognition, reconstruction and palaeoenvironmental interpretation, Widdowson M, Editor. 1997, Geological Society of London: London, United Kingdom. p 25–35.

Saari J, 1992. A review of the seismotectonics of Finland. YJT-92-29, Nuclear Waste Commission of Finnish Power Companies (YJT).

Sauber J, Plafker G, Molina B F, Bryant M A, 2000. Crustal deformation associated with glacial fluctuations in the eastern Chugach Mountains, Alaska. Journal of Geophysical Research, B, Solid Earth and Planets. Vol 105: p 8055–8077.

Scherneck H-G, Johansson J M, Elgered G, 1996. Application of space geodetic techniques for the determination of intraplate deformations and movements in relation with the postglacial rebound of Fennoscandia. SKB TR 96-19, Svensk Kärnbränslehantering AB.

Scherneck H G, Johansson J M, Elgered G, Davis J L, Jonsson B, Hedling G, Kovula H, Ollikainen M, Poutanen M, Vermeer M, Mitrovica J X, Milne G A, 2002. BIFROST: Observing the Three-Dimensional deformation of Fennoscandia, in Ice Sheets, Sea Level and the Dynamic Earth, Mitrovica J X, Editor. 2002, AGU: Washington DC. p 69–93.

Scholz C H, 1990. The mechanics of earthquakes and faulting. 1990, USA: Cambridge University Press USA. ISBN.

Schroeder J, Beaupre M, Cloutier M, 1986. Ice-push caves in platform limestones of the Montreal area. Canadian Journal of Earth Sciences = Journal Canadien des Sciences de la Terre. Vol 23(11): p 1842–1851.

Seeber L, Armbruster J G, 1993. Natural and induced seismicity in the Lake Erie-Lake Ontario region; reactivation of ancient faults with little neotectonic displacement, in Neotectonics of the Great Lakes area, Wallach J L and Heginbottom J A, Editors. 1993, Presses de l'Universite de Montreal: Montreal, PQ, Canada. p 363–378.

Shilts W W, 1984. Sonar evidence for postglacial tectonic instability of the Canadian Shield and Appalachians. Paper – Geological Survey of Canada. Vol 84–1a: p 567–579.

Shilts W W, Clague J J, 1992. Documentation of earthquake-induced disturbance of lake sediments using subbottom acoustic profiling. Canadian Journal of Earth Sciences = Journal Canadien des Sciences de la Terre. Vol 29(5): p 1018–1042.

Shilts W W, Rappol M, Blais A, 1992. Evidence of late and postglacial seismic activity in the Temiscouata-Madawaska Valley, Quebec-New Brunswick, Canada. Canadian Journal of Earth Sciences = Journal Canadien des Sciences de la Terre. Vol 29(5): p 1043–1069.

Shilts W W, Rappol M, Blais A, 1993. Erratum; Evidence of late and postglacial seismic activity in the Temiscouata-Madawaska Valley, Quebec-New Brunswick, Canada. Canadian Journal of Earth Sciences = Journal Canadien des Sciences de la Terre. Vol 30(1): p 201.

Sigmundsson F, Einarsson P, 1992. Glacio-isostatic crustal movements caused by historical volume change of the Vatnajoekull ice cap, Iceland. Geophysical Research Letters. Vol 19(21): p 2123–2126.

Sims J D, 1975. Determining earthquake recurrence intervals from deformational structures in young lacustrine sediments. Tectonophysics. Vol. 29(Recent crustal movements): p 141–152.

Sissons J B, 1972. Dislocation and non-uniform uplift of raised shorelines in the western part of the Forth Valley. Transactions, Institute of British Geographers. New Series. Vol 55: p 145–159.

Sissons J B, Cornish R, 1982a. Rapid localized glacio-isostatic uplift at Glen Roy, Scotland. Nature (London). Vol 297(5863): p 213–214.

Sissons J B, Cornish R, 1982b. Differential glacio-isostatic uplift of crustal blocks at Glen Roy, Scotland. Quaternary Research (New York). Vol 18(3): p 268–288.

Sjöberg R, 1994. Bedrock caves and fractured rock surfaces in Sweden. Occurrence and origin, Paleogeophysics & Geodynamics Stockholm University Stockholm Sweden:

SKB, 1990. Granskning av Nils-Axel Mörners arbete avseende postglaciala strukturer på Äspö. SKB AR 90-18, Svensk Kärnbränslehantering AB.

SKB, 2004a. Preliminary site description Forsmark area – version 1.1. SKB R-04-15, Svensk Kärnbränslehantering AB.

SKB, 2004b. Interim main report of the safety assessment SR-Can. SKB TR-04-11, Svensk Kärnbränslehantering AB.

Slunga R, Norrman P, Glans A-C, 1984. Seismicity of Southern Sweden. FOA Rapport C2 C 20543-T1, National Defence Research Institute (FOA) Dept. 2 Stockholm.

Slunga R S, 1991. The Baltic Shield earthquakes. Tectonophysics. Vol 189(1–4): p 323–331.

Smith D G, Jol H M, 1995. Wasatch Fault (Utah), detected and displacement characterized by ground penetrating radar. Environmental & Engineering Geoscience. Vol 1(4): p 489–496.

Sollid J L, Sorbel L, Tolgensbakk J, 1988. Rock glaciers in Norway, Svalbard included, in Permafrost, fifth international conference, Senneset, K, Editor. 1988, (publisher varies): (location varies), International. p 64.

Sowers J M, Noller J S, Lettis W R, 1998. Dating and earthquakes: Review of Quaternary geochronology and its application to paleoseismology. NUREG CR-5562, US Nuclear Regulatory Commission.

Spada G, Sabadini R, Yuen D A, 1991. Viscoelastic responses of a hard transition zone; effects on postglacial uplifts and rotational signatures. Earth and Planetary Science Letters. Vol 105(4): p 453–462.

Stein S, Cloetingh S, Sleep N H, Wortel R, 1989. Passive margin earthquakes, stresses and rheology, in Earthquakes at North-Atlantic passive margins; neotectonics and postglacial rebound, Gregersen, S. and Basham, P.W, Editors. 1989, D. Reidel Publishing Company: Dordrecht-Boston, International. p 231–259.

Stewart I S, Firth C R, Rust D J, Walker A B, 1999. Interactions between glacial unloading, postglacial faulting and present-day seismcity in the Scottish Highlands in European Geophysical Union 10. 1999. Strasbourg.

Stewart I S, Sauber J, Rose J, 2000. Glacio-seismotectonics: ice-sheets, crustal deformation and seismicity: Quaternary Science Reviews. Vol 19: p 1367–1389.

Sykes L R, 1971. Post-glacial faulting in competent rock in the Saint Lawrence seismic zone of New York State. Earthquake Notes. Vol 42(3–4): p 15.

Tanner V, 1930. Studier över kvartärsystemet i Fennoskandias nordliga delar IV. Bulletin de la Commission Géologique de Finlande. Vol 88: p 594 pp.

Thorson R M, 1996. Earthquake recurrence and glacial loading in western Washington. Geological Society of America Bulletin. Vol 108(9): p 1182–1191.

Tirén S A, Beckholmen M, Isaksson H, 1987. Structural analysis of digital terrain models, Simpevarp area, South-Eastern Sweden. Method study EBBA II. SKB HRL Progress report 25-87-21, Svensk Kärnbränslehantering AB.

Tirén S A, Beckholmen M, 1988. Structural analysis of contoured maps. Äspö and Ävrö, Simpevarp area, Southeastern Sweden. SKB HRL Progress report 25-87-22, Svensk Kärnbränslehantering AB.

Tröften P E, Mörner N A, 1997. Varved clay chronology as a means of recording paleo-seismic events in southern Sweden, in Paleoseismology; understanding past earthquakes using Quaternary geology, Hancock Paul L and Michetti Alessandro M, Editors. 1997, Pergamon Press: Oxford – New York, International. p 249–258.

Tullborg E-L, Larson S Å, Morad S, 2001. Dating methods and geochronology of fractures and movements in bedrock: a review. SKB R-01-25, Svensk Kärnbränslehantering AB.

Tushingham A M, Peltier W R, 1991. ICE-3G; a new global model of late Pleistocene deglaciation based upon geophysical predictions of post-glacial relative sea level change. Journal of Geophysical Research, B, Solid Earth and Planets. Vol 96(3): p 4497–4523.

Tushingham A M, Peltier W R, 1992. Validation of the ICE-3G model of Wuerm-Wisconsin deglaciation using a global data base of relative sea level histories. Journal of Geophysical Research, B, Solid Earth and Planets. Vol 97(3): p 3285–3304.

Wahlström R, Linder S-O, Holmqvist C, 1987. Near-distance seismological monitoring of the Lansjärv neotectonic fault region. SKB TR 88-12, Svensk Kärnbränslehantering AB.

Wahlström R, 1988. Earthquake dynamics and seismotectonics in the Baltic Shield, in Abstracts; Thrust tectonics in Fennoscandia; Tornebohm memorial meeting; annual meeting 1988 of the Geological Society of Sweden. 1988, Lunds Univ, Geol Inst Lund, Sweden. p 25.

Wahlström R, Linder S-O, Holmqvist C, Mårtensson H-E, 1989. Near-distance seismological monitoring of the Lansjärv neotectonic fault region. Part II: 1988. SKB TR 89-01, Svensk Kärnbränslehantering AB.

Wahlström R, 1995, Earthquake-generating hypotheses for Fennoscandia, in International Union of Geodesy and Geophysics; XXI general assembly; abstracts, Anonymous, Editor. 1995, (publisher varies): (location varies), International. p 360–361.

Walcott R I, 1970. Flexural rigidity, thickness, and viscosity of the lithosphere. Journal of Geophysical Research. Vol 75(20): p 3941–3954.

Walcott R I, 1972. Flexural Rigidity, Thickness, and Viscosity of the Lithosphere, in Plate Tectonics. 1972, American Geophysical Union: Washington, DC, United States. p 281–294.

Wallach J L, Mohajer A A, McFall G H, Bowlby J R, Pearce M, McKay D A, 1993. Pop-ups as geological indicators of earthquake-prone areas in intraplate eastern North America, in Neotectonics; Recent advances, Owen L A, Stewart I and Vita Finzi C, Editors. 1993, Quaternary Research Association: Cambridge, United Kingdom. p 67–83.

Vanneste K, Meghraoui M, Camelbeek T, 1999. Late Quaternary earthquake-related soft-sediment deformation along the Belgian portion of the Feldbiss fault, lower Rhine Graben system, Tectonophysics. Vol 309: p 57–79.

Weber J, 1975. Magnitude of global sea level changes over the past 17,000 years, in Northeastern Section, 10th Annual Meeting. 1975, Geological Society of America (GSA): Boulder, CO, United States. p 132.

Wilson A W G, 1902. Some recent folds in the Lorraine shales.

Woodworth J B, 1905. Ancient water levels of the Champlain and Hudson valleys [New York]. Bulletin of the New York State Museum. 1905, Albany, NY, United States: New York State Museum. p 265. ISBN.

Woodworth J B, 1907. Postglacial faults of eastern New York. Bulletin of the New York State Museum. Vol p 5–28.

Wu P, 1997. Effect of viscosity structure on fault potential and stress orientations in eastern Canada. Geophysical Journal International. Vol 130: p 365–382.

Wu P, 1998a. Will earthquake activity in Eastern Canada increase in the next few thousand years? Canadian Journal of Earth Sciences = Revue Canadienne des Sciences de la Terre. Vol 35(5): p 562–568.

Wu P, 1998b. Intraplate earthquakes and postglacial rebound in eastern Canada and northern Europe, in Dynamics of the Ice Age Earth: A Modern Perspective, Wu P, Editor. 1998b, Trans Tech Publications. p 603–628.

Wu P, Johnston P, 2000. Can deglaciation trigger earthquakes in N. America? Geophysical Research Letters. Vol 27(9): p 1323–1326.

Vuorela P, Kuivamäki A, Paananen M, 1987. Neotectonic bedrock movements. A preliminary survey of the Pasmajärvi fault. YST-57, Geological Survey of Finland Nuclear Waste Disposal Research Espoo.

Wänstedt S, 2000. Geophysical and geological investigations of the Boda area. SKB R-00-23, Svensk Kärnbränslehantering AB.